Human research ethics during commercial spaceflight p. 1408

Lessons from 30 years of genetics in Darwin's finches p. 1427

Solid delivery of gaseous fluorocarbons p. 1455

Science

$15
29 SEPTEMBER 2023
SPECIAL ISSUE
science.org
AAAS

HEAT AND HEALTH

Global warming's toll on the body p. 1386

SPARK the solutions for **TOMORROW.**

AAAS has been a leading voice for science for 175 years, and we've just begun.

Scan the QR code to donate today!

In honor of our anniversary, **help us shape the course of science and society for years to come** by making a generous, tax-deductible gift to the AAAS Catalyst Fund today.

aaas.org/**ignite**

CALL FOR PAPERS

SPJ
SCIENCE PARTNER JOURNALS

spj.science.org/bmef

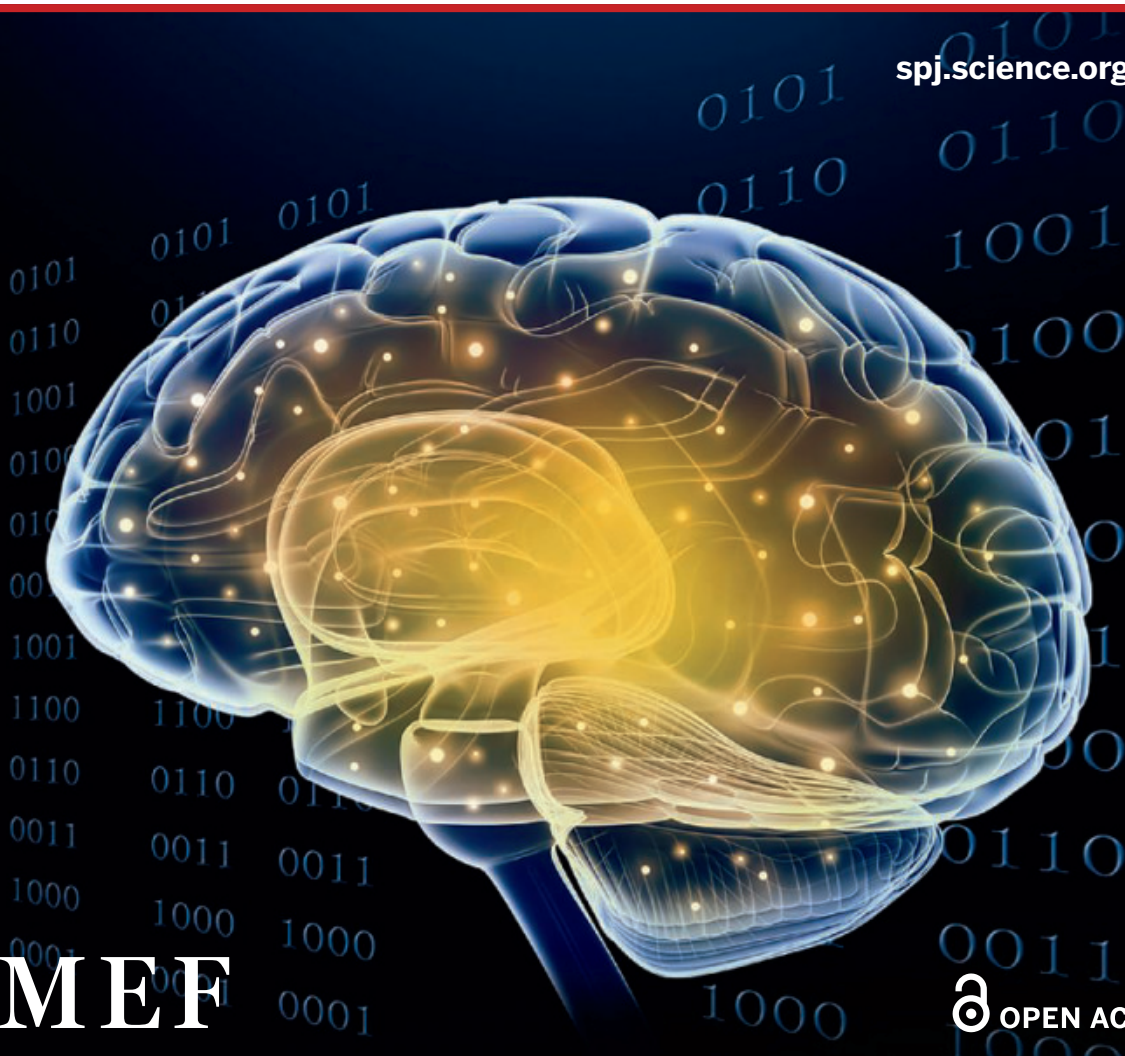

BMEF

OPEN ACCESS

BMEF is a **Science Partner Journal** distributed by the **American Association for the Advancement of Science** (AAAS) in collaboration with the **Suzhou Institute of Biomedical Engineering and Technology, Chinese Academy of Sciences** (SIBET CAS). *BMEF* serves the multidisciplinary community of biomedical engineering by publishing breakthrough original Research Articles, Rapid Reports, Reviews, Perspectives, and Editorials. The journal also publishes research in the fields of pathogenic mechanisms as well as disease prevention, diagnosis, treatment, and assessment.

The Science Partner Journals (SPJ) program was established by the American Association for the Advancement of Science (AAAS), the nonprofit publisher of the *Science* family of journals. The SPJ program features high-quality, online-only, open access publications produced in collaboration with international research institutions, foundations, funders and societies. Through these collaborations, AAAS expands its efforts to communicate science broadly and for the benefit of all people by providing top-tier international research organizations with the technology, visibility and publishing expertise that AAAS is uniquely positioned to **offer as the world's largest general science membership society**.

Submit your research to *BMEF* today!
Learn more at: **spj.science.org/bmef**

ARTICLE PROCESSING CHARGES WAIVED UNTIL 2023

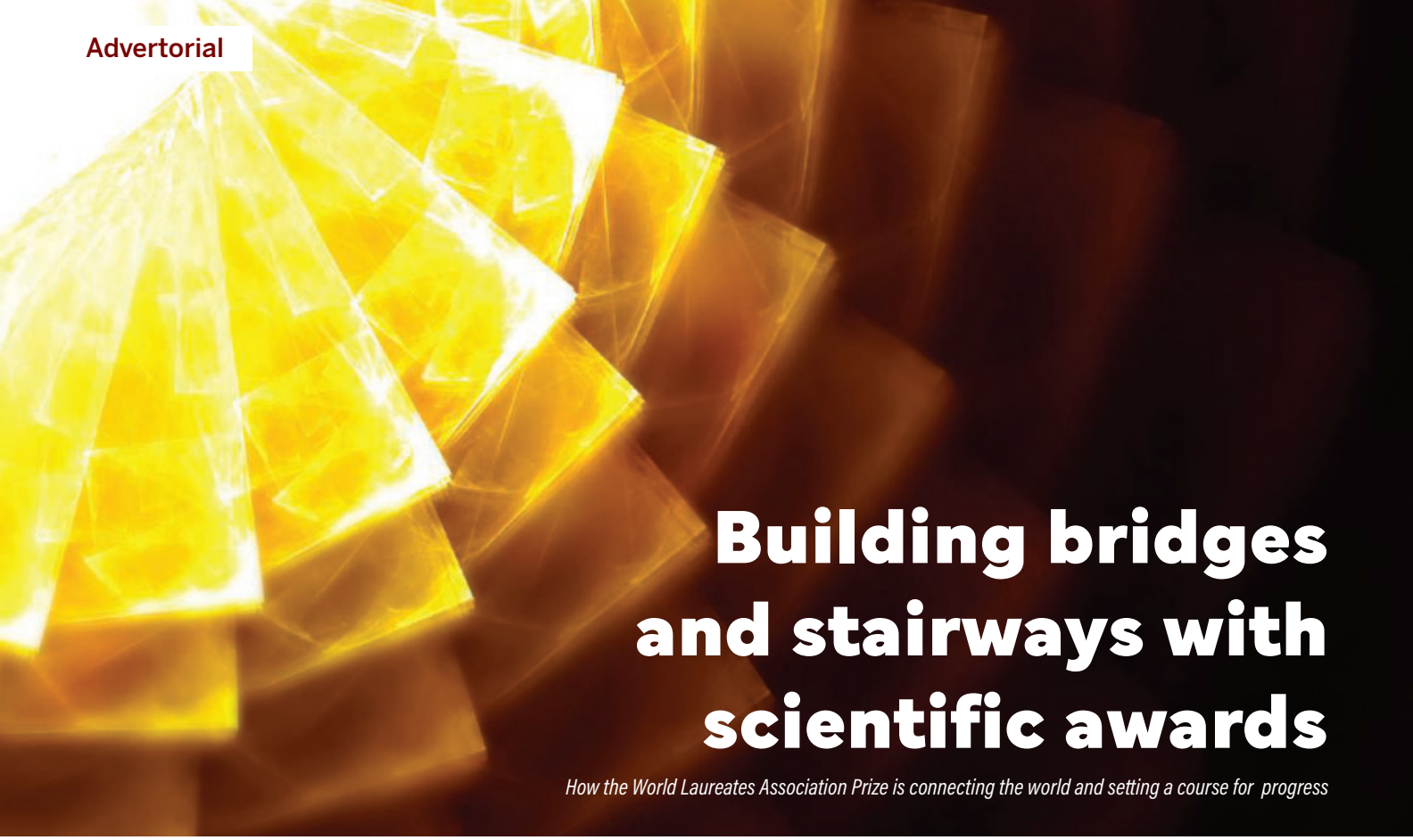

Building bridges and stairways with scientific awards

How the World Laureates Association Prize is connecting the world and setting a course for progress

Scientific progress has immeasurable value for human health and happiness. However, there is often too little recognition for the scientists whose hard work drives that progress forward. Except for a few household names like the Nobel Prize, most scientific awards are unfamiliar to those outside the field they celebrate. Prizes foster a spirit of friendly competition, build community, and reward researchers whose world-changing accomplishments would otherwise go unknown to the public. They shape science, says Ada Yonath, an Israeli chemist and Nobel laureate crystallographer best known for her pioneering work on the structure of ribosomes, by sharing the creativity, impact, and excitement of recent and longstanding advances "with a wide range of individuals."

The founders of the non-governmental and non-profit international organization World Laureates Association (WLA), mostly winners of prestigious science prizes such as the Nobel Prize, felt that there were vast gaps in the geographic and subject matter landscapes of scientific awards. So, in 2021, they introduced the World Laureates Association Prize (WLA Prize). The prize covers two categories—Computer Science or Mathematics, and Life Science or Medicine—that both offer an RMB 10 million (USD 1.4 million) cash prize.

"The WLA Prize acknowledges leadership, cooperativity, professionalism, and diversity as fundamental aspects of excellence, points that are less emphasized, hence maybe underpaid by other prizes," says Yonath.

Recognizing international collaboration

In addition to the broad gaps in scientific awards, there are also specific disparities between nations. Most existing awards come out of North America or Europe, with a smaller number coming from Asia.

"The overarching goal of the WLA is to build a bridge between Asia, America, and West Europe to nurture essential international collaborations in spite of political differences," says Randy Schekman, Chair of the 2023 WLA Prize Selection Committee in Life Science or Medicine and 2013 Nobel Physiology or Medicine laureate. "We feel very strongly that science is an international activity."

The 2023 WLA Prize in Computer Science or Mathematics was awarded jointly to:

Arkadi Nemirovski,
Georgia Institute of Technology, USA

Yurii Nesterov,
Université Catholique de Louvain, Belgium

For their seminal work in convex optimization theory, including the theory of self-concordant functions and interior-point methods, a complexity theory of optimization, accelerated gradient methods, and methodological advances in robust optimization.

IMAGE:© R.T. WOHLSTADTER/SHUTTERSTOCK.COM; PHOTO: COURTESY OF THE WLA PRIZE

In an era when scientific endeavors transcend borders, the WLA Prize seeks to recognize the contributions of scientists from all over the world, says Michael I. Jordan, the UC Berkeley professor who chairs the WLA Prize Selection Committee this year for the Computer Science or Mathematics category. He was also the inaugural prize laureate in the same category for his research on the foundations and applications of machine learning.

By bringing together scientists from around the world, the prize hopes to create a platform for exchange and collaboration. That focus on international cooperation underscores the interconnectedness of scientific progress, Jordan says. "The WLA Prize aims to have a broader vista," he adds.

Spotlight on emerging disciplines

To avoid piling attention onto scientists whose work has already been widely recognized, the WLA Prize rules specifically exclude from consideration those who have already won top-tier awards. Instead, the prize committees must find emerging scientists in less visible fields.

"Too many prize committees are looking to identify someone who they think will go on to win the Nobel Prize," says Schekman. "That, unfortunately, overemphasizes certain areas of science at the expense of other achievements that have been overlooked."

Theoretical mathematics is a good example. Long regarded as a prestigious discipline, it tends to outshine the newer field of computer science. Rather than see them as separate, the WLA Prize highlights the fascinating intersection of mathematics and computer science. "It's a very interesting and thoughtful choice," Jordan says. By acknowledging the historical connection between these fields, from the genesis of computer science in the deductive branch of mathematics, to the shared emphasis in recent years on probability, statistics, and data-intensive science, the prize celebrates the ongoing convergence of mathematics and computation, and their impact on society.

Dirk Görlich, the inaugural WLA Prize laureate in Life Science or Medicine and a director at the Max Planck Institute for Multidisciplinary Sciences, exemplifies underrecognized excellence according to Schekman. "For many years, I have been really impressed and have admired the quality of his scholarship. He has done one spectacular thing after another, and yet, he had not been appropriately recognized for it," he says. Görlich won the inaugural prize for fundamental discoveries elucidating the mechanism and selectivity of protein transport between the cytoplasm and nucleus.

Shaping the future

Scientific prizes have the power to influence conversations in academia, the media, and society. They inspire the next generation of scientists, guiding them toward important future research directions. Both of this year's chairs agree that looking at emerging fields and real-world challenges that inspire younger researchers is an excellent way to shape the scientific landscape. "We want to bring new voices into the conversation," says Jordan.

Through the prize, the WLA intends to facilitate meaningful discussions and collaboration. That mission is served by bringing together laureates from different fields, including previous WLA Prize winners, Nobel laureates, and other distinguished scientists, at the WLA Forum. In November 2022, the 5th WLA Forum was held in Shanghai with the theme of "Science Forward: Create a Bright Future." "By fostering dialogue in an international context, the Forum creates a setting full of opportunity for multidisciplinary collaboration and breakthroughs. I learned a great deal from those conversations," Jordan says.

At the core of every nomination is a fundamental scientific discovery that has led to broad community impact. "We are specifically looking for candidates who have not received major international awards; younger people in an ascending limb of their research, who've already had an impact and who will pave the way for the next generation," Schekman said.

The 2023 WLA Prize in Life Science or Medicine was awarded jointly to:

Karolin Luger,
University of Colorado Boulder,
USA

Daniela Rhodes,
MRC Laboratory of Molecular Biology,
Cambridge, UK

Timothy J. Richmond,
ETH Zürich
Zürich, Switzerland

For elucidating the structure of the nucleosome at the atomic level, providing the basis for understanding chromatin, gene regulation, and epigenetics.

https://www.thewlaprize.org/

Sponsored by

WLA PRIZE
世界顶尖科学家协会奖

PHOTO: COURTESY OF THE WLA PRIZE

CONTENTS

29 SEPTEMBER 2023
VOLUME 381
ISSUE 6665

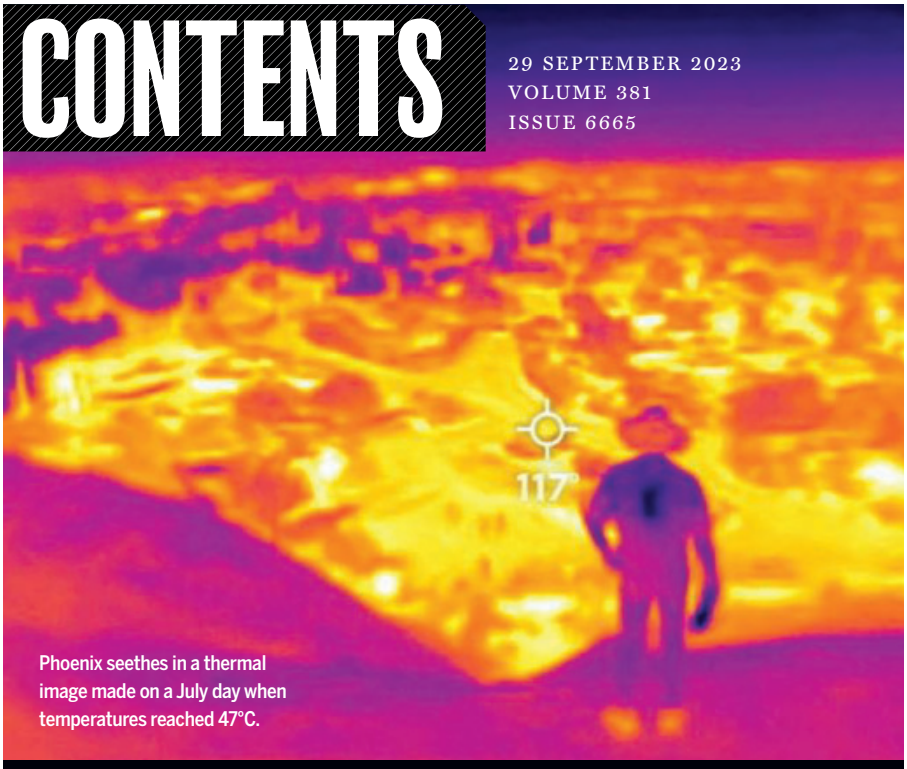

Phoenix seethes in a thermal image made on a July day when temperatures reached 47°C.

SPECIAL SECTION

HEAT AND HEALTH

This special issue of *Science* was supported by the Pulitzer Center and the Vapnek Family Foundation.

1386 An unhealthy climate
By T. Appenzeller

1388 Feeling the heat
Researchers struggle to convey the complex impacts of climate warming on infectious disease
By K. Kupferschmidt

1389 Will flu outbreaks ease in a warming world?

1391 A time of cholera

1392 Will fungal diseases come in from the cold?

1393 Heat-proofing India
Cities in India are testing measures that could help urban populations worldwide cope with rising temperatures
By V. Chandrashekhar
PODCAST

1399 Expecting extremes
Intense heat is a particular hazard in pregnancy. New studies are probing why
By M. Wadman

1402 Flight risks
Migratory birds efficiently ferry pathogens around the world. As a warming climate reshapes their journeys, infectious disease experts are on guard for new threats to humans *By J. Cohen*

1405 Gulls, floods, and superbugs

1406 Lurking in the deep freeze?
Climate change may release dangerous pathogens frozen for centuries in Arctic permafrost *By J. Cohen*

ON THE COVER

A summer scene in India captures how Earth's warming climate is pushing the limits of human endurance. Besides straining the body's ability to cool itself, global warming is fostering the spread of vector- and waterborne diseases and is perhaps bringing other pathogens out of hiding. This special issue examines the threats to human health and how they can be mitigated. See page 1386. *Image: Raj K. Raj/ Hindustan Times via Getty Images*

NEWS

IN BRIEF

1378 News at a glance

IN DEPTH

1380 NASA delivers bounty of asteroid samples to Earth
Bennu's rocks could reveal origin of organic molecules and Solar System evolution
By P. Voosen

1381 Mars Sample Return gets a new price tag. It's big

1382 Deadly avian flu hits Galápagos
Concerns rise for boobies, finches, and other endemic species *By E. Stokstad*
RESEARCH ARTICLE p. 1427

1383 Molecular 'sponges' could be hydrogen fuel tanks
Cheap chemical cages could expand the use of the clean-burning gas as an industrial fuel
By R. F. Service

1384 Faults teamed up 1100 years ago to produce Seattle megaquake—and could do so again
Tree rings give precise dates for ancient temblors, painting a more alarming picture of seismic risk *By M. Price*

1385 MRI study charts organ damage months after COVID-19
Imaging revealed no signs of lingering heart problems *By C. Offord*

INSIGHTS

POLICY FORUM

1408 Ethically cleared to launch?
Rules are needed for human research in commercial spaceflight *By V. Rahimzadeh* et al.

PERSPECTIVES

1412 Cellular coupling in the heart
Fibroblasts in scar tissue elicit myocyte excitation and promote arrhythmia in mouse hearts *By P. Camelliti and D. J. Stuckey*
RESEARCH ARTICLE p. 1480

1413 Widening the use of 3D printing
A light-triggered fabrication method extends the functionality of printable nanomaterials
By D. M. Balazs and M. Ibáñez
RESEARCH ARTICLE p. 1468

1414 Genetics of coral resilience
Genome-wide study in staghorn coral identifies markers of disease resistance
By L. D. Mydlarz and E. M. Muller
RESEARCH ARTICLE p. 1451

PHOTO: CARLOS BARRIA/REUTERS

1416 An epigenetic clock in plants
DNA methylation can identify evolutionary relationships among close plant lineages *By P. R. V. Satyaki*
RESEARCH ARTICLE p. 1440

BOOKS *ET AL.*

1417 Sheltering in place
An orphaned owl's convalescence inspired an ecologist's reflections during COVID-19 lockdown *By B. J. King*

1418 Pandemics and their lessons
Distrust and xenophobia have long been stumbling blocks during public health crises *By M. A. Goldman*

LETTERS

1419 Combat plastics in the Qinghai-Tibetan Plateau
By X. Wang and Y. Zhou

1420 Are algorithmic bias claims supported?
By S. Messing

1420 Response
By S. González-Bailón and D. Lazer

RESEARCH

IN BRIEF

1423 From *Science* and other journals

REVIEW

1426 Neuroscience
Integrative neurocircuits that control metabolism and food intake
J. C. Brüning and H. Fenselau
REVIEW SUMMARY; FOR FULL TEXT: DOI.ORG/10.1126/SCIENCE.ABL7398

RESEARCH ARTICLES

1427 Adaptation
Community-wide genome sequencing reveals 30 years of Darwin's finch evolution
E. D. Enbody et al.
RESEARCH ARTICLE SUMMARY; FOR FULL TEXT: DOI.ORG/10.1126/SCIENCE.ADF6218
NEWS STORY p. 1382

1428 Evolution
Cycles of fusion and fission enabled rapid parallel adaptive radiations in African cichlids *J. I. Meier* et al.
RESEARCH ARTICLE SUMMARY; FOR FULL TEXT: DOI.ORG/10.1126/SCIENCE.ADE2833

1429 Nanophotonics
Valley-addressable monolayer lasing through spin-controlled Berry phase photonic cavities *X. Duan* et al.

1433 Polymer chemistry
Diverse functional polyethylenes by catalytic amination *N. R. Ciccia* et al.

1440 Plant epigenetics
An evolutionary epigenetic clock in plants *N. Yao* et al.
PERSPECTIVE p. 1416

CREDITS: (PHOTO) MOTE MARINE LABORATORY; (ILLUSTRATION) ROBERT NEUBECKER

1446 Geology
A Bayesian inversion for emissions and export productivity across the end-Cretaceous boundary *A. A. Cox and C. B. Keller*

1451 Genomics
Genomic signatures of disease resistance in endangered staghorn corals *S. V. Vollmer* et al.
PERSPECTIVE P. 1414

1455 Fluorine chemistry
Handling fluorinated gases as solid reagents using metal-organic frameworks
K. T. Keasler et al.

1461 Mycoses
A *Candida auris*–specific adhesin, Scf1, governs surface association, colonization, and virulence *D. J. Santana* et al.

1468 Nanomaterials
3D printing of inorganic nanomaterials by photochemically bonding colloidal nanocrystals *F. Li* et al.
PERSPECTIVE p. 1413

1474 Organic chemistry
Aromatic nitrogen scanning by *ipso*-selective nitrene internalization *T. J. Pearson* et al.

1480 Heart disease
Fibroblasts in heart scar tissue directly regulate cardiac excitability and arrhythmogenesis *Y. Wang* et al.
PERSPECTIVE p. 1412

DEPARTMENTS

1377 Editorial
Proudly nonprofit *By H. H. Thorp*

1490 Working Life
Finding a different path *By G. Louloudis*

Science Staff 1376
AAAS News & Notes 1421
Science Careers 1488

SCIENCE (ISSN 0036-8075) is published weekly on Friday, except last week in December, by the American Association for the Advancement of Science, 1200 New York Avenue, NW, Washington, DC 20005. Periodicals mail postage (publication No. 484460) paid at Washington, DC, and additional mailing offices. Copyright © 2023 by the American Association for the Advancement of Science. The title SCIENCE is a registered trademark of the AAAS. Domestic individual membership, including subscription (12 months): $165 ($74 allocated to subscription). Domestic institutional subscription (51 issues): $2411; Foreign postage extra: Air assist delivery: $107. First class, airmail, student, and emeritus rates on request. Canadian rates with GST available upon request, GST #125488122. Publications Mail Agreement Number 1069624. **Printed in the U.S.A.**
Change of address: Allow 4 weeks, giving old and new addresses and 8-digit account number. **Postmaster:** Send change of address to AAAS, P.O. Box 96178, Washington, DC 20090–6178. **Single-copy sales:** $15 each plus shipping and handling available from backissues.science.org; bulk rate on request. **Authorization to reproduce** material for internal or personal use under circumstances not falling within the fair use provisions of the Copyright Act can be obtained through the Copyright Clearance Center (CCC), www.copyright.com. The identification code for *Science* is 0036-8075. *Science* is indexed in the *Reader's Guide to Periodical Literature* and in several specialized indexes.

Science AAAS

Editor-in-Chief Holden Thorp, hthorp@aaas.org

Executive Editor Valda Vinson

Editor, Research Jake S. Yeston **Editor, Insights** Lisa D. Chong **Managing Editor** Lauren Kmec

DEPUTY EDITORS Gemma Alderton (UK),Stella M. Hurtley (UK), Phillip D. Szuromi, Sacha Vignieri **SR. EDITORS** Caroline Ash (UK), Elisa Collado Fregoso (UK), Michael A. Funk, Brent Grocholski, Di Jiang, Priscilla N. Kelly, Marc S. Lavine (Canada), Sarah Lempriere (UK), Mattia Maroso, Yevgeniya Nusinovich, Ian S. Osborne (UK), L. Bryan Ray, H. Jesse Smith, Keith T. Smith (UK), Jelena Stajic, Peter Stern (UK), Valerie B. Thompson, Brad Wible **ASSOCIATE EDITORS** Bianca Lopez, Sarah Ross (UK), Madeleine Seale (UK), Corinne Simonti, Yury V. Suleymanov, Ekeoma Uzogara **SENIOR LETTERS EDITOR** Jennifer Sills **NEWSLETTER EDITOR** Christie Wilcox **RESEARCH & DATA ANALYST** Jessica L. Slater **LEAD CONTENT PRODUCTION EDITORS** Chris Filiatreau, Harry Jach **SR. CONTENT PRODUCTION EDITOR** Amelia Beyna **CONTENT PRODUCTION EDITORS** Anne Abraham, Robert French, Julia Haber-Katris, Nida Masiulis, Abigail Shashikanth, Suzanne M. White **SR. EDITORIAL MANAGERS** Carolyn Kyle, Beverly Shields **SR. PROGRAM ASSOCIATE** Maryrose Madrid **EDITORIAL ASSOCIATES** Aneera Dobbins, Joi S. Granger, Lisa Johnson **SR. EDITORIAL COORDINATORS** Jeffrey Hearn, Ronmel Navas, Jerry Richardson, Alice Whaley (UK), Anita Wynn **EDITORIAL COORDINATORS** Maura Byrne, Clair Goodhead (UK), Alexander Kief, Isabel Schnaidt, Qiyam Stewart, Brian White **ADMINISTRATIVE COORDINATOR** Karalee P. Rogers **ASI DIRECTOR, OPERATIONS** Janet Clements (UK) **ASI OFFICE MANAGER** Victoria Smith **ASI SR. OFFICE ADMINISTRATORS** Dawn Titheridge (UK), Jessica Waldock (UK) **COMMUNICATIONS DIRECTOR** Meagan Phelan **DEPUTY DIRECTOR** Matthew Wright **SENIOR WRITER** Walter Beckwith **WRITERS** Joseph Cariz, Abigail Eisenstadt, Nyla Hussain **SENIOR COMMUNICATIONS ASSOCIATE** Zachary Graber **COMMUNICATIONS ASSOCIATES** Kiara Brooks, Haley Riley, Mackenzie Williams, Sarah Woods

News Editor Tim Appenzeller

NEWS MANAGING EDITOR John Travis **INTERNATIONAL EDITOR** David Malakoff **DEPUTY NEWS EDITORS** Rachel Bernstein, Shraddha Chakradhar, Elizabeth Culotta, Martin Enserink, David Grimm, Eric Hand, Kelly Servick, Matt Warren (Europe) **SR. CORRESPONDENTS** Daniel Clery (UK), Jon Cohen, Jeffrey Mervis, Elizabeth Pennisi **ASSOCIATE EDITORS** Jeffrey Brainard, Michael Price **NEWS REPORTERS** Adrian Cho, Jennifer Couzin-Frankel, Jocelyn Kaiser, Rodrigo Pérez Ortega (Mexico City), Robert F. Service, Erik Stokstad, Paul Voosen, Meredith Wadman **CONTRIBUTING CORRESPONDENTS** Warren Cornwall, Andrew Curry (Berlin), Ann Gibbons, Sam Kean, Kai Kupferschmidt (Berlin), Andrew Lawler, Mitch Leslie, Virginia Morell, Dennis Normile (Tokyo), Elisabeth Pain (Careers), Charles Piller, Gabriel Popkin, Joshua Sokol, Richard Stone, Emily Underwood, Gretchen Vogel (Berlin), Lizzie Wade (Mexico City) **CAREERS** Katie Langin (Associate Editor) **INTERN** Phie Jacobs **COPY EDITORS** Julia Cole (Senior Copy Editor), Hannah Knighton, Cyra Master (Copy Chief) **ADMINISTRATIVE SUPPORT** Meagan Weiland

Creative Director Beth Rakouskas

DESIGN MANAGING EDITOR Chrystal Smith **GRAPHICS MANAGING EDITOR** Chris Bickel **PHOTOGRAPHY MANAGING EDITOR** Emily Petersen **MULTIMEDIA MANAGING PRODUCER** Kevin McLean **WEB CONTENT STRATEGY MANAGER** Kara Estelle-Powers **DESIGN EDITOR** Marcy Atarod **DESIGNER** Noelle Jessup **SENIOR SCIENTIFIC ILLUSTRATOR** Noelle Burgess **SCIENTIFIC ILLUSTRATORS** Austin Fisher, Kellie Holoski, Ashley Mastin **SENIOR GRAPHICS EDITOR** Monica Hersher **GRAPHICS EDITOR** Drew An-Pham **SENIOR GRAPHICS SPECIALISTS** Holly Bishop, Nathalie Cary **SENIOR PHOTO EDITOR** Charles Borst **PHOTO EDITOR** Elizabeth Billman **SENIOR PODCAST PRODUCER** Sarah Crespi **SENIOR VIDEO PRODUCER** Meagan Cantwell **SOCIAL MEDIA STRATEGIST** Jessica Hubbard **SOCIAL MEDIA PRODUCER** Sabrina Jenkins **WEB DESIGNER** Jennie Pajerowski

Chief Executive Officer and Executive Publisher Sudip Parikh

Publisher, Science Family of Journals Bill Moran

DIRECTOR, BUSINESS SYSTEMS AND FINANCIAL ANALYSIS Randy Yi **DIRECTOR, BUSINESS OPERATIONS & ANALYSIS** Eric Knott **MANAGER, BUSINESS OPERATIONS** Jessica Tierney **MANAGER, BUSINESS ANALYSIS** Cory Lipman **MANAGER, WEB ANALYTICS** Samantha Cressman **BUSINESS ANALYSTS** Kurt Ennis, Maggie Clark **FINANCIAL ANALYST** Isacco Fusi **BUSINESS OPERATIONS ADMINISTRATOR** Taylor Fisher **SENIOR PRODUCTION MANAGER** Jason Hillman **SENIOR MANAGER, PUBLISHING AND CONTENT SYSTEMS** Marcus Spiegler **CONTENT OPERATIONS MANAGER** Rebecca Doshi **SENIOR CONTENT & PUBLISHING SYSTEMS SPECIALIST** Jacob Hedrick **SENIOR PRODUCTION SPECIALIST** Kristin Wowk **PRODUCTION SPECIALISTS** Kelsey Cartelli, Audrey Diggs **DIGITAL PRODUCTION MANAGER** Lisa Stanford **SENIOR DIGITAL ADVERTISING SPECIALIST** Kimberley Oster **ADVERTISING PRODUCTION OPERATIONS MANAGER** Deborah Tompkins **DESIGNER, CUSTOM PUBLISHING** Jeremy Huntsinger **SR. TRAFFIC ASSOCIATE** Christine Hall **SPECIAL PROJECTS ASSOCIATE** Shantel Agnew

ASSOCIATE DIRECTOR, BUSINESS DEVELOPMENT Justin Sawyers **GLOBAL MARKETING MANAGER** Allison Pritchard **DIGITAL MARKETING MANAGER** Aimee Aponte **JOURNALS MARKETING MANAGER** Shawana Arnold **MARKETING ASSOCIATES** Ashley Hylton, Mike Romano, Lorena Chirinos Rodriguez, Jenna Voris **SENIOR DESIGNER** Kim Huynh

DIRECTOR AND SENIOR EDITOR, CUSTOM PUBLISHING Erika Gebel Berg **ASSISTANT EDITOR, CUSTOM PUBLISHING** Jackie Oberst **PROJECT MANAGER** Melissa Collins

DIRECTOR, PRODUCT & PUBLISHING DEVELOPMENT Chris Reid **DIRECTOR, BUSINESS STRATEGY AND PORTFOLIO MANAGEMENT** Sarah Whalen **DIRECTOR, PRODUCT MANAGEMENT** Kris Bishop **PRODUCT DEVELOPMENT MANAGER** Scott Chernoff **PUBLISHING PLATFORM MANAGER** Jessica Loayza **SR. PRODUCT ASSOCIATE** Robert Koepke **PRODUCT ASSOCIATES** Caroline Breul, Anne Mason

ASSOCIATE DIRECTOR, INSTITUTIONAL LICENSING MARKETING Kess Knight **BUSINESS DEVELOPMENT MANAGER** Rasmus Andersen **ASSOCIATE DIRECTOR, INSTITUTIONAL LICENSING SALES** Ryan Rexroth **INSTITUTIONAL LICENSING MANAGER** Marco Castellan, Claudia Paulsen-Young **SENIOR MANAGER, INSTITUTIONAL LICENSING OPERATIONS** Judy Lillibridge **SENIOR OPERATIONS ANALYST** Lana Guz **SYSTEMS & OPERATIONS ANALYST** Ben Teincuff **FULFILLMENT ANALYST** Aminta Reyes

ASSOCIATE DIRECTOR, US ADVERTISING Stephanie O'Connor **US MID WEST, MID ATLANTIC AND SOUTH EAST SALES** Chris Hoag **US WEST COAST SALES** Lynne Stickrod **ASSOCIATE DIRECTOR, ROW** Roger Goncalves **SALES REP, ROW** Sarah Lelarge **SALES ADMIN ASSISTANT, ROW** Victoria Glasbey **DIRECTOR OF GLOBAL COLLABORATION AND ACADEMIC PUBLISHING RELATIONS, ASIA** Xiaoying Chu **ASSOCIATE DIRECTOR, INTERNATIONAL COLLABORATION** Grace Yao **SALES MANAGER** Danny Zhao **MARKETING MANAGER** Kilo Lan **ASCA CORPORATION, JAPAN** Rie Rambelli (Tokyo), Miyuki Tani (Osaka)

DIRECTOR, COPYRIGHT, LICENSING AND SPECIAL PROJECTS Emilie David **RIGHTS AND PERMISSIONS ASSOCIATE** Elizabeth Sandler **LICENSING ASSOCIATE** Virginia Warren **RIGHTS AND LICENSING COORDINATOR** Dana James **CONTRACT SUPPORT SPECIALIST** Michael Wheeler

EDITORIAL
science_editors@aaas.org

NEWS
science_news@aaas.org

INFORMATION FOR AUTHORS
science.org/authors/science-information-authors

REPRINTS AND PERMISSIONS
science.org/help/reprints-and-permissions

MULTIMEDIA CONTACTS
SciencePodcast@aaas.org
ScienceVideo@aaas.org

MEDIA CONTACTS
scipak@aaas.org

PRODUCT ADVERTISING & CUSTOM PUBLISHING
advertising.science.org/products-services
science_advertising@aaas.org

CLASSIFIED ADVERTISING
advertising.science.org/science-careers
advertise@sciencecareers.org

JOB POSTING CUSTOMER SERVICE
employers.sciencecareers.org
support@sciencecareers.org

MEMBERSHIP AND INDIVIDUAL SUBSCRIPTIONS
science.org/subscriptions

MEMBER BENEFITS
aaas.org/membership/benefits

INSTITUTIONAL SALES AND SITE LICENSES
science.org/librarian

AAAS BOARD OF DIRECTORS
CHAIR Gilda A. Barabino
PRESIDENT Keith R. Yamamoto
PRESIDENT-ELECT Willie E. May
TREASURER Carolyn N. Ainslie
CHIEF EXECUTIVE OFFICER Sudip Parikh
BOARD Cynthia M. Beall, Janine Austin Clayton, Kaye Husbands Fealing, Kathleen Hall Jamieson, Jane Maienschein, Robert B. Millard, Babak Parviz, William D. Provine, Juan S. Ramírez Lugo, Susan M. Rosenberg, Vassiliki Betty Smocovitis

Science serves as a forum for discussion of important issues related to the advancement of science by publishing material on which a consensus has been reached as well as including the presentation of minority or conflicting points of view. Accordingly, all articles published in *Science*—including editorials, news and comment, and book reviews—are signed and reflect the individual views of the authors and not official points of view adopted by AAAS or the institutions with which the authors are affiliated.

BOARD OF REVIEWING EDITORS (Statistics board members indicated with **(S)**)

Erin Adams, *U. of Chicago*
Takuzo Aida, *U. of Tokyo*
Leslie Aiello, *Wenner-Gren Fdn.*
Deji Akinwande, *UT Austin*
Marcella Alsan, *Harvard U.*
James Analytis, *UC Berkeley*
Paola Arlotta, *Harvard U.*
Delia Baldassarri, *NYU*
Nenad Ban, *ETH Zürich*
Christopher Barratt, *U. of Dundee*
Franz Bauer, *Pontificia U. Católica de Chile*
Ray H. Baughman, *UT Dallas*
Carlo Beenakker, *Leiden U.*
Yasmine Belkaid, *NIAID, NIH*
Philip Benfey, *Duke U.*
Kiros T. Berhane, *Columbia U.*
Joseph J. Berry, *NREL*
Alessandra Biffi, *Harvard Med.*
Chris Bowler, *École Normale Supérieure*
Ian Boyd, *U. of St. Andrews*
Malcolm Brenner, *Baylor Coll. of Med.*
Emily Brodsky, *UC Santa Cruz*
Ron Brookmeyer, *UCLA* **(S)**
Christian Büchel, *UKE Hamburg*
Johannes Buchner, *TUM*
Dennis Burton, *Scripps Res.*
Carter Tribley Butts, *UC Irvine*
György Buzsáki, *NYU School of Med.*
Mariana Byndloss, *Vanderbilt U. Med. Ctr.*
Annmarie Carlton, *UC Irvine*
Simon Cauchemez, *Inst. Pasteur*
Ling-Ling Chen, *SIBCB, CAS*
Wendy Cho, *UIUC*
Ib Chorkendorff, *Denmark TU*
Chunaram Choudhary, *København Univ.*
Karlene Cimprich, *Stanford U.*
Laura Colgin, *UT Austin*
James J. Collins, *MIT*
Robert Cook-Deegan, *Arizona State U.*
Virginia Cornish, *Columbia U.*
Carolyn Coyne, *Duke U.*
Roberta Croce, *VU Amsterdam*
Molly Crocket, *Princeton U.*
Christina Curtis, *Stanford U.*
Ismaila Dabo, *Penn State U.*
Jeff L. Dangl, *UNC*
Nicolas Dauphas, *U. of Chicago*
Frans de Waal, *Emory U.*
Claude Desplan, *NYU*
Sandra Díaz, *U. Nacional de Córdoba*
Samuel Díaz-Muñoz, *UC Davis*
Ulrike Diebold, *TU Wien*
Stefanie Dimmeler, *Goethe-U. Frankfurt*
Hong Ding, *Inst. of Physics, CAS*
Dennis Discher, *UPenn*
Jennifer A. Doudna, *UC Berkeley*
Ruth Drdla-Schutting, *Med. U. Vienna*
Raissa M. D'Souza, *UC Davis*
Bruce Dunn, *UCLA*
William Dunphy, *Caltech*
Scott Edwards, *Harvard U.*
Todd Ehlers, *U. of Tübingen*
Nader Engheta, *UPenn*
Tobias Erb, *MPI Terrestrial Microbiology*
Karen Ersche, *U. of Cambridge*
Beate Escher, *UFZ & U. of Tübingen*
Barry Everitt, *U. of Cambridge*
Vanessa Ezenwa, *U. of Georgia*
Toren Finkel, *U. of Pitt. Med. Ctr.*
Natascha Förster Schreiber, *MPI Extraterrestrial Phys.*
Peter Fratzl, *MPI Potsdam*
Elaine Fuchs, *Rockefeller U.*
Caixia Gao, *Inst. of Genetics and Developmental Bio., CAS*
Daniel Geschwind, *UCLA*
Lindsey Gillson, *U. of Cape Town*
Gillian Griffiths, *U. of Cambridge*
Simon Greenhill, *U. of Auckland*
Nicolas Gruber, *ETH Zürich*
Hua Guo, *U. of New Mexico*
Taekjip Ha, *Johns Hopkins U.*
Daniel Haber, *Mass. General Hos.*
Sharon Hammes-Schiffer, *Yale U.*
Wolf-Dietrich Hardt, *ETH Zürich*
Louise Harra, *UCL*
Kelley Harris, *U. of Wash*
Carl-Philipp Heisenberg, *IST Austria*
Janet G. Hering, *Eawag*
Christoph Hess, *U. of Basel & U. of Cambridge*
Heather Hickman, *NIAID, NIH*
Hans Hilgenkamp, *U. of Twente*
Janneke Hille Ris Lambers, *ETH Zürich*
Kai-Uwe Hinrichs, *U. of Bremen*
Deirdre Hollingsworth, *U. of Oxford*
Christina Hulbe, *U. of Otago, New Zealand*
Randall Hulet, *Rice U.*
Auke Ijspeert, *EPFL*
Gwyneth Ingram, *ENS Lyon*
Darrell Irvine, *MIT*
Akiko Iwasaki, *Yale U.*
Erich Jarvis, *Rockefeller U.*
Peter Jonas, *IST Austria*
Matt Kaeberlein, *U. of Wash.*
Daniel Kammen, *UC Berkeley*
Kisuk Kang, *Seoul Nat. U.*
V. Narry Kim, *Seoul Nat. U.*
Nancy Knowlton, *Smithsonian*
Etienne Koechlin, *École Normale Supérieure*
Alex L. Kolodkin, *Johns Hopkins U.*
LaShanda Korley, *U. of Delaware*
Paul Kubes, *U. of Calgary*
Chris Kuzawa, *Northwestern U.*
Laura Lackner, *Northwestern U.*
Gabriel Lander, *Scripps Res.* **(S)**
Mitchell A. Lazar, *UPenn*
Hedwig Lee, *Duke U.*
Fei Li, *Xi'an Jiaotong U.*
Ryan Lively, *Georgia Tech*
Luis Liz-Marzán, *CIC biomaGUNE*
Omar Lizardo, *UCLA*
Jonathan Losos, *WUSTL*
Ke Lu, *Inst. of Metal Res., CAS*
Christian Lüscher, *U. of Geneva*
Jean Lynch-Stieglitz, *Georgia Tech*
David Lyons, *U. of Edinburgh*
Fabienne Mackay, *QIMR Berghofer*
Zeynep Madak-Erdogan, *UIUC*
Vidya Madhavan, *UIUC*
Anne Magurran, *U. of St. Andrews*
Ari Pekka Mähönen, *U. of Helsinki*
Asifa Majid, *U. of Oxford*
Oscar Marín, *King's Coll. London*
Charles Marshall, *UC Berkeley*
Christopher Marx, *U. of Idaho*
David Masopust, *U. of Minnesota*
Geraldine Masson, *CNRS*
Jennifer McElwain, *Trinity College Dublin*
Rodrigo Medellín, *U. Nacional Autónoma de México*
C. Jessica Metcalf, *Princeton U.*
Tom Misteli, *NCI, NIH*
Jeffery Molkentin, *Cincinnati Children's Hospital Medical Center*
Alison Motsinger-Reif, *NIEHS, NIH* **(S)**
Danielle Navarro, *U. of New South Wales*
Daniel Neumark, *UC Berkeley*
Thi Hoang Duong Nguyen, *MRC LMB*
Beatriz Noheda, *U. of Groningen*
Helga Nowotny, *Vienna Sci. & Tech. Fund*
Pilar Ossorio, *U. of Wisconsin*
Andrew Oswald, *U. of Warwick*
Isabella Pagano, *Istituto Nazionale di Astrofisica*
Giovanni Parmigiani, *Dana-Farber* **(S)**
Sergiu Pasca, *Standford U.*
Daniel Pauly, *U. of British Columbia*
Ana Pêgo, *U. do Porto*
Julie Pfeiffer, *UT Southwestern Med. Ctr.*
Philip Phillips, *UIUC*
Matthieu Piel, *Inst. Curie*
Kathrin Plath, *UCLA*
Martin Plenio, *Ulm U.*
Katherine Pollard, *UCSF*
Elvira Poloczanska, *Alfred-Wegener-Inst.*
Julia Pongratz, *Ludwig Maximilians U.*
Philippe Poulin, *CNRS*
Lei Stanley Qi, *Stanford U.*
Simona Radutoiu, *Aarhus U.*
Trevor Robbins, *U. of Cambridge*
Joeri Rogelj, *Imperial Coll. London*
John Rubenstein, *SickKids*
Mike Ryan, *UT Austin*
Miquel Salmeron, *Lawrence Berkeley Nat. Lab*
Nitin Samarth, *Penn State U.*
Erica Ollmann Saphire, *La Jolla Inst.*
Joachim Saur, *U. zu Köln*
Alexander Schier, *Harvard U.*
Wolfram Schlenker, *Columbia U.*
Susannah Scott, *UC Santa Barbara*
Anuj Shah, *U. of Chicago*
Vladimir Shalaev, *Purdue U.*
Jie Shan, *Cornell U.*
Beth Shapiro, *UC Santa Cruz*
Jay Shendure, *U. of Wash.*
Steve Sherwood, *U. of New South Wales*
Brian Shoichet, *UCSF*
Robert Siliciano, *JHU School of Med.*
Lucia Sivilotti, *UCL*
Emma Slack, *ETH Zürich & U. of Oxford*
Richard Smith, *UNC* **(S)**
John Speakman, *U. of Aberdeen*
Allan C. Spradling, *Carnegie Institution for Sci.*
V. S. Subrahmanian, *Northwestern U.*
Naomi Tague, *UC Santa Barbara*
Eriko Takano, *U. of Manchester*
A. Alec Talin, *Sandia Natl. Labs*
Patrick Tan, *Duke-NUS Med. School*
Sarah Teichmann, *Wellcome Sanger Inst.*
Rocio Titiunik, *Princeton U.*
Shubha Tole, *Tata Inst. of Fundamental Res.*
Maria-Elena Torres Padilla, *Helmholtz Zentrum München*
Kimani Toussaint, *Brown U.*
Barbara Treutlein, *ETH Zürich*
Li-Huei Tsai, *MIT*
Jason Tylianakis, *U. of Canterbury*
Matthew Vander Heiden, *MIT*
Wim van der Putten, *Netherlands Inst. of Ecology*
Ivo Vankelecom, *KU Leuven*
Judith Varner, *UC San Diego*
Henrique Veiga-Fernandes, *Champalimaud Fdn.*
Reinhilde Veugelers, *KU Leuven*
Bert Vogelstein, *Johns Hopkins U.*
Julia Von Blume, *Yale School of Med.*
David Wallach, *Weizmann Inst.*
Jane-Ling Wang, *UC Davis* **(S)**
Jessica Ware, *Amer. Mus. of Natural Hist.*
David Waxman, *Fudan U.*
Alex Webb, *U. of Cambridge*
Chris Wikle, *U. of Missouri* **(S)**
Terrie Williams, *UC Santa Cruz*
Ian A. Wilson, *Scripps Res.* **(S)**
Hao Wu, *Harvard U.*
Li Wu, *Tsinghua U.*
Amir Yacoby, *Harvard U.*
Benjamin Youngblood, *St. Jude*
Yu Xie, *Princeton U.*
Jan Zaanen, *Leiden U.*
Kenneth Zaret, *UPenn School of Med.*
Lidong Zhao, *Beihang U.*
Bing Zhu, *Inst. of Biophysics, CAS*
Xiaowei Zhuang, *Harvard U.*
Maria Zuber, *MIT*

EDITORIAL

Proudly nonprofit

H. Holden Thorp
Editor-in-Chief, *Science* journals.
hthorp@aaas.org;
@hholdenthorp

Science is fortunate that so many authors seek to publish with us. We shoulder enormous responsibility from both our outsized influence on research across many fields and from the journal's impact on the careers of scientists who publish in our pages. Although there can be some cynicism about the role of highly selective "glam journals," we understand why we are part of conversations that sometimes center around "CNS" (*Cell*, *Nature*, *Science*) periodicals. All three have considerable importance and prominence in the scientific community. But there is a major difference that often gets lost. Whereas *Cell* and *Nature* generate revenue for their parent for-profit companies, Elsevier and Springer Nature, *Science* is published by a nonprofit organization, the American Association for the Advancement of Science (AAAS), and produces no revenue for shareholders. We don't get the word out about this distinction frequently or overtly enough. It's an important contrast because decisions that we make at *Science* and AAAS are driven by putting scientists ahead of profit.

> **"...*Science* is published by a nonprofit organization... We don't get the word out about this distinction frequently or overtly enough..."**

Although our business environments are very different, *Science* shares many commonalities with *Nature*. Both are widely read, weekly journals that are broad in the scope of research published, and both have outstanding news and commentary sections.

Despite these similarities, the fact that *Science* is a nonprofit journal makes a big difference in how we operate. The margin that the *Science* family of journals (six in total) generates—orders of magnitude less than what commercial publishers make off thousands of journals—does not go to corporate shareholders. Rather, it goes to seed work of the AAAS in advocating for science in the United States and around the world, such as providing policy experiences for scientists and cultivating science diplomacy. This modest investment is multiplied many times over by the grants and philanthropic donations that the AAAS programs garner to support its mission to serve society.

Moreover, when we decide to start a new journal, it is because we think it will be of value to the scientific community, not that it will produce a profit. Meanwhile, our commercial peers have mechanisms to conveniently generate new journals every year. Many of these are fine publications, but there is a profit associated with each of them.

And *Science* has a different view of open access publishing compared to commercial journals. Consistent with its commitment to put the scientific community first, AAAS does not favor a publishing ecosystem driven by article processing charges—the fees that authors must pay so that their articles are freely available once published ("gold" open access). An environment dominated by this approach drains laboratory resources and favors well-funded investigators, institutions, and disciplines. These inequities are coming into ever starker contrast, including through a recent AAAS survey of over 400 researchers in the United States. Rather, AAAS favors an ecosystem that does not put the cost burden for access on scientists. It has become an open access publisher by adopting a "green" policy for its subscription journals, including *Science*, whereby accepted manuscripts are made immediately available in repositories of the author's choice. This approach—one that AAAS is excited to pursue alongside the American Medical Association—is consistent with open access policies in the United Kingdom, Europe, and the United States. But for now, AAAS still has one gold open access journal, *Science Advances*, as an option for scientists or funders that prefer this mechanism.

For most of the time that open access has been debated by publishers and librarians, investigators have largely stayed on the sidelines. But as the AAAS survey shows, scientists are beginning to grasp the implications of different publishing models on their careers and on the scientific enterprise. It is therefore vital that scientists engage in discussions about open access because publishing is rapidly changing, and at the moment, there are no certain outcomes in the long run.

Everything that is written on this page and elsewhere in *Science* starts with asking what our readers want from this journal. The unusual set of circumstances that allow us to do this—nonprofit status, support from AAAS society members (individuals and institutions), high-impact research articles, widely circulated news and commentary—is not something we take for granted.

–H. Holden Thorp

10.1126/science.adk9900

PHOTO: CAMERON DAVIDSON

> “In the name of protecting free speech, the scientific community is not allowed to speak.”
>
> **Health communication scientist Dean Schillinger,** in *The Washington Post*, about NIH’s suspension of a program to study health misinformation after legal threats from conservatives.

IN BRIEF

Edited by **Jeffrey Brainard**

INNOVATION

China leads in number of S&T clusters

In another sign of China’s growing research clout, the country now leads in a top 100 ranking of metropolitan areas based on their science and technology productivity. The annual Global Innovation Index, curated by the World Intellectual Property Organization, ranks these S&T clusters based on numbers of patent applications and scientific papers produced by their inventors and scientists. In 2022, China’s 24 clusters in the top 100 beat the 21 from the United States, the second most. “Vibrant local clusters are critical hubs of national competitiveness,” and the new ranking suggests the United States has been slipping, says Mark Muro, a regional innovation specialist at the Brookings Institution. The ranking’s top cluster is the Tokyo-Yokohama region, followed by Shenzhen-Hong Kong-Guangzhou, Seoul, Beijing, Shanghai-Suzhou, and San Jose-San Francisco. The clusters in Cambridge, England, and San Jose-San Francisco have the most intensive science and technology activity, a measure that accounts for the region’s population.

EU eyes extending glyphosate use

HERBICIDES | The European Commission last week recommended extending the approval of the controversial herbicide glyphosate for 10 more years, a proposal that faces a final vote in October. EU approval for the substance, the main ingredient in the commercial product Roundup, expires in December, and some environmentalists and scientists have campaigned to outlaw its use. The World Health Organization has classified it as a possible carcinogen, and Roundup’s maker, Bayer, has spent billions settling U.S. lawsuits by people who claimed it caused their cancers. But the U.S. Environmental Protection Agency has said the substance is safe for people. And in July, a review by the European Food Safety Authority of glyphosate’s risks to the health of humans, animals, and the environment found “no critical areas of concern.” To approve or block reauthorization, a qualified majority of EU member countries must agree in the 13 October vote. Otherwise, the decision falls to the Commission. Officials in Austria, France, and Germany have said they do not support reauthorization.

Grant supports Arecibo’s future

FACILITIES | The U.S. National Science Foundation (NSF) this week awarded a consortium a 5-year grant to create and operate an interdisciplinary center for science education and research at the Arecibo Observatory site in Puerto Rico. NSF decided last year not to rebuild the storied radio telescope facility after parts of it collapsed in 2020. The consortium receiving the grant totaling $5 million comprises Cold Spring Harbor Laboratory; the University of Maryland, Baltimore County; the University of Puerto Rico, Río Piedras; and the University of the Sacred Heart in Puerto Rico. The project will include a public science center with an exhibit describing the observatory’s accomplishments.

Group wants probe of Neuralink

RESEARCH ETHICS | Animal research opponents last week requested a government investigation of whether Neuralink’s CEO and founder Elon Musk committed securities fraud in describing rhesus monkeys used in studies of its implanted brain device. The company last week also won approval from an ethics committee for human trials to evaluate the device, a brain-computer interface system, for patients with quadriplegia. As first reported by *Wired*, the Physicians Committee for Responsible Medicine (PCRM) wrote the U.S. Securities and Exchange Commission alleging that Musk lied to investors and the public in a 10 September social media post. Musk stated that “no monkey has died as a result of a Neuralink implant” and that studies sponsored by the company used only “terminal mon[k]eys (close to death).” But medical records PCRM obtained from the University of California, Davis, where the experiments were conducted, show that several previously healthy young monkeys were euthanized because of problems with the implant. Neuralink did not respond to requests for comment.

Thank an earthworm for bread

AGROECOLOGY | If earthworms were a country, they would be the world’s fourth largest producer of grain, a study has determined. The first estimate of the wrigglers’ worldwide contribution to crop harvests, published this week in *Nature Communications*, says they help farmers grow more than 140 million tons of food each year. For wheat harvests alone, their impact is roughly equivalent to one slice in every loaf of bread. Earthworms help make soil more fertile by burrowing, which renders it more porous, and by digesting dead plant matter. A research team derived the estimates by combining a global atlas of earthworm abundance with maps of agricultural harvests. Farmers can make their soils more friendly for earthworms by

Scientists haven't determined what causes the patterns called fairy circles, such as these in the Gerebes Plain in Namibia.

BIOGEOGRAPHY

Fairy circles abound in dry regions of many countries

Mysterious patches of vegetation called fairy circles are well documented in the drylands of Australia and Namibia. Now, a study that combines machine learning and satellite images that span the continents reports examples in 13 other countries, mainly in Africa. Many of the 263 sites identified—in the Sahara and Madagascar, for example—have never before been recorded by scientists. Fairy circles consist of a ring of tall grass surrounding a patch of bare soil up to 12 meters in diameter. Researchers have attributed them to various causes, including patterns of water runoff and plants whose defensive chemicals ward off other vegetation. This year, a study based on Aboriginal knowledge highlighted the role of termites in Australia (*Science*, 7 April, p. 14). The new investigation, published this week in the *Proceedings of the National Academy of Sciences*, shows that fairy circles tend to occur in poor, sandy soil, and confirms that they are restricted to arid landscapes.

reducing plowing, which can kill them, says study co-author Steven Fonte, an ecologist at Colorado State University.

Elephant trunks' muscular secrets

ANATOMY | Using its trunk, an elephant can lift logs and pick up a potato chip without breaking it. The musculature that enables this combination of brute force and soft touch is among the most complex known. Now, researchers have published the most detailed examination to date of the tiny, muscle fiber bundles involved. They studied a trunk belonging to a baby Asian elephant that zookeepers had euthanized because the animal had a broken leg. The scientists used an x-ray scanning technique, microcomputed tomography, to map and count the bundles, almost 90,000 in all. Elephants get their fine control from the large number and surprisingly small size of these bundles, the team reports this week in *Current Biology*—those at the trunk's tip measure only 2 millimeters long. The findings could help scientists develop robots with more flexible, nimble appendages.

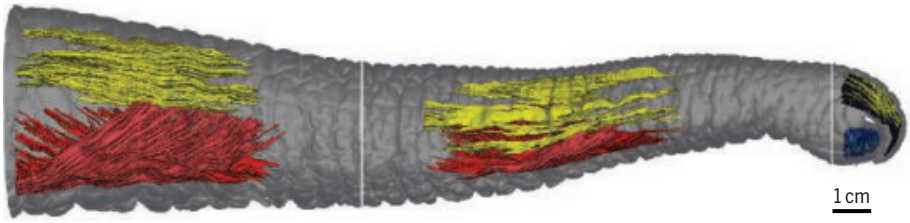

X-ray scanning allowed researchers to segment an elephant's trunk into bundles of muscle fibers (colored).

France to give birds flu shot

AGRICULTURE | In a first for Europe, France plans to start vaccinating poultry next week against highly pathogenic avian influenza (HPAI) viruses. The compulsory inoculations will begin at commercial duck farms, French agricultural officials said, and are expected to be expanded to other poultry. The effort aims to stop a variant of the flu virus that has devastated the continent's poultry industry since 2020 and killed many wild birds and sea mammals around the world. Europe has not previously used vaccines against HPAI outbreaks because of trade concerns; in theory, vaccination could mask symptoms of infections, leading to unwitting importation of the highly lethal virus. Instead, European countries combated HPAI outbreaks by culling infected flocks and stepping up biosecurity. But those methods have not stopped this flu variant.

Silkworms spin spider fibers

MATERIALS SCIENCE | Researchers have used gene editing to make silkworms that produce fibers tougher than the Kevlar used in bulletproof vests. Last week in *Matter*, researchers reported inserting DNA coding for spider fibers in the silkworms. The spider fibers are much tougher than ones naturally produced by silkworms, but spiders are difficult to cultivate. The new fibers could be used to create lightweight structural elements for fuel-efficient vehicles, for example. But it remains to be seen whether the inserted spider genes will persist when the silkworms are bred.

IMAGES: (TOP TO BOTTOM) EDWIN REMSBERG/VWPICS/UNIVERSAL IMAGES GROUP VIA GETTY IMAGES; LUKE L. LONGREN *ET AL.*, *CURRENT BIOLOGY*, 33 (2023)

PLANETARY SCIENCE

NASA delivers bounty of asteroid samples to Earth

Bennu's rocks could reveal origin of organic molecules and Solar System evolution

By **Paul Voosen**

Most of the small asteroids that enter Earth's atmosphere end their plunge in screaming, fiery violence. But on 24 September, after detaching from NASA's OSIRIS-REx spacecraft, a capsule carrying asteroid samples descended gently by parachute before touching down in the Utah desert. The cupful of pebbles and grit it delivered—the culmination of 7 years in space and $1 billion of expense—is only the third sample of an asteroid ever returned to Earth, and it's the largest haul of extraterrestrial material NASA has collected since the Apollo Moon missions.

Scientists say the material, which predates our planet, promises to offer new insights into the early Solar System and how the stage was set for life on Earth. "These samples are some of the oldest and most pristine materials we'll have available," says Jessica Barnes, a cosmochemist at the University of Arizona (UA).

It only took some 10 minutes for the suitcase-size capsule to fall through the clear skies of the western United States. Hovering helicopters quickly pounced on the scene so they could transport it to a temporary clean room at the Utah Test and Training Range, where it was sealed in a nitrogen atmosphere. At the landing site, researchers sampled the air, soil, and water to catalog potential contaminants, including organic molecules and microbes, just in case any find their way into the sample canister.

After arriving in 2018, OSIRIS-REx spent 2 years orbiting its target, Bennu, a carbon-rich, near-Earth asteroid 500 meters across. The asteroid was not smooth and solid, but a set of boulders and gravel "barely held together by their own microgravity," says Dante Lauretta, the mission's principal investigator and a UA planetary scientist.

That made sample collection in 2020 somewhat harrowing: the spacecraft's sampling arm plunged unexpectedly deep into Bennu's rubble pile. But it nevertheless sucked up some 250 grams of rocks and dust—so much that particles began to leak from the sample container, requiring spacecraft controllers to stow it quickly. The spacecraft then took 3 years to realign with the orbit of Earth so it could release the capsule.

The day after landing in Utah, the sample container was flown to Johnson Space Center, and the team began to open it in glove boxes inside a new clean room. But first, they took advantage of the leak by collecting a swab of the stray dust, which could give them a glimpse of Bennu's makeup within a week.

Once the container is fully opened, the team will sort through the collected pebbles, using instruments built into the glove boxes to measure the rocks' volume, shape, mass, and porosity. NASA will hold back 70% of the rocks for future scientists, who might have better experimental tools. It will send between 4% and 5% of the haul to collaborators in Canada and Japan. The remaining 25% will be reserved for detailed analysis by the mission's science team, which consists of more than 200 people spread across four continents. "We are fully ready for the unexpected," says Daniel Glavin, an astrobiologist at NASA's Goddard Space Flight Center.

Glavin leads the mission's 50-person organics team, which will explore the role of asteroid impacts in setting the stage for life. Whereas some have proposed that crucial organic molecules, such as amino acids, arose through chemical reactions at deep-sea vents, others have suggested asteroids could have seeded early Earth with them. So far, only 12 of the 20 amino acids necessary for life have been detected in meteorites, most of which are asteroid fragments. But Glavin and his colleagues have found that most extraction methods, which rely on warm water and mechanical stirring to dissolve the rock compounds within a "meteorite tea," can actually de-

PHOTO: KEEGAN BARBER/NASA

Disassembly of a sample capsule began in a temporary clean room at the Utah Test and Training Range.

stroy some of the amino acids. They've devised a gentler technique, using cool water and sound waves, and they are confident it can capture all 20. "We call it the cold brew," Glavin says.

In particular, Glavin wants to see whether Bennu has an excess of "left-handed" amino acids. Amino acids can occur in two mirror-image forms, but life exclusively uses left-handed ones. Some researchers believe this disparity emerged on Earth through molecules' exposure to magnetic fields, but polarized ultraviolet light striking asteroids during their long journeys in space could also have favored the left-handed forms. Glavin's team will also search for even more complex organic molecules used by living things, such as peptides—short protein segments—and sugars like ribose.

Lauretta says mission scientists also wonder whether Bennu's composition will be anything like it appears in telescopes. In 2020, Japan's Hayabusa2 spacecraft returned some 5 grams of material from Ryugu, another carbon-rich, near-Earth asteroid, which was thought to be relatively dry. Instead, the samples suggested it was fully altered by water. "We were all terribly wrong about Ryugu," says Edward Young, a cosmochemist at the University of California, Los Angeles.

If they are wrong about Bennu, it will be the opposite mistake. Remote observations suggest some 10% of Bennu's mass is made up of water locked in clays. "We don't have something more volatile rich in our collections," says Sara Russell, a cosmic mineralogist at the Natural History Museum in London who believes Bennu could represent a wholly new class of asteroid.

As it orbited Bennu, OSIRIS-REx glimpsed another sign of a watery past: meter-long veins of carbonate, a mineral that precipitates out of solution. The water may have flowed on Bennu's parent body, which likely formed beyond Jupiter's orbit, at the Solar System's very beginning 4.56 billion years ago. Short-lived radioactive aluminum in its interior could have provided a heat source powerful enough to keep water liquid. If carbonate is present in the returned samples, researchers will gain a window on this epoch, and perhaps learn just how that water originated in the first place, Barnes says. "We have a whole arsenal [of techniques] to use."

Until spacecraft began to collect samples, scientists could only analyze asteroid material in the form of meteorites, and Ryugu and Bennu now suggest they present a biased view. To survive their fall to Earth, meteorites have to be dense and durable, unlike the friable mix seen by the two missions, says Yurimoto Hisayoshi, a planetary scientist at Hokkaido University who has led analysis of the Ryugu samples. "These could very well be the standard type of Solar System composition."

Although it has accomplished its main goal of delivering samples, the work of the OSIRIS-REx spacecraft is not yet over. Operators have set a new trajectory to visit and orbit Apophis in 2029, just after the stony asteroid makes a close flyby of Earth. But Lauretta, who has worked on OSIRIS-REx for several decades, will remain focused on the Bennu samples. "The spotlight is going to move," he says. "I think I'm ready." ■

Mars Sample Return gets a new price tag. It's big

NASA's audacious Mars Sample Return (MSR) mission is overbudget and behind schedule, an independent review has found. Originally estimated to cost some $4 billion, the mission could end up costing as much as $11 billion, the reviewers found, and launch could happen no sooner than 2030, 2 years later than planned. "MSR was established with unrealistic budget and schedule expectations from the beginning," says the 21 September report from a NASA-commissioned, 16-person advisory panel.

The top priority in planetary science, MSR would gather rocks collected by the Perseverance rover, which has been drilling samples since it landed on Mars in 2020. MSR would rocket the samples off the planet and ferry them to Earth, where scientists would study them for signs of past life.

The reviewers say one solution to the schedule crunch is to delay launch from 2028 to 2030. But that would raise costs from $8 billion to $9.6 billion and increase the strain on smaller missions, which have been delayed to accommodate MSR and other large, overbudget missions (*Science*, 15 September, p. 1143). Lower annual costs could be achieved by splitting the mission up and staggering its launches, but that could raise overall costs to $11 billion and push the mission further into the 2030s.

The review, led by Orlando Figueroa, NASA's former director of Mars exploration, also recommends giving NASA centers clearer authority over their parts of the project, merging MSR back into the agency's Mars Exploration Program, and selecting one leader to shepherd the project, with direct access to NASA leadership.

MSR's future is far from assured. The U.S. Senate has already expressed skepticism about its rising costs and raised the specter of cancellation. In the wake of the report, NASA has pledged to complete by early next year a review of the program. —*P.V.*

Technicians collecting carcasses to test for avian flu stop to examine a juvenile red-footed boobie.

PHOTO: GALÁPAGOS NATIONAL PARK DIRECTORATE

CONSERVATION

Deadly avian flu hits Galápagos

Concerns rise for boobies, finches, and other endemic species

By **Erik Stokstad**

In a development that has alarmed conservation biologists, the avian flu strain that has devastated birds and marine mammals on five continents has reached Ecuador's Galápagos National Park, home to species that are found nowhere else.

"It is extremely concerning," says Marcela Uhart, a wildlife veterinarian at the University of California (UC), Davis. "Outbreaks could pose an acute threat to the future of these endemic species."

So far only a few animals have tested positive for the H5N1 virus, which migratory birds can carry long distances. But the highly contagious pathogen is likely to spread fast through the Galápagos Islands' dense colonies of seabirds, seals, and sea lions. Warmer seas caused by an imminent El Niño climate pattern could make species even more vulnerable by depleting the ocean life that sustains them. Park authorities are already restricting access to some areas to prevent people from spreading of the virus, raising concerns among residents that outbreaks could depress tourism.

The H5N1 virus has circulated in Europe, Africa, and Asia for decades, sometimes causing large losses of poultry. In late 2021, a new, especially aggressive subvariant appeared in North America and soon spread—for the first time—to South America. In the Galápagos, "We were just waiting, wondering when an outbreak is going to happen?" says Gustavo Jiménez-Uzcátegui, a wildlife veterinarian with the Charles Darwin Foundation.

Last week, tourist guides noticed dead seabirds, including frigatebirds and red-footed boobies, on two islands. Park rangers and technicians from Ecuador's Galápagos Biosecurity Agency collected five carcasses; three tested positive. "We know this is the tip of the iceberg," Jiménez-Uzcátegui says. "We have eyes watching the whole archipelago."

The birds were likely infected with 2.3.4.4b, the new highly pathogenic H5N1 variant, says virologist Thijs Kuiken of Erasmus University Medical Center. That strain "is raging through South America," says wildlife virologist Wendy Puryear of Tufts University. Farmers have been ordered to kill millions of infected poultry, and sea lions and fur seals have been hit hard in Peru, Chile, Argentina, and Uruguay.

Managers have few options for slowing H5N1's spread on the Galápagos. Removing carcasses quickly appears to have helped in some outbreaks elsewhere, Puryear says. And because the virus can be spread on shoes, park authorities have already closed visitor sites on Genovesa and San Cristóbal islands where dead birds were found. They have also closed two important breeding colonies on Española Island, even though no birds have tested positive there.

Researchers studying the colonies are taking precautions, including keeping their distance from the birds. Park and biosecurity officials will be meeting with universities and others to coordinate monitoring and research efforts. The California Academy of Sciences is considering postponing an expedition to Floreana Island planned for November, although a large annual survey of Galápagos seabirds and sea lions is still scheduled for that month.

One continuing concern is that the virus will jump from highly susceptible species, such as gulls, to others so far less afflicted. The 18 species of Galápagos finches made famous by Charles Darwin, for example, live in close contact with large seabird colonies. (Researchers continue to study the finches, including a large genomic study on p. 1427 of this issue of *Science*.)

Disease is not a common cause of extinction, but contagious pathogens can push small populations to the point of no return, Kuiken says. Extinction risk is higher for species that only occur in one place, such as the Galápagos lava gull—the world's rarest gull with just 300 breeding pairs. The Galápagos penguin is also only found on the islands, but it is related to the Humboldt penguin, which has had high mortality from H5N1 in South America.

The coming El Niño is adding to concerns. El Niño often disrupts populations of fish, squid, and other prey for penguins, cormorants, and sea lions, and hunger can weaken immune systems and make animals more susceptible to disease. Luckily, this El Niño is not forecast to be especially severe, and penguin and cormorant populations are robust after 3 years of a La Niña weather pattern, which brought abundant prey.

To help reduce stress on species facing outbreaks, Uhart says, managers should step up conservation efforts, such as by reducing fisheries bycatch and preventing unregulated tourism. "Affected wildlife will need all the help we can provide."

Jaime Chaves, an evolutionary biologist at San Francisco State University who has studied birds on the Galápagos Islands for more than a decade, is coping with his worries by planning research. The Galápagos have always been a laboratory of evolution, and he wants to monitor how the virus, too, evolves there. "Evolution," he says, "is taking its course yet again in this new setting."

For now that's not much consolation. ■

With reporting by Jon Cohen.

CHEMISTRY

Molecular 'sponges' could be hydrogen fuel tanks

Cheap chemical cages could expand the use of the clean-burning gas as an industrial fuel

By **Robert F. Service**

Hydrogen seems like the perfect fuel. By weight it packs more punch than any other fuel. It can be made from water, meaning supply is almost limitless, in principle. And when burned or run through a fuel cell, it generates energy without any carbon pollution. But hydrogen takes up enormous volume, making it impractical to store. Compressing it helps, but is expensive and essentially turns hydrogen storage tanks into high-pressure explosives.

Now, a molecular sponge made of organic compounds and cheap aluminum promises a practical solution, holding significant amounts of hydrogen at low pressures. Described in a paper accepted last week at the *Journal of the American Chemical Society* (*JACS*), it is the latest in a series of promising metal-organic frameworks (MOFs), and it suggests that the materials could be close to a mass market application, serving as fuel depots for backup power sources at industrial operations.

"For the first time ever, we have sorbents that are potentially cheaper than compressed gas in a realistic application," says Hanna Breunig, a chemical engineer at Lawrence Berkeley National Laboratory who helped analyze the economics of using the aluminum MOF. To Omar Farha, a chemist at Northwestern University who wasn't involved in the new work, it shows that "this field is progressing at a really incredible speed."

Hydrogen is already in wide use as an industrial chemical, and storage has been a long-standing problem. The primary solution to date has been to compress hydrogen at up to 700 bar, some 50 times the pressure of an outdoor grill's propane tank. But the high-pressure tanks are costly, and energy-guzzling compressors are needed to fill them. And even then, a liter of hydrogen compressed to 700 bar stores less than one-fifth of the energy of a liter of gasoline.

Some researchers are exploring storing hydrogen in underground caverns carved out of salt formations—but that geology is rare, and subterranean microbes might eat up the hydrogen. Compounds such as metal hydrides or ammonia can store hydrogen chemically (*Science*, 13 July 2018, p. 120). But these compounds must undergo reactions to unshackle the hydrogen, and recharging the material can be difficult.

MOFs are now emerging as an alternative. These porous solids look like molecular Tinkertoys. Metal atoms serve as hubs that are tied together with organic linkers—carbon-bearing molecular chains. The result is a chemical cage with passageways and voids that trap gases injected under mild pressures. When the pressure is lifted, the hydrogen flows back out.

In 2014, Jeffrey Long, a chemist at the University of California (UC), Berkeley, and his colleagues reported a nickel-based MOF that could store a record amount of hydrogen: 23 kilograms per cubic meter, about half as much as a high-pressure tank, but without the danger and expense of added pressure.

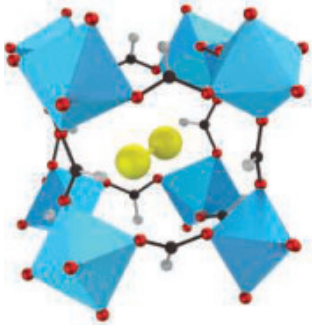

A metal-organic framework made with aluminum could store hydrogen (yellow) in voids.

IMAGE: CRAIG BROWN/NATIONAL INSTITUTE OF STANDARDS AND TECHNOLOGY

An MOF not only needs to soak up lots of hydrogen; it must also release it easily. The ideal binding strength—measured as the heat of absorption—is between 15 and 25 kilojoules per mole of hydrogen (kJ/mol). Below that range the grip is too loose, and the natural energy of hydrogen is enough for it to wriggle free of the cage. Above that range, the grip is too tight, and the system must be heated to push hydrogen out. "It's like a Goldilocks zone," says Hayden Evans, a chemist at the National Institute of Standards and Technology.

The nickel-based MOF has a near ideal binding energy of 14 kJ/mol, because the nickel atoms attract the slightly polar hydrogen molecule through weak electrostatic forces, Long explains. Baker Hughes, an offshoot of General Electric, is exploring using the material to store hydrogen and carbon dioxide captured from industrial furnaces.

In 2021, Long and colleagues followed up with a vanadium-based MOF that grabs hydrogen molecules more tightly at 21 kJ/mol, in the heart of the Goldilocks zone. But these MOFs store less hydrogen than their nickel-based cousins, because only a subset of the vanadium atoms have the right number of positive charges to attract hydrogen.

Competition is now rising from aluminum, which costs just over 1/10 as much as nickel and 1/13 as much as vanadium. In 2022, Anthony Cheetham, a UC Santa Barbara chemist, and his colleagues laid the groundwork when they reported an aluminum-based MOF that looked promising for capturing carbon dioxide. The aluminum MOF requires less energy to release the captured carbon than more conventional liquid carbon-capture compounds, and its small pore size naturally excludes nitrogen gas, the primary component of the atmosphere.

Now, in the *JACS* paper, Cheetham, Evans, and colleagues have tested the aluminum MOF for hydrogen storage. It stores just two-thirds as much gas as the nickel MOF. And with a binding energy of just 8.6 kJ/mol, it must be chilled to about –100°C to store its maximum amount of hydrogen. Nevertheless, Cheetham says the raw materials are so cheap that he expects the MOF to cost just $2 per kilogram. That would easily beat a $10 per kilogram community goal for the production cost of MOFs made from nickel and other more expensive metals. "It's hard to imagine any MOF being as cheap as this one," says Zeric Hulvey, who heads hydrogen storage at the U.S. Energy Department's Office of Energy Efficiency and Renewable Energy.

The modest storage capacity means the new MOF isn't likely to work for storing hydrogen in fuel cell vehicles, where volume and weight are critical constraints. However, the combination of low cost, mild operating pressures, and a manageable cooling requirement already points to a practical use, Hulvey says: storing hydrogen for backup power sources that could replace diesel generators at industrial operations, such as data centers.

Cheetham says he and his team want to show they can produce the aluminum MOF in large amounts, beyond the kilograms they can already synthesize. They're also working on tweaking the structure of the MOF, spiking it with small amounts of iron and other metals to see whether they can further increase its hydrogen storage capacity. Cheetham says: "There is lots of chemistry to explore." ■

U.S. Geological Survey divers in Price Lake, in northern Washington state, with a fresh cross section from a Douglas fir tree felled in an earthquake exactly 1100 years ago.

SEISMOLOGY

Faults teamed up 1100 years ago to produce Seattle megaquake—and could do so again

Tree rings give precise dates for ancient temblors, painting alarming picture of seismic risk

By **Michael Price**

In oral histories, the Salish people of the U.S. Pacific Northwest tell of a formative event in which a great serpent spirit, *a'yahos*, shook the earth, carving out cliffs and forming new lakes. The story mirrors geologic evidence that roughly between 900 C.E. and 930 C.E., whole forests were swept into lakebeds and new lakes appeared in the Seattle fault zone. But seismologists couldn't say whether the drowned forests, some more than 100 kilometers apart, died in independent temblors separated by decades, or whether the region's faults had linked up to produce a terrifying megaquake, bigger than anything a single fault could generate.

A study published this week in *Science Advances* supports the more dramatic scenario. It harnesses tree ring science and state-of-the-art radiocarbon dating methods to pin the tumult to a 6-month period bridging the years 923 C.E. and 924 C.E., suggesting a potent linked-fault earthquake.

The finding underscores the seismic risk to the populous Seattle area: If the faults simultaneously ruptured violently once, the authors say, they could do so again. "If faults rupture together, it raises the potential for larger earthquakes," explains geologist Lydia Staisch of the U.S. Geological Survey (USGS), who wasn't involved with the study.

In 2002, for example, a massive magnitude 7.9 earthquake struck along three connected fault lines near Alaska's Denali National Park. It was the United States's largest earthquake in 37 years and was felt as far away as Seattle. But linked fault quakes "would be unique for the Pacific Northwest," says Brian Sherrod, a Seattle-based geologist with USGS. "We have not experienced one [here] historically."

Sherrod has spent his career studying the region's seismic risk. Some elements of that risk are well mapped. Deep faults along the Cascadia Subduction Zone, a meeting of two tectonic plates off the coast, have ruptured in massive earthquakes in past centuries, and popular accounts have spelled out the immense devastation that would befall the region if it happened again. "We kind of know what might happen during a Cascadia Subduction Zone event," Sherrod says. "But the big unknown is these crustal faults."

The crustal fault zones near Seattle run directly under densely populated areas including Tacoma and Olympia and are much shallower than the Cascadia fault zone. So a big quake would transmit more energy to the surface within a smaller area. "That's just going to rock and roll," Sherrod says.

To find out whether the faults had linked

PHOTO: BRYAN BLACK

up in the past, Sherrod and Bryan Black, a tree ring scientist at the University of Arizona, studied trees felled by the ancient cataclysm. Tree ring scientists match annual growth ring patterns between living and dead trees, and can establish a continuous chronology for thousands of years. But Black also uses a new approach that relies on rare, dateable spikes in carbon-14 deposited in the rings by cosmic rays. Scientists have pinned a handful of those spikes, known as Miyake events, to single calendar years. Counting rings out from a dated Miyake event to the bark's edge yields the exact year a tree died.

By getting precise dates from Douglas fir trees swept into lakes by the ancient quake or quakes, Black says, he and Sherrod hoped "to see if these quakes were linked and happened in rapid synchrony." They used existing archives of ancient wood pulled from lakes as well as new cross sections obtained by USGS divers operating underwater hydraulic chainsaws. Some submerged forests were in the Seattle fault zone and others in the nearby Saddle Mountain fault zone.

In rings from several of the longer lived trees, Black spotted the telltale radiocarbon spike of a Miyake event at 774–775 C.E. Counting outward left no doubt: "Boom, 923," Black says. "That's the date."

He and Sherrod concluded that both fault zones ruptured between late fall 923 C.E. and early spring 924 C.E. Given the severity of the landscape shifts, they say the most likely scenario is that a single, massive earthquake around magnitude 7.8 ruptured across multiple faults all at once. The team can't rule out a series of earthquakes over 6 months, but statistics from past quakes suggest the linked-fault scenario is about three times more likely.

"This paper has been a long time coming, and it's really exciting," says Harvey Kelsey, a paleoseismologist at Humboldt State University.

Sherrod is now working to estimate how often such linked faulting may occur in the region, and what the risk of such a quake is today. In 2005, seismologists modeled the destructive potential of a magnitude 6.7 earthquake on the Seattle fault and found it would kill at least 1600 people and cause $50 billion in damages. A linked earthquake of magnitude 7.8 across the Seattle and Saddle Mountain faults would release about 38 times more energy and would likely trigger a local tsunami, the authors note.

The findings bolster the need for earthquake preparedness in the Seattle area, such as planning evacuation routes, Sherrod says. "If you're going to live here, you need to anticipate this and get ready." ■

COVID-19

MRI study charts organ damage months after COVID-19

Imaging revealed no signs of lingering heart problems

By **Catherine Offord**

Physicians have known since early in the pandemic that COVID-19 can affect multiple organs. But how long does the damage linger, and what does it mean for patients' recovery? In one of the most comprehensive post–COVID-19 MRI studies to date, scientists have found that about 6 months after infection, some 60% of hospitalized patients showed abnormalities in multiple organs, compared with 27% of people who never had the disease. Yet patients' hearts looked similar to those of uninfected people—a surprising result given previous research suggesting SARS-CoV-2 can wreak havoc on the organ.

"This is an intriguing study [that] adds to the growing literature on multiorgan impacts after severe COVID-19 infection," says Linda Geng, a clinician-researcher at Stanford University School of Medicine, adding that the findings "highlight the need for [a] multidisciplinary whole-person approach to post-COVID care." She cautions that the study only reveals associations between COVID-19 and organ damage, not cause and effect. Differences between the study's hospitalized and control groups could also explain some of the results, she and others note.

The study used data from 259 unvaccinated patients who were hospitalized with COVID-19 in 2020 or 2021. Roughly 5 months after being discharged, they underwent MRIs and blood and physiological tests, and answered symptom questionnaires. Researchers ran the same evaluations for 52 people who had no evidence of current or past SARS-CoV-2 based on polymerase chain reaction and antibody tests.

An interim analysis the team published last week in *The Lancet Respiratory Medicine* shows COVID-19 is associated with abnormalities in several organs. After researchers adjusted for confounding factors such as body mass index, patients were approximately three times as likely as uninfected people to have brain abnormalities, such as lesions in white matter. In scans of the lungs, heart, brain, kidneys, and liver, they were about three times as likely to show abnormalities in at least two organs.

The finding that hospitalized patients and controls had similar rates of heart abnormalities was counterintuitive, says study co-author and University of Oxford cardiologist Betty Raman, because clinicians do observe heart complications from COVID-19. The results may suggest the heart recovers relatively quickly from any damage.

Alternatively, heart abnormalities might be less strongly linked to COVID-19 than previously thought, says Steffen Petersen, a cardiologist at Queen Mary University of London who was not involved in the research. That 20% to 25% of both controls and hospitalized patients had unusual cardiac MRIs suggests many abnormalities in COVID-19 patients "must have been there beforehand." Patients with lingering cardiac symptoms might have disorders that weren't visible with MRI, or dysfunction in other organs, he adds.

MRIs were a poor predictor of how patients were faring overall. Kidney and brain abnormalities weren't associated with any patient-reported symptoms, for example. However, lung abnormalities correlated with coughing and chest tightness, and people who reported severe overall physical and mental impairment were more likely to have multiorgan abnormalities.

Such abnormalities can't be decisively attributed to COVID-19, says University of Washington biostatistician Daniela Witten. People in the control group were on average younger and healthier, and may have been less susceptible to organ damage. Without preinfection MRIs to compare against the postinfection ones, it's impossible to know which abnormalities were present already. And preexisting problems likely would have predisposed some patients to severe disease.

Nevertheless, studies like this one provide important data on how hospitalized patients fared, says Tanayott Thaweethai, a biostatistician at Massachusetts General Hospital. He adds he would like to see how the findings compare with MRIs of people hospitalized more recently, now that vaccinations are widespread and the dominant SARS-CoV-2 variants have changed.

Raman's team is still collecting data, and plans to investigate whether these MRI results can predict a person's need for hospital care in the future from COVID-19 or other illnesses. If so, MRIs for people who have had severe COVID-19 might help improve treatment and even speed up recovery. ■

AN UNHEALTHY CLIMATE

By **Tim Appenzeller**

This special issue of *Science* was supported by the Pulitzer Center and the Vapnek Family Foundation.

PHOTO: KYLE GRILLOT/BLOOMBERG/GETTY IMAGES

July's unprecedented heat in Palm Springs, California, drove people to a cooling center.

Earth scientists often call climate change a "great global experiment," which humanity is heedlessly performing as we pump greenhouse gases into the atmosphere. The dire consequences are already becoming clear—not just for the workings of the planet, but for our own health. The stories in this special package explore the threats, and how we can minimize them.

Vector-borne diseases are a special worry (p. 1388). A warmer climate favors the mosquito that spreads dengue and may already be fueling a worldwide surge in the debilitating disease. Warming may also have enabled malaria-carrying mosquitoes to flourish in Africa's cooler highlands and ticks that carry Lyme disease to advance northward. Migratory birds, which ferry cargoes of pathogens such as West Nile virus and influenza across continents, are changing the timing and routes of their journeys, with consequences that have yet to emerge (p. 1402).

Then there are the direct effects of heat on the human body. The worsening toll of heat waves is unmistakable, with thousands dying every summer, but researchers are also discerning subtler impacts. Among the most vulnerable to extreme heat are pregnant people and their fetuses. Epidemiological studies have already revealed links to preterm birth, low birth weight, stillbirth, and other complications, and now scientists are trying to understand the mechanisms (p. 1398).

As always when it comes to climate change, the health effects are likely to hit hardest in hotter, poorer parts of the world. But even in countries where air conditioning and window screens are scarce, adaptation is possible, as cities in India are now showing with efforts to plan for heat waves and promote cooler houses and public spaces (p. 1393). And when it comes to infectious diseases, we are far from powerless in the face of the growing threats. "Climate change matters," disease ecologist Colin Carlson told *Science*. "But public health interventions [are] 200 times more important."

Warming is making many places more suitable for the dengue-carrying mosquito *Aedes aegypti*.

FEELING THE HEAT

Researchers struggle to convey the complex impacts of climate warming on infectious disease

By **Kai Kupferschmidt**

In early July, on one of the hottest days ever recorded globally, Colin Carlson walked into a radio studio in Washington, D.C., to answer some questions about how a warming climate is affecting infectious diseases. Cases of locally transmitted malaria in Florida and Texas—not seen in decades—had made the national news. The radio host, Jenn White, asked Carlson whether these cases were linked to climate change.

Carlson, a disease ecologist just shy of his 27th birthday and already on the faculty at Georgetown University, was wearing flip-flops, shorts, and a heavy metal style T-shirt demanding "Medicare for all." On his left hand he had scrawled a reminder in large letters: "Don't swear."

The day before, in his office at Georgetown, Carlson's alarm about the planet's trajectory had boiled over. He recalled a paper he had read years ago: a modeling study suggesting that if the carbon dioxide levels in the atmosphere rose above 1200 parts per million, Earth's clouds could start to disappear. "It is not small potatoes, it is not this small, incremental change in the way that the world works," he said, stabbing the tip of his pencil into his notebook. "It's what if our planet didn't have fucking clouds?"

Infectious diseases, too, could undergo a dramatic shift as the globe warms, Carlson says. The list of plausible catastrophes is long. Mosquitoes and ticks carrying pathogens could multiply faster and spread farther, endangering ever more people. More frequent droughts and floods, a consequence of warming, could expose more people to deadly waterborne microbes such as the cholera-causing bacterium *Vibrio cholerae*. Migrating animals could mingle with species they have not encountered before, allowing pathogens to spread to new animal hosts and eventually humans. Respiratory infections could change their patterns, and fungi usually warded off by body heat could adapt to the world's higher temperatures and become more adept at infecting humans.

Disease ecologist Colin Carlson says the influence of climate change on diseases is powerful but nuanced.

But in the studio, Carlson explained calmly that the malaria cases in Florida and Texas probably could not be blamed on climate change. If cases of dengue had appeared in Washington, D.C., it would be much easier to make the link, he told White, because that disease is spread by different mosquitoes: "If we see something like that, it's very easy for us to say, 'OK, climate brought the mosquitoes, the mosquitoes brought dengue.'" But mosquitoes able to carry malaria have always lived in southern states. A traveler returning from abroad with the parasite in their blood is all it takes to seed local spread. "I think this is one of those weird edge cases," Carlson says. "This is just something that happens, but it looks a lot like the things that climate change will probably bring."

It is a position researchers like Carlson constantly find themselves in: caught between the nuance of now and the threat of tomorrow.

Defining that threat is not simple. The challenge is to do for infectious diseases what other researchers can now do for droughts or hurricanes: "attribute" events to climate change. "The very cutting edge right now is actually trying to start doing attribution … to say, for each degree of temperature change, how many more cases do we get?" says Erin Mordecai, an infectious disease ecologist at Stanford University.

Carlson and Mordecai are just two researchers working on this, but the complexity is staggering. Climate change influences temperature, humidity, and rainfall patterns as well as animal and human behavior. Each factor could affect a disease differently—and that effect could vary depending on whether the disease is caused by a virus, bacterium, parasite, or fungus and whether it is spread by mosquitoes, ticks, or another vector; through water; or through the air. One question is what will happen to a disease already prevalent in a region as its climate shifts. A different one is whether diseases will spread into new regions as the climate changes. And those are just the diseases we know about. Will new diseases be more likely to emerge?

The answers are important if the world is to prepare for the public health challenges that lie ahead. But linking climate and disease is a scientific problem wrapped in a communications challenge.

Researchers have made the most progress on the disease Carlson was talking about that morning on the radio: malaria, which kills more than half a million people every year. He believes he has made the best case yet that climate changes have increased malaria in some parts of Africa. But the broader story emerging from the work of Carlson, Mordecai, and others isn't straightforward.

DISEASE FORECASTING

Will flu outbreaks ease in a warming world?

From cold viruses to influenza to respiratory syncytial virus, viruses that spread through the air cause billions of infections each year. That makes it important to understand how they will respond to climate change. But little is known so far, except that different viruses will react differently. Measles, for instance, spreads efficiently in all climates, suggesting global warming will make little difference to its transmission.

For influenza, animal studies point to a different outcome. "We can place guinea pigs in environmental chambers and unpick the dependencies," says Jessica Metcalf, a disease ecologist at Princeton University. Humidity has emerged as a crucial factor: The virus transmits best in cold and dry environments, which may help explain winter flu outbreaks. As the climate warms, allowing the air to take up more water vapor, seasonal influenza epidemics are likely to become milder in most places.

But there is a catch. Today, transmission of influenza often falls to near zero between epidemics. As epidemics become less severe in a warming climate, the virus is more likely to circulate year-round in some places. That could have an effect on its evolution, says Brown University epidemiologist Rachel Baker. Without the periodic pauses, flu evolution may speed up, meaning for instance that vaccines might need to be updated more frequently.

As for the respiratory virus that has turned the world upside down for more than 3 years, SARS-CoV-2, so far scientists have no clue how it will respond. *–K.K.*

PHOTOS: MICHAEL A. MCCOY/THE NEW YORK TIMES/REDUX; (OPPOSITE PAGE) FERNANDO DA CUNHA/SCIENCE SOURCE

Some like it hotter

How fast mosquito-borne diseases spread depends in part on temperature, peaking at an optimum warmth and declining above and below it. Different combinations of diseases and vectors have different peaks. Carried by its usual mosquito vector, the most dangerous form of malaria peaks at 25°C, cool enough that climate change could decrease transmission in some regions. But dengue and Zika could burgeon in a warmer world.

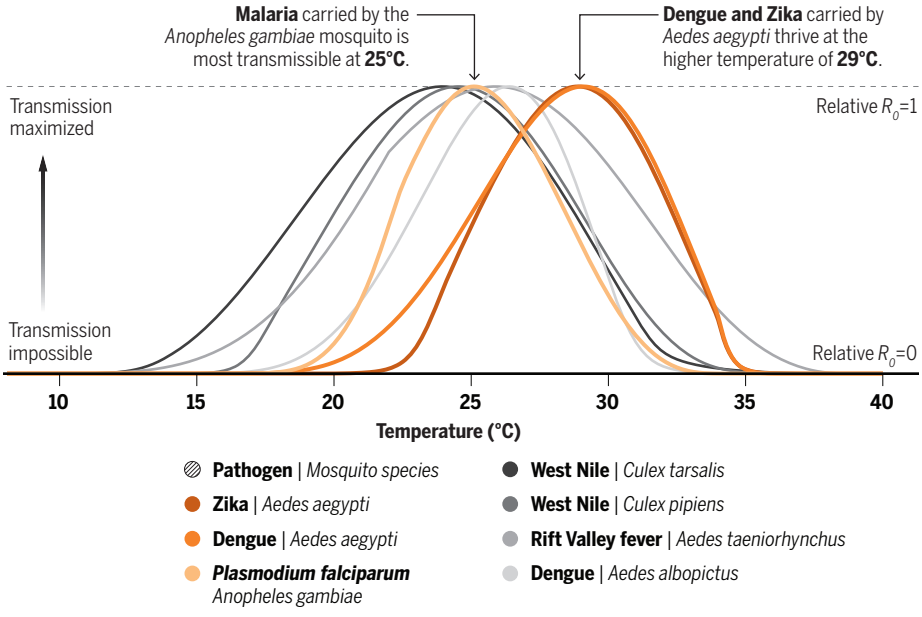

Building a transmission curve

Scientists start by measuring the effect of temperature on many different traits of a specific pathogen and a mosquito species that carries it: how long the mosquito lives, for instance, and how fast the pathogen replicates in the mosquito. The result is a series of curves, which are mathematically combined into a single curve relating temperature to disease transmission.

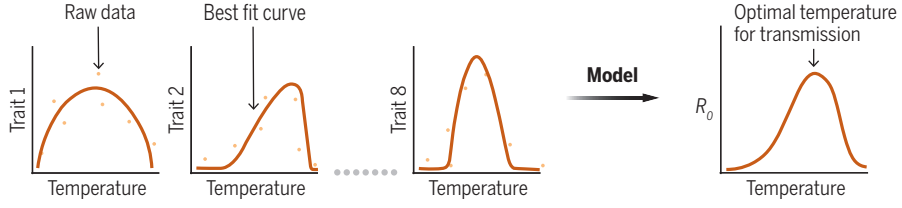

MORDECAI WAS STUDYING grasses when her interest in malaria began. As a graduate student at the University of California, Santa Barbara, in love with both math and biology, she focused on how plant pathogens spill over from invasive grass species to native ones. Then a paper by her adviser, ecologist Kevin Lafferty, raised an issue that seemed more urgent. He argued that the relationship between human diseases and climate would not be linear. Mordecai was intrigued. "And frankly, I got kind of sick of trying to explain to people why we should care about the coexistence of grass species, and I wanted to do something that was a little more directly relevant to people."

Mordecai set out to dissect how temperature affects both mosquitoes and the pathogens they carry. Mosquitoes are cold-blooded animals, and so temperature influences almost everything about their lives and potential to spread disease: how long they live, how many eggs a female lays per day, and how likely it is to bite. It also influences mosquito-borne pathogens, determining for instance how likely they are to establish themselves in the insect after it consumes blood from an infected person or animal and how long that takes.

In the lab researchers can study how temperature affects each trait. The relationship generally seems to be hump-shaped: an optimum at a certain temperature and an exponential decline as the temperature increases or decreases from that optimum. The same goes for humans, says Courtney Murdock, an infectious disease ecologist at Cornell University. "There are some temperatures that you experience that are too cold, and some temperatures that are too bloody hot. And there's the temperature that you'd like to hang out at, usually around 75°[F]," she says. "It's kind of the same thing for mosquitoes and for the parasites that they transmit."

Researchers like Mordecai mathematically merge all these measured temperature-dependent traits for a mosquito and a certain pathogen it carries into a single curve that shows how that disease's transmission changes with temperature (see graphic, left). That curve, too, is hump-shaped—which has some important implications.

"The baseline assumption is that warmer climate will make vector-borne disease worse because people observe that most [such] diseases occur in the tropics, and in more temperate places they occur in the summer," Mordecai says. But studies like hers show, she says, that "the effect of rising temperatures can go either way."

For many years the temperature optimum for malaria was pegged at about 31°C. But in a 2012 paper in *Ecology Letters*, Mordecai and others showed that was wrong. They concluded that the temperature optimum was dramatically lower: just 25°C. Above 28°C, transmission decreases rapidly. "If anything, climate warming is actually decreasing malaria transmission in a lot of sub-Saharan Africa," Mordecai says. In the highlands of South America and southern Africa, on the other hand, temperatures increasingly favor malaria transmission. And in once-malarial regions of Europe and North America that have controlled the disease, keeping it in check may become more challenging.

But zooming in on the relationship between a mosquito, a disease, and temperature leaves out many other climate-related factors. Rainfall patterns are changing, extreme weather events like droughts or floods are more frequent, and people are migrating in response to these global changes. All will put a stamp on disease patterns.

THAT'S WHY SOME scientists trying to tease out climate-disease links are looking to the past, combing historical data for signs that climate change has already affected disease incidence in the real world. One set of data on malaria, from the Kericho tea estates in the eastern highlands of Kenya, has sparked an academic fight that has been raging for decades.

The company running the estates, Brooke Bond Kenya Ltd., provided health care for all employees and their families and kept meticulous records. In the late 1990s, a scientist at the U.S. Army Medical Research Unit in Nairobi named Dennis Shanks "climbed up into a loft in the Kericho tea estate and managed to identify some boxes of malaria admissions and cases going all the way back to 1965," says Robert Snow, a malaria researcher at the Kenya Medical Research Institute.

Shanks, Snow, and others digitized and

CREDITS: (GRAPHIC) M. HERSHER/*SCIENCE*; (DATA) E. MORDECAI *ET AL*., *ECOLOGY LETTERS*, **22**, (2019)

A woman in Lagos, Nigeria, is one of hundreds of millions of people who develop malaria each year. Warming has likely increased malaria in sub-Saharan Africa, one analysis shows.

PHOTO: SADAK SOUICI/ZUMA PRESS WIRE

analyzed the records, reporting in 2000 that they revealed a dramatic increase in malaria during the 1990s. But the mean monthly temperature in the region had not changed significantly in this time, the researchers noted. "It seems plausible to assume that factors other than climate change would have led to the precipitous rise in malaria warranting inpatient care during the 1990s at the Kericho tea estates," they wrote, pointing to lapsed mosquito control programs and an "epidemic of drug-resistant malaria" sweeping the region.

The paper kicked off a heated back and forth. In 2006, Mercedes Pascual, a computational ecologist at New York University, published a new look at the estates' temperature data, showing there was indeed a warming trend there if a longer time period was considered. The dispute was important, she says, because "it was clear that one of the places where we should see the strongest impact of climate change [on malaria] were the highlands."

The medical data, one of the few long-term records of malaria, were reanalyzed again and again. "Everyone and their tennis partner have sort of downloaded it and tried to match it to climate data," says Snow, one of the authors of the original paper. In a 2002 paper reiterating that climate had played no role in the resurgence of malaria, Snow and others wrote that they hoped their work would "help focus attention on the real and immediate causes of these malaria resurgences."

He and other malaria researchers worry that the growing focus on climate change is a distraction from more pressing questions about how to deliver antimalarial measures to those who most need them. "I don't for one minute doubt the significance to the planet of global warming," Snow says. "But in the malaria space, I do feel that it gets more attention than it deserves."

Pascual disagrees. "The research efforts, the funding, everything related to malaria has been much, much bigger for public health in general than it is for climate change. It is only recently that some of this research on climate and disease is attracting more real attention."

CARLSON'S RECENT WORK is drawing some of that attention, because he claims to have pinned down the influence of climate on malaria. A child prodigy who started at the University of Connecticut at 12 years old, he originally studied how likely parasites were to go extinct because of climate change, then shifted to how climate change would affect the diseases that parasites cause. "Parasites led me to disease and

DISEASE FORECASTING

A time of cholera

When the World Health Organization called attention in 2022 to a surge in cholera outbreaks around the globe, it listed the usual factors that favor waterborne diseases: lack of sanitation, humanitarian crises, and conflict. But it also said climate change was worsening the situation.

Cholera is caused by *Vibrio cholerae*, a bacterium that can produce a toxin and spreads when the stool of infected people contaminates drinking water and food. Microbiologist Rita Colwell has long argued that warmer surface waters can favor the emergence of the bacterium. Whether this plays any role in the large outbreaks around the globe is contested. But another climate link is clear. Floods can aid spread by causing latrines to overflow into water sources, for instance, and droughts can boost the concentration of the bacterium in shrinking ponds and streams and force people to use unsafe water.

Climate change is making such extreme weather events more frequent, so cholera is likely to surge in a warming world, says Andrew Azman, an epidemiologist at Johns Hopkins University. But there is little consensus on the magnitude of the effect. "It is really, really hard to attribute any of the current cholera cases to climate change," Azman says—in large part because there are few good long-term data on cholera. The same caveat applies to other waterborne diarrheal diseases, which some researchers suspect will also increase in a warmer world. —*K.K.*

disease led me here," Carlson says. There is a personal element in his interest in climate change. Given his age, Carlson says, "I am going to live through more of climate change than most of my colleagues."

He decided to investigate the role of climate in malaria with methods from a field known as climate econometrics, which has been used, for instance, to estimate how human-caused climate change has affected food production and conflict. The method is essentially an elaborate game of scientific "what if." Using a new and larger data set covering 115 years of malaria in sub-Saharan Africa that Snow had published in 2017, Carlson and his colleagues developed 1000 plausible models of how temperature shifts, floods, and droughts could have contributed to the changes in the disease's incidence. With them, the team then simulated thousands of alternative worlds with no climate change, allowing comparisons of malaria incidence in those "what if" worlds with the real world. That let them estimate the odds that climate change has worsened the disease.

In a preprint earlier this year, Carlson's team reported a 66% likelihood that humanmade climate change has already increased malaria in sub-Saharan Africa as a whole. They estimate that for every 100,000 children there between ages 2 and 10, 84 cases of malaria can be attributed to climate change at any time. That may not sound like a lot, but with about 300 million children in that age range in sub-Saharan Africa, "there are probably right now more than 200,000 children who have malaria, who would not have it without climate change," Carlson says. "That's a huge impact, not just in terms of total mortality, but also cumulative impact of that burden of disease." That impact is highest in eastern and southern Africa, whereas climate change has probably reduced malaria in west and central Africa over time, he and his colleagues concluded.

"Our study resolves a decades-old debate about one of the earliest health impacts of global warming," Carlson writes in the preprint's abstract. But the study has not been peer reviewed yet. And there are important caveats. One is that even in the regions with the highest impact of climate change, the malaria increase pales in comparison with the reduction that public health measures such as bed nets, vector control, and treatments have achieved. "We can hold in our head both thoughts," Carlson says. "Climate change matters. But public health interventions have been 200 times more important."

Carlson's study also offers hope, suggesting that as the climate keeps warming, the trend will reverse and actually lead to a net reduction in malaria across the continent by the middle of the century even if global warming is curbed at 2°C.

THAT MAY SOUND reassuring, but the outcome may be very different for other mosquito-borne diseases, Mordecai's transmission curves show. Some have much higher temperature optimums than the most deadly form of malaria, which is caused by the *Plasmodium falciparum* parasite carried by the mosquito *Anopheles gambiae*. "Everything to the right of *falciparum* malaria [on the temperature diagram]—Rift Valley fever, Ross River virus, dengue, Zika—that is going to have experienced and will experience much greater increase due to climate change," Carlson says.

Dengue is a particular worry. The virus already causes hundreds of millions of infections a year and an estimated 20,000 deaths, and the threat is only likely to increase as the world warms. "Whereas climate change is driving malaria in different directions in different places, it's kind of driving dengue in the same direction in every place," Mordecai says. On top of that, urbanization and a lapse in mosquito control have led to a resurgence of dengue-carrying *Aedes aegypti* in many places. "Dengue is the one that's really predicted to get worse and is getting worse."

Even for malaria the respites may be transient. The mosquito and parasite could adapt to higher temperatures. And another mosquito carrying the same parasite, *Anopheles stephensi*, could become more important, Murdock says. "*Stephensi*, which is the urban malaria that's now expanding throughout Africa, actually tolerates much higher temperatures," she says.

The complexities are no less daunting for diseases that don't depend on insects to spread (see sidebars, left and pp. 1389 & 1391). Influenza, for instance, follows a seasonal pattern, surging in winter—and not just because people collect indoors, but also because cold, dry air favors its transmission. Changes in air temperature and humidity will surely affect the spread of the virus, and perhaps even its evolution, but just how isn't clear. "It's an unbelievably tortured tangled thing," says Jessica Metcalf, a disease ecologist at Princeton University.

COMMUNICATING ALL THIS complexity and uncertainty is challenging. Broad and easily understood statements such as "mosquito-borne pathogens will thrive in a warming world" can be seductive but misleading, Carlson acknowledges. Yet conveying the nuances—that climate change may end up causing more malaria in some places and less in others—risks blurring the urgent message that climate change is a threat to public health. "I don't think the science is getting walked back," Carlson says. "I think that there is this impossibly high rhetorical bar that we've created for what the science is supposed to look like for it to be a dramatic health impact."

Just a few weeks after Carlson's radio interview, the next communication challenge arose: Another locally transmitted malaria case was reported in the United States, this time in Maryland, which had not seen such a case in 40 years. "I mean that is just really weird," Murdock says. Still, climate change probably isn't behind this malarial threat.

At least not yet. ■

DISEASE FORECASTING

Will fungal diseases come in from the cold?

It came as a nasty surprise when *Candida auris* suddenly started to cause deadly infections in 2011. The yeast was resistant to major classes of drugs and killed more than one-third of known patients who developed invasive infections. Even more surprising, *C. auris* infections had apparently emerged simultaneously around the world. "There was just no good explanation," says Arturo Casadevall, a microbiologist at the Johns Hopkins Bloomberg School of Public Health. "Why should a fungus that is not known to medicine all of a sudden appear in three continents at the same time?"

Casadevall had a hypothesis ready to go: climate change. In a 2010 paper in *mBio* he and Mónica García-Solache, then at Yeshiva University, laid out a simple argument: Humans are largely protected from fungal infections by their high body temperature, which slows fungal growth. But as the climate heats up, this "thermal barrier" could erode as fungi in the environment adapt to higher temperatures. That happened with *C. auris*, Casadevall now says—and the same thing might be expected of other fungal diseases.

For now, he says, it is just a hypothesis. But in 2021 *C. auris* was found in the environment, on an island in the Indian Ocean. The discovery suggested the infectious strain could have originated in the soil, not an animal host. These environmental samples grew poorly at body temperature, suggesting it took an evolutionary leap—perhaps propelled by climate change—for the fungus to turn deadly. —*K.K.*

HEAT-PROOFING INDIA

Cities in India are testing measures that could help urban populations worldwide cope with rising temperatures

Cities like Nagpur are experiencing more frequent and longer heat waves.

By **Vaishnavi Chandrashekhar**, *in Mumbai, India; Photography by* **Atul Loke**

In Lal Matti, an informal settlement of tin-roofed homes in this coastal city, summer can be unbearable. Before the monsoon rains arrive, temperatures can top 37°C, with humidity at a sweltering 95%. The hot, muggy afternoons are particularly oppressive, says Tamrunissa, a young woman who lives with her extended family in a large room above a shop, accessed by a ladder. Despite running three small ceiling fans all day—the family can't afford an air conditioner—she often gets headaches from the heat, and her children fall sick. Her elderly father, who has diabetes and high blood pressure, retreats to an alcove below the apartment to nap. "He can't handle the heat up here," she says.

Sometimes, Mumbai's heat becomes deadly. In April, on a day the temperature reached 36°C, 11 people sitting through an hourslong outdoor ceremony died from heat stroke. At least 20 others were hospitalized.

Indians are increasingly at risk from extreme heat and heat waves that are more frequent and last longer. The country saw a 55% rise in heat-related deaths between 2000–04 and 2017–21, according to research published last year in *The Lancet*. Global warming will continue to elevate the risks, particularly in India's fast-growing urban areas, where heat-absorbing tar and concrete boost temperatures. By 2025, cities are expected to house more than half of India's population, now at 1.7 billion.

Architect Rajashree Kotharkar (top) runs one of India's longest running urban heat studies, in the city of Nagpur. Sensors deployed there (bottom) have helped identify neighborhoods and populations most at risk from heat.

PHOTOS: ATUL LOKE

"It is a very clear story of increasing hazard," says social scientist Chandni Singh, a climate researcher with the Indian Institute for Human Settlements. "The combination of climate change–driven heat and urban heat, generated by buildings and roads, means that many more cities are going to suffer from extreme heat." The most affected, she adds, will be the millions of urban poor who can't afford air conditioning or labor outdoors.

Historically, India's disaster planning efforts focused on addressing cyclones and floods. It wasn't until 2015 that officials designated heat waves as a natural disaster at the national level. But now, India is emerging as a laboratory for a world coping with climate change, as researchers try to better understand the risks posed by heat and find ways to prevent the worst outcomes.

In some cities, researchers have been working with authorities to improve emergency response plans that guide decisions on when to issue heat alerts and open cooling centers. Some are also experimenting with inexpensive ways to retrofit dwellings to make them cooler. Others are studying how land use and architecture influence temperatures in different neighborhoods, producing insights that could reduce the impact of future urban expansion.

It's urgent to turn such research into action, says Rajashree Kotharkar, an architect and urban planner at the Visvesvaraya National Institute of Technology who leads one of the country's longest running heat studies. Science must "evolve, keep pace," Kotharkar says. "We aren't mathematicians doing something abstract that will find application hundred years down the line. Whatever research we do should also provide some solutions for this particular time."

KOTHARKAR'S URBAN HEAT research project is based in one of India's hottest cities: Nagpur. The city of 3 million sits in the semiarid plains of central India, where summer temperatures can reach nearly 49°C.

One morning in May, on a narrow lane lined with apartment buildings in Nagpur's Mahal neighborhood, researcher Parikshit Dongarsane clambered up a wall to retrieve a sensor attached to a slender pole. A colleague then plugged the sensor, which had been recording temperatures and humidity levels for a month, into a laptop and downloaded its data.

It was just the first stop on a long, blazingly hot day in the field. Equipped with hats, water bottles, and even packages of oral rehydration solution, the young researchers retrieved data from 14 sensors across the city. Kotharkar set up the network as part of a decadelong effort to map how temperatures vary across the city and

gain insight into how the built environment shapes microclimates.

Some of the results have been surprising. One might assume, for instance, that daytime temperatures would be highest in relatively dense and treeless neighborhoods like Mahal, which sits near the city's center. But the sensors often record the highest daytime readings in the less built-up and slightly greener areas on Nagpur's outskirts. That's likely because more open land is directly exposed to the Sun there, Kotharkar says. Those fringe areas are usually cooler at night, she adds. Downtown, denser buildings block trapped heat from radiating into the sky, and the nights remain hotter.

That daily pattern has implications for human health, Kotharkar notes. Research has shown that unusually warm nights can contribute to health problems, especially when they follow hot days, because the body gets no respite from the heat. And consecutive hot days and hot nights are becoming more frequent in India, studies have found.

Kotharkar's team is also examining how other meteorological factors—such as humidity and wind speed—affect heat stress. And it is looking at how infrastructure and socioeconomic factors can shape vulnerability to that stress. Poorer people may not be able to afford air conditioners or other cooling devices, for example, and the elderly may have ailments that make them more susceptible to heat. (Most of those who died in Mumbai's April heat tragedy were older.) Some neighborhoods lack the water supplies or health clinics that can help tackle heat-related illness. Nagpur's outlying areas might experience cooler nights, for example, but they also have less access to health services.

How people perceive heat can also be important, Kotharkar's team has found. During a heat wave last year, researchers set up mini–weather stations on sidewalks and interviewed passing pedestrians, to see how objective data such as temperatures lined up with the subjective experience. Even at temperatures of 45°C, many of those interviewed expressed little concern. "People would say: 'It's always been like this,'" Kotharkar says.

The nonchalance is worrying, she says, because it suggests people are not aware of the dangers posed by heat—and might not pay heed to official heat wave warnings. One take-home message, Kotharkar says, is "people who live in hot regions are not always able to see heat as a risk."

Nagpur, India, residents quench their thirst at a roadside refreshment stand. Adequate access to drinking water can help vulnerable populations cope with extreme heat.

PHOTO: ATUL LOKE

SUCH FINDINGS have important practical applications, particularly in helping cities develop or improve heat wave response plans.

These heat action plans, or HAPs, have been proliferating in India in the past few years. In general, an HAP spells out when and how officials should issue heat warnings and alert hospitals and other institutions. Nagpur's plan, for instance, calls for hospitals to set aside "cold wards" in the summer for treating heatstroke patients, and advises builders to give construction laborers a break from work on very hot days.

The first HAP was introduced in 2013 in the arid western Indian city of Ahmedabad, with the help of local scientific institutions as well as the nonprofit Natural Resources Defense Council (NRDC). That plan's success—a study published in 2018 estimated it had saved at least 1190 lives—spurred the creation of more. India's disaster management agency is now working with 23 of India's 28 states to develop HAPs.

But implementation of existing HAPs has been uneven, according to a March report from the Centre for Policy Research (CPR), a prominent Indian think tank. It reviewed 37 plans adopted by cities, states, or administrative districts.

Many lack adequate funding, it found. And their triggering thresholds often are not customized to the local climate, says Dileep Mavalankar, director of the Indian Institute of Public Health, who has been closely involved in Ahmedabad's HAP. In some areas, high daytime temperatures alone might serve as an adequate trigger for alerts. Ahmedabad, for example, set its threshold for initial alerts at 41°C based on data showing that heat-related deaths began to climb at that point. But in other places, nighttime temperatures or humidity might be as important a gauge of risk as daytime highs.

Mumbai's April heat stroke deaths highlighted the need for more nuanced and localized warnings, researchers say. That day's high temperature of roughly 36°C was 1°C shy of the heat wave alert threshold for coastal cities set by national meteorological authorities. But the effects of the heat were amplified by humidity—an often neglected factor in heat alert systems—and the lack of shade at the late-morning outdoor ceremony. Ironically, the state of Maharashtra, which includes Mumbai, had adopted its own HAP just 2 months before the tragedy. It advised shifting outdoor events to early mornings on hot days.

To help improve HAPs, Kotharkar's team is working on a model plan that outlines best practices and could be adapted to local conditions. Among other things, she says, all cities should create a vulnerability map to help focus responses on the populations most at risk. (The CPR study found that only two of the 37 HAPs it examined identified the most vulnerable populations.)

Such mapping doesn't need to be complex, Kotharkar says. "A useful map can be created by looking at even a few key parameters." For example, neighborhoods with a large elderly population or informal dwellings that cope poorly with heat could get special warnings or be bolstered with cooling centers. The Nagpur project has already created a risk and vulnerability map, which enabled Kotharkar to tell officials which neighborhoods to focus on in the event of a heat wave this summer.

HAPs shouldn't just include short-term emergency responses, researchers say, but also recommend medium- to long-term measures that could make communities cooler. In Nagpur, for example, Kotharkar's team has been able to advise city officials about where to plant trees to provide shade. HAPs could also guide efforts to retrofit homes or tweak building regulations. "Reducing deaths [in an emergency] is good target to have, but it's the lowest [target]," Singh says.

Traditional architectural features, such as shaded porches (left), can help keep homes cool. In Jodhpur, India, heat mitigation programs provide poorer residents with special reflective white paint to cool their roofs (right).

IN THE LONG RUN, cooling India's cities will mean changing the way they are built. One possibility is to look to the past, when structures were designed to insulate people from their local climates.

In Nagpur, Kotharkar likes to show her students—and visiting reporters—a one-story, 300-year-old mansion in Mahal. It is built of brick, stone, and wood, not the concrete and plastics that make nearby modern apartment blocks absorb and radiate heat. The walls are thick, delaying heat gain. A double-layered roof provides extra shade and ventilation, and a courtyard allows hot air to float into a natural sink—the sky. Smaller windows on the external walls, along with the courtyard, help create differences in air pressure that keep air moving and cool temperatures.

On a May morning, the outdoor temperature is 39°C, but the ground-floor rooms feel comfortable and the interior courtyard, with its fountain flowing, is almost cool. "When the temperature outside is highest, at say 2 p.m., the inside isn't so hot," Kotharkar says. "And by the time the inside temperature peaks, the outside has started cooling down."

In recent years, India's housing ministry has produced detailed guidelines for constructing climate-resilient buildings, which include some principles drawn from traditional architecture. But the recommendations remain largely on paper, with builders and local government slow—or reluctant—to change their practices. To make cool building easier, Kotharkar's dream is to create a predictive model, perhaps even an app, that local officials can use to forecast the impact of a new building or development policy on local temperatures—and plan for mitigation if needed.

Given the rapid pace of development in India's large cities, Singh warns that "there's a narrowing space" to erect cooler architecture. Still, Kotharkar sees hope in smaller towns where growth is just beginning to accelerate. "We're so focused on the big cities," she says, "we forget the smaller ones are still manageable."

FOR MANY LOW-INCOME Indians living in cities, the possibility of moving to a newly constructed, climate-resilient residence is remote. That is why some groups are retrofitting existing homes.

The most popular retrofit involves covering roofs with white reflective paint. Ahmedabad was the first city to experiment with this technique in 2017, as part of its HAP. The project, which was supported by NRDC and the Mahila Housing Trust, a local women's group, has had encouraging results. One assessment found that homes with painted tin roofs were at least 1°C cooler than nonpainted ones, and more

PHOTOS: (LEFT TO RIGHT) ATUL LOKE; REBECCA CONWAY/GETTY IMAGES

expensive roofing technologies produced cooling of up to 4.5°C.

In 2020, Ahmedabad expanded its cool roof program to cover 15,000 low-income homes. This year, the desert city of Jodhpur launched a similar initiative, and in April the state of Telangana pledged to create 300 square kilometers of cool roofs by 2028.

In Mumbai and other cities, meanwhile, a private firm called cBalance is testing other low-cost passive cooling interventions for poorer households. Among those selected for the experiment this year: Tamrunissa's family in Lal Matti.

To cool her house, cBalance workers lined her ceiling with aluminum foil, providing insulation against the heat from the tin roof. But the bigger intervention was the installation of a second roof, made of panels of recycled plastic waste, a little above the original. From her kitchen window, Tamrunissa can reach out to pull a lever to close the panels in the morning, creating a shield against the Sun, and then open them again at night, allowing heat to radiate.

"It's like wearing a hat," says environmental engineer Vivek Gilani, the firm's founder. "The [extra] barrier doesn't allow heat to accumulate in the roof, and what does accumulate gets released into the sky at night."

The new roof has made a real difference for Tamrunissa and her family. This summer has been more comfortable than usual, she says. "We can sleep better."

A philanthropic foundation provided the funding for those improvements. But finding money to pay for cooling solutions remains a challenge, says Abhiyant Tiwari, NRDC's lead climate resilience and health consultant in India. The special paint, for example, can cost several thousand rupees, a large outlay for poorer families. To save money, some have tried painting their roofs with regular white paint. But it has a different formulation and doesn't work, says Savitaben, who worked on a cool roof project in New Delhi with the Mahila Housing Trust and goes by one name.

In Mumbai's slums, Gilani and cBalance have encountered obstacles beyond funding. Shading panels can't be installed on some roofs because they are crisscrossed by power lines or being used for other purposes. They've also had to ensure that roof modifications don't interfere with the waterproofing measures that protect homes against the intense rains of the annual monsoon.

Despite these challenges, researchers and engineers remain motivated to find cooling solutions for India's cities, especially for their most vulnerable inhabitants. "Cooling is not a matter of luxury," Tiwari says. "It's a matter of justice." ■

Vaishnavi Chandrashekhar is a journalist based in Mumbai, India.

Mercy, 7 months pregnant, walked 35 minutes to collect water in rural Kilifi County in Kenya last year. Pregnant women in the county regularly work outdoors in intense heat.

EXPECTING EXTREMES

Intense heat is a particular hazard in pregnancy. New studies are probing why

By **Meredith Wadman**, *in Sydney*

Jem Cheng was soaked with sweat by the time she climbed off the stationary bike at the University of Sydney last month. The work of pedaling wasn't the problem; the 30-year-old pushes herself much harder during her own regular workouts. But this ride took place in a "climate chamber," a large, high-ceilinged room that on this day was heated to 36°C. During Cheng's 86 minutes of pedaling, the humidity in the chamber gradually ramped up from 38% to a deeply uncomfortable 56%, making the air feel more like 46°C. "I feel like I could have stayed in there for a little bit longer," she said later, after weighing in to discover she had sweated off nearly 1 kilogram. "But I probably wouldn't have wanted to."

Cheng is a postdoc at the university's Heat and Health Research Incubator (HHRI), and her ride was just a demonstration. But starting soon, dozens of pregnant women will be pedaling in the same climate chamber. The groundbreaking study seeks to replicate what tens of millions of pregnant people experience every day in a warming world: physical exertion in intense heat. The trial is funded by £2 million from the Wellcome Trust, which awarded £16.5 million this year to projects probing why heat is a risk during pregnancy.

That risk is already undeniable. Dozens of epidemiological studies have linked heat exposure to poor outcomes including preterm birth, low birth weight, stillbirth, and congenital anomalies in the fetus. Premature birth is the most commonly documented: A 2020 literature review found that each 1°C increase brought a 5% increase in the risk of prematurity in hot areas or seasons—and a 16% increase during heat waves. That means climate change could exacerbate a major risk: Globally, prematurity is already the leading cause of death for children younger than 5.

A smaller number of studies, almost all from high-income countries, has suggested heat exposure also imperils the pregnant person: It has been associated with gestational diabetes and preeclampsia, a dangerous condition marked by high blood pressure. And a study of more than 400,000 pregnancies in Southern California published this month in *JAMA Network Open* found long-term heat exposure during pregnancy increased the risk of severe maternal illness during labor by 27%. The impacts may be worse in low-income countries in the Global South that face the greatest threats from climate change—and where pregnant people are more likely to be exposed to prolonged physical labor in hot environments. But, "There is very little data from regions we know are particularly vulnerable," says Ana Bonell, a clinician and epidemiologist at the Medical Research Council Unit The Gambia at the London School of Hygiene & Tropical Medicine. Bonell has studied heat stress in pregnant Gambian subsistence farmers and has Wellcome funding to expand her work there.

A pregnant woman in a climate chamber at the University of Sydney, where researchers are planning a study to define safe heat exposure limits for pregnancy.

PHOTOS: UNIVERSITY OF SYDNEY/STEFANIE ZINGSHEIM; (OPPOSITE PAGE) CLIMATE HEAT MATERNAL NEONATAL HEALTH AFRICA CONSORTIUM

Even in wealthy nations that are investing heavily to prepare for climate change, specific risks to pregnant people are rarely acknowledged in heat or disaster plans and related documents. There is little research to go on. How pregnant people respond biologically to heat stress, how fetal risk varies across the weeks of pregnancy, and the safe limits for heat exposure are all uncertain.

Those unknowns helped inspire the new application for the HHRI climate chamber, which the Sydney researchers have used to study heat exposure among athletes, children, and the elderly, and to simulate conditions on garment factory floors in Bangladesh. Having finished a small initial trial, the team will spend the next several years recruiting pregnant participants to cycle in the chamber. "We're very passionate about trying to get evidence that is applicable to women in pregnancy," says Adrienne Gordon, a neonatologist and stillbirth researcher at Sydney and the Royal Prince Alfred Hospital, who is co–lead investigator on the climate chamber study.

The Sydney team will combine its data with measurements from a companion study of pregnant women wearing temperature sensors, run by collaborators in urban India and rural Bangladesh. The result will be a first-of-its-kind model aimed at designating safe limits for heat exposure during pregnancy. Such concrete advice is vital, says the study's other co-lead, Ollie Jay, a thermal physiologist at Sydney who directs HHRI. "Otherwise, all we have is: 'Avoid extreme

heat,' or 'Avoid hot weather,' or 'Avoid exercise,'" he says. "That's very difficult for many of the most vulnerable."

PREGNANT OR NOT, humans normally maintain their core temperature—the temperature of their internal organs—at about 37°C. To keep that temperature from rising, we must lose heat as fast as it is produced by the body and absorbed from the environment. Our most efficient mechanism for losing heat is sweating.

Much of what scientists know about the body's response to heat comes from studying men. "Healthy, young, white males [are] the classic sort of test subjects for understanding thermoregulatory response," says Caitlin Wyrwoll, a reproductive physiologist at the University of Western Australia who is also embarking on a Wellcome-funded study of extreme heat and pregnancy complications. For instance, a model called the Universal Thermal Climate Index (UTCI) is widely used to gauge heat stress in different environmental conditions—including for studies of pregnancy. But it's based on a 73.5-kilogram man with 14% body fat. In the U.S., women of reproductive age who don't have overweight or obesity typically carry between 20% and 31% body fat, a percentage that bumps up during pregnancy, making the model's assumptions far from fit for purpose.

This matters because it's vital that pregnant people maintain normal core temperatures. The evidence comes not just from data linking heat exposure and poor pregnancy outcomes, but also from studies showing that running a high fever in pregnancy, especially in the first trimester, is linked to fetal abnormalities, including neural tube defects, heart malformations, and oral clefts. These studies helped establish 39°C as the "teratogenic" threshold. (Teratogens are factors that cause fetal malformations.) Yet studies of core temperature regulation in pregnancy are scarce. What's more, virtually all research on heat and pregnancy has involved only cisgender women.

Scientists have long assumed that pregnant people don't thermoregulate as well as others. They gain substantial weight, which means that relative to their body mass, they have less skin surface to dissipate heat. More than one-quarter of that additional weight is fat, which, compared with other tissues, requires less heat to raise its temperature. Fat also insulates the body, making it harder to offload heat. And the task of building another human being is itself an energy-intensive process that generates a lot of internal heat (see image, below).

Yet pregnant people have additional tools that apparently aid thermoregulation. By the third trimester, the volume of plasma, the noncellular, fluid component of blood, has increased by 50% or more. That allows more fluid to be shunted to vessels in the skin that dilate in response to heat stress, releasing heat into the environment to cool the blood. (This works as long as the air is cooler than the body; if not, sweating kicks in.) Small arteries and arterioles in the limbs also relax over the course of pregnancy, enhancing blood flow and cooling. One 32-year-old study suggested pregnancy also lowers the body's threshold for sweating. That study and others also found a woman's core temperature ticks steadily downward during pregnancy. And the Sydney researchers' smaller study, of 15 pregnant women who cycled at 32°C in the HHRI climate chamber during their second and third trimesters, showed that they safely regulated their internal temperatures, performing as well as or better than nonpregnant controls. None of their core temperatures even hit 38°C.

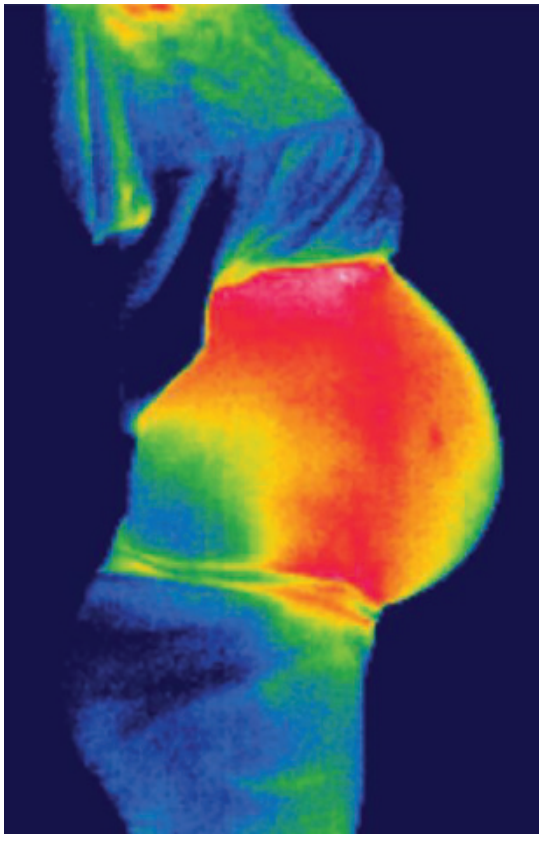

Internal heat generated by a growing fetus penetrates all the way to the skin, as shown by the red zone in this thermal scan.

UNCOMFORTABLE INDOOR cycling hardly captures the kinds of heat exposure facing women in rural Kilifi County in Kenya, one site in a multicountry study called Climate, Heat and Maternal and Neonatal Health in Africa, better known as CHAMNHA. There, a team led by medical anthropologist Adelaide Lusambili of Africa International University conducted interviews with dozens of pregnant women, new mothers, male partners, mothers-in-law, community health care workers, and community leaders in 2021.

In this drought-ridden region where high temperatures average 31°C for months at a time, most women have no choice but to work in direct sun, collecting firewood, farming, and walking daily to ever-scarcer water holes, while trying to avoid those shared with animals for fear contaminants will harm their fetuses. (That reluctance puts both mother and fetus at risk of dehydration.) Pregnant women experienced sleeplessness, racing hearts, and faintness, and described their bodies as "boiling" or "on fire." Some men said they had seen their wives having difficulty breathing because of the heat. Anecdotally, community health workers reported, pregnancies in the hottest months were more likely to be complicated by high blood pressure, or to end in miscarriages or premature birth.

Lusambili found that extreme heat also has indirect effects on pregnant women's health, because it is "likely to compromise safe behaviors." For example, her team learned that pregnant women are less likely to use bed nets when it's hot, increasing their exposure to mosquitoes that can transmit malaria. The heat makes them fearful of walking kilometers across nearly shadeless terrain to health facilities for prenatal care or delivery. "With climate change we are going to have to rethink some of these behaviors that are harmful to the mom in the heat," Lusambili says. "These women need help."

Jay and his group hope to delineate where behaviors cross into danger. For the new study, they aim to recruit 270 pregnant women and 90 age-matched, nonpregnant women as controls. Pregnant women's participation will stretch from late in their first trimester—when the risk of fetal malformations has largely passed—to late in the third. They will ride the cycle ergometer for up to 1 hour during each trimester, one-third of the participants at 30°C, another third at 35°C, and the rest at 40°C. After 30 minutes of exercise, the chamber's relative humidity will gradually increase.

Several hours before the study, the women will swallow a temperature-sensing pill that sits in their intestines during the ride, wirelessly conveying core temperature to an external recorder every 15 seconds and later

PHOTO: ANASTASIA TOPALIDOU

leaving their bodies by the usual route. These measurements will enable the scientists to identify the crucial inflection point when a participant can no longer maintain a steady state and their core temperature begins to climb steeply. (The researchers will halt the session then.)

They will then analyze how various factors—including temperature, pregnancy stage, maternal age, heart rate, and body shape and size—influence that inflection point. Those data will inform a biophysical model and, ultimately, a prototype online tool that will use the weather forecast at a pregnant person's location and other individual metrics such as their age and week of pregnancy "to then say … 'The maximum temperature that you can be exposed to is X for X number of minutes, exercising at this intensity,'" Gordon says. "It will have that level of detail." The researchers hope the tool will eventually be used in the Global South, to protect pregnant people like those in Lusambili's survey from excessive heat stress.

"It's admirable that they are trying to do this study," says Anne Drapkin Lyerly, an obstetrician and bioethicist at the University of North Carolina School of Medicine. "So much of pregnancy advice is based on fear and a 'better safe than sorry' sort of framework." Admonitions such as "don't exercise" and regimes of bed rest to avoid premature labor have shown no benefit and carry risks of their own, she says.

Still, Lyerly notes the sensitivities that come with studying pregnant people. "I think the jury is likely out on whether pregnant women would be willing to participate and who these pregnant women are," she says. "This is a context where it would be extremely important to make sure that women were given every opportunity to say 'No.'"

Jay and Gordon say they're prioritizing safety. As with any research study, participants will be able to drop out at any time for any reason. Anticipating defections, the team is recruiting three times as many pregnant women as controls. The women must have low obstetrical risk; recent, normal fetal ultrasound scans; and be cleared by their doctors to participate. A participant's session will be halted if her core temperature reaches 38°C. That leaves a 1°C buffer between her temperature and the 39°C teratogenic threshold, which Jay calls "very conservative." Throughout the trial, a research midwife will be present to answer participants' questions and monitor the fetal heart rate. Any pregnant woman who does drop out, or whose fetus' heart rate raises concern, will be offered an immediate ultrasound scan to gauge fetal well-being at the nearby Royal Prince Alfred Hospital. The pregnant participants "are probably safer in our lab than they are just on a regular summer day," Jay says.

"We're very conscious that we need to make it extremely safe," Gordon adds, "but we're also very conscious that these things are happening to pregnant women all over the world in terms of exercise and heat exposure, and nobody's measuring anything."

A FEW PIONEERS are trying. Bonell and her team recently conducted the first field study probing the physiological impacts of heat stress on mother and fetus, published in December 2022. Her team tracked 92 pregnant women who were subsistence farmers in the Gambia and found they were frequently exposed to extreme heat. It led directly to fetal strain, which the scientists defined as reduced blood flow in the umbilical artery—indicating a placenta not functioning properly—or a fetal heart rate outside the normal range of 115 to 160 beats per minute. Bonell and her team found that the likelihood of the fetus experiencing strain grew by 17% for each 1°C increase in temperature as measured by the UTCI, which adjusts for the effects on the body of air temperature, humidity, wind speed, and heat radiating off nearby objects.

"We are going to have to rethink some of these behaviors that are harmful to the mom in the heat. These women need help."

Adelaide Lusambili, Africa International University

How such effects lead to outcomes such as premature birth, stillbirth, and low birth weight isn't clear. "There is very limited definitive evidence," a 2022 review concluded. But hypotheses are plentiful. High temperatures may prompt embryonic or fetal cells to switch key genes off or on at the wrong times, as suggested by studies in embryonic mice and newborn piglets. Cells under stress also produce heat shock proteins, which help stabilize the cells. But these proteins may go into overdrive, causing inflammation; and some also regulate the coordinated, forceful uterine muscle contractions during labor. Both mechanisms, it's hypothesized, could lead to preterm birth. Another pair of possible culprits is oxytocin, the primary hormone triggering labor, and prostaglandins, which speed it along. Studies from the 1990s showed that they are secreted in pregnant farm animals exposed to heat stress.

Perhaps highest on the list of potential causes is reduced blood flow to the placenta. Studies in pregnant ewes have shown that chronic heat stress leads to smaller placentas and smaller, ill-nourished fetuses. It also reduces uterine blood flow, which feeds the placenta, by up to 30%, potentially triggering preterm labor or stillbirth. The picture is much the same in pregnant cows.

Bonell hopes her new Wellcome-funded study will help clarify what's happening in humans. Her team will recruit 762 pregnant women in the Gambia and compare levels of chronic heat stress between those living on the country's relatively cooler coast and those in the much hotter interior. She and her team will measure placental blood flow at regular check-ins. They will track maternal physiology and pregnancy outcomes including the health of the mothers and conduct neurodevelopmental tests on the newborns. Placental tissue samples will be shipped to physiologist Amanda Sferruzzi-Perri at the University of Cambridge, who will study whether differences in the organ's vasculature or gene expression correlate with poor outcomes.

Jay and Gordon's team will also add to the evidence base from women's on-the-ground lives in the Global South. Working with partners at the Sitaram Bhartia Institute of Science and Research and the International Centre for Diarrhoeal Disease Research, they hope to enroll nearly 6000 women in urban India and rural Bangladesh, early in their pregnancies, for a prospective study that will use wearable temperature sensors to regularly track their levels of heat exposure. The primary outcome measure will be premature birth, though the team will also examine rates of other severe consequences such as stillbirth and low birth weight, as well as maternal complications including gestational diabetes and preeclampsia.

In a subset of 1000 women, the team will periodically assess heart rate, dehydration, and core temperature. These measurements will strengthen the model the Sydney group develops using the climate chamber. As a whole, the field study will offer "much more accurate data on the effect of individual level heat exposure on pregnancy outcomes," says Camille Raynes-Greenow, a perinatal epidemiologist at Sydney who is co-leading the Bangladeshi arm of the study.

Ultimately, she would like to see effective and culturally acceptable measures available everywhere to protect pregnant people and their newborns from extreme heat. These might include education about the most sensitive weeks of pregnancy, trees planted where shade is most needed, and changes in building regulations to require insulation and cooler construction. But untangling the mechanisms of harm will be critical to these efforts, she says. "If we don't know what is causing harm, how can we ever develop interventions to mitigate it?" ■

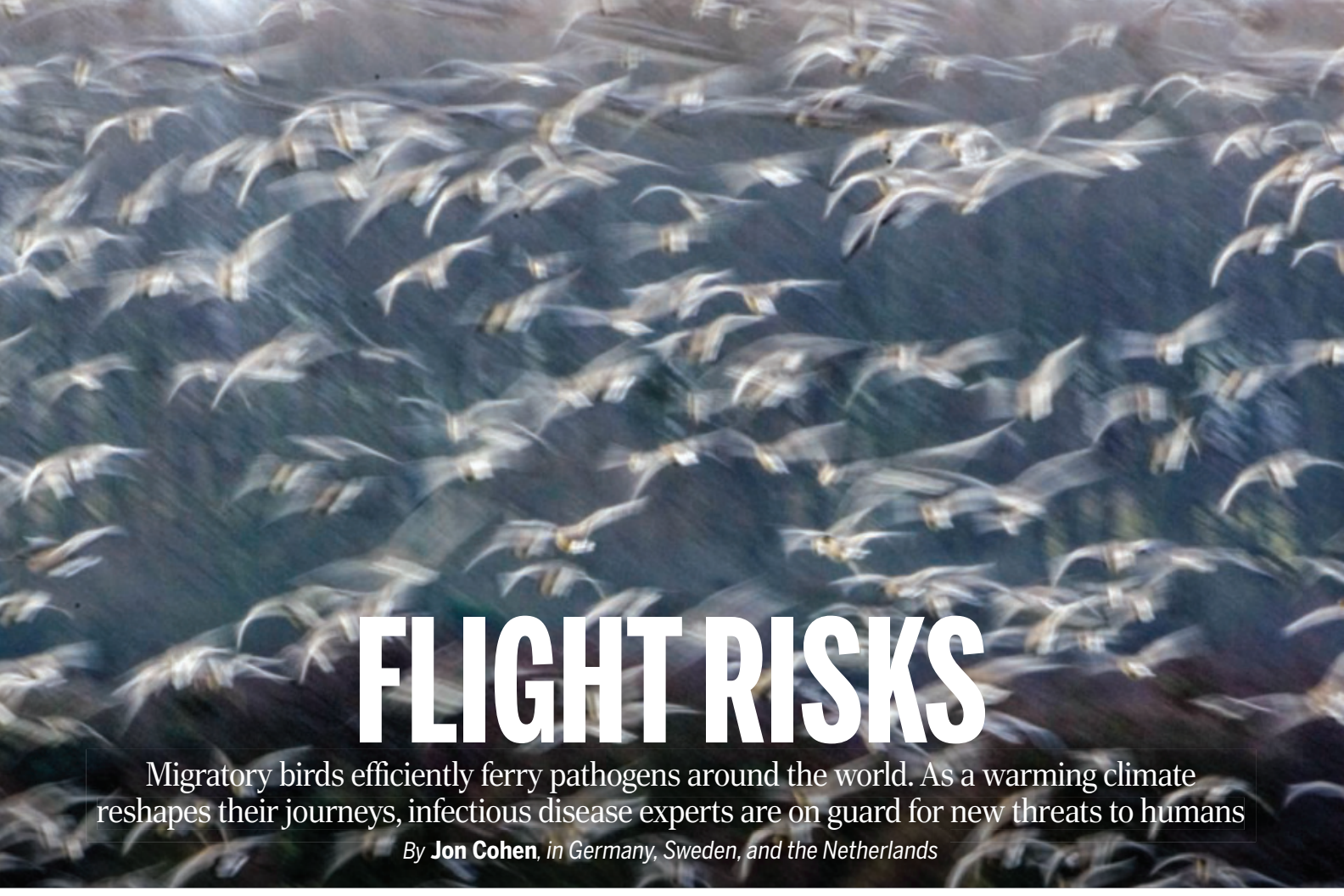

FLIGHT RISKS

Migratory birds efficiently ferry pathogens around the world. As a warming climate reshapes their journeys, infectious disease experts are on guard for new threats to humans

By **Jon Cohen**, *in Germany, Sweden, and the Netherlands*

One day in May, a team of scientists parked their cars in a German nature park near the Baltic Sea and stared at the top of a 30-meter-tall black poplar tree. They were seeking eagles—and clues to the stream of viruses and other pathogens coursing along Europe's flyways in the guts of migratory birds. These white-tailed eagles don't migrate much. But the adults capture and eat birds that do, and feed the prey to their offspring.

It was a month or so into the breeding season, and the scientists hoped to find nestlings—far easier to trap than adult eagles. A local eagle watcher pointed to a nest at the top of the tree. The signs were good. In the distance, a white-tailed eagle soared in the clear sky, and Anne Günther, the veterinarian leading the project, smiled as she pointed to plaques of white goop staining the grass: fresh eagle feces. It was time to take a closer look at the nest.

Veterinarian Oliver Krone, who is based at the Leibniz Institute for Zoo and Wildlife Research and has studied white-tailed eagles for 23 years, deftly hovered a drone over the nest and saw three eaglets. A tree climber dressed in camouflage slingshotted a rope over a sturdy branch and scurried up it, carrying a sack. Soon the fluffy gray eaglets and the dead prey in the nest had been lowered to the ground. The researchers banded, swabbed, and drew blood from the eaglets, all to be analyzed for pathogens they might have picked up from their migratory prey and for antibodies from their mother, signs of past infections. They also sampled the carcass of a wigeon, a dabbling duck, that was found in the nest.

Ducks and other migratory birds efficiently transport all kinds of microbes around the world, including novel influenza strains that threaten poultry and humans, West Nile virus, and a wide range of bacteria that can sicken people and harbor antimicrobial resistance genes (see sidebar, p. 1405). Günther's project, which has already detected a devastating bird flu strain in the eagles, is funded by the Versatile Emerging infectious disease Observatory (VEO). A $30 million Europe-wide collaboration, VEO aims to improve the early warning system that tracks key pathogens, potentially thwarting pandemics. "We're trying to figure out what do hot spots look like for human risk," says VEO project coordinator Marion Koopmans of the Erasmus Medical Center.

Pink-footed geese breed in the Arctic and winter on the U.K. coast. But warming could alter their travels.

A staggering number of variables influence the risks: bird behavior, the nature of the pathogens, the insects and other vectors that help spread them, and humans' own habits and effects on the landscape. And as the world warms there's a new variable to consider, says Martin Beer, a veterinarian at the Friedrich Loeffler Institute (FLI) who is Günther's Ph.D. supervisor. "Bird migration, breeding, and everything is connected to climate change."

As birds migrate to feed or breed, rising temperatures and changing moisture patterns are likely to affect where they go, how long they stay, and what pathogens they meet. The VEO group is on particularly high alert for birds that travel through Europe to the Arctic, which is warming faster than any other part of Earth and serves as a mixing pot for many species.

Already climate change is shaping some birds' journeys. What that implies for the airborne traffic of pathogens, and ultimately the risk to people, remains uncertain,

PHOTO: TIM GRAHAM/GETTY IMAGES

however. "It's not as simple as when this happens, that will happen," Koopmans says. But untangling the relationships—and learning what warning signs to watch for—is critical, she adds. "Can we narrow down the multitude of factors that do drive disease emergence to a set of indicators that you can build into a monitoring system?" Koopmans asks. "I've spent decades now chasing outbreaks. It's not good enough. Once it starts spreading, it's too late."

THE FIRST STEP is to learn where specific birds go and what they're carrying. Each morning this spring, a dozen college-age students who live at the Ottenby Bird Observatory in Sweden repeatedly walked around the nature preserve, clapping their hands in unison. What from a distance resembles a New Age ritual serves a most practical function: It compels any nearby birds—in this case small migrants called wheatears—to fly down large funnels so they can be captured for measurements and banding.

The observatory sits at the tip of Öland, an island in the Baltic Sea about 300 kilometers as the wigeon flies from the park in Germany where the white-tailed eagles reside. Each spring and summer, birds arrive in Ottenby's 340 hectares of lush coastal grassland. For some, it's a final destination to breed, but for many others it's a stopover on their way north to breeding grounds in Iceland or the White Sea in Russia. On their way south in the fall, the birds often stop in Ottenby again, before continuing as far as Africa.

During both seasons the birds foul water bodies with the viruses in their guts, infecting other birds that then travel on different flyways. The result is a global relay system for transmission. "You can easily imagine that [wild birds] have the potential to bring new pathogens to new areas," says ornithologist and microbiologist Jonas Waldenström, who works about a 1-hour drive away at Linnaeus University (LNU) and sometimes collaborates with VEO researchers.

For over 2 decades, Waldenström has sampled more than 100 species of birds at Ottenby. He has found a gallery of pathogens that threaten poultry, humans, or both: influenza and Newcastle disease virus, *Campylobacter*, *Salmonella*, *Yersinia*, tick-borne encephalitis virus, Candidatus, *Babesia*, *Rickettsia*, and papillomavirus.

Waldenström and his colleagues have also spotted signs that a warming climate is beginning to affect the birds' travels. "We are quite poor at remembering how things were 20, 30 years ago, unless we have some notes," he says, as barnacle geese bark in flight above him. But this observatory has trapped and recorded birds—140 species at current count—for 77 years.

The staff band the animals, trusting that the enormous international community of birders will report where they are spotted next. Birders are obsessive observers. Once you become fascinated with birds, Waldenström says, "in a way you will never be alone again, because there are all these little fluffy dinosaurs around at all times. When people get this disease, there is no real cure for it." Many share what they find on websites, and the crowdsourced data have traced annual flyways. They are also revealing changes.

A 2006 *Science* paper Waldenström coauthored analyzed data from 1980 to 2004 to show long-distance passerine birds were arriving earlier in the spring at Ottenby and four other European observatories, likely as a result of climate change. During that period, the spring "green up" came about half a day earlier each year on average, and April and May were typically warmer, likely leading to more of the insects that many of the birds eat. "They're good heralds of what is going on," Waldenström says. "We all see that climate change is happening. But long before we started to see and feel these changes, you can see those types of changes in the bird community."

Waldenström's team now equips black-headed gulls and mallards with transmitters that cellphone towers and satellites can track. "Bird banding is a rather blunt tool," he says. "Typically, you only get few recoveries, and in most cases it is just the site of banding and the site of recovery." The transmitters should give a fuller picture of migration routes and timing—but they cost about $1000 each and are cumbersome, which limits the number and types of birds they can follow. Smaller birds cannot wear the tags at all.

An eaglet was lowered from its nest in Germany to be banded and tested for pathogens from the migratory birds it dines on.

PHOTO: J. COHEN/*SCIENCE*

JUST HOW CLIMATE-DRIVEN changes in bird migration affect human, or even avian, disease risk depends on an intricate web of factors. Many long-distance migrants start their journeys in response to signals unaffected by climate, such as changes in daylight or internal cues. Keeping to their traditional timing, they might reach a breeding area when spring is more advanced, encountering a changed ecosystem and, perhaps, different pathogens. Others, responding to temperature and humidity, might speed up their migrations, expending more energy, which might also make them more apt to pick up diseases. "Migration is energetically expensive, and studies show that this suppresses the immune system," says Mariëlle van Toor, a movement ecologist who works with Waldenström at LNU.

For some birds, climate change might convert what once was a stopover spot into their primary breeding grounds, which could make them more likely to pick up certain pathogens. An evolutionary theory known as the dilution effect holds that a diversity of species, expected at a stopover point, can reduce the ability of a pathogen to spread, because an infected bird is more likely to transmit it to a different species in which it does not thrive. But if large numbers of one species settle in to breed, this safeguard may diminish.

Changing climate could also make some pathogens more dangerous. "If you have globally higher temperatures, it means that certain species are going to migrate less, and then the pathogens that they have become more virulent," says Thijs Kuiken, a flu and coronavirus specialist at Erasmus who is also a serious birder. The idea is that a highly virulent virus in migratory birds will force infected individuals to lag behind, so they will have fewer opportunities to transmit the infection to others. But if whole flocks begin to stay put, the odds grow that when highly pathogenic variants emerge, they will more easily be able to jump from bird to bird and persist.

Climate change could influence pathogen spread in other ways. Warming could lead to booms in mosquito or tick populations, some of which can spread novel microbes to birds. At birth birds have little immunity, and if they hatch in new locales, they may pick new pathogens and pass them to other populations or species. And climate may directly hamper or aid pathogens, which have preferred temperatures and humidity themselves.

"An inherent problem is so many things change at the same time," Waldenström says.

RESEARCHERS WIDELY AGREE that the most damaging avian pathogen today, a variant of the influenza virus subtype known as H5N1, emerged because of human actions unrelated to greenhouse emissions. The spread of the virus, which has killed unprecedented numbers of wild birds across the world, devastated some mammal populations, and stoked pandemic fears, "has much more to do with the expansion of the poultry industry," Kuiken says. Large poultry farms, which can have millions of birds massed together, provide a paradise for viruses to persist and evolve into more deadly variants. Many countries also have lax surveillance and control programs for these highly pathogenic avian influenza viruses. "The virus has been given so much opportunity to spread to wild bird populations from poultry," Kuiken says.

For researchers worried about other bird-borne pathogens, however, the international effort to document the flu virus' spread shows the value of surveillance. It mapped in exquisite detail how this nightmarish variant, designated 2.3.4.4b, originated in an outbreak in South Korean poultry in 2014, then made a global journey in migratory birds, spreading through Europe to different flyways—one through the Bering Strait, the other via Iceland—that brought it to both coasts of North America by 2022 and then all the way to Chile (*Science*, 7 April, p. 24).

And although climate change may not have spurred the evolution of the variant, Kuiken expects it will affect where the virus travels in the future and which species of birds suffer the most harm. An ambitious VEO project in remote regions of Greenland this summer found the variant in birds on that fast-warming island, where white-fronted geese that winter in Europe may mix with Canada geese that head south to North America. "What happens in these areas that are undergoing this climate change?" Koopmans asks. "There's very little knowledge right now."

Besides tracking bird migrations, VEO researchers are monitoring and modeling other factors that might influence the diseases they carry. Several members of Koopmans's team are delving into how climate change might affect the Netherlands, much of which is below sea level and prone to flooding. If wetlands expand, will they attract new bird species, which might pick up more tick- and mosquito-borne viruses such as West Nile and spread them to cities? If seas rise and rivers grow more saline, will the salt-sensitive freshwater invertebrates that prey on mosquitoes decline, leading to more insect vectors and more infections in birds? VEO researchers are feeding data from their field studies of waterways and animals into a database to probe for answers.

Reina Sikkema, a veterinarian on the Erasmus team who specializes in viral jumps between species, says human attempts to cope with climate change can create new risks. "When you have a drought, people keep their own rain barrels, so you would have more breeding sites for mosquitoes," which could spread microbes to and from birds, Sikkema says. Many cities are also aggressively planting trees to cool the streets. "Greening our cities is good, but what if that attracts more mosquitoes and creates much higher risks for public health?" she asks.

Similarly, physical oceanographer Julie Pietrzak and her colleagues at the Delft University of Technology, along with Koopmans, are modeling how changes to the country's elaborate dike system to prepare for rising seas might boost disease risks. Introducing different locks and gates to improve water control could create new wetlands in the Rhine-Meuse delta, altering the gathering places for birds and the prevalence of mosquitoes and other vectors that infect them. "I'd never thought about viruses spreading in the delta and the roles of birds," Pietrzak says. "As you understand how the complex system works, to a certain level, then you can make better decisions."

Nnomzie Atama, a veterinarian from the A.P. Leventis Ornithological Research Institute in Nigeria, and other VEO researchers are seeking clues to bird-borne human disease by watching a proxy pathogen. Usutu virus, first found in South Africa in 1959, is related to West Nile virus and is transmitted by the same mosquitoes and the same species of birds. A team including Koopmans

Crowded skies

Many migratory species stop in the coastal meadows around Sweden's Ottenby Bird Observatory on their annual journeys between Arctic breeding grounds and winter habitat. Banding and tags have traced some species' routes and revealed early signs of change.

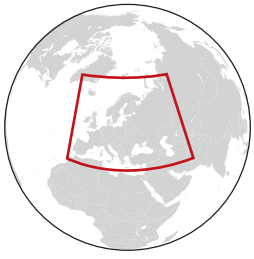

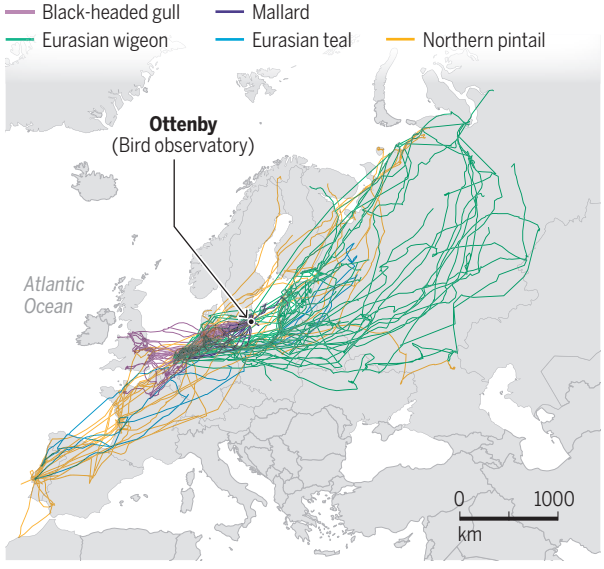

GRAPHIC: C. BICKEL/*SCIENCE*; DATA: M. VAN TOOR, LINNAEUS UNIVERSITY

first reported the appearance of Usutu in the Netherlands in 2016, when it killed a large number of blackbirds.

Usutu virus rarely causes disease in humans, but the first Dutch case of West Nile was in 2020. The VEO researchers hope Usutu can give them a jump on what West Nile might do next. They have been aggressively monitoring for Usutu by testing trapped birds, shed feathers (which have microscopic drops of blood on the shaft), and dead birds that come to the lab. "There hasn't been much study done of Usutu, so we're trying to cover the gap," says Atama, who is working on his Ph.D. at Erasmus.

If Usutu becomes more prevalent with climate change, it could provide warnings far beyond the Netherlands, and for viruses other than West Nile. "You might also get the introduction of more exotic arboviruses like Dengue," says Bas Oude Munnink, a molecular virologist at Erasmus. Alerted by Usutu, "We potentially can try to slow down, or perhaps even stop, the spread" of its deadlier relatives.

STANDING IN THE WAY of these plans are not just the dauntingly complex interactions of birds, microbes, and climate, but also mundane challenges. On their May outing, Günther and her German colleagues managed to retrieve and sample just six eaglets. A 3-week Greenland expedition in July sampled 85 geese, which averages out to about four per day invested. At FLI, which has long focused on farm animal health, "I see other Ph.D. students who come back from the pig stables with 200 samples at once, and I'm like, 'Well, I got two today,'" Günther says. Wild birds are simply difficult to monitor for pathogens.

The long-term studies needed to discern trends are also expensive. "In order to know what's new and novel you need to know what is normal," Waldenström says. "But the funding cycle that researchers experience is not really good for long-term monitoring and surveillance." Trapping birds and collecting samples requires large teams, and then there's the cost of analyzing the material. Waldenström's freezers have 60,000 bird samples collected over the past 25 years, the vast majority untested. "We have a shitload of samples lying in our freezers," he says. "It's like a biobank of bird viromes."

But climate change makes such studies that much more urgent, Koopmans says. The ultimate goal is to predict, with the precision of weather forecasting, where spillovers from birds to people are most likely to occur. "It ain't easy," Koopmans says. "But I'm convinced we have to start embracing the complexity." ■

PHOTO: J. COHEN/*SCIENCE*

Mariëlle van Toor, Jonas Bonnedahl, and Jonas Waldenström (left to right) teach an aide to tag a gull.

Gulls, floods, and superbugs

Just as viruses wash back and forth between species, so do genes that enable bacteria to shrug off antibiotics. Arising in people and livestock that are heavily dosed with the drugs, bacteria that evolve antimicrobial resistance (AMR) are spread far and wide by birds. "In this part of the world, it's definitely the gulls," says Jonas Bonnedahl, an infectious disease clinician based at Linköping University in Sweden. "They really enjoy to feed from the wastewater treatment plants and the landfills."

Bonnedahl traps black-headed gulls, samples their feces for bacteria carrying AMR genes, and affixes tracking tags to their backs to follow their migrations. The work, done with his longtime collaborator Jonas Waldenström, an ornithologist at Linnaeus University, offers a way to gauge the prevalence and travels of these genes. When bird droppings contaminate food or water supplies, humans can be at risk from either the resistant bacteria or the AMR genes, which can spread to other microbes.

The studies might also reveal an impact of climate change. Floods could supercharge the spread of the genes by dispersing sewage or manure, and droughts could do the same by causing birds and other animals to congregate and share microbes at water sources. "If we identify the point sources for AMR and its distribution in the environment, it's much easier to identify mitigation strategies," Bonnedahl says.

An estimated 1.27 million people worldwide died in 2018 because AMR made their infections untreatable, according to a recent report in *The Lancet*. Monika Dolejská, a microbiologist at the University of Veterinary Sciences Brno who studies AMR in wild birds, says the Swedish researchers have provided "direct evidence" that birds help spread the genes and "an opportunity to quantify the associated risks to public health."

In a May paper in *Science of the Total Environment*, for example, Bonnedahl and collaborators reported on sampling done in gulls strolling in a Swedish park and at a nearby wastewater plant. Eight percent of their fecal samples carried AMR genes also found at the wastewater plant. The genes code for enzymes that cripple carbapenems, which have become last-resort antibiotics to combat multidrug-resistant bacterial infections. "When I'm working in the clinic, these are the most frightening resistance genes," Bonnedahl says.

The birds can carry AMR genes across continents, the team reported in 2021. Working with investigators from the U.S. Geological Survey, they took 773 fecal samples from seven communities of gulls in Alaska, most of which dined on waste landfills, and found an AMR gene in 16% of the samples. Tags on 42 of the birds revealed that within days, some flew northwest to the coast of Chukotka, Russia, whereas others flapped southeast to California's San Francisco Bay.

"We shouldn't blame the gulls," Bonnedahl says. "We should blame us for releasing AMR in a way that they get it." Different wastewater treatment methods, better covers at landfills, or strategies that scare off birds might all help. But the weather extremes that a warming climate is bringing willmake curbing AMR spread more difficult. —*J.C.*

LURKING IN THE DEEP FREEZE?

Climate change may release dangerous pathogens frozen for centuries in Arctic permafrost

By **Jon Cohen**

In 1733, an Inuit boy and girl who had been sent to Denmark for the king's coronation 2 years earlier sailed back home to Greenland. Both were in a "sickly state of health" during the trip, according to an account written a few decades later by a missionary, and the girl died on the way. Shortly after reaching his native land that September, the boy also died, of "a cutaneous disorder." He had brought smallpox with him, and the disease raced around the island, killing Inuits and Europeans alike. Another missionary wrote of "houses tenanted only by the corpses of their former occupants, and dead bodies lying unburied on the snow." The outbreak lasted until at least June of the next year, killing maybe half of Greenland's already sparse population.

In the summer of 2022, a team of researchers visited Greenland to take soil samples from heaps of human and animal waste, or middens, dating from the smallpox epidemic and before. Their goal is to assess the risk that, as the Arctic warms and the permafrost thaws, long-frozen soil could release dangerous pathogens. Such "zombie viruses" are fodder for Hollywood, but they are not science fiction. Temperatures in the Arctic are rising twice as fast as in the rest of the world. And viable pathogens are clearly lurking in the soil, says Marion Koopmans, a virologist at the Erasmus Medical Center who runs a European consortium dubbed the Versatile Emerging infectious disease Observatory (VEO) that's studying how northern-latitude warming might influence infectious diseases (see related story, p. 1402). "What you see now is studies that find infectious viruses from permafrost."

The odds are low that smallpox or anything comparably dangerous will spring from the soil after centuries in the deep freeze, says veterinary microbiologist Frank Aarestrup, who heads the VEO project with Koopmans and whose lab at the Technical University of Denmark has been screening the midden samples for DNA. "But it's better that we should investigate it now rather than after something has been released." Yet some scientists do worry that the effort itself could unleash a human pathogen.

Researchers from Aix-Marseille University were the first to isolate viruses from ancient permafrost, reporting in 2014 and 2015 that

PHOTO: CHRISTIAN KOCH MADSEN/GREENLAND NATIONAL MUSEUM AND ARCHIVES

When archaeologists excavate waste piles, or middens, left centuries ago by Norse settlers on Greenland (left), microbiologists retrieve soil samples, which they store and later analyze for pathogens (right).

PHOTO: J. COHEN/*SCIENCE*

samples of Siberian soil frozen for 30,000 years harbored two large DNA viruses that could infect amoebae but posed no threat to humans. In the 18 February issue of *Viruses*, the same team, led by genomicist Jean-Michel Claverie and materials scientist Chantal Abergel, revealed 13 more permafrost megaviruses that infect amoebae, one dating back 48,500 years.

A more alarming pathogen may have already emerged naturally from frozen ground. In the unusually hot summer of 2016, *Bacillus anthracis*, a bacterium that lurks in soil worldwide and causes anthrax, killed 2649 reindeer in Siberia. It also sickened 36 people, including a 12-year-old boy who died. But linking the outbreak and climate change is not easy, as archaeologist Alexander Volkovitskiy from the Russian Academy of Sciences noted at an international workshop on microbial threats in the Arctic held in 2019. More than a century ago, anthrax outbreaks repeatedly killed Siberian reindeer, which led the Soviet Union to begin to vaccinate the animals in 1930. The elimination of cases led the Russian government to end the vaccination program in 2007, which could have helped set the stage for the 2016 outbreak.

The Ukraine war has ended outside collaborations in Siberia, which holds much of the world's permafrost, making VEO's work in Greenland more important. "Permafrost in the rest of the Arctic is a substitute, and all studies and investments in this are valuable," says Birgitta Evengård, an infectious disease specialist at Umeå University who specializes in Arctic health.

The VEO team collected 360 soil samples during its visit in the summer of 2022, concentrating on the middens, where waste sometimes reached 3 meters in height. "They're kind of hot spots," Aarestrup says. The group's studies to date have found several bacteria from the genus *Clostridium*, including ones that cause food poisoning, toxic shock, and botulism. Many samples are still being analyzed.

The researchers take precautions to avoid infection. In the field, they wear protective gear and only visit sites where archaeologists are already taking samples. "We cannot say that nothing is going to be released [from the permafrost], but it should not be because of us," Aarestrup said. In the lab, the samples are studied under sterile conditions with strict biosafety protocols.

Claverie isn't reassured. He hopes the VEO researchers do not attempt to revive pathogens that might have the potential to cause outbreaks in humans. Claverie says he chose to focus on viruses that infect amoebae for safety reasons, "thinking that 2 billion years of diverging evolution is a much better barrier against human accidental infection than the walls and safety protocols." Aarestrup and Koopmans note that they chemically treat samples to kill any organisms before studying them. "We are collecting a relatively small number of samples, by people who understand possible risks," Koopmans says.

There are also worries that permafrost pathogens could infect livestock—and then spill over into humans. The Norse brought sheep when they settled the island around 1000 B.C.E., but both the animals and the Norse were gone by 1450. "With climate change, Greenland expects to start having sheep farming again," Aarestrup says. "As a vet, this is something that you immediately start getting concerned about because this potentially is bringing a completely immunenaïve population of animals into an area."

If the VEO team does find dangerous pathogens, Greenland could close certain areas to tourists and stop archaeological excavations, Aarestrup says. "I don't think something will happen, but I do think that it's good to be prepared for it," he says. "You should never say never." ■

INSIGHTS

POLICY FORUM

SPACEFLIGHT

Ethically cleared to launch?

Rules are needed for human research in commercial spaceflight

By **Vasiliki Rahimzadeh[1], Jennifer Fogarty[2], Timothy Caulfield[3], Serena Auñón-Chancellor[4], Pascal Borry[5], Jessica Candia[6], I. Glenn Cohen[7], Marisa Covington[8], Holly Fernandez Lynch[9], Henry T. Greely[10], Michelle Hanlon[11], James Hatt[12], Lucie Low[13], Jerry Menikoff[14], Eric M. Meslin[15], Steven Platts[16], Vardit Ravitsky[17,18], Tara Ruttley[19], Rachael D. Seidler[20,21], Jeremy Sugarman[22], Emmanuel Urquieta[2], Michael A. Williams[23,24], Paul Root Wolpe[25], Dorit Donoviel[2], Amy L. McGuire[1]**

Massive public and private investment in scientific research has enabled the commercial spaceflight industry to expand opportunities in space beyond primarily government-sponsored missions (*1*). Commercial companies endeavor to fly thousands of commercial spaceflight participants (cSFPs) and workers to space in the decades ahead (*2*). Although the future of safe commercial spaceflight depends on rigorous and inclusive research, the ethical conduct of such research is complicated by scientific uncertainty, high attendant risks (*3*), and poorly defined rules for research ethics oversight within the commercial spaceflight industry. Now is the opportune time to develop clear rules for ethical cSFP

PHOTO: JOE RAEDLE/GETTY IMAGES

The SpaceX Falcon 9 rocket with the Crew Dragon spacecraft lifts off from the Kennedy Space Center in Cape Canaveral, Florida, on 21 May 2023.

research while space activities are ramping up and the regulatory environment for commercial spaceflight is actively being shaped. We propose an ethical framework based on terrestrial human research that is anchored in four guiding principles—social responsibility, scientific excellence, proportionality, and global stewardship—and is applicable to the responsible conduct of research in commercial spaceflight.

Well-established norms, policies, and national regulations guide the ethical conduct of most traditional research involving humans on Earth. There is also consensus on ethical principles guiding research with government astronauts (*4*). However, there are no clear frameworks that govern privately funded research with civilians on commercial space vehicles. Existing research ethics safeguards may not apply because of gaps in how research regulations govern private industry, and international space research must contend with interjurisdictional issues. Many of the regulatory and ethics challenges we identify for commercial spaceflight research are amplified by the rare opportunity cSFPs have to travel to space and the outsized social value that only they can provide through research participation (see the box).

The emerging commercial spaceflight sector will have global impact, but the United States currently leads the world in overall spending on space programs, including investment in developing the commercial arm of spaceflight. We therefore highlight ethical tensions posed by the regulatory vacuum for responsible research conduct, primarily in the United States. For example, the US Federal Aviation Administration (FAA) moratorium on occupant safety regulations aboard commercial space vehicles is set to sunset in October 2023 (*5*). The FAA is working to encourage the development of industry consensus standards and revise the US government's human spaceflight safety practices (*6*), and has established an aerospace rule-making committee to garner industry input on a new safety framework. Meanwhile, the Biden administration confirmed that the United States will decommission the International Space Station as soon as 2030, which effectively ends decades of collaboration on the only microgravity research platform shared with other spacefaring nations. International agreements, including the Outer Space Treaty (OST)—signed and ratified by 112 countries—are silent on whether principles for peaceful human space exploration apply to human research sponsored by commercial firms (*7*), and diverse research partners and complex funding and sponsorship relationships can lead to redundancies in the science and provide insufficient oversight.

Gaps in policy intended to protect cSFP health and safety in commercial spaceflight research threaten the industry, hamstring scientific collaboration between public and private partners, and limit the translation of research benefits to society. To foster research safety and utility, our primary objectives are twofold: (i) create an expectation that commercial spaceflight companies provide the infrastructure and resources necessary to engage in high-quality human research, and (ii) inform approaches to safe and effective commercial spaceflight research by advocating for robust ethical principles and standards that reflect consensus among diverse stakeholders and account for the distinct research environments to which future cSFPs will be exposed.

GUIDING PRINCIPLES

Social responsibility

Most commercial flights currently depend on cofunding from the government and private sources. Additionally, commercial spaceflight services are only possible now because of substantial public investment in past research. Therefore, the public has an important role in helping to shape the commercial interests of companies, and data that builds on initial public investments in spaceflight research should be treated as community resources. What we learn in the early years of commercial spaceflight will be critical for ensuring the safety of future missions, and research with cSFPs has the potential to improve human health not only in space but also on Earth (*8*). Thus, early cSFPs arguably have a heightened social responsibility to help advance research to build the evidence base.

Appealing to principles of social responsibility differs from preexisting ethical frameworks that give primacy to autonomy because it explicitly calls on those privileged to have the opportunity to travel into space to contribute to research activities that benefit society at large.

Scientific excellence

Poorly designed, duplicative, and low-priority studies beget poor-quality data. They cloud the evidence base, endanger participants, and waste resources. Bad science is also bad for business. It can misguide strategy, permit inefficiency, and expose organizations to liability. By adhering to standards of excellence, those who sponsor and conduct research in commercial spaceflight show by example how rigorous science drives successful business practice.

Proportionality

Spaceflight research, like all research that involves humans, is only permissible if it maximizes social value and minimizes the likelihood and severity of harms to participants, crew members, and other personnel. Spaceflight is a high-risk activity, and research procedures that pose minimal risks on Earth could pose substantially increased risk when performed in space. The add-on risks of research participation should therefore be evaluated against the baseline risks of spaceflight, minimized to the extent possible, and proportionately balanced in relation to the anticipated benefits to the individual cSFP and to society.

Global stewardship

The benefits of human space exploration and its resources should be enjoyed by all (*7*). Spaceflight research should therefore engage, and be conducted by, individuals and communities representative of humankind's diversity. We draw on stewardship principles and concepts advanced in space governance (*9*), the environmental sciences, and natural resource fields to inform how we might fairly distribute the knowledge benefits of commercial spaceflight research. We emphasize responsible use of time, data, and natural resources in ways that take full and balanced account of the interests of society, future generations, and other species, as well as of private interests to advance the science of safe human space exploration (*10*).

NEW APPLICATIONS OF EXISTING POLICIES AND PRACTICES

Free and informed consent

If we take seriously the principle of social responsibility, we might condition commercial spaceflight on informed research participation focused on improving human health or safety, at least in the early years. Although all astronauts are thoroughly briefed on research protocols and voluntarily consent to participate, many view their participation as an occupational responsibility to support longitudinal health surveillance that benefits future crew. Privately funded cSFPs may not be motivated by the same occupational responsibility but rather could be moved to participate in minimally invasive or minimal risk studies under the principle of social responsibility.

To compel cSFP participation in research as a condition of spaceflight in the commercial context could undermine

the business interests of privately funded companies, including their ability to attract future customers. It could also violate cSFP autonomy by providing an excessive benefit that challenges voluntariness. Travel to space can present an opportunity so compelling that cSFPs could opt in to risky research not customarily tolerated on Earth without appropriate safeguards. Furthermore, some cSFPs are employees of commercial space companies, and conditioning employment on research participation is generally impermissible.

All prospective cSFPs should be fully informed about the social value of any proposed research protocols and be encouraged to participate. Incentivizing participation may be justified, so long as the incentive is calibrated with the risks and does not create undue inducement (*11*). Commercial companies may give preference to those cSFPs willing to participate in research, but further ethical attention is needed to determine whether cSFPs should remain flight eligible even if they decline research participation.

Maximizing benefits to society

The social value of research increases proportionately to the usefulness of new knowledge gained. Well-annotated datasets—including information about the flight protocol, operational endpoints, and adverse events—should be of sufficient scientific quality to substantiate social value. Those who conduct research in space should share these data to ensure findability, accessibility, interoperability, and reusability for the scientific community and society well into the future. Indeed, private companies must commit to openly sharing scientific data if they are operating on behalf of a signatory to the 2020 Artemis Accords (*10*), which includes Australia, Canada, Italy, Japan, Luxembourg, the United Arab Emirates, the United Kingdom, and the United States.

Minimizing risks

Known physiological effects of spaceflight stem from research principally performed with government astronauts and other highly trained personnel who cleared stringent medical tests before flight. Prospective cSFPs may not undergo the same tests, and commercial companies indeed plan to fly cSFPs with preexisting health conditions (such as cancer) and physical disabilities (for example, the European Space Agency parastronaut program). The attendant risks of cSFP research participation are expected to compound as a result. This is particularly true for cSFPs with less experience managing adverse events that affect fellow crew or responding to operational emergencies during spaceflight. Missions that enable quick and safe return to Earth could thus be prioritized for crews composed mostly of cSFPs without prior spaceflight experience. Competent adults ought nevertheless to be able to assume risks for the advancement of knowledge and betterment of society.

cSFPs may participate in multiple studies, each with their own set of risks and safeguards against adverse events. Future planned studies are likely to reflect different types of research (ranging from noninvasive, to minimally invasive, to invasive), with a broad spectrum of risk potential. Companies, principal investigators, and ethics committees therefore need to consider the portfolio of risks for cSFPs individually, as well as in the aggregate (*3*). Different risk thresholds may be justifiable for different crew members. Companies may, for example, limit a crew medical officer or commander from participating in research that could lead to impairment or incapacitation because their role is essential to the safety and welfare of the entire crew.

To further substantiate spaceflight safety and enhance informed consent for prospective cSFPs, a formal system for reporting adverse events should be developed like what is required of pharmaceutical drug companies. Such a system should be focused on adverse events related to research involving cSFPs, separate from adverse events from operational failures or crew error.

Data protections and governance

Some instances of research data sharing can be in tension with the proprietary interests of commercial companies or their customers. The commercial spaceflight industry would benefit from direct engagement with regulators to develop and

Ongoing cSFP research related to spaceflight-associated neuro-ocular syndrome (SANS).

SANS is associated with long-duration spaceflight and is thought to be the result of increased intracranial pressure (ICP). Symptoms include optic disc edema, changes in near vision, and possible reductions in cognitive functions that could compromise mission-critical tasks (*15*). Nearly 70% of NASA astronauts develop some degree of SANS, underscoring the need to identify its pathophysiologic mechanisms and find effective countermeasures. Commercial companies have a vested interest in management and prevention of SANS and support cSFP participation in studies of the issue. The most accurate method for measuring ICP—inserting a probe directly into the brain or cerebral ventricles—is too risky for spaceflight. Investigators developed a less risky method: a catheter surgically implanted in the lumbar cerebral spinal fluid space and attached to a subcutaneous telemetric ICP sensor that would enable ICP readings before, during, and after flight. After NASA concluded that the risks of the modified implant on long-duration missions were also too high, this approach was pursued by the Translational Research Institute for Space Health and a competitively selected experienced research team in coordination with a commercial spaceflight company to include a healthy cSFP in this study (https://taskbook.nasaprs.com/tbp/index.cfm?action=public_query_taskbook_content&TASKID=15266).

[1]Center for Medical Ethics and Health Policy, Baylor College of Medicine, Houston, TX, USA. [2]Translational Research Institute for Space Health, Baylor College of Medicine, Houston, TX, USA. [3]Faculty of Law and School of Public Health, University of Alberta, Edmonton, AB, Canada. [4]Louisiana State University Health Science Center Baton Rouge Campus, Baton Rouge, LA, USA. [5]Centre for Biomedical Ethics and Law, Department of Public Health and Primary Care, KU Leuven, Leuven, Belgium. [6]Component Office of Human Research Protections, Air Force Medical Readiness Agency, Department of the Air Force, Falls Church, VA, USA. [7]The Petrie-Flom Center for Health Law Policy, Biotechnology, and Bioethics at Harvard Law School, Cambridge, MA, USA. [8]Office of Research Assurance, Office of the Chief Health and Medical Officer, National Aeronautics and Space Administration, Houston, TX, USA. [9]Department of Medical Ethics and Health Policy, Perelman School of Medicine, University of Pennsylvania, Philadelphia, PA, USA. [10]The Center for Law and the Biosciences, Stanford University, Stanford, CA, USA. [11]Center for Air and Space Law, University of Mississippi, Oxford, MS, USA. [12]Space Policy Division, Office of Commercial Space Transportation, Federal Aviation Administration, Washington, DC, USA. [13]Axiom Space, Houston, TX, USA. [14]Centre for Biomedical Ethics, National University of Singapore, Republic of Singapore. [15]Council of Canadian Academies, Ottawa, ON, Canada. [16]Human Research Program, NASA Johnson Space Center, Houston, TX, USA. [17]School of Public Health, University of Montreal, Montreal, Canada. [18]Harvard Medical School, Boston, MA, USA. [19]Orbital Reef, Blue Origin, Washington, DC, USA. [20]Department of Applied Physiology and Kinesiology, University of Florida, Gainesville, FL, USA. [21]Department of Neurology, University of Florida, Gainesville, FL, USA. [22]Berman Institute of Bioethics and Department of Medicine, Johns Hopkins University, Baltimore, MD, USA. [23]Department of Neurology, University of Washington School of Medicine, Seattle, WA, USA. [24]Department of Neurological Surgery, University of Washington School of Medicine, Seattle, WA, USA. [25]Center for Ethics, Emory University, Atlanta, GA, USA. Email: amcguire@bcm.edu

implement methods to share data for research purposes without compromising intellectual property. An industry-wide database should be created to securely store and manage controlled access to relevant study data for research purposes [for example, (*12*)]. Robust data governance mechanisms—including penalties or sanctions to hold users accountable for data misuse—should be developed simultaneously with data infrastructures and should reflect the interests of contributors as well as downstream users of the data.

Similar data types may be collected to monitor cSFPs' health and welfare while in space and later repurposed for space health research (*13*), with appropriate consent. Privacy and confidentiality of these data rely heavily on the ability to deidentify them. However, the small sample size per mission and extensive data linkages needed to support robust data analyses means that cSFP privacy could be compromised even for minimal risk studies (*14*). Limits to data privacy should be disclosed to cSFPs at the time of consent, and prospective cSFPs should demonstrate that they fully comprehend the realistic risks that research data could be attributed to individual cSFPs and other privacy-related consequences of participation.

EXTENSION OF EXISTING POLICIES AND PRACTICES

Setting research priorities

Research investigating the effects of spaceflight on cSFPs can be expensive, risky, and difficult to reproduce because opportunities are rare, and only a select few cSFPs can be accommodated on space vehicles. Such extreme resource constraints have both practical and ethical consequences for setting research priorities, which places a premium on prioritizing scientifically rigorous studies that add the most social value, address questions about which there is genuine uncertainty, and can only be carried out in space as opposed to an Earth analog.

There may also be competing priorities for commercial spaceflight companies and sponsors of research in terms of what scientific questions to ask and where to invest research dollars. Those who conduct commercial spaceflight research should develop a transparent research agenda that meaningfully incorporates input from diverse stakeholders, including the public, scientists, regulators, funding agencies, and other industry partners. To avoid redundancy and increase scientific impact, research sponsors should consolidate studies that ask similar scientific questions or call for participation from cSFPs with similar health and demographic profiles whenever possible. This will require collaboration within a competitive space and sharing data for the public good as gestures of responsible stewardship, while protecting trade secrets to stimulate commercial investment.

Scientific and ethics review

Independent ethics review of research involving humans in space is expected, as it is on Earth. Although federally funded research is legally required to obtain ethics review, research funded entirely by private organizations is not. Legal authorities can also be unclear for research that involves cSFPs funded through multinational space agency collaborations, in which each agency maintains their own requirements. Research that involves cSFPs should nevertheless undergo independent ethics review that is free of any real or perceived investigator conflict of interest even if not strictly required by law because it is a longstanding ethical obligation that predates many legal requirements.

Given the specialized research focus, many research ethics committees will not have the necessary expertise to conduct quality, comprehensive reviews of spaceflight research. A specialty body could be named, external experts could be consulted, or membership on ethics committees could be expanded to include human spaceflight experts.

Promoting diversity of cSFPs and researchers

cSFPs have not so far been representative of society in terms of gender, age, genetic ancestry, health, and socioeconomic status. Where such individual attributes are known or suspected to have physiological ramifications for spaceflight, findings from research with less diverse cSFPs may not be generalizable. This raises at least two justice concerns: inequity in knowledge gained for those living on Earth, and inequity in evidence collected to support safe spaceflight for more diverse cSFPs in the future.

Investigators should be encouraged to consider diversity when designing research protocols, but ultimately, sample diversity will be driven by the specific research questions. With proper oversight, commercial spaceflight research presents a historic opportunity to address prior underrepresentation and redefine who can safely experience the wonders of spaceflight. Companies that fly their own staff as well as prospective customers on research missions should therefore also invest in the training, recruitment, and retention of researchers and cSFPs from diverse backgrounds to sustain a thriving commercial spaceflight workforce (*2*) and participant pool.

CONCLUSION

To demonstrate trustworthiness and reduce their own risk and liability, companies should issue policies and develop best practices to ensure that sponsored research is performed in a socially responsible and ethical manner. To demonstrate their commitment to global cooperation and responsible stewardship of space resources, regulatory agencies will need to strategize how to effectively implement and ensure accountability for ethical research standards across public and private sectors. We believe that there is ample opportunity for collaboration on both fronts that is consistent with our proposed ethical framework. Future work should focus on identifying specific responsible actors and determining what level of policy is appropriate for ensuring implementation of the framework. ■

REFERENCES AND NOTES

1. R. Skibba, "Spaceflight companies promised to do science—So how's it going?" *Wired,* 28 December 2022; https://www.wired.com/story/spaceflight-companies-promised-to-do-science-so-hows-it-going.
2. M. Marge *et al.*, *J. Space Saf. Eng.* **10**, 22 (2023).
3. E. L. Antonsen *et al.*, *npj Micrograv.* **8**, 1 (2022).
4. Institute of Medicine, *Health Standards for Long Duration and Exploration Spaceflight: Ethics Principles, Responsibilities, and Decision Framework* (National Academies Press, 2014).
5. E. Mahoney, Ed., "NASA provides updated International Space Station transition plan" (NASA, 2022); http://www.nasa.gov/feature/nasa-provides-updated-international-space-station-transition-plan.
6. FAA, "Recommended practices for human space flight occupant safety" (FAA, 2014).
7. United Nations Office of Outer Space Affairs, "Treaty on principles governing the activities of states in the exploration and use of outer space, including the Moon and other celestial bodies" (United Nations, 1967).
8. M. Shelhamer *et al.*, *npj Micrograv.* **6**, 5 (2020).
9. T. Aganaba, *Albany Law Rev.* **85**, 409 (2022).
10. The Artemis program, "The Artemis Accords: Principles for cooperation in the civil exploration and use of the moon, Mars, coments and asteroids for peaceful purposes" (NASA, 2020).
11. I. Seane-Viaño, J. J. Ong, A. W. Basit, A. Goyanes, *Int. J. Pharm. X* **4**, 100121 (2022).
12. E. Urquieta, J. Wu, J. Hury, D. Donoviel, *Nat. Med.* **28**, 611 (2022).
13. R. T. Scott *et al.*, *Nat. Mach. Intell.* **5**, 196 (2023).
14. E. L. Antonsen, R. D. Reed, *Houston J. Health Law Pol.* **19**, 1 (2020).
15. J. Ong *et al.*, *Br. J. Ophthalmol.* **107**, 895 (2023).

ACKNOWLEDGMENTS

The views expressed in this article are the authors' own and do not necessarily reflect those of their affiliate institutions. This work is supported by the Translational Research Institute for Space Health through NASA Cooperative Agreement NNX16AO69A. The ethical principles and their applications that comprise this framework were produced after a workshop held at the Banbury Center, Cold Spring Harbor Laboratory. The authors wish to sincerely thank R. Leshan and the Banbury Center, Cold Spring Harbor Laboratory for their combined financial and coordination support.

10.1126/science.adh9028

PERSPECTIVES

PHYSIOLOGY

Cellular coupling in the heart

Fibroblasts in scar tissue elicit myocyte excitation and promote arrhythmia in mouse hearts

By **Patrizia Camelliti**[1] *and* **Daniel J. Stuckey**[2]

Traditionally, cardiac electrophysiology has focused on myocytes—the heart muscle cells that generate action potentials and are electrically excitable. Nonmyocytes within the heart are often considered barriers to action potential propagation. Typically defined as extracellular matrix–producing cells, cardiac fibroblasts are one of the largest nonmyocyte cardiac populations. However, they have been recognized to be important for maintaining normal cardiac function and for mediating cardiac remodeling during pathology, when their number substantially increases (*1*). The presence of electrical coupling between fibroblasts and myocytes has been established in vitro and more recently demonstrated in situ (*2*–*4*). But definitive in vivo evidence has been lacking. On page 1480 of this issue, Wang *et al.* (*5*) report that fibroblasts and myocytes are electrically coupled in living mice. This finding could transform the understanding of cardiac connectivity and arrhythmogenesis, with profound implications for the management of heart disease patients.

Wang *et al.* engineered an optogenetic transgenic mouse that expressed the light-sensitive channelrhodopsin 2 (CHR2) in fibroblasts, enabling real-time stimulation of membrane depolarization specifically in resident fibroblasts by illumination with blue light. In animals subjected to coronary occlusion to mimic myocardial infarction, blue light illumination of the resulting fibroblast-rich scar drove organ-wide cardiac excitation in vivo and in excised perfused hearts. Increasing the frequency of the illumination increased the heart rate with a 1:1 response, demonstrating functional electrical coupling between CHR2-expressing fibroblasts and myocytes. When optical pacing ceased, a subset of hearts did not return to normal sinus rhythm and displayed ectopic beats and atrioventricular conduction block, which suggests that depolarization of fibroblasts can initiate arrythmia.

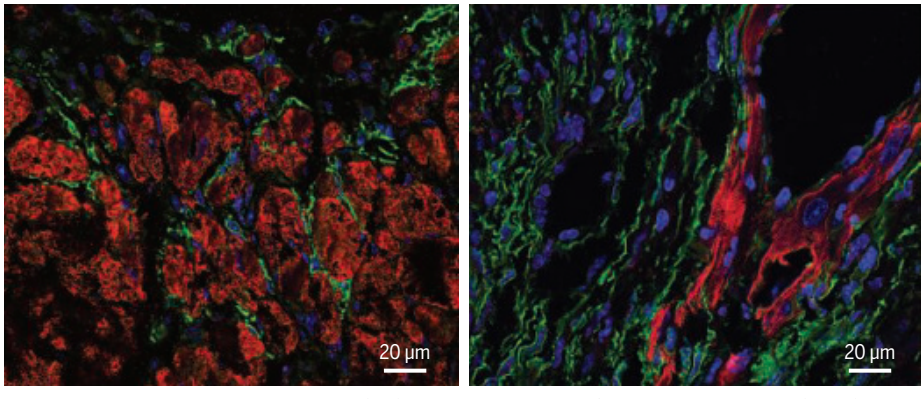

Immunofluorescent images show myocytes (red) and channelrhodopsin 2–expressing fibroblasts (green) in the uninjured myocardium (left) and in the scar (right) 10 days after myocardial infarction in mice.

Cardiac arrhythmia is an important complication in patients with myocardial infarction and can lead to sudden cardiac death. Fibrotic tissue promotes arrhythmia by acting as a physical barrier to action potential conduction between myocytes. Cocultures of fibroblasts and myocytes have demonstrated that coupling between the two cell types can alter myocyte excitability, repolarization, and conduction, promoting arrhythmogenic conditions (*6*). Wang *et al.* showed that fibroblast-myocyte coupling can promote arrhythmia in vivo. Although the exact mechanism leading to the observed arrhythmia remains elusive, the authors suggest that changes in myocyte excitability and conduction driven by the depolarization of scar fibroblasts could induce arrhythmia after myocardial infarction.

It is important to note that Wang *et al.* used synchronous, global depolarization of scar fibroblasts to drive organ-wide cardiac excitation and promote arrhythmogenesis. Although local changes in fibroblast depolarization could occur in response to mechanical stretch or ischemia in the scar (*7*), global depolarization of fibroblasts in vivo is unlikely owing to the heterogeneous nature of the infarcted myocardium. In vitro and computational studies indicate that a substantial number of fibroblasts functionally coupled to myocytes is required to promote arrhythmogenesis (*6*). Whether local depolarization of a small number of fibroblasts in the scar or border zone would be sufficient to alter cardiac excitation and trigger arrhythmia remains to be determined. But focal activation using a micrometer-diameter light source in the model developed by Wang *et al.* could start to address this question.

Electrical coupling between fibroblasts and myocytes is generally thought to be mediated by gap junctions, which directly connect the cytoplasm of neighboring cells (*1*). Using conditional deletion of the gap junction protein connexin 43 (CX43) in fibroblasts, Wang *et al.* show that this gap junctional protein is not essential for fibroblast-myocyte communication in vivo. It would be interesting to see whether loss of CX43 in fibroblasts would affect arrhythmogenicity. In vitro experiments performed in fibroblasts deficient in CX40, CX43, CX45, and pannexin 1 (PANX1) suggest that these membrane channel proteins are also unnecessary for heterocellular coupling. Follow-up computational studies indicated that ephaptic coupling—a non–gap junctional coupling mechanism that facilitates cell-to-cell transfer of electrical activation through the extracellular space (*8*)—may be sufficient to couple cells. Proving the presence of ephaptic coupling in vivo and dissecting its contribution to arrhythmogenesis will be challenging but essential to develop therapies to block fibroblast-mediated cardiac arrhythmia.

The findings of Wang *et al.* have important implications for ablation procedures that are commonly used to treat arrhythmia. The frequent recurrence of ventricular tachycardia in these patients (*9*) could result from the coupling of fibroblasts with residual myocytes at the ablation site, leading to new arrhythmogenic substrates. Targeting fibroblast-myocyte coupling in this setting could be a promising strategy to prevent recurrence. Conversely, interventions that enhance fibroblast-myocyte coupling and conduction might be beneficial in bridging scar tissue and reducing conduction block,

[1]School of Biosciences, University of Surrey, Guildford, UK. [2]Centre for Advanced Biomedical Imaging, University College London, London, UK. Email: p.camelliti@surrey.ac.uk

PHOTO: YUJIE WANG AND SIVAKUMAR RAMADOSS IN ARJUN DEB LABORATORY

therefore preventing reentrant ventricular tachycardia (*7*). The prevalence of diffuse and focal fibrosis in many other forms of heart disease further widens the relevance of these findings, with potential roles of fibroblast-myocyte coupling in hypertrophic and arrhythmogenic right ventricular cardiomyopathies, which are common causes of sudden cardiac death in young people.

These results will also be important for cardiac cell therapies that are being developed to replace myocardium lost in disease (*10*). Electrical coupling between resident scar fibroblasts and transplanted myocytes could alter donor myocyte excitability, repolarization, and conduction, promoting substrates for focal or reentrant arrhythmia (*11*). Alternatively, fibroblasts could assist donor myocyte integration by forming passive conduction connections to the host's myocardium, promoting electrophysiological synchronization.

Advances in genetic tools (*12*) coupled with biomedical imaging (*13*) now make it possible to track and manipulate the function of individual cell types, allowing molecular processes and pathways to be investigated and multicellular contributions to complex organ systems to be disentangled in situ and even in vivo. The approach used by Wang *et al.* highlights only the beginning of what will be possible using these advanced genetic systems. The exact number and location of fibroblasts required to initiate arrhythmia and the contribution of other nonmyocytes and transplanted donor cells to cardiac electrophysiology can now be investigated and controlled in model organisms. This could initiate a step change in our understanding of cardiac electrophysiology and uncover therapeutic targets for heart failure, arrythmia, and sudden cardiac death. ■

REFERENCES AND NOTES

1. R. D. Johnson, P. Camelliti, *Int. J. Mol. Sci.* **19**, 866 (2018).
2. T. A. Quinn *et al.*, *Proc. Natl. Acad. Sci. U.S.A.* **113**, 14852 (2016).
3. V. M. Mahoney *et al.*, *Sci. Rep.* **6**, 26744 (2016).
4. M. Rubart *et al.*, *Cardiovasc. Res.* **114**, 389 (2018).
5. Y. Wang *et al.*, *Science* **381**, 1480 (2023).
6. A. Simon-Chica, E. M. Wülfers, P. Kohl, *Am. J. Physiol. Heart Circ. Physiol.* **325**, H475 (2023).
7. R. G. Gourdie, S. Dimmeler, P. Kohl, *Nat. Rev. Drug Discov.* **15**, 620 (2016).
8. R. G. Gourdie, *Anat. Rec.* **302**, 93 (2019).
9. L. Quinto *et al.*, *Heart Rhythm* **18**, 896 (2021).
10. R. J. Jabbour *et al.*, *JCI Insight* **6**, e144068 (2021).
11. R. D. Johnson, M. Lei, J. H. McVey, P. Camelliti, *Cell. Mol. Life Sci.* **80**, 276 (2023).
12. J. Joshi, M. Rubart, W. Zhu, *Front. Bioeng. Biotechnol.* **7**, 466 (2020).
13. B. M. Helfer *et al.*, *Cytotherapy* **23**, 757 (2021).

ACKNOWLEDGMENTS

P.C. receives support from the British Heart Foundation (BHF) (FS/17/33/32931 and PG/22/11172) and the Royal Society (RSG/R1/180198). D.J.S. is a BHF Senior Research Fellow (FS/SBSRF/21/31020).

10.1126/science.adk3408

GRAPHIC: A. MASTIN/*SCIENCE*

NANOMATERIALS

Widening the use of 3D printing

A light-triggered fabrication method extends the functionality of printable nanomaterials

By **Daniel M. Balazs** *and* **Maria Ibáñez**

Three-dimensional (3D) printing has reshaped manufacturing paradigms by providing customized on-demand object fabrication. To unlock 3D printing's full range of applications, material versatility is necessary. Presently, the range of available 3D-printing materials is limited to mostly metals and polymers because of their ease in forming chemical bonds as they convert from ink into a solid object. Recently, complex 3D structures of semiconducting nanoparticles were printed by light-induced reactions between the nanoparticles and molecules at their surface (*1*). This strategy relies on the properties of the nanoparticle and the surface molecules, limiting the printable materials. On page 1468 of this issue, Li *et al.* (*2*) report a material-independent strategy for 3D-printing nanoparticles, which uses an additive that decomposes, upon light irradiation, into a reactive species that binds together two stabilizing molecules connected to the nanoparticle surface (capping molecules). This provides flexibility in the material used, which only requires the ability to form surfactant-stabilized dispersions.

3D-printed structures are formed by creating chemical bonds at the desired location between building blocks—atoms, molecules, or small pieces of material. The most important advance in 3D printing has been the use of light to trigger the connection between building blocks dissolved or suspended in liquids to manufacture complex 3D structures with high spatial resolution (*3*). This approach is based on a light-induced chemical reaction that occurs within a limited volume of the liquid where the light is focused, forming bonds between the building blocks. By tracing the desired structure design with the light beam, the final object is built up within the liquid. Such a strategy has been mainly used for creating plastic (polymeric) objects in a process called photopolymerization. For other materials, such as semiconductors, light-triggered conversion from liquid precursors to solids is not possible because of the materials' complex composition, internal structure, and high atomic binding energies. These peculiarities re-

Three-dimensional (3D)–printing new materials

(Left) A light source is used to initiate the reaction within a nanoparticle suspension containing a light-sensitive additive (**1**). (Top right) The additive, a bisFPA [bis(perfluorophenyl azide)] compound, reacts with light to form a reactive molecule, the binder (Nitrene). (Bottom right) The binder reacts with the capping molecules linked to the nanoparticles (**2**).

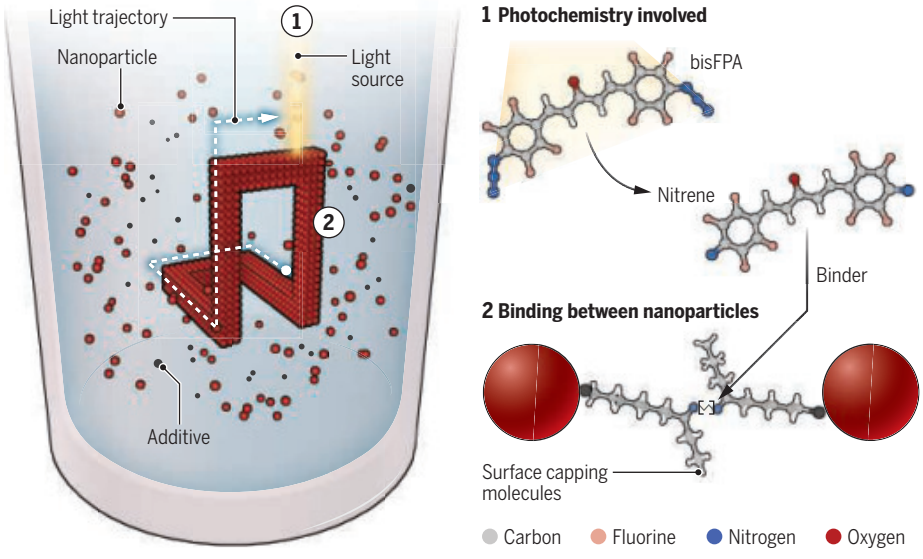

quire demanding processing conditions, such as high pressure or temperature, that are often incompatible with 3D printing.

A solution to bypass this problem is using nanoparticles as solid building blocks in the ink. The nanoparticles should have uniform sizes to warrant high spatial resolution and to take advantage of their size-dependent properties in an optimal ink (*4*). Surfactant-assisted colloidal synthesis has been used to produce such nanoparticle ensembles (*5*). This synthetic method relies on the use of long organic molecules, called ligands, to guide the formation of the nanoparticles, allowing control over their size and shape, among other properties. After their role during nanoparticle synthesis, those ligands or derivatives formed during the synthesis (*6*) remain on the nanoparticle surface, helping to form stable suspensions, (*7*) a crucial characteristic for high-quality printing. The challenge is then to find the right chemistry to form bonds between the nanoparticles.

Li *et al*. designed a nanoparticle printing strategy that interconnects the ligands between different nanoparticles to create 3D structures. A molecular additive is mixed into the nanoparticle suspension, which then decomposes upon irradiation with light, creating a highly reactive and symmetric species called the binder, which is able to bridge the ligands (see the figure). The bond formation can happen either within two ligands of the same nanoparticle, reducing the local colloidal stability and bringing the particles closer together, or between two ligands of different nanoparticles, indirectly creating interparticle links. In addition, the binding occurs through the ligand hydrocarbon chains, providing complete freedom from the properties of the surface-anchoring group of the ligand. Hence, a large variety of ligands can be used, simplifying the ink preparation. Overall, the light-triggered sequence of reactions results in a build-up of solid material defined by the path of the focal point of the light through the liquid. The 3D-printed structures have remarkable mechanical strength and maintain the functionality of the individual nanoparticles. In some configurations, collective phenomena, such as chiral or plasmon-enhanced photoluminescence, can be observed.

Another advantage of this printing method is the small amount of organic content present in the final 3D structures, especially compared with previous methods in which nanoparticles were encapsulated in polymer matrices (*3*). Ideally, the final structure should be only made of the solid material intended to be printed, that is, the nanoparticles. The presence of organic molecules is usually detrimental for applications in which the nanoparticles need to be in close proximity to one another, such as those involving charge transfer (electronics, catalysis, among others) (*8, 9*). The high nanoparticle content used in Li *et al*.'s approach also allows the removal of the organic network after printing by thermal or chemical stripping without compromising the object's shape and strength. Yet, in this regard, there are still some challenges to be addressed, especially in understanding the effect of organic molecules and their thermal decomposition products upon the functionality of the printed structures.

Li *et al*.'s method achieves outstanding spatial resolution, which depends on the wavelength and the optical setup used to trigger the reaction, similar to the resolution limit of optical microscopy. Moreover, the printing setup resembles those used in commercial 3D printers, meaning that the method can be easily and widely adopted in existing systems after a chemical safety evaluation. However, a disadvantage of this method compared to polymer 3D printing is the printing speed, which is limited by the diffusion of the nanoparticles into the exposed volume. The viscosity of the solution, the particle size, and the type of ligand affect the ink stability. Managing the variables that influence printing speed presents a challenge within the realm of chemical engineering.

Highly dense, mechanically robust 3D structures made of a vast array of materials can now be produced by the method presented by Li *et al*. This is an important step toward reaching additive manufacturing's true potential as a transformative technology to 3D-print full devices, including substrates, electric contacts, active elements, and encapsulating layers in one setup, simplifying device fabrication and broadening the functionality of printable materials. ■

REFERENCES AND NOTES

1. S.-F. Liu *et al*., *Science* **377**, 1112 (2022).
2. F. Li *et al*., *Science* **381**, 1468 (2023).
3. S.-F. Liu *et al*., *Adv. Funct. Mater*., 2211280 (2022).
4. A. L. Efros, L. E. Brus, *ACS Nano* **15**, 6192 (2021).
5. M. V. Kovalenko *et al*., *ACS Nano* **9**, 1012 (2015).
6. M. Calcabrini *et al*., *JACS Au* **1**, 1898 (2021).
7. M. A. Boles, D. Ling, T. Hyeon, D. V. Talapin, *Nat. Mater*. **15**, 141 (2016).
8. C. R. Kagan, C. B. Murray, *Nat. Nanotechnol*. **10**, 1013 (2015).
9. M. Liu *et al*., *Nat. Electron*. **4**, 548 (2021).

ACKNOWLEDGMENTS

The authors thank the Werner-Siemens-Stiftung and the Institute of Science and Technology Austria for financial support.

10.1126/science.adk3070

Institute of Science and Technology Austria, Klosterneuburg, Austria, Email: mibanez@ist.ac.at

GENOMICS

Genetics of coral resilience

Genome-wide study in staghorn coral identifies markers of disease resistance

By **Laura D. Mydlarz**[1] *and* **Erinn M. Muller**[2]

Present in every population of plants and animals are distinct individuals who are resistant to disease. An important question is what genetic insights can be obtained from studying these individuals. In the case of coral, many of which are on the brink of regional extinctions largely because of disease outbreaks, information on resistant individuals has the potential to prevent ecosystem collapse. On page 1451 of this issue, Vollmer *et al*. (*1*) report genome sequencing results for staghorn coral (*Acropora cervicornis*) populations in Florida and Panama that have been exposed to disease. They identified gene variants that are associated with disease resistance. These variants could be used to identify resilient populations for use in coral restoration efforts. This is important because climate change and disease outbreaks continue to prevent many existing restoration programs from achieving long-term success.

Over the past 50 years, reef-building corals have experienced unprecedented declines globally, leaving their spectacular biodiversity and contributions to ecosystem function hanging in the balance. Populations of the *Acropora* genus of branching corals, including *A. cervicornis* and elkhorn coral (*Acropora palmata*), have experienced widespread declines throughout their geographical range, which extends from Florida throughout the Caribbean. Regional die-offs of *Acropora* species began in the late 1970s because of ocean warming, hurricanes, and white band disease (*2*). The latter is likely a bacterial disease, although a singular pathogen has not been identified, and is so named because it causes rapid tissue loss that exposes the white skeleton and eventually kills the coral.

To prevent population and ecosystem collapse, massive efforts are underway to restore corals within depleted reefs. To do this, tens of thousands of coral fragments (broodstock) are grown in coral nurser-

Shown are four-year-old outplants of nursery-grown staghorn coral (*Acropora cervicornis*) in Florida Keys, USA.

PHOTO: MOTE MARINE LABORATORY

ies and then transported and attached to reef substrate (outplanted) within Florida's coral reef each year. One major restoration program predicts that hundreds of thousands to millions of corals will need to be outplanted to regain appropriate coral cover over just ~70 acres (~0.3 km^2) (*3*). *A. cervicornis* is the most common species for outplanting (*3*) because it is fast growing and easy to propagate in underwater nurseries. However, sustained disease outbreaks, in combination with unrelenting climate change and hurricanes, have caused major setbacks in these restoration efforts, particularly within Florida. White band disease remains a substantial threat to these corals, and, given the largely clonal genetic structure of *Acropora*-dominated reefs, the disease can lead to chronic coral loss (*4*, *5*).

Vollmer *et al.* performed a genome-wide association study on mixed-genotype populations of *A. cervicornis* from Florida (nursery corals) and Panama (wild corals). They identified 73 single-nucleotide polymorphisms (SNPs) on seven chromosomes that are associated with disease resistance and used these data to calculate a polygenic score for disease resistance. Of the resistance-associated SNPs, four resulted in identifiable protein-coding changes in genes that have known roles in immunity and in other pathways relevant to disease resistance. The identification of these genes not only highlights potential resistance pathways but also provides information on processes that are critical to the coral immune response.

There is a plethora of omics data that compares health and disease states in coral (*6*). However, these studies can fall short in distinguishing between effective immune responses and reactive inflammation and tissue loss. The genes identified by Vollmer *et al.* are promising in this regard. For example, some of these genes are involved in the regulation of lysosomal and vesicular trafficking and the initiation of endocytosis, both of which play a pivotal role in disease responses (*6*). The knowledge that variants in specific genes within these pathways contribute to disease resistance could substantially advance understanding of the coral immune system.

The identification by Vollmer *et al.* of biomarkers of disease resistance for a restoration target species is the type of research that is needed to facilitate interventions that will encourage population-level resilience in restored coral populations. Indeed, introducing intervention strategies that are designed to overcome disease and climate risks is likely the only way to continue conducting restoration with any hope of long-term efficacy. Long-standing tropes that focus on only encouraging genetic diversity within restored populations without thoughtfully integrating resistant traits to promote population- and community-level resilience will simply not be enough to promote long-term recovery in the face of unprecedented anthropogenic threats to coral health.

With this aim in mind, the findings of Vollmer *et al.* could facilitate the outplanting of more-resistant broodstock. Techniques such as selective breeding for heritable resistance traits or the use of gene-editing tools will be necessary to create additional resistant variants while maintaining genetic diversity. To build on the work by Vollmer *et al.*, further studies should explore the potential for trade-offs that are associated with disease resistance. For example, restoration cannot move forward with disease-resistant broodstock if these genotypes are sterile, less temperature tolerant, or highly susceptible to other common and unavoidable stress events. To date, few, if any, trade-offs between important life history traits, such as heat tolerance, growth, survival, and disease resistance, have been identified within *A. cervicornis* (*4*, *7*). However, trade-offs between disease resistance and heat tolerance have been documented within other coral species (*8*, *9*). Additionally, coral diseases are a complex interaction between host, microbiome, and environment; therefore, any discoveries of disease resistance in the host need to be considered alongside contributions from these other elements. In particular, it will be important to determine how environmental conditions, such as temperature stress, interact with genetics to influence disease resistance (*10*, *11*). Regardless, massive efforts to conduct restoration will fail if global carbon dioxide and other local anthropogenic stressors are not mitigated.

Vollmer *et al.*'s identification of adaptive polygenic variation in disease resistance in Florida and Panama populations of *A. cervicornis* indicates that the genetic variation for disease resistance is present across the Caribbean, which brings hope for the persistence of this critically endangered species. Will this new information be used to develop more-informed disease-management strategies and prioritize conservation and recovery efforts? The threats to the future of these reefs are outside of expected norms, and thus efforts to preserve them must be as well. ■

[1]Department of Biology, University of Texas at Arlington, Arlington, TX, USA. [2]Mote Marine Laboratory, Sarasota, FL, USA. Email: mydlarz@uta.edu; emuller@mote.org

REFERENCES AND NOTES

1. S. V. Vollmer, J. D. Selwyn, B. A. Despard, C. L. Roesel, *Science* **381**, 1451 (2023).
2. K. L. Cramer *et al.*, *Sci. Adv.* **6**, eaax9395 (2020).
3. L. Boström-Einarsson *et al.*, *PLOS ONE* **15**, e0226631 (2020).
4. E. M. Muller, E. Bartels, I. B. Baums, *eLife* **7**, e35066 (2018).
5. A. L. Brown *et al.*, *Sci. Rep.* **12**, 19286 (2022).
6. N. Traylor-Knowles *et al.*, *Front. Mar. Sci.* **9**, 952199 (2022).
7. H. R. Koch, Y. Azu, E. Bartels, E. M. Muller, *Front. Mar. Sci.* **9**, 958500 (2022).
8. A. Shore-Maggio, S. M. Callahan, G. S. Aeby, *Coral Reefs* **37**, 507 (2018).
9. B. Cornwell *et al.*, *eLife* **10**, e64790 (2021).
10. Z. L. Fuller *et al.*, *Science* **369**, eaba4674 (2020).
11. R. L. Vega Thurber *et al.*, *Front. Ecol. Evol.* **8**, 575927 (2020).

10.1126/science.adk2492

EVOLUTIONARY BIOLOGY

An epigenetic clock in plants

DNA methylation can identify evolutionary relationships among close plant lineages

By **P. R. V. Satyaki**

Molecular clocks are analytical tools that count the DNA sequence differences between orthologous genomic regions of related organisms to identify when their evolutionary lineages diverged (*1*). This approach assumes that mutations that do not affect an organism's fitness (neutral mutations) accumulate at a constant rate. Over the past ~60 years, molecular clocks have helped fill gaps in the fossil record, assisted in conservation programs (*2*), and enabled the tracking of severe acute respiratory syndrome coronavirus 2 (SARS-CoV-2) variants (*1*, *3*). However, current molecular clocks struggle to map relationships between recently diverged populations with few DNA sequence differences. On page 1440 of this issue, Yao *et al*. (*4*) describe a molecular clock that overcomes this shortcoming in self-pollinating (selfing) and clonal (vegetatively propagated) plant populations by counting epigenetic mutations (epimutations), which occur faster than DNA sequence mutations. The new tool has potential applications in plant breeding and the study of ecology, evolution, and archaeology.

The epimutations examined by Yao *et al*. are changes to the methylation of CpG sites in DNA. During DNA replication, CpG methylation status is copied to newly synthesized DNA by DNA methyltransferases (*5, 6*). CpG methylation can also be removed by DNA demethylases to maintain epigenetic homeostasis by preventing DNA hypermethylation (*5*, *6*). Inaccuracies or "noise" in DNA methylation and demethylation can lead to epimutations whereby CpGs gain or lose methylation compared with those in the previous generation of cells (*5*, *6*). In plants, these epimutations accumulate largely during mitotic cell division in the genomes of a stem cell population called the meristem (*5*). Meristems give rise to both somatic tissues and to gametes that, in turn, transmit the epimutations to the progeny of the plant.

Studies in the model plant *Arabidopsis thaliana* and in other plant species show that the methylation status of individual cytosines at many sites, including within genes, seems to have no functional consequence (*5*), and thus these epimutations are similar to neutral mutations. CpG epimutations in plants also occur at a rate up to five orders of magnitude higher than genetic mutations and can thus be used to identify the evolutionary relationships between recently diverged lineages (*5*).

To test if these neutral epimutations could be used to calibrate a molecular clock, Yao *et al*. analyzed changes in genome-wide DNA methylation between multiple *A. thaliana* pedigrees that had been selfed and had accumulated mutations for up to 32 generations with or without exposure to stresses such as bacterial infections, drought, and salinity. They identified genomic regions that exhibited epimutation-driven molecular clock-like behavior that was not influenced by exposure to stress. The epimutations dated the evolutionary divergence of their experimental *A. thaliana* pedigrees with much higher accuracy than genetic differences. This approach was used to identify the evolutionary relationships between *A. thaliana* strains in North America using epimutations from present *A. thaliana* strains as well as from herbarium samples, some of which were collected in the 19th century. They also used the epigenetic clock to identify the relationships between clonal lines of the seagrass *Zostera marina*.

> **"...epimutations dated the evolutionary divergence of... *Arabidopsis thaliana* pedigrees..."**

It should be noted that the technique described by Yao *et al*. differs from the epigenetic aging clocks observed in mammals. Mammalian epigenetic clocks can measure an individual's age but not evolutionary time because DNA methylation is reset during mammalian reproduction (*5*).

The epigenetic clock could be used in ecological research. Many plant species are migrating in response to climate change (*7*), and selfing and clonal plants are likely to be more successful than cross-pollinating plants to colonize new areas (*8*). Therefore, the capability of the epimutation clock to accurately date the recent evolutionary history of selfing and clonal species could be used to improve the planning of ecological restoration projects (*9*) by determining the source of plant species and their rates of migration.

The clock developed by Yao *et al*. could aid the breeding of crops such as potatoes, soybean, and strawberries by providing information on the pedigree of genetic resources such as seeds or tissues. In addition, the epimutation clock might play an important role in archaeology, where it could provide accurate estimates of when a crop was domesticated or when archaeological sites exchanged agricultural products (*10*). In the field of archaeogenomics, the clock could be applied to genomic analysis of plant remains found at archaeological sites (*10*).

Epimutation-based molecular clocks may also be useful for "resurrection genomics" (*11*), in which seeds recovered from archaeological sites are germinated. The resulting plants can provide fresh material for DNA extraction and sequencing. Although the efficacy of this technique is limited by seed longevity, a pioneering effort that germinated 2000-year-old date palm seeds and sequenced their genomes highlights its potential (*11*).

Combining the information from genetic and epigenetic changes was previously proposed to produce a more accurate molecular clock than either type of change alone (*5*). Long-read sequencing technology such as nanopore-based methods that simultaneously read DNA sequences and CpG methylation (*12*) could be pivotal in developing this combined clock. ■

Department of Biological Sciences, University of Toronto Scarborough, Toronto, ONT, Canada. Email: satyaki.rajavasireddy@utoronto.ca

REFERENCES AND NOTES

1. S. Kumar, *Nat. Rev. Genet.* **6**, 654 (2005).
2. Y. Hu *et al*., *Sci. Adv.* **7**, eabd5725 (2021).
3. J. Pekar, M. Worobey, N. Moshiri, K. Scheffler, J. O. Wertheim, *Science* **372**, 412 (2021).
4. N. Yao *et al*., *Science* **381**, 1440 (2023).
5. N. Yao, R. J. Schmitz, F. Johannes, *Trends Genet.* **37**, 699 (2021).
6. R. R. Hazarika *et al*., *Nat. Plants* **8**, 146 (2022).
7. S. Fei *et al*., *Sci. Adv.* **3**, e1603055 (2017).
8. J. R. Pannell *et al*., *New Phytol.* **208**, 656 (2015).
9. J. L. Mijangos, C. Pacioni, P. B. S. Spencer, M. D. Craig, *Mol. Ecol.* **24**, 22 (2015).
10. L. Kistler *et al*., *Annu. Rev. Plant Biol.* **71**, 605 (2020).
11. M. Gros-Balthazard *et al*., *Proc. Natl. Acad. Sci. U.S.A.* **118**, e2025337118 (2021).
12. J. T. Simpson *et al*., *Nat. Methods* **14**, 407 (2017).

10.1126/science.adk2696

Alfie (left) and one of her chicks survey their surroundings from their nest box.

BOOKS *et al.*

ANIMAL BEHAVIOR

Sheltering in place

An orphaned owl's convalescence inspired an ecologist's reflections during COVID-19 lockdown

By **Barbara J. King**

"Show me what you are grateful for, and I will know what you believe," writes behavioral ecologist Carl Safina in *Alfie and Me: What Owls Know, What Humans Believe*. Safina's expansive gratitude for the natural world illuminates every page: gratitude for the wild animals who live near the Long Island home he shares with his wife; for the dogs, chickens, snake, and parrots who also share that home; and for the little eastern screech owl he named Alfie whose convalescence on Safina's property transcended any border between wild and domestic. Alfie blurred, in fact, the very notion of such a border as she became for Safina "a portal to the parallel reality adjacent to our human experience."

Alfie and Me: What Owls Know, What Humans Believe
Carl Safina
Norton, 2023. 384 pp.

As an orphaned chick, filthy and weak, Alfie was rescued by Safina from almost certain death. Safina's plan was to allow her some recovery time, then release her. When her flight feathers did not fully develop on schedule, Alfie unexpectedly required a "prolonged, unplanned captivity" in an outdoor coop. Her confinement overlapped with the worldwide period of COVID-19 pandemic lockdown, creating a rare opportunity for the usually overscheduled Safina to closely observe an owl's physical and behavioral growth.

Screech owls are tiny: Alfie stood five inches tall, plus three inches of tail. Her eyes and bill shone a light yellow green, while her body was colored brick red with "vertical streaks of dark chocolate" that aided her camouflage when in the trees. When her feathers did come in, they enabled the awesome silent flight that aids owl predation on birds, small mammals, and insects. "Alfie could fly right past our faces without us hearing anything," writes Safina.

Ethical questions arose and persisted. Safina repeatedly grappled with tough decisions—how much to help Alfie, how much to allow her to absorb free-living risks on her own—and it is a mark of integrity that he reports what he considers his occasional mistakes as well as his joyful successes.

Those successes make up the beautiful heart of the book, because what happened between Alfie and Safina exceeded scientific observation. The two created with each other bonds of mutual trust and entered partway into each other's worlds. Telling this intimate story becomes an insightful extension of Safina's earlier books on the intelligence, emotion, and culture of animals ranging from elephants to scarlet macaws.

Alfie and Me is not a work of fiction. Why then do I feel reluctant to reveal in any detail the events that unfolded as Alfie became bolder in her own wild world? Perhaps because, just like humans' lives, the lives of owls follow a narrative arc, and it is a pure joy to discover, chapter by chapter, Alfie's own arc as she matures, mates, and raises a family. Especially entrancing are descriptions of her three fledglings' first days out of the nest near Safina's house. The owlets discover the hard way that songbirds despise the presence of predators in their airspace: In an encounter with blue jays, a youngster is smacked hard "and plummets like a falling apple" from tree to ground.

Interspersed with this owl ethnography are lengthy passages describing historical perspectives on nature and animals. Plato becomes a central figure, described as the author of "history's biggest intellectual mistake": the dualist opposition of mind and matter.

Because the charming owl sections alternate in quick fashion with insights about society's persistent devaluing of animals, indeed about our "planetary rape culture," the emotional experience is whipsawing at times. But heroes and hope are here too. The terrible acts against nature and the views from which they spring are Western in origin; Indigenous and Asian cultures, on the other hand, see the world as webs of relationships. They represent not only a different past but also a better way forward.

Safina continuously loops back to his theme of gratitude, for Alfie and her family and for other animals who cross his path. Upon hearing a dove and a woodpecker early one morning, then enjoying a squirrel's acrobatics, Safina notes that the day ahead "felt nourishing and delicious."

There is abundant appreciation, too, for fishes in the sea who, for Safina, nonetheless become "gifts" of food. Knowing that fishing causes pain, Safina explains that he fishes apologetically. He does so in part to avoid factory-farmed food but mainly because taking his boat onto the ocean among creatures of the sea and air is vital to his life. This honest appraisal reveals that, while we have come a long way since Plato's dualism, it is still the case that some animal lives matter more than others. ■

10.1126/science.adj4265

The reviewer is professor emerita of anthropology at William & Mary, Williamsburg, VA 23185, USA. Email: bjking@wm.edu

PHOTO: CARL SAFINA

HISTORY OF MEDICINE

Pandemics and their lessons

Distrust and xenophobia have long been stumbling blocks during public health crises

By **Michael A. Goldman**

Foreign Bodies: Pandemics, Vaccines, and the Health of Nations
Simon Schama
Ecco, 2023. 480 pp.

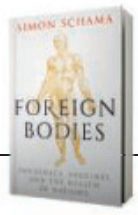

"The matter filling million upon millions of pages of recorded history—wars and revolutions, the rise and fall of cities and empires, fevers of faith, the heaping up and the emptying out of wealth—has been circumscribed by what we have done to nature and what it has done to us," writes historian Simon Schama in his latest volume, *Foreign Bodies*. This conflict between natural forces and humankind, although it may be more intense today, has erupted many times before, and many times before we have failed to heed the lessons of the past to avoid repeating our mistakes. As the reverberations of COVID-19 recede, Schama presents an eloquent picture of our past encounters with other pathogens, in the process illustrating our unfolding relationship with SARS-CoV-2.

Schama is well known for his scholarship on Jewish history and world history, and this new work addresses some similar themes, revealing how nationalism and xenophobia intersect with science, medicine, and the history of both. The "foreign bodies" to which the book's title refers are not just the microbial invaders that infect us but also the outsiders and global figures who have contributed to humankind's collective understanding of infectious disease pathology, etiology, treatment, and prevention.

In the 1800s, steamships and steam engines made international travel possible. One consequence of this mobility, however, was that the rest of the world could not easily ignore a raging cholera pandemic in India. Nor, it turns out, could curious British scientists resist the fertile vaccination testing grounds the colony afforded. During this period, there were regular disagreements over new ideas in bacteriology and virology. Tensions between French microbiologists, adherents to old customs in the Ottoman Empire, the British medical establishment, and traditional medicine practitioners of India raged, often fueled more by nationalism than by evidence. Parallels exist in attitudes today toward COVID-19, which are often informed by xenophobia and inherent distrust of authority.

Schama drills deep on a few other historical epidemics—smallpox in France in the late 1700s and bubonic plague in India in the late 1800s, for example. Often the same countries and characters pervade the stories. Despite the author's selectivity, the book spans more than 400 lively pages, telling the story of some of the unsung heroes of virology and vaccination, from the English writer Mary Wortley Montagu, who wrote home about Turkish smallpox inoculation practices in 1717, to the French physician Adrien Proust (father of Marcel) whose 1873 *Essay on International Hygiene* advocated for human agency in the spread of cholera. Schama tells each of these stories with characteristic eloquence, but I will mention here one such figure—the microbiologist Waldemar Mordechai Wolff Haffkine.

Born in Odessa, in what is now the country of Ukraine, Haffkine had his first brush with fame as a Jewish defense fighter in the Odessa pogroms. Training at the Pasteur Institute, he helped to bring "French science" to Britain and India and contributed substantially to the development of the cholera and plague vaccines, even as he faced discrimination and distrust as a result of his nation of origin. He is remembered today through the Haffkine Institute for Training, Research and Testing in Mumbai, India, and the Haffkine Bio-Pharmaceutical Corporation, which produced the COVID-19 vaccine Covaxin in 2021.

The interplay between humanity and nature is not confined to the pages of history but rather is etched in our genes and in the genes of the organisms with which we interact. Certain alleles may become more or less common in future generations, for example, because of the resistance or susceptibility to infectious disease they confer during times of rampant infection (*1*–*3*). Selective pressures from COVID-19 are already in evidence (*4*, *5*). That genetics does not figure into Schama's account is a missed opportunity in an otherwise important book on epidemics, pandemics, and human history.

"Truth," observes Schama, "always seems on the verge of overtaking error, when its exhilarating progress is sandbagged by indignation about foreign substances deviously introduced into our bodies." This observation resonates today, as so many people choose to believe ivermectin and hydroxychloroquine will treat or cure COVID-19, eschewing vaccination. Solving such a seemingly intractable problem will depend increasingly on interdisciplinary approaches, deployed on a global scale, without borders. Are we ready? History, unfortunately, suggests we are not. ■

The reviewer is at the Department of Biology, San Francisco State University, San Francisco, CA 94132, USA.
Email: goldman@sfsu.edu

REFERENCES AND NOTES

1. A. C. Allison, *Br. Med. J.* **1**, 290 (1954).
2. E. K. Karlsson, D. P. Kwiatkowski, P. C. Sabeti, *Nat. Rev. Genet.* **15**, 379 (2014).
3. A. P. Galvani, M. Slatkin, *Proc. Natl. Acad. Sci. U.S.A.* **100**, 15276 (2003).
4. F. Barmania, J. Mellet, M. A. Holborn, M. S. Pepper, *Adv. Exp. Med. Biol.* **1412**, 119 (2023).
5. D. G. Augusto *et al.*, *Nature* **620**, 128 (2023).

10.1126/science.adj8933

SCIENCE, SEX, AND GENDER

This block in New Belgrade was designed to meet families' needs.

PHOTO: KRISTEN GHODSEE

PODCAST

Everyday Utopia: What 2,000 Years of Wild Experiments Can Teach Us About the Good Life
Kristen R. Ghodsee
Simon and Schuster, 2023. 352 pp.

The nuclear family and its attendant (and often unequal) gender roles may be a commonly accepted organizing principle for human society, but it is far from the only option available to us. This week on the *Science* podcast, Kristen Ghodsee explores how humanity has experimented with other frameworks for cultivating community and the lessons these experiments hold for those hoping to foster a more egalitarian future. bit.ly/460SJW0

10.1126/science.adk6940

Plastic use in the Qinghai-Tibetan Plateau could affect water quality throughout much of Asia.

PHOTO: WULINGYUN/GETTY IMAGES

Edited by **Jennifer Sills**

Combat plastics in the Qinghai-Tibetan Plateau

The Ecological Protection Law of the Qinghai-Tibetan Plateau (QTP), approved by China's National People's Congress Standing Committee in April, took effect on 1 September (*1*). The law includes measures to address biodiversity loss, climate change, and carbon neutrality in the QTP, but it does not sufficiently control plastic pollution. Plastic products are intertwined with industry, agriculture, animal husbandry, and daily life on the QTP (*2*), and regulating plastic effectively in the region is crucial to human and ecological health across a vast area of Asia.

The QTP provides a home to diverse flora and fauna (*3*), and its ecosystems are unique in the world. Microplastic pollution (plastic debris less than 5 mm in size) is ubiquitous in the air, rivers, lakes, soil, and snow and ice throughout the QTP (*4*–*6*). The transfer of microplastics through the food chain threatens biological organisms (including humans), undermining the region's contribution to the protection of wildlife habitats and biodiversity (*3*).

As the largest frozen reservoir in the world, the QTP serves as a vital water source for about 2 billion people (*7*). Microplastic pollution in the QTP may affect the drinking water safety of downstream regions and countries, including eastern China and India (*8*). Moreover, greenhouse gas emissions generated by plastic use (*9*) in the QTP—such as tourism, farming, and construction—have not been determined, introducing uncertainties about the effectiveness of national climate change legislation.

The Ecological Protection Law's plastics policies rely on voluntary actions by residents, tourists, and construction organizations to mitigate plastic pollution. The law suggests that individuals appropriately dispose of waste, and it requires full life-cycle environmental monitoring for major construction projects. However, it provides no enforcement mechanisms. Without strong legislation, local governments in the QTP, which covers a quarter of China's area, cannot take legal action against plastic pollution.

To ensure effective plastic management in the QTP, China should pass additional legislation that establishes a specific timetable for plastic control, including measurable midterm goals and penalties for inaction. Guidelines and strategies that facilitate the development of biodegradable plastic substitutes and disposal of recyclable plastics should be tailored to each local community and ecosystem. The national government should also educate QTP residents about plastic use and recycling (*10*). Controlling plastic use in the QTP will benefit the region itself as well as the people and ecosystems that depend on it.

Xiaoping Wang[1,2]* and Yunqiao Zhou[1]
[1]State Key Laboratory of Tibetan Plateau Earth System, Resources and Environment, Institute of Tibetan Plateau Research, Chinese Academy of Sciences, Beijing 100101, China. [2]University of Chinese Academy of Sciences, Beijing 100049, China.
*Corresponding author.
Email: wangxp@itpcas.ac.cn

REFERENCES AND NOTES

1. "Law of the People's Republic of China on Ecological Conservation on the Qinghai–Tibet Plateau, issued by the National People's Congress Standing Committee on 27 April 2023" (2023); https://www.mee.gov.cn/ywgz/fgbz/fl/202304/t20230427_1028458.shtml [in Chinese].
2. S. Borrelle *et al.*, *Science* **369**, 1515 (2020).
3. Y. Lu *et al.*, *Sci. Adv.* **6**, eabd0952 (2020).
4. H. Dong *et al.*, *Environ. Sci. Technol.* **57**, 2362 (2023).
5. H. Dong *et al.*, *Environ. Sci. Technol.* **55**, 12951 (2021).
6. T. Wang *et al.*, *J. Hazard. Mater.* **457**, 131711 (2023).
7. T. Yao *et al.*, *Nat. Rev. Earth. Environ.* **3**, 618 (2022).
8. F. Zhang *et al.*, *Nat. Rev. Earth. Environ.* **3**, 611 (2022).
9. R. Meys *et al.*, *Science* **374**, 71 (2021).
10. Y. Zhou, G. Yuan, Z. Cong, X. Wang, *Fund. Res.* **1**, 329 (2021).

10.1126/science.adk2906

Are algorithmic bias claims supported?

In their Special Issue Research Article, "Asymmetric ideological segregation in exposure to political news on Facebook" (28 July, p. 392), S. González-Bailón *et al.* analyzed links to news that US Facebook users shared and viewed during the 2020 election and found substantial ideological segregation in content on Facebook. They claim that Facebook's news feed algorithm increases ideological segregation. However, the evidence suggests that news feed ranking does not increase partisan segregation overall, at least for the sample and timeframe under study.

González-Bailón *et al.* analyzed data aggregated both by source (i.e., domain or website) and by URL (i.e., the specific webpage). Source-level analysis pools both liberal and conservative webpages from the source together, artificially reducing estimates of segregation. This aggregation bias can be particularly problematic on non-news websites, such as Youtube, Twitter, and Reddit, where users encounter twice the partisan content (*1*) they see on news sites. Indeed, González-Bailón *et al.* point out this problem in their discussion section: "[A] focus on domains rather than URLs will likely understate, perhaps substantially, the degree of segregation in news consumption online."

In Figure 2, B and C, González-Bailón *et al.* show the ideological segregation of all content that users were eligible to see (potential audience) compared with the segregation of content users actually see as a result of news feed ranking (exposed audience). On the basis of the domain-level analysis (Figure 2B), they argue that algorithmic news feed ranking increases ideological segregation. However, the URL-level analysis (Figure 2C), which includes the ideological slant of individual webpages, reveals that the ideological segregation of the overall sample is higher than the domain analysis reflects. As a result, in the URL-level analysis, there is no meaningful difference in ideological segregation before and after news feed ranking. [There are traces of algorithmic segregation in content shared by users and pages but not groups (figure S14) and when looking only at the subset of users classified as having high political interest (figure S19B compared with figure S19D)].

The observational URL-level analysis is consistent with the causal evidence in the related Special Issue Research Article (*2*), in which A. M. Guess *et al.* analyze an experiment that compares news feed ranking to a simple reverse chronological algorithm. In contrast to the conclusions of González-Bailón *et al.*, Guess *et al.* find that news feed ranking decreases, rather than increases, exposure to like-minded political content (table S20) and political news from partisan sources relative to reverse chronological feed (supplementary text S3.3).

Although evidence in both of these papers suggests that news feed ranking has limited effects on partisan content delivery, caution is warranted when drawing conclusions about the effects of ranking algorithms on ideological segregation. As González-Bailón *et al.* point out, friend, page, and group recommendation algorithms may serve to polarize the network of relationships that users form on the platform. Future work should attempt to more broadly understand social media as a complex ecosystem.

Solomon Messing
Center for Social Media and Politics, New York University, New York, NY, USA.
Email: solomon.messing@nyu.edu

REFERENCES AND NOTES

1. M. Wojcieszak *et al.*, *Polit. Commun.* 10.1080/10584609.2023.2238641 (2023).
2. A. M. Guess *et al.*, *Science* **381**, 398 (2023).

10.1126/science.adk1211

Response

Messing asserts that data at the URL level do not support our claims that algorithmic curation affects ideological segregation on Facebook. However, he acknowledges the presence of statistically significant differences in segregation levels at the potential and exposed levels in subsets of the data. These differences serve as evidence that algorithmic curation increases segregation but also that this increase reveals complex dynamics, contingent on platform features.

Messing acknowledges that there is evidence of increased algorithmic segregation in content shared by users [consistent with his own work (*1*)] and pages (figure S14, A, B, D, and E). Messing describes the size of these effects as "trace," but the differences are substantively and statistically significant, as the confidence intervals around the time trends (based on a local polynomial regression) suggest. Messing states that there is no evidence of algorithmically driven increased segregation for Facebook groups, but the evidence suggests that algorithmic curation actually drives a very large and statistically significant reduction, rather than an increase, in segregation levels (figure S14C). Although the reasons behind the conflicting results are unclear, the data confirm that Facebook's purposeful choices about how algorithmic curation operates shape the content users see on the platform.

Messing also acknowledges a small difference for users with high political interest but minimizes the value of this observation. Focusing on this subgroup, compared with users that are uninterested in politics, can provide important information regarding the relationships between political preferences and Facebook's feed algorithm. As Messing notes, segregation at the URL-level increases as we move down the "funnel of engagement" from potential to exposed audiences (see tables S10 and S14 and figure S19B). The difference is substantively and statistically significant for most of the observation period.

Although Messing analyzes Figure 2C, he overlooks Figure 2F. This panel shows that polarization (i.e., the extent to which the distribution of ideology scores is bimodal and far away from zero) goes up after algorithmic curation. In particular, the size of the homogeneous "bubble" on the ideological right grows when shifting from potential to exposed audiences. This is true both for URL- and domain-level analyses (Figure 2, E and F).

Messing argues that our results are inconsistent with the findings in Guess *et al.* (*2*). However, that study of about 23,000 Facebook users compares exposure with the standard Facebook algorithm versus reverse chronological ordering. It was not designed to evaluate 208 million Facebook users' platform-wide patterns of segregation in news consumption or compare potential and actual exposure. In addition, Guess *et al.* did find an algorithmic feed effect, noting that it increases exposure to like-minded posts more than it decreases crosscutting posts.

As we repeatedly state in our Research Article, algorithmic bias requires nuanced assessment, and our results do suggest a complex intertwining of algorithms and platform features that affect ideological segregation, especially on the political right. We agree that more research is essential, especially given that Facebook has introduced purely algorithm-driven content into feeds since 2020 (*3*).

Sandra González-Bailón[1]* and David Lazer[2]
[1]Annenberg School for Communication, University of Pennsylvania, Philadelphia, PA, USA. [2]Network Science Institute, Northeastern University, Boston, MA, USA.
*Corresponding author.
Email: sandra.gonzalez.bailon@asc.upenn.edu

REFERENCES AND NOTES

1. E. Bakshy, S. Messing, L. A. Adamic, *Science* **348**, 1130 (2015).
2. A. M. Guess *et al.*, *Science* **381**, 398 (2023).
3. A. Heath, "Facebook is changing its algorithm to take in TikTok, leaked memo reveals," *The Verge* (2022).

COMPETING INTERESTS

S.M.'s disclosures are available at https://solomonmg.github.io/disclosures/

10.1126/science.adk4899

Moments and people who shaped AAAS as it turns 175

By **Becky Ham**

In 2022, the American Association for the Advancement of Science unveiled a new strategic vision with four focused and refined goals, which will guide the organization for years to come. They include advancing scientific excellence and achievement; fostering equity and inclusion for scientific excellence; building trust among scientists and communities; and catalyzing progress where science meets policy.

The AAAS of today, which celebrates 175 years this month, was shaped by visionaries throughout the association's storied history, as a look back at AAAS history shows. This history is part of what will inform how AAAS ignites progress and continues to serve at the forefront of advancing science to serve society.

"Now more than ever, science is essential to the decisions that will determine the prospects for future health, prosperity, and peace," AAAS CEO Sudip S. Parikh wrote in a 15 September 2023 editorial in *Science*. "The scientific enterprise and AAAS must help shape the next 175 years and not be bystanders as history unfolds before us."

Advancing scientific excellence

By bringing together scientists from disparate fields, the founders of AAAS recognized the importance of a multidisciplinary approach to advancing scientific excellence.

Since 1874, AAAS has annually honored as fellows many scientists who broke barriers in their time. Sociologist W.E.B. Du Bois, the first Black American to earn a doctorate from Harvard University; astronaut Ellen Ochoa, the first Hispanic and second woman director in the history of the Johnson Space Center; and Admiral Grace Hopper, a pioneer in computer software development and programming languages, are among the honorees of the program as it nears its 150th anniversary.

The *Science* family of journals is critical to the association's mission of advancing scientific excellence. The association's oldest award, the AAAS Newcomb Cleveland Prize, was established in 1923 to recognize the year's most outstanding research paper in *Science*. First funded by advertising executive Newcomb Cleveland and now supported by The Fodor Family Trust, the prize has recognized key discoveries in quantum entanglement, draft genomes of the fruit fly and the Neanderthal, Bose-Einstein condensates, the first views of extrasolar planets, and the impact of radiation on genes and chromosomes, among other work.

Upon his death, the *New York Times* said the prize "was inspired by Mr. Cleveland's belief that it was the scientist who counted and who needed the encouragement an unexpected monetary award could give." That belief is carried forward today by the Mani L. Bhaumik Breakthrough of the Year Award, which supports a $250,000 annual cash prize for the scientists behind *Science*'s Breakthrough of the Year.

"The Breakthrough of the Year is done by people—it just doesn't fall from the sky," said Bhaumik, who has pledged $11.4 million for the award. "People are really at the center of the Breakthrough."

Science for all

In 1973, the AAAS Board of Directors appointed a Committee on Opportunities in Science to advise the association on achieving greater representation of women and scientists from marginalized communities across AAAS and the scientific enterprise. As part of that effort, AAAS's Shirley Malcom and colleagues produced "The Double Bind" report after a groundbreaking meeting in 1975 of 30 women scientists representing diverse backgrounds.

"Most of us experienced strong negative influences associated with race or ethnicity as children and teenagers but felt more strongly the handicaps for women as we moved into post-college training in graduate schools or later in careers," wrote Malcom and her colleagues.

The report offered a blueprint for change that could lead to a dramatic increase in women and minority participation in the sciences, but it also exposed the continuing systemic barriers to participation in the sciences.

The organization's early efforts have given it the credibility to launch new programs that address these systemic issues, said Malcom, who now directs one of those programs, called SEA Change. Now with 27 members, the program aims to expand the talent pool in science, technology, engineering, mathematics, and medicine (STEMM) by partnering with colleges and universities to take steps to identify and remove barriers to diversity, equity, and inclusion in those fields.

AAAS is also leading the national initiative to attain fundamental, systemic change to close the opportunity gap within STEMM through the STEMM Opportunity Alliance (SOA), launched in 2022 with founding support from the Doris Duke Foundation. More than 125 partners in industry, education, research infrastructure, community organizations, and philanthropies have committed $1.5 billion to the alliance, which will launch and begin implementing a national strategy in 2023 to achieve equity and inclusive excellence in STEMM by 2050.

Where science meets policy

The AAAS Science & Technology Policy Fellowships (STPF) program, now celebrating its 50th anniversary, demonstrates the impact and reach of a more inclusive scientific enterprise. This celebrated initiative is more diverse than the nation's pool of STEMM

PHOTO: COURTESY OF STPF

The AAAS Science & Technology Policy Fellowships launched in 1973 with seven fellows on Capitol Hill.

NEWS FROM
Science
AAAS

Subscribe to **News from Science** for unlimited access to authoritative, up-to-the-minute news on research and science policy.

bit.ly/NewsFromScience

PhD holders and brings a similarly rich set of knowledge and skills to help inform, communicate, and implement policy solutions throughout all three branches of the federal government.

S&T Policy Fellows are known for not only bringing critical, science-based evidence to the table but also explaining it with simplicity and relevance. They work across the aisle to ensure that science-informed evidence regarding climate change, energy, health and technology, and other pressing issues is considered in the policy-making process. A 2019 survey of the program found that 95% of government staff respondents felt that the fellows made important contributions to critical policy decisions.

William T. Golden, who served as AAAS treasurer for 30 years, helped establish STPF, setting a precedent for the Golden Family Foundation's extensive support of the association, which today is memorialized at the AAAS headquarters, named the William T. Golden Center for Science and Engineering. In 2008, the Golden family helped AAAS build trusted relationships on an international scale with the launch of the Center for Science Diplomacy.

Among other long-standing AAAS policy efforts are the annual Forum on Science & Technology Policy and the R&D Budget and Policy Program, which has been a leading source of independent data and analysis of federal research funding since its initial support by the Alfred P. Sloan Foundation in 1976.

Building trust with communities

Building on the respect and trust that AAAS's national and international policy programs have garnered over decades, the association has made a significant effort in recent years to expand its state and local engagement activities.

"If you want to have a big policy-making impact, you can't ignore the federal government, but frankly there is a broader need for support and help in understanding evidence and the narrative around evidence that state and local regulators and policy-makers are evaluating to make policy decisions," said Michael Fernandez, the founding director of the AAAS Center for Scientific Evidence in Public Issues (EPI Center).

The EPI Center works with state and local policy-makers to share actionable evidence on topics from drinking water safety to voting machine security. Other recent additions to AAAS that focus on local engagement include the Local Science Engagement Network (LSEN), which mobilizes scientists and engineers to participate in civic engagement in their local communities, and SciLine, a free and independent service launched with founding support from the Quadrivium Foundation, which provides trusted sources and resources for journalists, with a special emphasis on the needs of local and general assignment reporters.

Over a quarter-century ago, establishing trust and partnership between US scientific and religious communities was the motivation for the founding of the AAAS Dialogue on Science, Ethics, and Religion (DoSER). Since 1995, the program has expanded with long-standing support from the John Templeton Foundation and other partners to include a variety of initiatives that bring scientists into faith communities to talk about issues like evolution, public health, societal justice, and climate change.

Like many AAAS programs, DoSER's deep roots support its vibrant new growth. As DoSER Director Emeritus Jennifer Wiseman noted, "The focus on building connections and longer-term relationships is what outlasts specific projects."

As AAAS embarks on the next era, it will build on these milestones to strive for its new vision to mobilize an inclusive and global scientific community to ignite, enable, and celebrate scientific excellence and science-informed decisions and actions.

RESEARCH

IN *SCIENCE* JOURNALS

Edited by **Michael Funk**

GEODESY

Rising seas and falling land

Sea-level rise threatens coastal regions globally, but the effects in a specific area depend on both sea-level changes in the oceans and vertical motions of the land surface in the form of subsidence or uplift. Buzzanga *et al.* show how modern remote sensing data can be used to quantify these vertical motions. The New York City metropolitan area is sinking overall at a rate of 1.6 millimeters per year, but high-resolution data help to pinpoint urban localities experiencing variable uplift or subsidence. Such information sharpens our understanding of local risks related to sea-level rise and leads to better mitigation strategies. —KVH

Sci. Adv. (2023) 10.1126/sciadv.adi8259

Much of the land in the New York City area is gradually sinking, a phenomenon that will exacerbate flood risk alongside climate change.

PHOTO: JAY LAZARIN/ISTOCKPHOTO

NANOPHOTONICS

Into the valley and spinning out

Light sources with dynamically controlled polarization states are valuable for applications in sensing, spectroscopy, and optical communication. Typically, a magnetic field is required to select the polarization state, but that is not practical in a nanophotonic setting. The band structure of two-dimensional materials can have a valley degree of freedom in which selection for a particular valley results in polarized emission. Duan *et al*. show that the integration of a monolayer of tungsten disulfide with a carefully designed photonic crystal cavity enhances the light-matter coupling, resulting in lasing with valley-addressable polarized output. Operation at room temperature without the need for a magnetic field should be useful in developing advanced nanophotonic light sources. —ISO

Science, adi7196, this issue p. 1429

CHEMOTHERAPY

Targeting RyR2 to prevent chemobrain

Cancer survivors often experience cognitive impairments after chemotherapy, a side effect commonly known as "chemo brain." Liu *et al.* treated breast cancer mice and wild-type mice with one of two chemotherapeutic regimens, doxorubicin or methotrexate and 5-fluorouricil, to investigate the role of ryanodine receptor type 2 (RyR2) in chemo brain. The authors identified chemotherapy-induced posttranslational modifications and increased calcium leakiness of RyR2. Treatment with a ryanodine receptor calcium release channel stabilizer (S107) prevented chemotherapy-induced RyR2 leakiness and ameliorated cognitive deficits in these breast cancer mice. The authors found similar chemotherapy-induced RyR2 modifications and cognitive deficits in cancer-free mice, indicating that chemotherapy without cancer was sufficient to induce chemo brain in mice. These preclinical results suggest that targeting RyR2 might be a promising target to prevent this unwanted side effect of chemotherapy. —DN

Sci. Transl. Med. (2023) 10.1126/scitranslmed.adf8977

MYCOSES

Fungal sticking power

Invasive and drug-resistant fungal infections in care facilities caused by the emerging pathogen *Candida auris* are of increasing concern. Infection readily spreads from contaminated skin, medical devices, and abiotic surfaces. Santana *et al*. explored the basis of adhesion in several isolates of this species. In addition to adhesins

resembling those found in other *Candida* species, *C. auris* has a specific and dominant adhesin called Surface Colonization Factor (SCF1), which adheres by cation-dependent interactions to a wide range of biotic and abiotic surfaces. Together with a complementary *Candida* adhesin, IFF4109, which attaches by hydrophobic interactions, these adhesins mediate colonization and biofilm formation. Several clinical phenotypes are seen, with different adhesion properties displaying correlated degrees of virulence. —CA

Science, adf8972, this issue p. 1461

GEOLOGY

A model extinction

The end-Cretaceous mass extinction, which included the elimination of all nonavian dinosaurs, occurred after the impact of a meteorite and during a stretch of large-scale volcanism. Although it is known that the impact is temporally linked to the extinction, the relative roles are hard to disentangle. Cox and Keller used an inversion scheme that is agnostic about what occurred geologically but provides best guesses for a number of variables, including carbon and sulfur dioxide release. These gases cause environmental changes, and the results may argue for a two-stage extinction related to the volcanism. This approach should be useful for disentangling other complex events in Earth systems and elsewhere. —BG

Science, adh3875, this issue p. 1446

FLUORINE CHEMISTRY

Solid introduction of fluorinated gases

Gaseous fluorocarbons are hazardous reagents that can be especially challenging to deliver in parallel high-throughput experimental conditions. Keasler *et al*. report that a magnesium-based metal organic framework can stably host these gases in solid powders that are easy to weigh and distribute. Moreover, encapsulation of the powder in wax prevents the unintended release of the gas before sonication in the reaction solvent. The authors demonstrate the utility of this strategy for the synthesis of a wide variety of fluorinated styrene derivatives. —JSY

Science, adg8835, this issue p. 1455

IMMUNOLOGY

B cells need the physical touch

The activation of B cells upon the binding of antigens to the B cell receptor is important for vaccine-based antibody production. Kwak *et al*. show that the mechanosensitive cation channel Piezo1 is required for B cells to respond to antigens that are membrane presented, but not to those that are soluble. Piezo1-mediated changes in calcium ion flux enabled B cells to sense contact with a solid, antigen-bearing surface, leading to B cell receptor activation. These findings may lead to vaccines that better stimulate antibody production by B cells. —JFF

Sci. Signal. (2023) 10.1126/scisignal.abq5096

POLYMER CHEMISTRY

Adding nitrogen to enhance polyethylene

Different plastics are often used in combination with each other and multiple additives to achieve desired performance properties, and this approach can complicate efforts to recycle or reprocess constituents of the mixture. Ciccia *et al*. report that a simple chemical modification to the backbone of polyethylene, the most common plastic, can also tune a wide variety of characteristics. Copper catalysis oxidatively replaces about 1 to 2% of the carbon–hydrogen bonds with nitrogen substituents, which in turn confer varying toughness, adhesion, and solubility properties. A hydrophobic ligand avoids competing chain scission pathways that plagued prior analogous approaches. —JSY

Science, adg6093, this issue p. 1433

IN OTHER JOURNALS

Edited by **Caroline Ash** *and* **Jesse Smith**

CANCER

One-click cancer cell destruction

Efficient targeting of cancer cells is an important goal for developing less generally toxic treatments. The enzyme aldehyde dehydrogenase 1A1 (ALDH1A1) is overexpressed within breast cancer cells but itself is not a direct target for treatment. To detect and selectively kill cancer stem-like cells, Bo *et al.* designed an azido sugar–like molecule that serves as a substate for ALDH1A1. The designed substrate causes a chemical tag to be linked to glycoproteins on the cell surface, signaling the presence of ALDH1A1. The surface azide tag is recognized in animals treated with dibenzocyclooctyne (used in "click" chemistry) conjugated to a toxin. The toxin kills cells and makes tumors regress. Small azido sugars and DBCO toxins have better tissue penetration than larger molecules such as antibodies. —LBR

Proc. Natl. Acad. Sci. U.S.A. (2023) 10.1073/pnas.2302342120

NEUROSCIENCE

Anchorage for AMPARs

Neuronal firing in the mammalian brain requires glutamate receptors called AMPARs for successful propagation, but how AMPARS are distributed and anchored to cells in the brain is unknown. Using high-resolution proteomics together with functional and morphological analyses, Boudkkazi *et al.* identified the highly conserved Noelin family of secreted proteins as being the AMPAR anchors. The Noelin proteins are abundant

PHOTO: CI PHOTOS/SHUTTERSTOCK

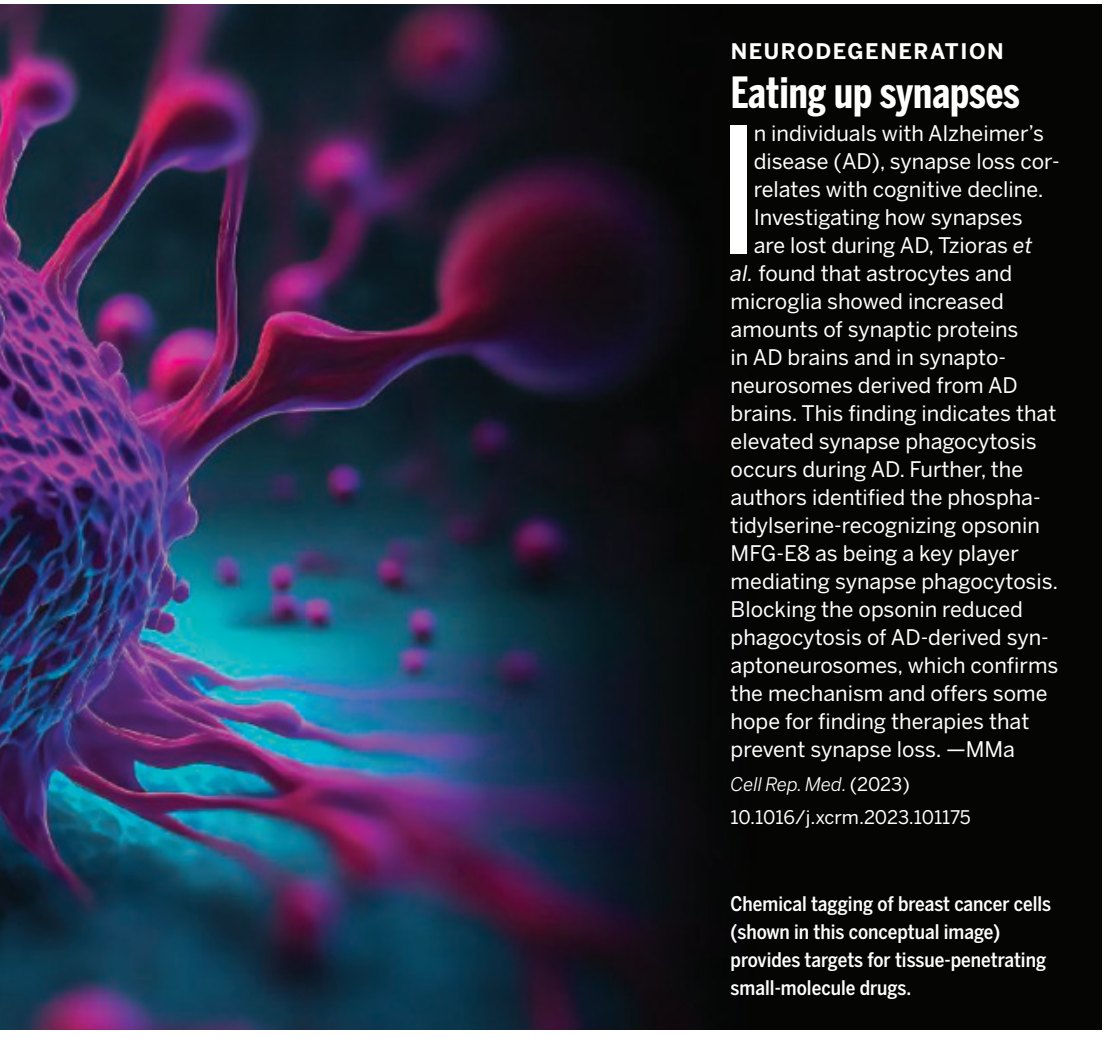

NEURODEGENERATION

Eating up synapses

In individuals with Alzheimer's disease (AD), synapse loss correlates with cognitive decline. Investigating how synapses are lost during AD, Tzioras *et al.* found that astrocytes and microglia showed increased amounts of synaptic proteins in AD brains and in synaptoneurosomes derived from AD brains. This finding indicates that elevated synapse phagocytosis occurs during AD. Further, the authors identified the phosphatidylserine-recognizing opsonin MFG-E8 as being a key player mediating synapse phagocytosis. Blocking the opsonin reduced phagocytosis of AD-derived synaptoneurosomes, which confirms the mechanism and offers some hope for finding therapies that prevent synapse loss. —MMa

Cell Rep. Med. (2023)
10.1016/j.xcrm.2023.101175

Chemical tagging of breast cancer cells (shown in this conceptual image) provides targets for tissue-penetrating small-molecule drugs.

throughout the brain and, as homo- and heterotetramers, bind to the extracellular portion of all AMPAR subunits. The Noelin-AMPAR complexes interact with a network of proteins in cell membranes to determine their number and density under steady-state and active conditions. —PRS

Neuron (2023)
10.1016/j.neuron.2023.07.013

IMMUNOLOGY

Chemokine cutback drives tolerogenic T cells

A subset of T cells called $CD4^+CD8\alpha\alpha^+$ intraepithelial lymphocytes (DP IELs) play an important immunoregulatory role in the gut. Unlike other types of regulatory T cells, which are primarily found in the lamina propria, DP IELs develop in the intraepithelial compartment after migrating from the periphery. Although the differentiation of this T cell subset has been extensively studied, the factors surrounding its tissue localization are unknown. Ono *et al.* report that differentiating mouse DP IELs down-regulate the chemokine receptor CCR9, which is known to play a role in homing to the lamina propria. Moreover, *Ccr9*-knockout mice show enhanced DP IEL differentiation, which correlates with thymic homing capacity. Curiously, neither overexpression of CCR9 nor lack of CCR9 ligand had any significant effect on DP IEL differentiation, indicating that reductions in CCR9 expression, rather than absolute expression, is key. —STS

Nat. Commun. (2023)
10.1038/s41467-023-40950-2

QUANTUM SENSING

A quantum route to enhanced sensing

Applications in sensing and metrology are benefiting from the ability to harness the quantum mechanical properties of the constituent quantum-two-level systems making up the systems. The nitrogen-vacancy defect (NV center) in diamond, for example, is sensitive to magnetic fields, as well as to stress and thermometry changes to its local environment. Arunkumar *et al.* show that an ensemble of such NV centers can be used for enhanced sensing capabilities and that quantum logical operations exploiting the coupling between the on-site nuclear spins and the electronic spin results in an enhancement of the signal-to-noise ratio. This approach is applicable to other quantum technology platforms for enhanced performance. —ISO

Phys. Rev. Lett. (2023)
10.1103/PhysRevLett.131.100801

STORMS

Warming up and changing speed

Extratropical cyclones often bring heavy precipitation, high winds, and large temperature swings to the middle and high latitudes. These storms can cause a great deal of damage, especially if they linger over a region. Crawford *et al.* used a suite of climate models to examine the response of Northern Hemisphere extratropical cyclones to global warming. They found that winter storms tend to move more slowly over midlatitude North America as the world warms but faster over the North Pacific Ocean and parts of Europe. These processes are becoming more dramatic as global warming intensifies. —HJS

J. Clim. (2023)
10.1175/JCLI-D-23-0082.1

PHYSICS

Intertwined orders

The members of the recently discovered family of kagome superconductors host several intertwined long-range orders that appear at different temperatures. One of them is a charge-stripe order that is a feature of the kagome superconductor CsV_3Sb_5, but not the related KV_3Sb_5. Li *et al.* used angle-resolved photoemission spectroscopy (ARPES) and scanning tunneling microscopy (STM) to study the interplay of these orders. The ARPES data suggested the formation of small Fermi surface pockets in all investigated compounds, with corresponding scattering wave vectors identified in the STM measurements. The differences in the behavior of these wave vectors, depending on the presence or absence of stripe order, point to an intrinsic nature of this property. —JS

Phys. Rev. X (2023)
10.1103/PhysRevX.13.031030

REVIEW SUMMARY

NEUROSCIENCE

Integrative neurocircuits that control metabolism and food intake

Jens C. Brüning* and Henning Fenselau

BACKGROUND: There is an ever-increasing population of overweight and obese individuals who exhibit the predisposition for a plethora of obesity-associated disorders, such as type 2 diabetes mellitus, cardiovascular diseases, certain types of cancers, as well as neurodegenerative disorders. Because both energy homeostasis and peripheral metabolism are coordinated through the brain, defining the basic neurobiological mechanisms of metabolic regulation and defining how alterations in these pathways promote obesity development and the onset of obesity-associated metabolic disorders are urgently needed to devise therapeutic interventions for these prevalent diseases. The arcuate nucleus (ARC) of the hypothalamus integrates multiple hormonal and neuronal inputs, signaling nutrient availability of the organism. The core of this hypothalamic control system comprises two neuronal populations, which exert almost opposite functions in the regulation of feeding behavior, energy expenditure, and fuel metabolism. Agouti-related peptide (AgRP) neurons are activated in conditions of energy deficit, are inhibited by the fuel communication signals leptin and insulin, and promote foraging and food consumption. Pro-opiomelanocortin (POMC) neurons are activated in states of positive energy balance and the associated hormonal changes and reduce food intake and increase energy expenditure. Intense research over the past 20 years has revealed that alterations in this circuitry are causally linked to obesity development in mouse models and humans.

ADVANCES: Recent developments of high-throughput single-cell and single-nucleus RNA-sequencing methods have enabled the definition of cellular subpopulations at unprecedented molecular resolution. Applying these technologies has recently led to the identification of numerous additional food intake and metabolism regulatory neuronal and non-neuronal cell populations in the hypothalamus. In parallel, functional molecular systems approaches have allowed the delineation not only of the functional role of these newly identified cell types in metabolism control but also definition of the neuronal network organization as well as assessment of their activity in freely behaving animals. These experiments revealed that metabolism regulatory neurons are modulated across different timescales, including upon sensory perception of food cues, post-ingestive signals that originate from the gastrointestinal tract, and more long-term hormonal mediators. The integration of these signals serves to fine-tune metabolic adaptation and associated behaviors in an allostatic manner. These studies have largely advanced our knowledge of the fundamental principles of central nervous system–dependent control of metabolism. They also allowed the definition of new strategies to combat metabolic diseases. These recent advances are highlighted in the Review.

OUTLOOK: Further expanding on these developments will allow a more holistic insight into the conserved metabolism regulatory cell types and neurocircuits not only in rodent models but also in humans. This new knowledge will aid the definition of how their deregulation is linked to the development of metabolic disturbances. Moreover, such studies will help clarify the mode of action of promising new anti-obesity therapeutics. These include glucagon-like peptide-1 (GLP-1) receptor agonists as well as newly developed polyagonists for different receptors of gut-derived peptides, for which clinical studies have provided evidence for promising efficacy in body weight reduction and metabolic improvement. Furthermore, deeper insights into the molecular signature of metabolism-regulatory cell types and into the synaptic mechanisms underlying their network interaction carry the potential to nurture the development of alternative therapeutic strategies for metabolic diseases. ■

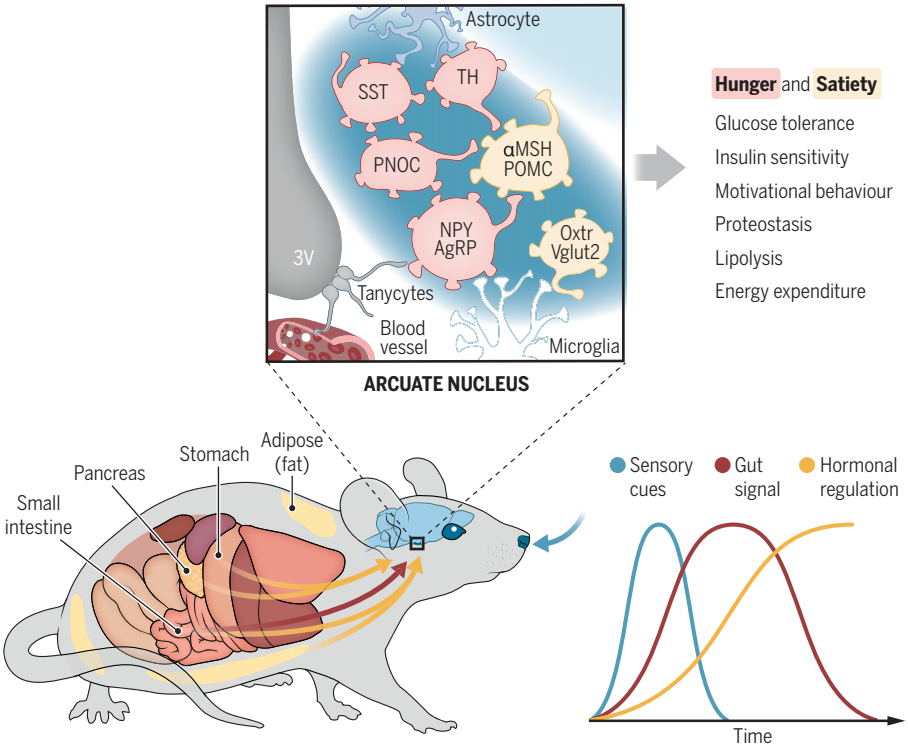

Hypothalamic integration of food-related signals in metabolic control. Key hunger- and satiety-promoting neuronal cell types in the hypothalamus integrate nutrient-related signals across different timescales: (i) upon sensory perception of food, (ii) post-ingestive gut-derived signals, and (iii) hormonal signals that communicate the energy state of the organism. In addition to feeding, these neurocircuits also adapt multiple behaviors and other physiological parameters in peripheral tissues in accordance to the energy state of the organism.

The list of author affiliations is available in the full article online.
*Corresponding author. Email: bruening@sf.mpg.de
Cite this article as J. C. Brüning, H. Fenselau, *Science* 381, eabl7398 (2023). DOI: 10.1126/science.abl7398

READ THE FULL ARTICLE AT
https://doi.org/10.1126/science.abl7398

CREDIT: (MOUSE IMAGE) N. BURGESS/*SCIENCE*

RESEARCH ARTICLE SUMMARY

ADAPTATION

Community-wide genome sequencing reveals 30 years of Darwin's finch evolution

Erik D. Enbody*, Ashley T. Sendell-Price, C. Grace Sprehn, Carl-Johan Rubin, Peter M. Visscher, B. Rosemary Grant, Peter R. Grant, Leif Andersson*

INTRODUCTION: Adaptive radiations are groups of organisms that have diverged ecologically from a common ancestor relatively rapidly. They have yielded important insights into the ecology, behavior, and genetics of speciation through inferences of the evolutionary processes that most likely gave rise to observed patterns of divergence. In a few cases, experiments have substantiated these inferences by testing hypotheses of causal mechanisms. Our understanding of evolutionary radiations has been transformed in the past decade by discoveries of the genomic variation underlying phenotypic divergence. The dynamic genomic variation responsible for rapid evolutionary change in contemporary populations in nature, and its connection with evolution in the past, is not well known.

RATIONALE: We set out to establish the link between contemporary and past evolution in a well-studied system, Darwin's finches in the Galápagos archipelago. Eighteen species have evolved from a common ancestor in the last million years. They diverged in beak morphology and body size, and to a small extent, in plumage. Two evolutionary processes, natural selection and introgressive hybridization, influenced the outcomes of phenotypic evolution in this adaptive radiation. We followed the fates of individually marked and measured birds of four *Geospiza* species on Daphne Major Island for 40 years to investigate contemporary evolution. We combined observations on fitness with whole-genome sequencing to reveal and interpret the genetic architecture of evolutionary change.

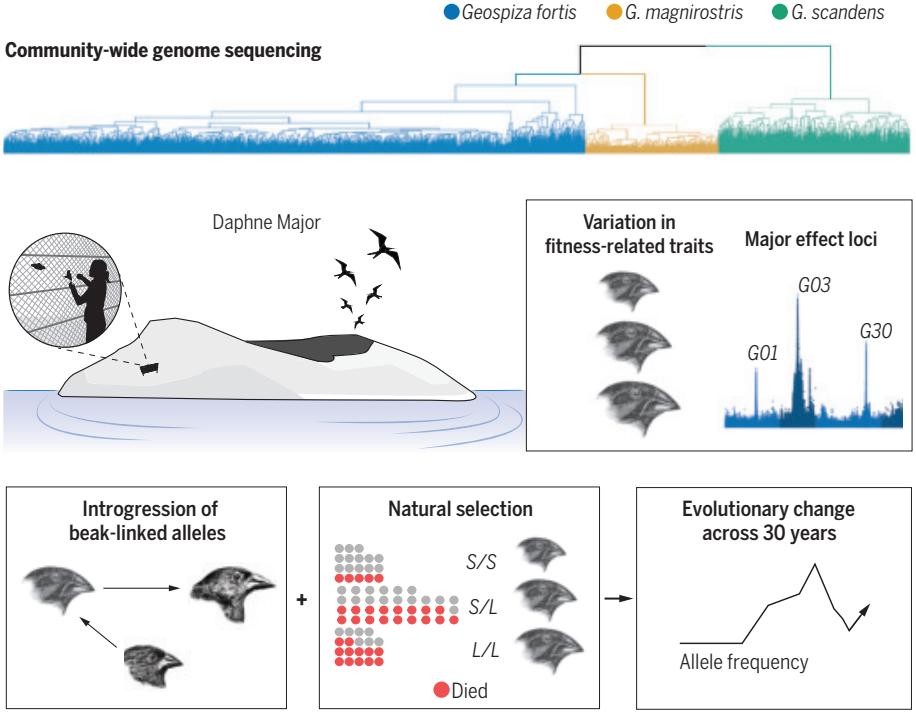

Evolutionary change revealed by community sequencing. Population monitoring over 30 years followed by genome-wide sequencing of ~4000 individuals of four Darwin's finch species (the fourth, *G. fuliginosa*, is not visible in the tree) on Daphne Major, Gálapagos Islands. Genome-wide association analysis identified major-effect loci on fitness-related traits, revealing alleles transferred among species by introgression and subject to natural selection. *S*, small beak-size allele *L*, large beak-size allele.

BIRD ILLUSTRATIONS: P.R.G. AND DARWIN, 1845

RESULTS: We used whole-genome resequencing data to track evolutionary change in 3955 finches of four *Geospiza* species. We identified six loci that together explain as much as 45% of variation in beak size of *G. fortis* (medium ground finch), a highly heritable and key ecological trait. One locus alone is responsible for 25% of variation in beak size and 13% of variation in body size, and is most likely a supergene comprising four genes that contain multiple adaptive mutations with phenotypic consequences for both traits. The haplotypes associated with large and small beak size were established before the divergence of *Geospiza* ground finches and *Camarynchus* tree finches. Abrupt changes in allele frequencies at these loci in *G. fortis* resulted from strong natural selection during an extreme drought and explained a large part of the shift in beak size. Introgression of small-beak alleles from the smaller *G. fuliginosa* influenced the outcome of natural selection by increasing the frequency of small alleles in *G. fortis*. In the cactus-feeding *G. scandens* population, we observed more gradual changes in allele frequencies over the study period resulting from introgression.

CONCLUSION: We show that a few loci of large effect have had a major impact on the trajectory of Darwin's finch populations on the small island of Daphne Major. They affect fitness through their association with survival in relation to competition for food, particularly during extreme climatic events, and have been passed between species through hybridization. A reasonable explanation for the presence of large-effect alleles in Darwin's finches is that these have evolved over time by the accumulation of multiple causal mutations as a response to diversifying selection. They contribute both to phenotypic differences between species and to phenotypic diversity within *G. fortis*. This genetic architecture differs from the one documented for many polygenic traits in other species lacking large-effect loci, such as beak morphology in some other birds and human stature, which is likely due to differences among species in selection regimes and the impact of gene exchange. These genetic changes at the population level reveal the dynamics of evolutionary change in this iconic adaptive radiation. ■

The list of author affiliations is available in the full article online.
*Corresponding author. Email: erik.enbody@gmail.com (E.D.E.); leif.andersson@imbim.uu.se (L.A.)
Cite this article as E. D. Enbody *et al.*, *Science* **381**, eadf6218 (2023). DOI: 10.1126/science.adf6218

READ THE FULL ARTICLE AT
https://doi.org/10.1126/science.adf6218

RESEARCH ARTICLE SUMMARY

EVOLUTION

Cycles of fusion and fission enabled rapid parallel adaptive radiations in African cichlids

Joana I. Meier*, Matthew D. McGee, David A. Marques, Salome Mwaiko, Mary Kishe, Sylvester Wandera, Dirk Neumann, Hilary Mrosso, Lauren J. Chapman, Colin A. Chapman, Les Kaufman, Anthony Taabu-Munyaho, Catherine E. Wagner, Rémy Bruggmann, Laurent Excoffier, Ole Seehausen*

INTRODUCTION: Much of species diversity is thought to have arisen during adaptive radiations—the process whereby many species arise in short succession and diversify in their ecological niche use. It is not understood why, when given ecological opportunity, some lineages readily undergo adaptive radiations, whereas others do not. A lineage with exceptional propensity to radiate is that of the cichlid fishes of the Lake Victoria region. In this instance, each major lake harbors highly ecologically diverse cichlid assemblages, ranging from algivores to zooplanktivores to predators that feed on other members of the radiation. We had previously shown that all of these radiations evolved from a hybrid population between two lineages that merged about 150,000 years ago.

RATIONALE: In the Pleistocene dry period, >20,000 to ~16,000 years ago, Lake Victoria was completely dry, and any previous radiation would have died out. The deeper Western Rift Lakes Edward, Kivu, and Albert may still have hosted parts of their cichlid radiations. It thus remained unclear whether the ecological guilds had colonized Lake Victoria from these deeper lakes or whether they evolved in a new adaptive radiation. In this work, we test whether the hundreds of ecologically diverse Lake Victoria cichlids in fact diverged from a common ancestor in less than 16,000 years and how they diversified so rapidly.

RESULTS: We generated a whole-genome dataset of 464 cichlids representing all major lakes in the region and several species of almost all the ecological groups in Lake Victoria. We find that the Lake Victoria cichlids evolved in the lake as an extremely rapid adaptive radiation. The process started from hybrid ancestry of at least three lineages that must have survived the dry period in swamps in the region. We find evidence that each of these parental lineages contributed ecologically relevant alleles that facilitated the rapid radiation in Lake Victoria. Hybridization between members of the emerging Lake Victoria Radiation additionally gave rise to yet more guilds and species. Cycles of hybridization leading to the fusion of lineages followed by diversification (lineage fission) thus occurred repeatedly throughout the evolutionary history. As shown previously, the hybridization event about 150,000 years ago facilitated the older radiations in the region, and in this work, we show that further cycles of fusion and fission allowed the lineage to retain large, phenotypically relevant genetic variation and thus to radiate extremely rapidly.

CONCLUSION: Multiple cycles of lineage fusion and fission likely explain the very high propensity of these cichlids to form parallel adaptive radiations across multiple trophic levels. It may be generally true that animal or plant lineages that have recently radiated are not only particularly prone to hybridize but are also prone to radiate again from the resulting hybrid populations, perpetuating and exacerbating the differences in diversification rates between lineages. The variation in radiation propensity is thus not a property of any one species but that of an evolving flock of species. This finding also suggests that we should grow beyond species-centric conservation strategies and aim to preserve entire species complexes to preserve their capacity to adapt and diversify. ■

The list of author affiliations is available in the full article online.
*Corresponding author. Email: joana.meier@sanger.ac.uk (J.I.M.); ole.seehausen@iee.unibe.ch (O.S.)
Cite this article as J. I. Meier *et al.*, *Science* **381**, eade2833 (2023). DOI: 10.1126/science.ade2833

READ THE FULL ARTICLE AT
https://doi.org/10.1126/science.ade2833

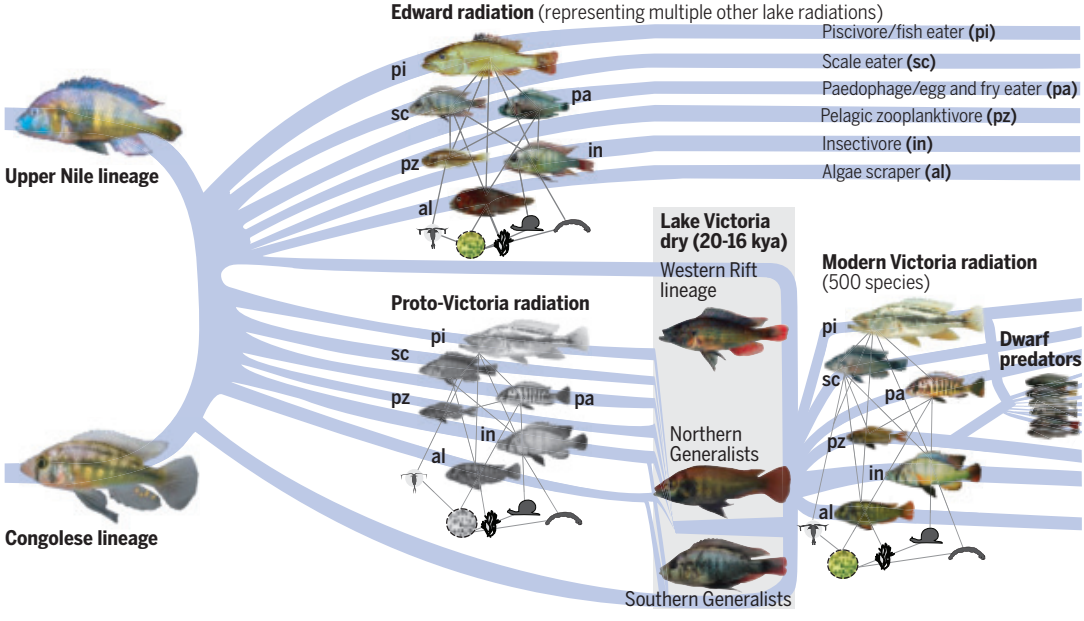

Multiple cycles of lineage fusion by hybridization and diversification led to increasingly rapid and extensive radiations of cichlid fishes, including the explosive evolution of 500 Lake Victoria species across four trophic levels in 16,000 years. The blue lines reflect lineage fusion and fission events inferred in this work. The fish photos visualize some ecological groups that evolved in parallel in each lake, making up entire trophic networks.

PHOTO CREDITS: NATHAN VRANKEN, PAEDOPHAGE OF LAKE EDWARD; ERWIN SCHRAML, WESTERN RIFT LINEAGE; FRANS WITTE/HEST, PISCIVORE OF THE VICTORIA RADIATION; ADRIAN INDERMAUR, CONGOLESE LINEAGE; VIANNY NATUGONZA/NAFIRRI, ALGAE SCRAPER OF THE VICTORIA RADIATION; M.D.M., NORTHERN GENERALIST; SEEHAUSEN GROUP, ALL OTHER PHOTOS

RESEARCH ARTICLES

NANOPHOTONICS

Valley-addressable monolayer lasing through spin-controlled Berry phase photonic cavities

Xiaoyang Duan[1]†, Bo Wang[2]†, Kexiu Rong[1]†, Chieh-li Liu[1], Vladi Gorovoy[1], Subhrajit Mukherjee[3], Vladimir Kleiner[1], Elad Koren[3], Erez Hasman[1]*

The spin-valley coupling between circularly polarized light and valley excitons in transition metal dichalcogenides provides the opportunity to generate and manipulate spin information by exploiting the valley degree of freedom. Here, we demonstrate a room-temperature valley-addressable tungsten disulfide monolayer laser in which the spin of lasing is controlled by the spin of pump without magnetic fields. This effect was achieved by integrating a tungsten disulfide monolayer into a photonic cavity that supports two orthogonal spin modes with high quality factors. The spin-pumped lasing effectively broke the population symmetry of valley excitons, resulting in highly coherent emission with valley-switchable radiation modes due to distinct laser thresholds. Our scheme provides a nanophotonic platform to develop versatile coherent spin-light sources operating at room temperature by actively manipulating spin-valley coupling in light-matter interactions.

Carrier spin, the intrinsic angular momentum in many forms of waves and particles, stands in the center of interest for various branches of modern physics (*1*–*6*). In particular, there has been a long-sought goal in nanophotonics to achieve coherent light sources with two dynamically controlled opposite spin states because they play intriguing roles in fundamental optics and applications such as chiral sensing (*4*), quantum encryption (*5*), and angular momentum–based communications (*6*). The physical foundation to achieve this objective involves two steps: (i) splitting a lasing mode into a pair of orthogonal spin modes using an artificial vector potential and (ii) regulating the spin modes using a real vector potential. Specifically, an artificial vector potential (Berry connection, $\boldsymbol{A}$) can stem from the structural inversion symmetry (IS) breaking together with the emergent spin-orbit interaction, which acts as a pseudomagnetic field (Berry curvature, $\boldsymbol{B} = \nabla \times \boldsymbol{A}$) and separates spin states in momentum ($\boldsymbol{k}$) space (*7*–*10*). This time-reversal symmetric method has shown extraordinary ability to manipulate the transport of spin-polarized light ($\sigma = \pm 1$). Typically, the photonic Rashba effect describes a momentum-space spin-split dispersion $\omega(\boldsymbol{k} + \sigma\boldsymbol{k}_R)$ of light, where $\sigma\boldsymbol{k}_R$ is an additional spin-dependent Rashba momentum $\sigma\boldsymbol{k}_R = \nabla\phi_g(\boldsymbol{r})$ and $\phi_g(\boldsymbol{r})$ is the Berry (geometric) phase in real ($\boldsymbol{r}$) space (*10*–*12*). In this case, the artificial vector potential manifests as the gradient of Berry phase, that is, $\boldsymbol{A} = \nabla\phi_g(\boldsymbol{r})$. In addition, incorporating Berry phase perturbations upon photonic crystals has provided opportunities to achieve spin modes with a configurable quality factor (Q-factor) (*13*).

To achieve selective control of the spin-split eigenstates, applying a magnetic field is commonly used to break the time-reversal symmetry of light-matter interactions through the Faraday or Zeeman effects (*14*–*16*). However, magnetic fields are not preferred for miniaturized devices due to the particularly weak magneto-optical effect in visible frequencies. Therefore, there is a high demand for a magnetic-free approach to generate and control the two orthogonal spin states in compact lasers.

Recently, two-dimensional transition-metal dichalcogenides (TMDs) have attracted much attention as an atomically thin gain medium for compact lasers (*17*–*19*) because of their large exciton binding energy and strong excitonic emission (*20*). Unlike conventional semiconductors, TMD excitons have a valley degree of freedom arising from structural IS breaking and electronic spin-orbit interaction. The $\pm K_e$ valley excitons belong to orthogonal states with opposite spin angular momenta, and they can be selectively populated for circularly polarized emission following a valley-dependent optical selection rule through a different pump spin. Therefore, this spin-valley locking effect offers a mechanism for spin-controllable lasers without magnetic fields. However, a TMD laser with valley-addressable spin-optical radiation is still lacking. This is mainly ascribed to fast depolarization processes (*20*) such as intervalley scattering, which randomly mixes excitons from opposite valleys and destroys valley information initialized from pump spin, and, more importantly, the lack of a high-Q optical cavity with a pair of degenerate but orthogonal spin modes.

Here, we demonstrate a valley-addressable surface-emitting laser by integrating a tungsten disulfide (WS_2) monolayer with a Berry phase photonic cavity under magnetic-free and room-temperature conditions (Fig. 1A). The measured TMD monolayer lasing exhibited strong temporal and spatial coherence and valley-switchable spin-optical radiation modes due to distinct spin-pumped laser thresholds.

Principle and characteristics of monolayer lasing

The planar photonic cavities are based on a valley photonic crystal (PhC), with each unit cell composed of a pair of nonequivalent artificial atoms ("A" and "B" in Fig. 1A) located on the corners of the honeycomb lattice (lattice constant a). The size difference between atoms A and B induces spatial IS breaking in the photonic system, which opens Dirac bandgaps at the corners ($\pm K_p$) of the first Brillion zone for transverse electric waves, forming photonic valley states at the band extrema [see section 3 in (*21*)]. We focused on the $\pm K_p$ valley states at the lowest-frequency band, which are guiding modes located below the light line with a theoretically infinite vertical Q-factor (colored bands in Fig. 1, E and G). $\pm K_p$ valley states exhibit opposite and near-perfect circular polarizations ($\sigma^{\pm}$), showing a photonic spin-valley locking effect in analogy to the valley excitons in TMD monolayers. We further modified A atoms by perturbating their geometry from circular to elliptical (Fig. 1, A to C) with customized local in-plane orientations $\theta(\boldsymbol{r})$. This gives rise to a Berry phase $-2\sigma\theta(\boldsymbol{r})$ that generates an in-plane Rashba momentum $\sigma\boldsymbol{k}_R = -2\sigma\nabla\theta(\boldsymbol{r})$ to recouple spin-dependent valley modes to the free space with predesigned radiation modes ($|\pm k_R\rangle$ in Fig. 1, E and G).

To achieve mode selection and a high Q-factor in a small-footprint cavity, we constructed a heterostructure PhC composed of core and cladding regions (Fig. 1B). Lateral mode confinement and spin modes selection were obtained by using band misalignment between core and cladding by enlarging the A atoms in the core [see section 3 in (*21*)], leading to a pair of spatially confined high-Q cavity modes with orthogonal spin polarizations ($Q > 1.5 \times 10^4$ in experiments).

Furthermore, a WS_2 monolayer was integrated into the cavity as an ultrathin spin-polarized gain medium [see section 1 in (*21*)].

[1]Atomic-Scale Photonics Laboratory, Russell Berrie Nanotechnology Institute, and Helen Diller Quantum Center, Technion – Israel Institute of Technology, Haifa 3200003, Israel. [2]State Key Laboratory of Advanced Optical Communication Systems and Networks, School of Physics and Astronomy, Shanghai Jiao Tong University, Shanghai 200240, China. [3]Faculty of Materials Science and Engineering, Russell Berrie Nanotechnology Institute, and Helen Diller Quantum Center, Technion – Israel Institute of Technology, Haifa 3200003, Israel.
*Corresponding author. Email: mehasman@technion.ac.il
†These authors contributed equally to this work.

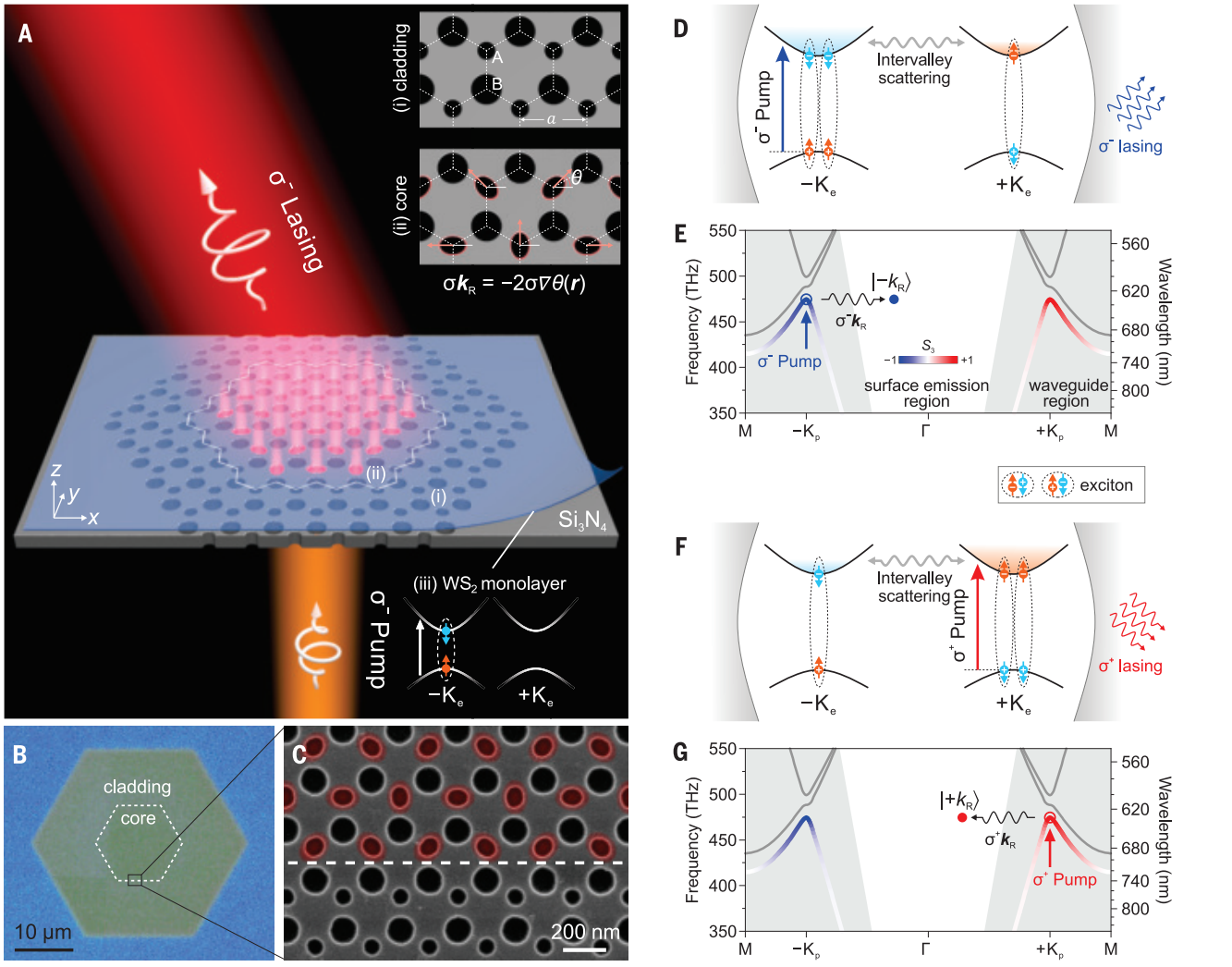

Fig. 1. Principle of the valley-addressable monolayer laser. (**A**) Schematic of the laser consisting of a Berry phase PhC cavity and a WS_2 monolayer. Inset: (i and ii) Top view of the PhC lattice in cladding and core region, respectively [see details in section 3.5 in (*21*)]; (iii) selective excitation of $-K_e$ (or $+K_e$) valley excitons for surface-emitting lasing with the same spin. (**B**) Microscopic image of a cavity integrated with a WS_2 monolayer encapsulated by a polymethyl methacrylate layer. (**C**) Enlarged scanning electron microscopic image of a fabricated cavity. The elliptical holes in the core are shown in red. (**D** and **F**) Valley-addressable spin lasing under σ^- (or σ^+) pump. The dominant $-K_e$ (or $+K_e$) valley excitons are coupled to the PhC spin mode at $-K_p$ (or $+K_p$) valley, promoting a spin lasing emission $|\pm k_R\rangle$ that bypasses the intervalley scattering. (**E** and **G**) Simulated band structure of a Berry phase PhC, where the lowest band is color coded to show the near-field optical spin (Stokes parameter S_3). The PhC spin mode at the $-K_p$ (or $+K_p$) valley is further routed into free space following $\sigma\boldsymbol{k}_R$.

The valley contrast of the WS_2 monolayer is quantified by the degree of valley polarization $D_{vp}(\lambda) = \frac{I^+(\lambda)-I^-(\lambda)}{I^+(\lambda)+I^-(\lambda)}$, where $I^{\pm}(\lambda)$ is the spin-dependent photoluminescence (PL) intensity at wavelength λ under spin pump. Note that the intervalley scattering severely destroys the valley information (low D_{vp}) at room temperature. We will show that by using the lasing mechanism, valley polarization can be substantially amplified near the lasing threshold, where the emission spin aligned with the pump spin is preferably coupled to the $\pm K_p$ valley mode of the cavity to enable spin-controlled lasing (Fig. 1, D and F).

To experimentally demonstrate lasing from the system, a series of cavities were fabricated and then covered by a WS_2 monolayer [section 7 in (*21*)]. A sample with a high *Q*-factor cavity mode at $\lambda_0 = 636.4$ nm was then pumped with a linearly polarized 594-nm continuous-wave laser (near-resonant pump), and the far-field emission pattern was captured. Figure 2, A and B, respectively, show the intensity pattern and the corresponding spin-resolved distribution in $\boldsymbol{k}$ space obtained from a relatively high pump power ($10P_{th}$, P_{th} as lasing threshold). Because of the linearly polarized pump, $-K_e$ and $+K_e$ valley excitons are equally populated ($D_{vp} = 0$). Therefore, two spin-dependent Gaussian spots ($|-k_R\rangle$ and $|+k_R\rangle$) with identical intensity and width [full width at half maximum (FWHM) $\Delta k = 0.050k_0$, corresponding to a divergence half-angle of 0.77°] but opposite S_3 values ($S_3 = \pm 0.96$) were observed at $(k_x, k_y) = (\pm 0.402k_0, 0)$, respectively. Here, $k_0 = 2\pi/\lambda_0$ is the free space wavenumber. The beam quality was quantitatively evaluated by a near-unity diffraction-limited value of $M^2 = 1.08$. Note that the Berry phase plays an important role in determining the radiation mode of the surface emission lasers. It can be further extended to achieve a more complex lasing mode with general implementations of the spin-dependent momentum $\sigma\boldsymbol{k}_R$, thus offering a compact approach to obtaining coherent emission with on-desired wave structures [see experimental demonstration in sections 12 and 13 in (*21*)]. The spatial coherence length can

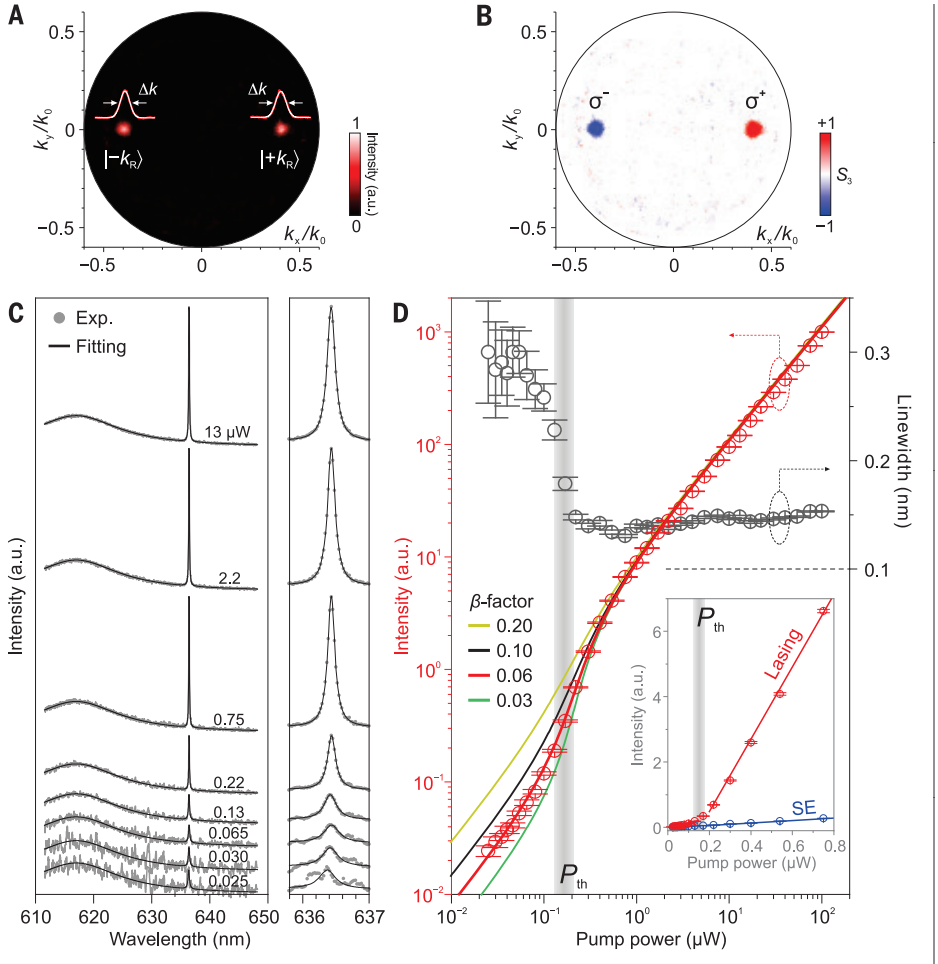

Fig. 2. Spatial and spectral characteristics of the monolayer lasing. (**A** and **B**) Observed far-field intensity (A) and S_3 (B) distributions for a linearly polarized pump ($10P_{th}$). The intensity is fitted by a radial Gaussian function with a FWHM $\Delta k = 0.050k_0$, equal to the diffraction limit of $1.0\lambda_0/D$ (D being the diameter of the core). (**C**) Observed emission spectra against pump power. The spectra (fitted by bi-Lorentzian functions) are normalized by the pump power and shifted vertically for clarity. (**D**) Measured power-dependent L-L curves and linewidths of the observed cavity resonance. Solid curves are fitted by using the laser rate equations with different β-factors. The gray shadow indicates the laser threshold P_{th} = 0.14 μW (17.8 W/cm^2). Inset shows the intensity evolution of lasing emission and SE in a linear scale near P_{th}.

be estimated as $L_{sc} = 8\ln 2/\Delta k = 11.23$ μm [see section 6 in (*21*)]. For comparison, the far-field emission pattern was also measured below threshold ($0.2P_{th}$), where a broader spot ($\Delta k = 0.075k_0$) corresponding to a shorter spatial coherence length (7.49 μm) was observed, indicating the spontaneous emission (SE)–lasing transition (*21*).

To further study the transition from SE to lasing, we measured the evolution of the emission spectra as a function of pump power (Fig. 2C). At very low pump power, we observed a broad PL spectrum centered at 616 nm corresponding to the SE of the WS_2 monolayer. As the pump power increased, a cavity resonance at 636.4 nm emerged and then surpassed the broad PL, indicating the onset of lasing. The cavity resonance and the broad PL were fitted using bi-Lorentzian curves to extract their intensity and linewidth (FWHM, Δλ) evolution. As shown in Fig. 2D, the light-in and light-out (L-L) evolution of the cavity resonance shows a clear "S" shape in log-log scale and a "kink" in linear scale. By comparison, no kink signature was observed from SE. We used spin-dependent laser rate equations [see section 14 in (*21*)] to fit the L-L curves for estimating the β-factor and the P_{th} of the monolayer laser. Here, β-factor is defined as the fraction of SE coupled into the cavity mode and D_{vp} is set to be 0 for linear pump. We found that the results were best fitted by β = 0.06. The threshold, P_{th} = 0.14 μW (17.8 W/cm^2), was derived by the second-order differentiation of the L-L curve, which agrees well with a quantum threshold analysis (*21*). Moreover, the spectral linewidth of the cavity resonance undergoes a significant narrowing (a factor of ~2 from ~0.28 to ~0.14 nm) when the excitation power exceeds the threshold. In addition, temporal and spatial coherence, as key figure-of-merits of a laser, were fully investigated using Michelson interferometers. Both the measured temporal and spatial coherence lengths showed a significant increase above the lasing threshold, evidencing the monolayer lasing [see sections 9 and 10 in (*21*)].

Observation of valley-addressable monolayer lasing

These two lasing modes $|\pm k_R\rangle$ were experimentally verified to be independent [see section 11 in (*21*)], which is a necessary condition for spin-controlled lasing. To showcase the valley-addressable feature of our laser, we characterized the two spin modes in Fig. 2A under spin-polarized ($\sigma^{\pm}$) pump, which can generate an unbalanced valley population and lead to gain anisotropy. To evaluate the spin-controlled properties, we defined a parameter D_R to quantify the modulation depth of the spin Rashba modes as $D_R = \frac{I(|+k_R\rangle)-I(|-k_R\rangle)}{I(|+k_R\rangle)+I(|-k_R\rangle)}$, where $I(|\pm k_R\rangle)$ is the emission intensity of the cavity mode $|\pm k_R\rangle$. Thus, the valley polarization amplification (VPA) from the lasing is expressed as VPA = D_R/D_{vp}. For clarity, we used labels $|\sigma^{\pm}/\pm k_R\rangle$ to discriminate the spin of pump/emission modes, with the same and opposite signs for co-circular (co) and cross-circular (cr) polarization measurements, respectively.

Figure 3A shows the far-field image captured by the σ^- pump with a power of 0.22 μW ($\sim P_{th}^{(cr)}$), in which an asymmetric emission distribution can be observed. In particular, the $|\sigma^-/-k_R\rangle$ spot exhibits a narrower profile ($\Delta k = 0.050k_0$) and an ~2-fold stronger intensity than those of the $|\sigma^-/+k_R\rangle$ spot ($\Delta k = 0.062k_0$). This spin contrast is also demonstrated by the spin-resolved spectra (Fig. 3B), where the $|\sigma^-/-k_R\rangle$ mode is ~2-fold stronger and narrower than that of the $|\sigma^-/+k_R\rangle$ mode. Consequently, a stronger emission probability for $|\sigma^-/-k_R\rangle$ mode (than that for $|\sigma^-/+k_R\rangle$ mode) was achieved without magnetic effects due to a spin pumping around the vicinity of the lasing threshold.

To establish an insightful picture of our valley-addressable laser, the intensities of the $|\sigma^-/-k_R\rangle$ and $|\sigma^-/+k_R\rangle$ spots were separately measured as a function of σ^- pump power (Fig. 3C). Two distinct thresholds, $P_{th}^{(co)}$ and $P_{th}^{(cr)}$, appeared for the co-circularly and cross-circularly polarized emission, respectively, consistent with their measured linewidth narrowing. The modulation depth D_R and the corresponding VPA were also plotted against pump power, revealing three distinct physical regions. First, for the pump power below $P_{th}^{(co)}$, both modes were subcritical and only SE was observed with a negligible D_R and

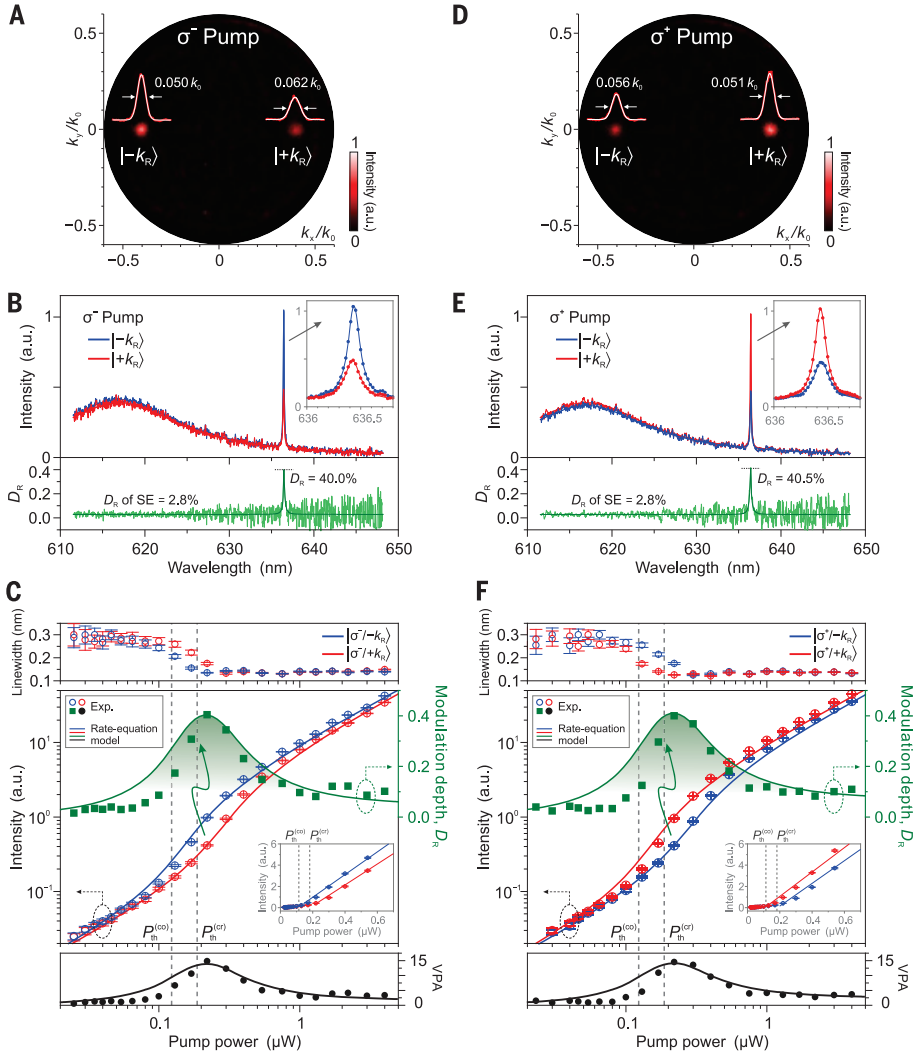

Fig. 3. Observation of the spin-controlled monolayer lasing. (**A**) Observed far-field emission distribution under σ^- pump with a power of 0.22 μW. Inset shows the intensity profiles of the $|\sigma^-/-k_R\rangle$ (or $|\sigma^-/+k_R\rangle$) emission spots with a FWHM of $0.050k_0$ (or $0.062k_0$). (**B**) Corresponding emission spectra of the two spots from (A) and a significant amplification of D_R from ~2.8% of SE background to ~40% of cavity emission (green line). (**C**) Intensity (*L*-*L*) and linewidth evolutions of $|\sigma^-/-k_R\rangle$ and $|\sigma^-/+k_R\rangle$ emission against σ^- pump power. Inset shows *L*-*L* curves in linear scale. The D_R (green squares) and VPA (black circles) are also plotted to show three distinct regions below, near, and above the thresholds. The slight discrepancy between experiments and fitting is attributed to the high sensitivity of the lasing intensity around the thresholds. The thresholds $P_{th}^{(co)}$ and $P_{th}^{(cr)}$ are 0.11 μW (14.0 W/cm^2) and 0.18 μW (22.9 W/cm^2), respectively. (**D** to **F**) Same measurements as in (A) to (C) but under σ^+ pump.

a near-unity VPA. Second, as the pump power crossed between $P_{th}^{(co)}$ and $P_{th}^{(cr)}$, only the pump-parallel mode $|\sigma^-/-k_R\rangle$ started to lase due to a sufficient optical gain, leading to a dominance of copolarized $|\sigma^-/-k_R\rangle$ emission over the cross-polarized $|\sigma^-/+k_R\rangle$ emission. As a result, the small valley contrast (D_{vp}= ~2.8%) was significantly enhanced, with an observed D_R up to ~40% (VPA ~15) as the pump power reached ~$P_{th}^{(cr)}$. Finally, for the pump power over $P_{th}^{(cr)}$, both modes started to lase, and D_R gradually decreased due to the rapidly increased cross-polarized lasing emission. Therefore, the cavity emission near the threshold exhibited the highest D_R and VPA. Similar results were observed with the spin-flipped component when the pump spin was changed from σ^- to σ^+ (Fig. 3, D to F).

Concluding remarks

These results verify that dynamically controlled spin-asymmetric lasing can be achieved under a spin-polarized pump, which overcomes the room-temperature intervalley scattering by effectively breaking the population balance between opposite valley excitons through the lasing mechanism. Moreover, a spin-dependent rate equations model has been used to simulate the spin-controlled lasing process, which agrees well with experimentally observed *L*-*L*, D_R, and VPA curves. It also confirms that both high D_{vp} of the WS_2 monolayer and low β-factor of the cavity will promote the D_R [see section 14.7 in (*21*)]. Our scheme illustrates the ability to actively enhance the spin contrast of light emission, offering a versatile platform for developing compact spin-polarized quantum sources and valley-based spin-optical devices at room temperature.

REFERENCES AND NOTES

1. E. Rashba, *Sov. Phys. Solid State* **2**, 1109–1122 (1960).
2. M. I. Dyakonov, V. I. Perel, *Phys. Lett. A* **35**, 459–460 (1971).
3. K. Y. Bliokh, Y. P. Bliokh, *Phys. Rev. Lett.* **96**, 073903 (2006).
4. E. Maguid *et al*., *Science* **352**, 1202–1206 (2016).
5. T. Stav *et al*., *Science* **361**, 1101–1104 (2018).
6. N. Carlon Zambon *et al*., *Nat. Photonics* **13**, 283–288 (2019).
7. M. V. Berry, *Proc. R. Soc. Lond. Ser. A* **392**, 45–57 (1984).
8. N. Shitrit *et al*., *Science* **340**, 724–726 (2013).
9. X.-T. He *et al*., *Nat. Commun.* **10**, 872 (2019).
10. K. Rong *et al*., *Nat. Nanotechnol.* **15**, 927–933 (2020).
11. Z. Bomzon, G. Biener, V. Kleiner, E. Hasman, *Opt. Lett.* **27**, 1141–1143 (2002).
12. N. Dahan, Y. Gorodetski, K. Frischwasser, V. Kleiner, E. Hasman, *Phys. Rev. Lett.* **105**, 136402 (2010).
13. A. C. Overvig, S. C. Malek, M. J. Carter, S. Shrestha, N. Yu, *Phys. Rev. B* **102**, 035434 (2020).
14. S. Klembt *et al*., *Nature* **562**, 552–556 (2018).
15. E. Maguid *et al*., *ACS Photonics* **5**, 1817–1821 (2018).
16. B. Wang, K. Rong, E. Maguid, V. Kleiner, E. Hasman, *Nat. Nanotechnol.* **15**, 450–456 (2020).
17. S. Wu *et al*., *Nature* **520**, 69–72 (2015).
18. Y. Ye *et al*., *Nat. Photonics* **9**, 733–737 (2015).
19. Y. Liu *et al*., *Sci. Adv.* **5**, eaav4506 (2019).
20. H. Zeng, J. Dai, W. Yao, D. Xiao, X. Cui, *Nat. Nanotechnol.* **7**, 490–493 (2012).
21. Materials and methods are available as supplementary materials.

ACKNOWLEDGMENTS

Fabrication was performed at the Micro-Nano Fabrication & Printing Unit of Technion. **Funding:** X.D., K.R., C.-l.L., V.G., V.K., and E.H. gratefully acknowledge financial support from the Israel Science Foundation (ISF grant 1170/20). X.D. is supported by a Technion-Guangdong Fellowship. B.W. is supported by the National Key R&D Program of China (grant 2022YFA1205100), the National Science Foundation of China (grant 12274296), Shanghai International Cooperation Program for Science and Technology (22520714300), and the Yangyang Development Fund. E.K. and E.H are supported by a joint NEVET grant from the Russell Berrie Nanotechnology Institute of Technion. **Author contributions:** All authors contributed substantially to this work. **Competing interests:** The authors declare no competing interests. **Data and materials availability:** All data are available in the main text or the supplementary materials.

License information: Copyright © 2023 the authors, some rights reserved; exclusive licensee American Association for the Advancement of Science. No claim to original US government works. https://www.science.org/about/science-licenses-journal-article-reuse

SUPPLEMENTARY MATERIALS

science.org/doi/10.1126/science.adi7196
Materials and Methods
Supplementary Text
Figs. S1 to S27
Tables S1 and S2
References (*22*–*25*)

Submitted 15 May 2023; accepted 25 August 2023
10.1126/science.adi7196

POLYMER CHEMISTRY

Diverse functional polyethylenes by catalytic amination

Nicodemo R. Ciccia[1,2], Jake X. Shi[1,2], Subhajit Pal[3], Mutian Hua[4], Katerina G. Malollari[3], Carlos Lizandara-Pueyo[5], Eugen Risto[6], Martin Ernst[6], Brett A. Helms[4,7], Phillip B. Messersmith[3,4], John F. Hartwig[1,2]*

Functional polyethylenes possess valuable bulk and surface properties, but the limits of current synthetic methods narrow the range of accessible materials and prevent many envisioned applications. Instead, these materials are often used in composite films that are challenging to recycle. We report a Cu-catalyzed amination of polyethylenes to form mono- and bifunctional materials containing a series of polar groups and substituents. Designed catalysts with hydrophobic moieties enable the amination of linear and branched polyethylenes without chain scission or cross-linking, leading to polyethylenes with otherwise inaccessible combinations of functional groups and architectures. The resulting materials possess tunable bulk and surface properties, including toughness, adhesion to metal, paintability, and water solubility, which could unlock applications for functional polyethylenes and reduce the need for complex composites.

A central challenge for the design, synthesis, and implementation of polymers is that each application necessitates a specific set of material properties. Consequently, numerous materials have been developed to meet demand, and the generation of new materials for emerging applications continues at a rapid pace (*1*).

Functionalized polyethylenes are a class of polyolefins used in applications ranging from packaging and film to sealants and enclosures (*2*–*6*). Functional groups along the hydrocarbon backbone endow the plastic with surface properties such as adherence to inks or glues that are valuable for such applications (*7*–*9*). However, functional polyethylenes lack diversity in structure, namely the available combinations of polymer architecture and different polar groups, thus limiting the tunability of their properties. Given the wide-ranging applications of plastics, these materials are commonly formulated with other polymers, but such composites complicate recycling and reuse (*10*, *11*). Functional polyethylenes with different combinations of properties could alleviate this need for composites, thereby indicating that polyethylenes with varying amounts and identities of polar groups along the hydrocarbon chains are important materials.

However, methods to prepare functional polyethylenes are limited. The production of functional polyethylenes is generally conducted by free-radical copolymerization, but this method generates only branched materials and the ratios of incorporated comonomers are difficult to control (*12*–*14*). The synthesis of such materials by copolymerizations catalyzed by transition-metal complexes suffers from poisoning by the polar comonomer, preventing the synthesis of more linear polyethylenes with polar groups (*3*–*5*, *15*–*17*). Thus, alternative methods are needed to create functional polyethylenes with controllable combinations of architectures and functional groups that imbue them with favorable properties.

The functionalization of polyolefins could generate a diverse range of materials and properties because the polar bonds are introduced after the polymer architecture has been established (*18*–*20*). By employing such methods, combinations of functional groups and polymer architectures could be generated rapidly, and the properties of these materials assessed. This approach offers advantages over the state of the art; although functionalization of polyethylene by radical chain processes or plasma treatments conducted industrially provide access to important materials, the high degree of cross-linking resulting from these reactions uncontrollably alters polymer architectures (*8*, *21*, *22*). Emerging functionalization strategies of polyethylenes have predominantly formed C–C, C–O, or C–X bonds on the polymer chain. However, such methods are inherently limited in the scope of substituents that can be incorporated, involve reagents that are expensive or require multiple steps to prepare, and are often accompanied by cross-linking or scission (*19*, *23*). Furthermore, new reaction conditions are typically required for each new material and may not universally apply to the broad range of polyethylene architectures currently available.

We envisioned that the catalytic conversion of C–H bonds to C–N bonds in polyolefins could serve as a general platform to prepare an array of functional polyethylenes because the nitrogen atoms in the reagents for amination can carry two of the same or different substituents, thereby enabling C–N bond formation to append multiple groups with varying polarity onto the polymer chains. Polyethylenes containing pendent nitrogen-based groups are currently underexplored because their synthesis by copolymerization is particularly challenging (Fig. 1A), and methods for intermolecular amination of the unactivated secondary C(sp^3)–H bonds in polyethylene (Fig. 1B) are limited to a single uncatalyzed process by insertion of a nitrene generated from 4-aminobenzenesulfonyl azide (*24*) and radical addition into an azodicarboxylate initiated by *N*-hydroxyphthalimide to form a hydrazide product (*25*). The installation of a series of different groups by these methods would be difficult to accomplish, and the reactions suffer from undesired cross-linking of the polymer chains. Instead, catalytic amination of the C–H bonds in polyethylene that occurs with a broad scope of common nitrogen-based compounds could enable access to polyethylenes possessing a range of pendent functionality with properties suitable for multiple applications.

Here, we report a Cu-catalyzed amination of polyethylenes possessing various molecular weights and architectures with a broad range of nitrogen-based functionality, including amide, carbamate, sulfonamide, and imide groups (Fig. 1C). Translation of the amination of small alkanes to the amination of polyethylene with high efficiency and generality and without chain cleavage required changes to the catalyst structure, and unusual effects of the length of alkyl substituents on the ligand made possible the controlled incorporation of 0.2 to 4 mol % of these carbamoyl-based functionalities, relative to monomer units. To highlight the ability of our approach to create materials for different applications rapidly, the properties of both monofunctional and bifunctional materials generated by the amination process were tested, including toughness, adhesion to metal surfaces, paintability, reversible cross-links, and water-solubility, and they were found to be comparable or superior to those of commercial functional polyethylenes. Thus, catalytic C–H amination unlocks established polyethylene feedstocks—even waste plastics—for the development of new materials and applications.

Development of reaction conditions for the amination of C–H bonds in polyethylenes

Our efforts to develop an amination of polyethylene began by investigating a series of reaction conditions known to promote the catalytic amination of aliphatic C–H bonds. Low-density polyethylene (LDPE) was used first for these studies because of its prevalence in commercial applications and its greater solubility in organic solvents than more linear, high-density polyethylene (HDPE). Conditions to catalyze nitrene insertion into the

[1]Department of Chemistry, University of California, Berkeley, Berkeley, CA 94720, USA. [2]Division of Chemical Sciences, Lawrence Berkeley National Laboratory, Berkeley, CA 94720, USA. [3]Departments of Materials Science and Engineering and Bioengineering, University of California, Berkeley, Berkeley, CA 94720, USA. [4]Materials Sciences Division, Lawrence Berkeley National Laboratory, Berkeley, CA 94720, USA. [5]BASF Corporation, Berkeley, CA 94720, USA. [6]BASF SE, 67056 Ludwigshafen am Rhein, Germany. [7]The Molecular Foundry, Lawrence Berkeley National Laboratory, Berkeley, CA 94720, USA.
*Corresponding author. Email: jhartwig@berkeley.edu

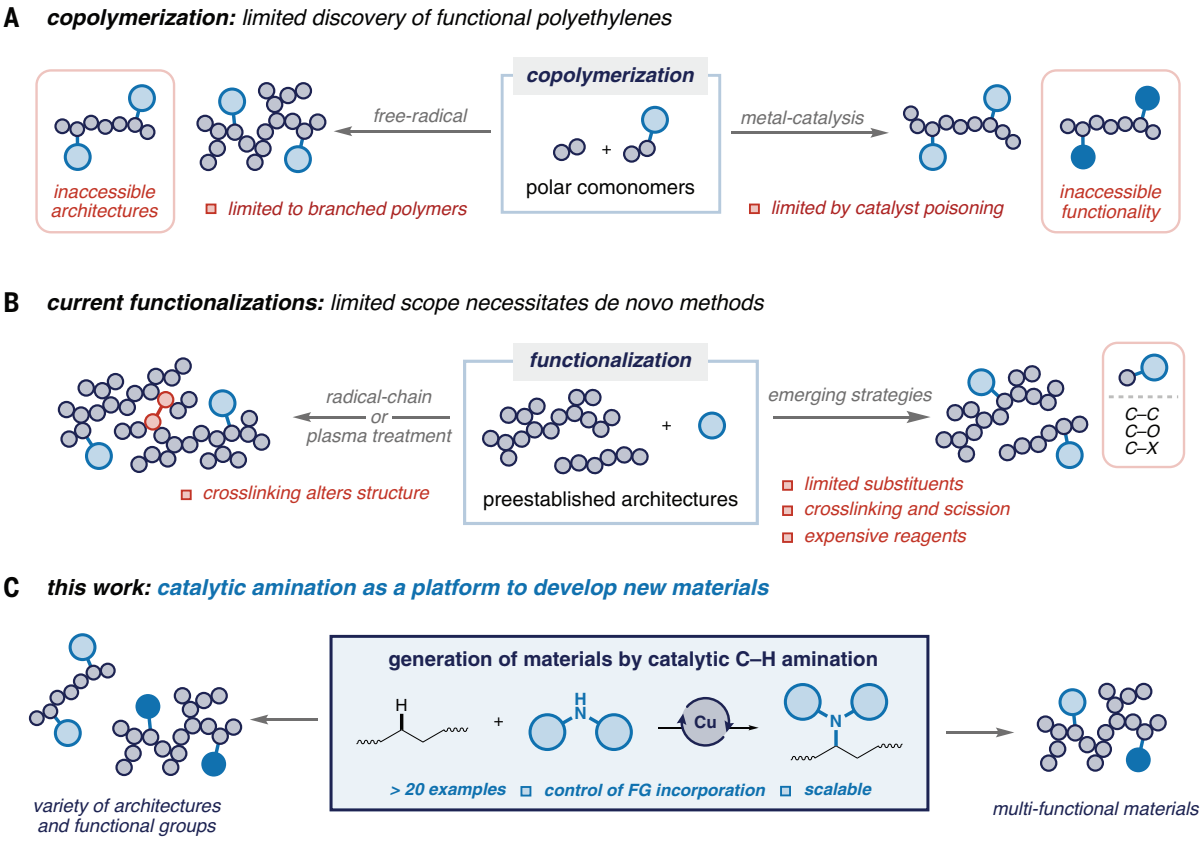

Fig. 1. Methods to access functional polyethylenes. (**A**) Synthesis of functional polyethylenes by copolymerizations. (**B**) Limitations of current functionalizations of polyethylene. (**C**) Catalytic C–N bond formation as a platform for the development of new materials.

C(sp^3)–H bonds of LDPE with manganese- and ruthenium-porphyrin complexes, as well as rhodium acetate, resulted in undetectable levels of incorporation of amide groups and competing incorporation of chlorine from the solvent (table S1). These data underscore how the high temperatures and nonpolar solvents needed to dissolve polyethylenes are incompatible with many common methods for the functionalization of C–H bonds in small molecules. Despite these challenges, we found that a copper-catalyzed amination with benzamide as the nitrogen-based reagent and di-*tert*-butyl peroxide (DTBP) as the oxidant led to the incorporation of amidyl groups into LDPE (Fig. 2A). While our previously reported method for the amination of small alkanes employed benzene as a solvent (*26*), 1,2-dichlorobenzene (1,2-DCB) was selected as the solvent for the amination of polyethylenes because its high boiling point enabled dissolution of the polymer at 120°C. Control experiments indicated that each component, including the copper catalyst, was required to achieve detectable levels of C–N bond formation (table S7).

The yields of amination reactions of small alkanes catalyzed by CuI and 1,10-phenanthroline (**L1**) or 4,7-dimethoxy-1,10-phenanthroline (**L2**) are high (*26*), but reactions of LDPE (M_n = 35.1 kg mol^{-1}) catalyzed by the same systems resulted in less than 1% incorporation of the amide functional group per monomer unit (Fig. 2A) and a significantly lower molecular weight of the resulting polymers than of the starting polyethylene. These data suggest that the alkyl radical intermediate, generated by abstraction of a C–H bond by an alkoxy radical, combines with a copper(II) amidate species more slowly than it undergoes β-scission.

To probe this hypothesis, we investigated the effect of ligand structure on the degree of functional-group incorporation and the molecular weight of the functionalized polyethylenes. We tested such ligands because solubilizing alkyl chains have enhanced the activity of polymerization catalysts that form high–molecular weight materials (*27*, *28*). Such substituents could render a polar Cu catalyst more compatible with nonpolar polyethylenes and improve the amination process.

Indeed, reactions with a series of phenanthrolines containing alkyl substituents led to greater incorporation of the amide functional groups (Fig. 2A). Reactions catalyzed by copper complexes of phenanthroline derivatives that contain alkyl substituents at the 3 and 8 positions (**L3** to **L5**) proceeded in higher yields (yields were defined as 100 × the ratio of the amount of amide incorporated onto the polymer versus the amount of amide added to the reaction mixture) than those catalyzed by complexes of the unsubstituted counterpart, and the ligand containing the longest chain (**L5**) led to the highest incorporation of the amidyl group onto the polymer (Fig. 2A and table S4). The amination with **L5** also occurred with the smallest decrease in M_n. These observations suggest that the alkyl substituent on the ligand accelerates the reaction of the copper(II) amidate with the polymeric alkyl radical, and this faster rate limits side reactions of the alkyl radical.

To probe the origin of this effect of ligand on reaction yield, we compared the catalytic amination of polyethylenes with **L1** and **L5** as ligand on copper to the amination of small alkanes with the same ligands. While the amination of *n*-hexane, cyclohexane, *n*-octane, cyclooctane, and *n*-octadecane occurred in similar or higher yields with **L1** as with **L5**, the amination of LDPE occurred in higher yields with **L5** (Fig. 2B and table S5). These data show that the relative rates of elementary steps on and off the catalytic cycle could depend on the molecular weight of the alkane, possibly because of the differences in the rates of diffusion of reactive intermediates in the medium

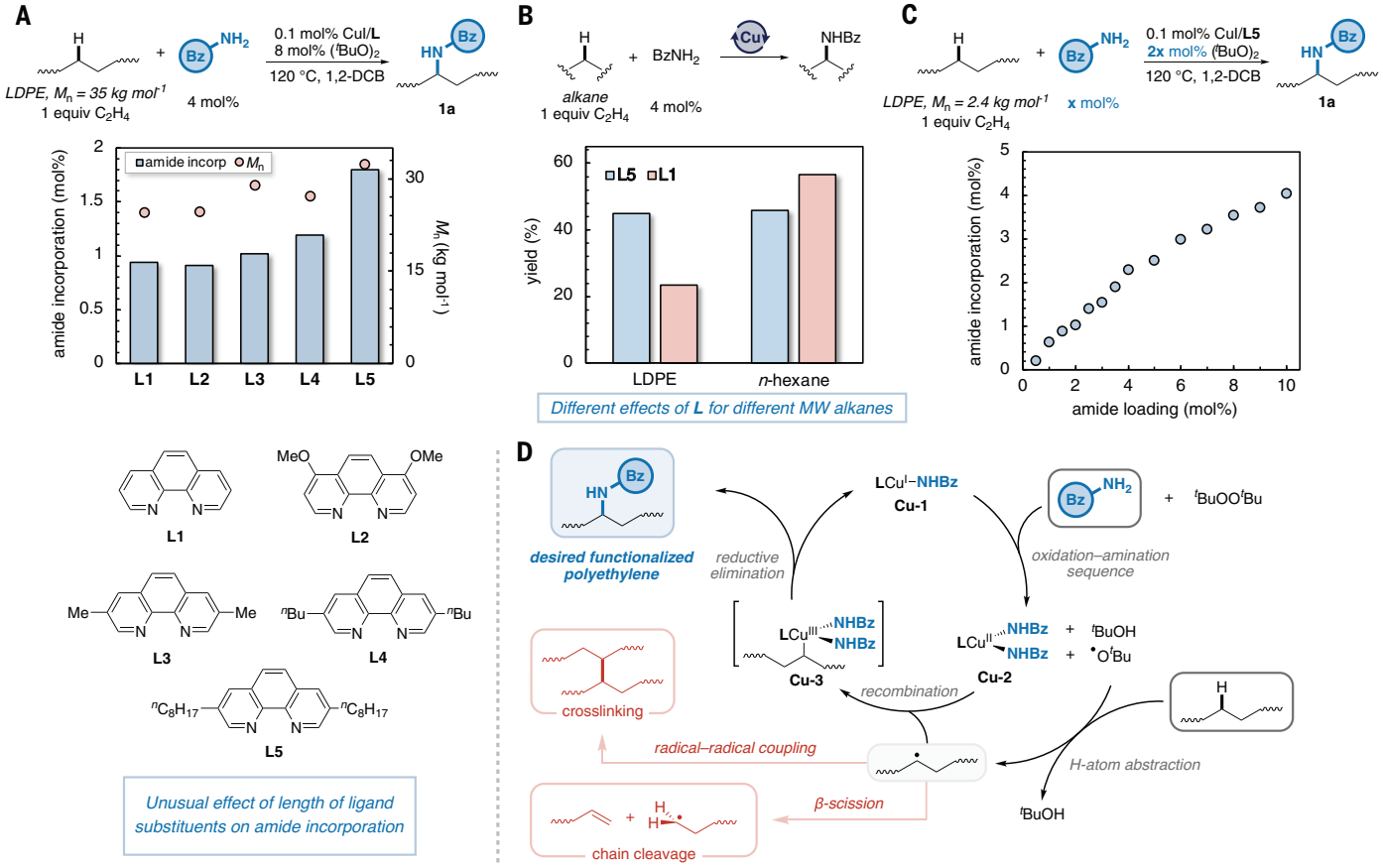

Fig. 2. Development of the catalytic amination of polyethylenes. (**A**) Investigation of the effect of ligands on the yield of amination and on the change in M_n of the polymers. Amide incorporation (mol %) was determined relative to unmodified C_2H_4 units. Reaction yields were calculated as the percentage of amide that was incorporated. DTBP, di-*tert*-butyl peroxide. 1,2-DCB, 1,2-dichlorobenzene. (**B**) Comparison of aminations of polyethylene and *n*-hexane with **L1** or **L5** as ligand. Conditions: 1 equiv C_2H_4 units, 4 mol % benzamide, 0.1 mol % CuI, 0.1 mol % **L1** or **L5**, 8 mol % DTBP, 1,2-DCB, 120°C. (**C**) Illustration of the range of amide incorporations accessible by this method. (**D**) Proposed mechanism for the catalytic amination of polyethylenes.

containing the polymer. Ongoing investigations in our laboratories seek to test this hypothesis.

The ability to incorporate specific levels of functional groups is crucial to tune the material properties of functional polyethylenes for specific applications. Figure 2C shows that our method generates polyethylenes with prescribed levels of amide incorporation between 0.20 and 4.1 mol % [amide incorporation was determined by ^{1}H nuclear magnetic resonance (NMR) spectroscopy, see Supplementary Materials Section 2 for details]. Although slightly nonlinear, a continuous increase in amide incorporation with increase in loading of the amide was observed. The turnover numbers of this copper-catalyzed amination (>40), although currently modest, exceed those for copper-catalyzed functionalizations of the tertiary C–H bonds in polyolefins to form C–C bonds, manganese-catalyzed oxidations of polyolefins to form C–O bonds, and iridium-catalyzed reactions of polyolefins to form C–C double bonds (*29*–*31*). Furthermore, analysis by inductively coupled plasma optical emission spectroscopy indicates that the amount of residual copper remaining in the functional polyethylenes can be reduced to less than 5 parts per million (ppm), which is below government-regulated migration limits for copper in food-contact plastics (see fig. S8 for details) (*32*).

These amination conditions can be compared with those for the synthesis of polyethylene with grafted maleates, a process which is conducted industrially (*21*, *33*, *34*). In both processes, peroxides are used to generate alkyl radical intermediates. Although industrial grafting involves peroxides in initiator quantities and our method involves such reagents in stoichiometric quantities, we demonstrate that reactions with as little as 5.3 wt % peroxide (relative to polymer) incorporate amide groups onto polyethylene (Fig. 2C), and we show that such materials with the corresponding levels of amide incorporation possess modified properties (vide infra). Furthermore, grafting of polyethylene is often performed with a large excess of maleates—up to 100 wt % relative to polymer—and the efficiencies of these reactions are often well below 20%. Our amination process includes just 4 mol % benzamide, relative to monomers (17 wt % relative to polymer), and incorporates nearly 50% of this amide, making the material balance of reactants in this catalytic amination comparable to those of well-established functionalizations. Finally, grafting reactions with maleic anhydride have been reported in solution, as well as polymer melts for large-scale applications (*35*). In the current, initial form, our solution-phase process has been conducted on a decagram scale to produce sufficient material for a range of experiments testing properties and potential applications. Although amenable to laboratory-scale experiments, the use of 1,2-DCB for commercial-scale processes could pose economic, environmental, or safety risks. To address such concerns, we conducted this amination in the polymer melt. Preliminary experiments indicate that the amination reaction with benzamide proceeds under solvent-free, melt conditions to produce functional polyethylenes in moderate yields (table S3).

Considering the high degree of branching in LDPE, we sought to determine the selectivity of this amination for the primary, secondary,

or tertiary C–H bonds in polyethylene. The potential for functionalization of the primary C–H bonds was assessed by comparing the ^{1}H NMR spectrum of the functionalized polymer to that of *N*-octylbenzamide. The potential for functionalization of the tertiary C–H bonds of LDPE was assessed by comparing the ^{13}C NMR spectrum of the functionalized polymer to that of *N*-[(1,1-dipropyl)butyl]benzamide and by comparing the integration of the methine proton to the amidyl protons in the ^{1}H NMR spectrum of the functionalized polymer. The absence of a ^{1}H resonance between 3.43 and 3.53 ppm for a methylene proton or a ^{13}C resonance at 59.4 ppm for a tetrasubstituted carbon α to the amidyl group, and the precise 1:2 ratio of methine to *ortho*-aryl protons, indicate that this transformation, similar to the amination of small alkanes (*26*), is selective for secondary C–H bonds (see figs. S5 to S7 for details).

In each of the aminations of polyethylene, internal olefins in much smaller amounts than the amide (generally 0.5 to 0.7 mol % versus monomer units) were detected by NMR spectroscopy. Control experiments show that internal olefins form by Cu-catalyzed dehydrogenation of alkane by peroxide, suggesting that some background process could lead to these units when conducting the Cu-catalyzed reaction (table S7). Oxidations of small alkanes with copper catalysts and peroxide reagents also lead to competitive formation of alkenes or products from oxidation of the resulting allylic C–H bonds (*36*, *37*). Although the amount of olefin introduced is low and does not change the polarity of the material, we have eliminated these groups by reduction. Simple reaction of **1a** with *p*-toluenesulfonyl hydrazide furnished benzamidyl-functionalized LDPE with no detectable amounts of olefin and no change in the level of amide incorporation (Supplementary Materials Section 13). We also envision that these groups could undergo additional reactions, such as hydrofunctionalization, oxidation, or vulcanization, to access multifunctional or cross-linked materials.

Scope of the amination of polyethylene C–H bonds

A major limitation of existing functionalizations of polyethylene is the narrow scope of substituents that can be incorporated onto the polymer chains and the changes that occur to the polymer architecture from these functionalizations. As such, materials with various combinations of functional groups and structures cannot be made by such methods. We hypothesized that our catalysts designed to react with polyolefins could enable functionalization of a range of polyethylene architectures and that the breadth of groups amenable to this C–N bond formation could, together, furnish an array of new materials with a range of properties.

Indeed, polyethylenes with varying molecular weights and architectures underwent the amination process (Fig. 3). These polyethylene functionalizations were conducted with a 1:25 ratio of amide to C_2H_4 units. Low molecular weight LDPE (M_n = 2.38 kg mol^{-1}) underwent functionalization in 45% yield to create a material in which 1.8 mol % of the monomer units contain an amide. Amination of high molecular weight LDPE (M_n = 35.1 kg mol^{-1}) occurred in the same 45% yield. Reactions of HDPE and linear low-density polyethylene (LLDPE) both occurred, but reactions of these polymers required lower concentrations than reactions of LDPE for functionalization to occur without solidification that, presumably, results from coupling of alkyl radicals. With these modified conditions, both HDPE and LLDPE underwent amination to give functional polyethylenes in which 0.89 and 0.72 mol % of the monomer units contained amides, respectively.

The amination also occurred with the C–H bonds of polyethylene in waste materials. Although the focus of this work is to illustrate the potential of this process to create a range of new materials, additional value could be gained by the conversion of waste plastic to functionalized materials with altered properties. Catalytic functionalization of post-consumer polyethylenes is more challenging than the functionalization of virgin materials because post-consumer materials often contain heterogeneous and unpredictable mixtures of dyes, plasticizers, or residues, which can inhibit reactivity. Despite the presence of these components, the reactions of post-consumer LDPE (resealable storage bag) or HDPE (milk jug) with benzamide gave a functionalized material in which 1.1 or 1.4 mol % of the monomers contained amides, respectively. This degree of amide incorporation in these waste-derived materials is comparable to that in the functional materials formed by amination of virgin LDPE (1.8 mol %) or HDPE (0.89 mol %), signifying the ability of our method to form *N*-containing polyethylenes from ubiquitous waste plastic.

A broad range of amides underwent this functionalization reaction with LDPE under conditions (1:25 ratio of amide to C_2H_4 units) analogous to those for the functionalizations with benzamide to create a wide array of materials (Fig. 3). Benzamides possessing electron-withdrawing groups, such as Cl, CN, and CF_3 (**2a** to **4a**), underwent the process to produce polyethylenes with functional-group incorporation between 1.2 and 2.0 mol % and no substantial change in the molecular weight distributions of the polymer chains. Benzamides possessing electron-donating groups, such as Me, *n*-Bu, *t*-Bu, and OMe (**6a** to **9a**), also underwent the reaction to give functional polyethylenes with good amide incorporation (1.7 to 2.3 mol % of monomers). In some reactions of electron-rich benzamides, an increase in M_n of the polymer was observed, suggesting that coupling of alkyl radicals competes with combination between the alkyl radical and an electron-rich copper(II) amidate (see Supplementary Materials Section 25). Reaction with isonicotinamide (**12a**) furnished functional polyethylenes with 2.1 mol % amide incorporation to introduce heteroarenes along the backbone of the polymer. Alkylamides (**13a** to **16a**) also underwent the process, showing that the aromatic unit of the benzamides is not necessary for the amination to occur, and even an alkylamide containing an unprotected alcohol (**17a**) was compatible. Finally, a carbamate (**18a**), sulfonamide (**19a**), and imide (**20a**) each reacted with LDPE to incorporate functional groups at 1.1 to 2.2 mol % of the monomer units, demonstrating the broad applicability of this reaction to the incorporation of carbamoyl-based functional groups. The yields for amination with each of the amides tested were comparable to or greater than those for established functionalizations of polyolefins (*19*).

Deprotection unveiled functional groups, such as a carboxylic acid, hydroxyl group, or amino group, that were otherwise incompatible with the catalytic process. Benzamides bearing CO_2Me or OTBS groups (**5a** and **10a**, respectively) underwent hydrolysis or desilylation to generate polymers containing a combination of amidyl units and pendent carboxylic acids or alcohols (**5b** and **10b**). Perhaps most notable, simple addition of acid to polymer **18a** containing *tert*-butyl carbamate units produced polymer **18b** in which 2 mol % of the monomer units contained NH_2 groups (Fig. 3). These various groups provide additional opportunities to generate new materials with distinct properties (vide infra).

Functional polyethylenes containing multiple types of groups, which are challenging to synthesize by terpolymerization or current functionalizations, were readily accessible by our method. Treatment of LDPE under standard conditions with 2 mol % of both benzamide and $BocNH_2$ (**21a**), $TsNH_2$ (**23a**), or phthalimide (**24a**) furnished bifunctional materials that contained similar amounts of each group (Fig. 3). Furthermore, reaction of 2 mol % $BocNH_2$ and 2 mol % *p*-(CO_2Me)-benzamide (**22a**) with LDPE furnished a bifunctional amino acid material that contained, upon deprotection, 1 mol % NH_2 groups and 1 mol % CO_2H groups (**22b**, Supplementary Materials). Measurements of the thermal transitions by differential scanning calorimetry (DSC) indicate that the melting point of the bifunctional material is significantly lower than that of a blend of two separate materials, showing that intramolecular noncovalent interactions could affect the properties of the material (fig. S14).

The broad scope of this catalytic amination also enables the synthesis of complex polymer architectures, including networks with

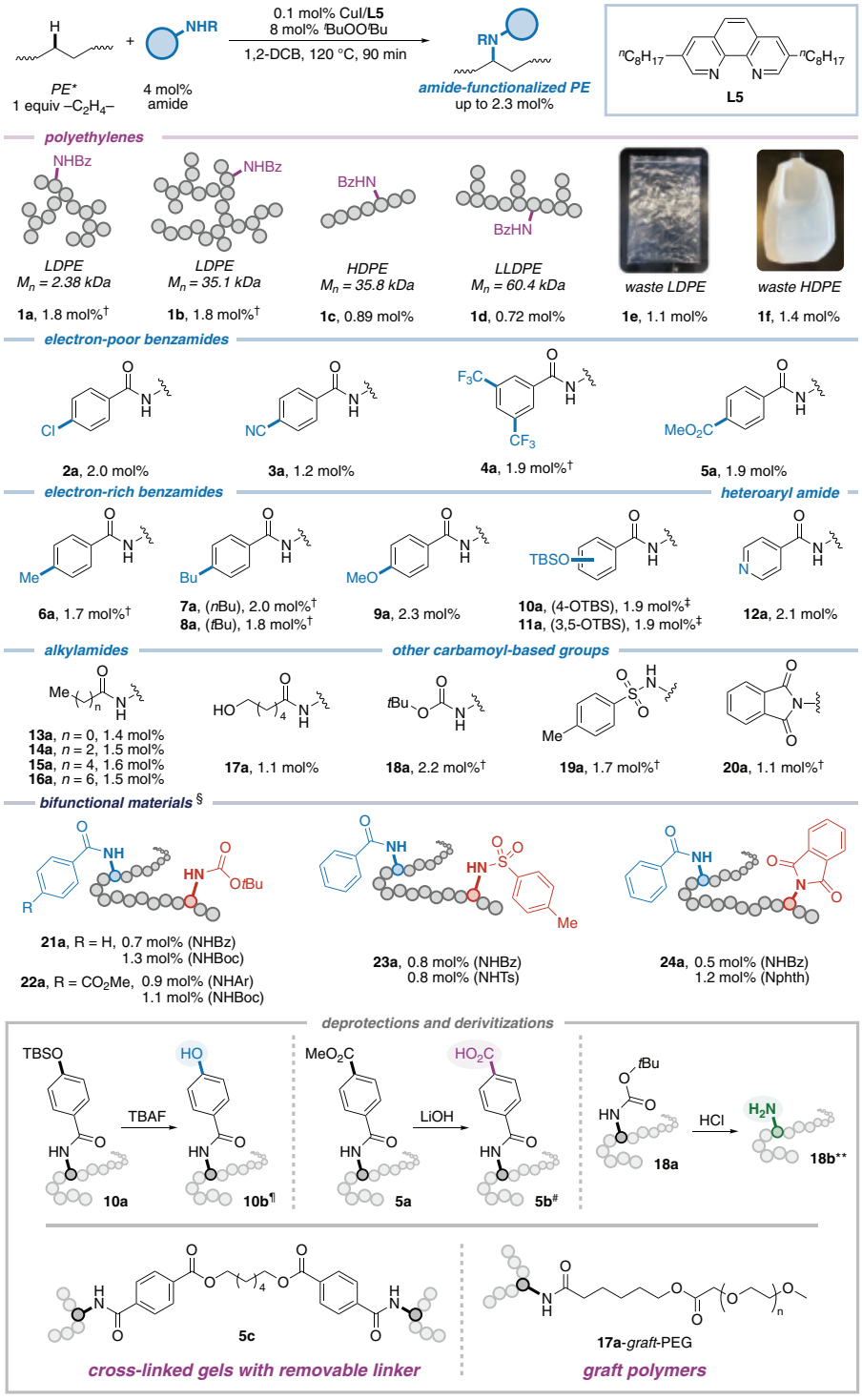

Fig. 3. Scope of polyethylenes and nitrogen-based groups that undergo catalytic amination. Amide incorporation (mol %) was determined relative to unmodified C_2H_4 units. DTBP, di-*tert*-butyl peroxide. 1,2-DCB, 1,2-dichlorobenzene. *Unless otherwise specified, starting PE was LDPE, M_n = 2.4 kg mol^{-1}. †Reaction time of 2 hours. ‡Performed on a 3.0-gram scale. §Amide loadings of 2 mol %. ¶Conditions: 1 equiv TBSO groups, 1.5 equiv TBAF, tetrahydrofuran (THF), 75°C. #Conditions: 1 equiv CO_2Me groups, excess LiOH, *t*-amyl alcohol, 90°C. **Conditions: 1 equiv BocNH groups, excess HCl, dichloromethane (DCM), 75°C.

removable cross-links and graft polymers. For example, reaction of polymer **17a**, which contains pendent aliphatic alcohols, with polyethylene glycol (PEG) derivatives furnished a graft polymer (Fig. 3). In addition, treatment of polymer **5b**, which contains pendent carboxylic acid groups, with 1,6-hexanediol and *p*-toluenesulfonic acid produced insoluble cross-linked networks (**5c**) with a gel content of 60%. Consistent with a removable cross-link, swelling in *t*-AmOH at 100°C and treatment with LiOH converted the insoluble **5c** into a fully soluble material after 1 hour and, upon workup, the starting polymer was recovered.

Selected properties of diverse materials from C–H amination

Because each application of polymers requires a specific combination of material properties, it is crucial that methods for the synthesis of functional polyethylenes can create multiple materials with distinct properties that can be selected and tuned for each application. Thus, we sought to highlight the ability of C–H amination to create various materials with a range of bulk and surface properties that could unlock innovative applications for polyethylenes, rather than to target a single set of properties.

We first evaluated the tensile properties of multiple polyethylenes containing carbamoyl-based groups to illustrate a range of mechanical properties that can be accessed by our method (Fig. 4A). Both the identity and the proportion of the functional groups affected these mechanical properties, illustrating the ability to use the catalytic process to tune properties. For example, the tensile strength of **1b** (16 ± 2 MPa) was 1.5 times higher than that of virgin LDPE (11 ± 1 MPa) and, notably, the elongation at break for **1b** (733 ± 131%) was ~320% that of LDPE (228 ± 97%). In addition, the Young's modulus of **1b** (80 ± 4 MPa) was lower than that of the starting LDPE (149 ± 17 MPa). This lower value could be attributed to lower levels of crystallinity in **1b** than in LDPE because the incorporation of large functional groups disrupts the crystalline domains of polyethylenes (*16*, *38*). DSC data corroborate this hypothesis; the melt transitions for each of the nitrogen-containing polyethylenes were lower and broader than that of virgin LDPE (figs. S9 to S13). Overall, the combined changes to tensile strength, elongation at break, and Young's modulus cause the toughness of **1b** (81 ± 21 MJ m^{-3}) to be 390% higher than that of virgin LDPE (21 ± 10 MJ m^{-3}). Similar tensile measurements of other polyethylenes with varying amounts of benzamidyl groups (0.3 to 2.5 mol %) demonstrate that the toughness of these materials can be finely tuned based on the amount of amide that is incorporated (Fig. 4A). Furthermore, other functional groups accessible by our method, such as alkylamido (**14b**) or phthalimidyl groups

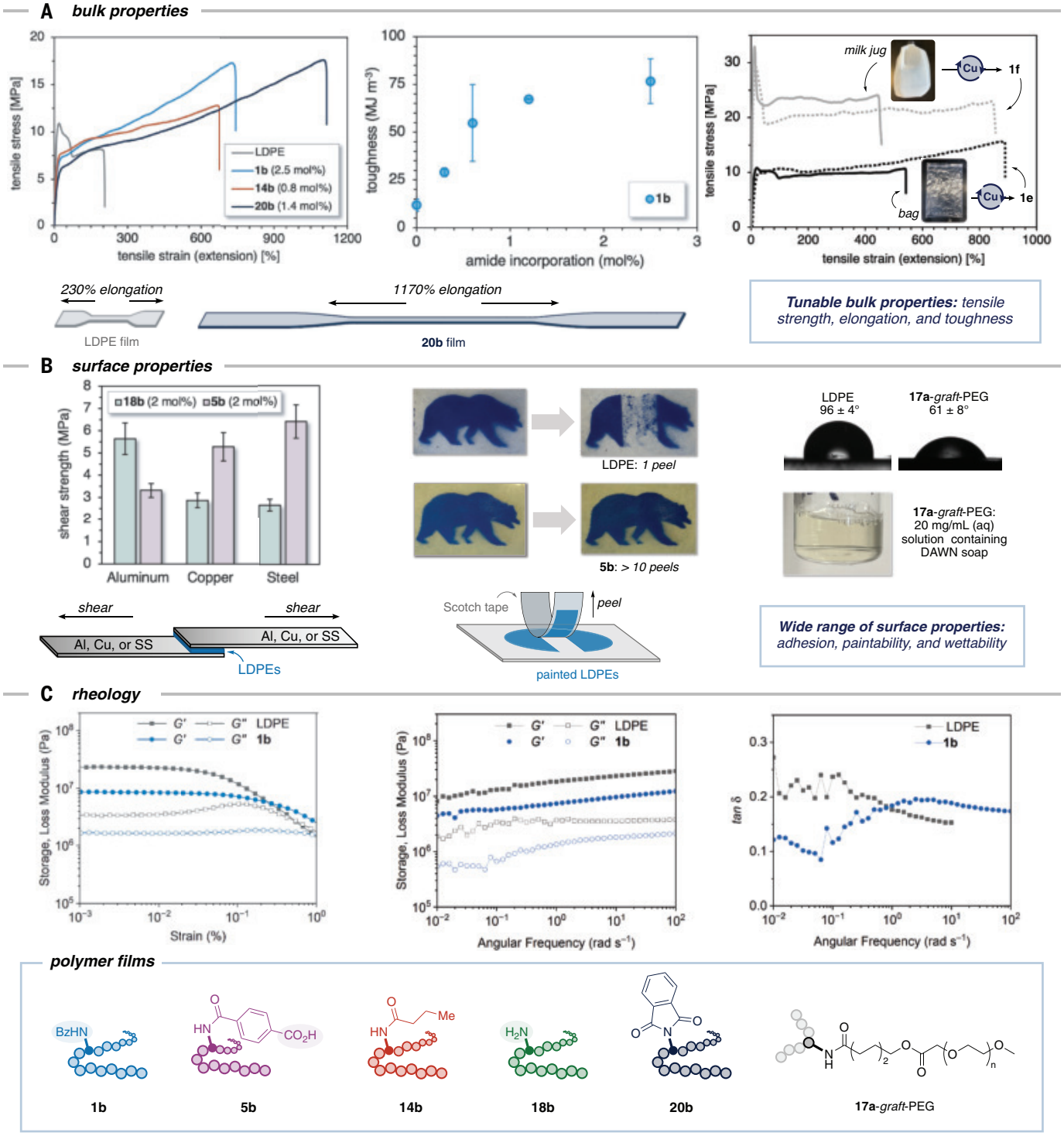

Fig. 4. Range of properties of selected functional polyethylenes. (**A**) Bulk properties of functional polyethylenes. (Left) Representative tensile tests of LDPE and *N*-containing polyethylenes (0.8 to 2.5 mol %). Strain rate = 50 mm min^{-1}. (Middle) Average toughness of **1b** with varying percentages of amide incorporation. Error bars represent standard deviation. (Right) Representative tensile tests of waste LDPE (resealable storage bag), waste HDPE (milk jug), **1e** (0.3 mol %), and **1f** (0.4 mol %). Strain rate = 50 mm min^{-1}. (**B**) Surface properties of functional polyethylenes. (Left) Lap-shear adhesion tests of **18b** (2 mol %) and **5b** (2 mol %) as the adhesive interlayers. Error bars represent standard deviation. (Middle) Peel tests of LDPE and **5b**. (Right) Water-contact angles of LDPE and **17a**-*graft*-PEG, and image of aqueous solution of **17a**-*graft*-PEG. (**C**) Rheological measurements. (Left to right) amplitude sweep, frequency sweep, and tan δ plot of LDPE and **1b** (2.5 mol %), respectively. Amplitude sweep frequency fixed at 10 rad s^{-1}, frequency sweep fixed at 0.01% strain, temperature 40°C.

(**20b**), also affect the tensile properties of the resulting materials (Fig. 4A). These examples represent just a small number of the functional polyethylenes accessible by our method but illustrate the ability of a single C–H amination protocol to create materials with varying properties.

Increases in these tensile properties were also observed for *N*-containing polyethylenes generated from waste materials (Fig. 4A). Specifically, incorporation of less than 0.4 mol % benzamidyl groups into waste LDPE (resealable storage bag) or waste HDPE (milk jug) led to a 1.7-fold increase in the toughness of the materials, relative to their respective precursors, in both cases. These examples highlight the opportunities created by our amination process to leverage waste plastics as potential feedstocks for these previously inaccessible materials.

We next investigated the interfacial adhesion of the functional polyethylenes to different metal surfaces, demonstrating the ability of our amination to create materials for potential coating or adhesive applications. To assess the effects of nitrogen-containing groups on adhesive strengths, we performed single-lap-shear tests with aluminum, copper, and stainless steel as substrates (Fig. 4B). All attempts to prepare a lap joint between two metal surfaces with unmodified LDPE (M_n = 2.38 kg mol^{-1}) were unsuccessful, indicating poor adherence of the starting LDPE to these metals. However, many *N*-containing LDPEs created by the amination reaction adhered to aluminum and, notably, other metal surfaces with varying adhesive strengths (Fig. 4B and table S11). Amine-functionalized LDPE **18b**, which contains just 2 mol % amine groups, adhered most strongly to aluminum (5.6 ± 0.7 MPa) and adhered to both copper (2.6 ± 0.3 MPa) and even stainless steel (5.3 ± 0.6 MPa) surfaces. Whereas **18b** adhered more strongly to aluminum, carboxylic acid–containing benzamide **5b** adhered more strongly than **18b** to copper and steel (Fig. 4B).

We also assessed additional surface properties of the functional polyethylenes, such as paintability. Specifically, the paintability of various polyethylene films was evaluated by a peel test (Fig. 4B, Supplementary Materials Section 19). Unfunctionalized LDPE poorly adhered to the applied coating, which was removed by a single peel of Scotch tape. By contrast, the painted image applied to functional LDPE **5b** withstood more than 10 peels of tape. These data creating multiple valuable surface properties highlight the advantages of C–H amination as a platform for the development of polyethylene materials for new applications.

The scope of our C–H amination reaction also enables the augmentation of polymer architectures to achieve other desired properties. Water-based polyolefin formulations are particularly important for coating and adhesive applications (*39*). As shown above, the reaction of functional polyethylene **17a** with modified PEG chains creates graft-polymer architectures. The static water-contact angle of a film of **17a**-*graft*-PEG was measured to be 61 ± 8°, and this material was even soluble in aqueous solutions containing commercial surfactants (dish soap) at concentrations up to 100 mg/mL (Fig. 4B, Supplementary Materials Section 20). Although PEG-grafted polyethylenes have been studied previously (*40*), our method enables access to such materials from polyethylenes possessing varying architectures in just two chemical steps.

Given that the properties of *N*-containing polyethylenes are largely underexplored because of their challenging synthesis, we also sought to investigate the origins of the effects of carbamoyl-based groups on the properties by conducting rheological studies at 40°C, 60°C, and 80°C. At 40°C, the linear viscoelastic region of LDPE **1b** persisted to higher strains than it did in pristine LDPE (Fig. 4C), indicating that the elastic characteristics of **1b** are more pronounced than those of LDPE. In addition, frequency sweeps between 10^{-2} and 10^{2} rad s^{-1} at 40°C showed that the onset of the increase in the loss modulus G'' occurred at a higher frequency for LDPE **1b** than it did for virgin LDPE at 40°C (Fig. 4C). Although the measurements at low frequencies contained significant noise, likely due to environmental fluctuation during the long duration of data acquisition in the low frequency region, the corresponding tan δ plot—which assesses the dampening properties of the polymer—distinguishes the characteristic mechanical responses of the polymers (Fig. 4C). Specifically, the characteristic mechanical response of **1b** clearly occurs at a higher frequency than that of virgin LDPE, based on the trends of the tan δ values. Data obtained across the entire temperature range corroborate this analysis at 40°C; the frequencies of the characteristic mechanical responses of **1b** at 60°C and 80°C were also higher than the corresponding values for LDPE at these temperatures, owing to enhanced bond and chain dynamics at higher temperatures (figs. S24 to S27). These data indicate that benzamidyl-functionalized LDPE **1b** stores more energy during deformation than do the unmodified materials. Considering these rheological data and the results from the tensile tests, we conclude that noncovalent interactions between chains at the sites of functionalization in the *N*-containing LDPEs rearrange to dissipate energy during deformation in the tensile tests and that the enhancement of mechanical properties is tied to the reversibility of these noncovalent interactions within the materials created by the amination chemistry.

Taken together, our results show that catalysts tailored for chemical reactions at the C–H bonds of polyolefins can enable the formation of a diverse set of functional materials that possess valuable properties that can be tuned and combined for desired applications. The modifications we made to our copper catalysts point toward the features of transition-metal catalysts that facilitate reactions in the viscous solution of polyethylene and suppress common side reactions, such as chain scission and cross-linking, and the effect of the carbamoyl-based functional groups show how a single-step amination process can create deep-seated changes in polymer properties. This ability to create diverse properties by low levels of amination should motivate and inform the translation of additional light alkane functionalizations to polyolefin functionalizations as a means to use existing polymers of varying architectures as precursors to create previously inaccessible materials for new applications.

REFERENCES AND NOTES

1. M. Bergmann *et al*., *Science* **376**, 469–470 (2022).
2. N. M. G. Franssen, J. N. H. Reek, B. de Bruin, *Chem. Soc. Rev.* **42**, 5809–5832 (2013).
3. L. S. Boffa, B. M. Novak, *Chem. Rev.* **100**, 1479–1494 (2000).
4. B. P. Carrow, K. Nozaki, *Macromolecules* **47**, 2541–2555 (2014).
5. L. K. Johnson, S. Mecking, M. Brookhart, *J. Am. Chem. Soc.* **118**, 267–268 (1996).
6. A. Kermagoret, A. Debuigne, C. Jérôme, C. Detrembleur, *Nat. Chem.* **6**, 179–187 (2014).
7. C. Tan, C. Zou, C. Chen, *Macromolecules* **55**, 1910–1922 (2022).
8. S. Wu, *Polymer Interface and Adhesion*. (Routledge, 1982).
9. R. J. Ashley, in *Adhesion 12*. (Springer 1988), pp. 239–247.
10. K. Ragaert, L. Delva, K. Van Geem, *Waste Manag.* **69**, 24–58 (2017).
11. J. N. Hahladakis, C. A. Velis, R. Weber, E. Iacovidou, P. Purnell, *J. Hazard. Mater.* **344**, 179–199 (2018).
12. A. Zarrouki, E. Espinosa, C. Boisson, V. Monteil, *Macromolecules* **50**, 3516–3523 (2017).
13. J. J. Filley, T. McKinnon, D. T. Wu, G. H. Ko, *Macromolecules* **35**, 3731–3738 (2002).
14. R. D. Burkhart, N. L. Zutty, *J. Polym. Sci. A* **1**, 1137–1145 (1963).
15. A. W. Waltman, T. R. Younkin, R. H. Grubbs, *Organometallics* **23**, 5121–5123 (2004).
16. S. E. Lehman Jr. *et al*., *Macromolecules* **40**, 2643–2656 (2007).
17. J. K. Leonard, Y. Wei, K. B. Wagener, *Macromolecules* **45**, 671–680 (2012).
18. N. K. Boaen, M. A. Hillmyer, *Chem. Soc. Rev.* **34**, 267–275 (2005).
19. C. M. Plummer, L. Li, Y. Chen, *Polym. Chem.* **11**, 6862–6872 (2020).
20. G. Menendez Rodriguez, M. M. Díaz-Requejo, P. J. Pérez, *Macromolecules* **54**, 4971–4985 (2021).
21. R. L. Tabor, G. M. Lancaster, Z. Jezic, G. P. Young, J. O. Biesser, Maleic anhydride grafts of olefin polymers (US Patent US4950541A, The Dow Chemical Company, 1988).
22. N. Sprang, D. Theirich, J. Engemann, *Surf. Coat. Tech.* **74-75**, 689–695 (1995).
23. T. J. Fazekas *et al*., *Science* **375**, 545–550 (2022).
24. S. A. Bateman, D. Y. Wu, *J. Appl. Polym. Sci.* **84**, 1395–1402 (2002).
25. H. Zhou *et al*., *Macromolecules* **50**, 3510–3515 (2017).
26. B. L. Tran, B. Li, M. Driess, J. F. Hartwig, *J. Am. Chem. Soc.* **136**, 2555–2563 (2014).
27. K. Matyjaszewski, T. E. Patten, J. Xia, *J. Am. Chem. Soc.* **119**, 674–680 (1997).
28. D. M. Haddleton *et al*., *Macromolecules* **32**, 2110–2119 (1999).
29. M. M. Diaz-Requejo *et al*., *Macromolecules* **38**, 4966–4969 (2005).
30. N. K. Boaen, M. A. Hillmyer, *Macromolecules* **36**, 7027–7034 (2003).
31. A. Ray *et al*., *Chem. Commun.* **3388**, 3388–3390 (2005).
32. European Union, COMMISSION REGULATION (EU) 2020/1245 of 2 September 2020 amending and correcting Regulation (EU) No 10/2011 on plastic materials and articles intended to come into contact with food (32020R1245, 2020); https://data.europa.eu/eli/reg/2020/1245/oj.
33. M. Aglietto, R. Bertani, G. Ruggeri, F. Ciardelli, *Makromol. Chem.* **193**, 179–186 (1992).
34. B. Lu, T. C. Chung, *J. Polym. Sci.* **38**, 1337–1343 (2000).
35. N. C. Liu, W. E. Baker, K. E. Russell, *J. Appl. Polym. Sci.* **41**, 2285–2300 (1990).
36. A. Conde *et al*., *J. Am. Chem. Soc.* **135**, 3887–3896 (2013).

37. B. L. Tran, M. Driess, J. F. Hartwig, *J. Am. Chem. Soc.* **136**, 17292–17301 (2014).
38. B. Crist, *Polymer* **44**, 4563–4572 (2003).
39. A. C. Neubauer *et al*., Dispersions of higher crystallinity olefins. (US20100255207A1, Dow Global Technologies LLC, 2010).
40. C. W. S. Yeung *et al*., *Macromolecules* **56**, 815–823 (2023).

ACKNOWLEDGMENTS

We thank B. Abel for use of the TA Discovery DSC 25 and TA Discovery TGA 550 and for helpful discussions. We acknowledge E. Dailing of the LBL Molecular Foundry for his assistance in acquiring GPC chromatograms of polyolefins reported herein. **Funding:** Catalyst development, rheology, and thermomechanical analysis were funded by the US Department of Energy, Office of Science, Office of Basic Energy Sciences, Materials Sciences and Engineering Division, under contract no. DE-AC02-05-CH11231, Unlocking Chemical Circularity in Recycling by Controlling Polymer Reactivity Across Scales program CUP-LBL-Helms. The initial aminations of polyethylene and studies on the scope of amides were supported by BASF through the California Research Alliance (CARA). N.R.C. and J.X.S. gratefully acknowledge the LBL Molecular Foundry (Proposal 7554) for technical and financial support. Work at the Molecular Foundry was supported by the Office of Science, Office of Basic Energy Sciences, of the US Department of Energy under Contract No. DE-AC02-05-CH11231. J.X.S. gratefully acknowledges the National Science Foundation for financial support. S.P. acknowledges the Swiss National Science Foundation for financial support. We acknowledge the UC Berkeley NMR facility and the National Institutes of Health for providing funding for the cryoprobe for the AV-600 spectrometer under grant S10OD024998. **Author contributions:** Conceptualization: N.R.C. and J.F.H. Methodology: N.R.C. Experimental design: N.R.C., C.L.P., E.R., M.E., B.A.H., P.M.B., and J.F.H. Investigation of methodology: N.R.C. and J.X.S. Investigation of material properties: N.R.C., S.P., K.M., and M.H. Writing – original draft: N.R.C. and J.F.H. Writing – Review and Editing: contributions and approval from all authors. **Competing interests:** A patent application (PCT/US2023/015456) has been filed on the process and composition of resulting materials with N.R.C., C.L.P., E.R., M.E., and J.F.H. as inventors. B.A.H. has a financial interest in Cyklos Materials and Sepion Technologies. **Data and materials availability:** All data are available in the main text or the supplementary materials. **License information:** Copyright © 2023 the authors, some rights reserved; exclusive licensee American Association for the Advancement of Science. No claim to original US government works. https://www.sciencemag.org/about/science-licenses-journal-article-reuse

SUPPLEMENTARY MATERIALS

science.org/doi/10.1126/science.adg6093
Materials and Methods
Supplementary Text
Figs. S1 to S179
Tables S1 to S12
References (*41*–*59*)

Submitted 10 January 2023; resubmitted 4 July 2023
Accepted 28 August 2023
10.1126/science.adg6093

PLANT EPIGENETICS

An evolutionary epigenetic clock in plants

N. Yao[1]†, Z. Zhang[2]†, L. Yu[3], R. Hazarika[2], C. Yu[2], H. Jang[1], L. M. Smith[4], J. Ton[4], L. Liu[5], J. J. Stachowicz[6], T. B. H. Reusch[3]*, R. J. Schmitz[1]*, F. Johannes[2]*

Molecular clocks are the basis for dating the divergence between lineages over macroevolutionary timescales (~10^5 to 10^8 years). However, classical DNA-based clocks tick too slowly to inform us about the recent past. Here, we demonstrate that stochastic DNA methylation changes at a subset of cytosines in plant genomes display a clocklike behavior. This "epimutation clock" is orders of magnitude faster than DNA-based clocks and enables phylogenetic explorations on a scale of years to centuries. We show experimentally that epimutation clocks recapitulate known topologies and branching times of intraspecies phylogenetic trees in the self-fertilizing plant *Arabidopsis thaliana* and the clonal seagrass *Zostera marina*, which represent two major modes of plant reproduction. This discovery will open new possibilities for high-resolution temporal studies of plant biodiversity.

Reconstructing the tree of life is a central goal in evolutionary biology. A key challenge is to infer the approximate date when two lineages diverged from each other in the past (*1*, *2*). In addition to fossil and archaeological evidence, molecular clocks have emerged as an important tool to perform such dating (*2*, *3*). Constant-rate clock calibrations such as those originally introduced by Zuckerkandl and Pauling (*4*) are based on the premise that neutral mutations in DNA (or proteins) accumulate at a fixed rate, so that nucleotide differences increase with time. If the mutation rate is known, it becomes possible to deduce the most recent common ancestor (MRCA) of two lineages. Although the modern use of molecular clocks relies on a number of strong modeling assumptions (*5*), in practice, they are often the only means to obtain temporal information for parts of a phylogeny where fossil or archaeological records are lacking (*3*).

The low mutation rate found in most species limits the use of DNA-based clocks. With a rate of ~10^{-9} to 10^{-8} mutations per site per year, these clocks may offer sufficient temporal resolution over larger timescales (~10^4 to 10^8 years) but are less accurate in recent time (<10^3 years from the present), as too few mutations accumulate to permit reliable tree inference and dating (*6*). However, it may be of interest to infer shallow divergence times of just a few decades to hundreds of years, for example, when assessing associations with species range shifts, colonization events, or environmental changes (*7*). In self-fertilizing (selfing) or clonal species with short life cycles, new lineages can diverge rapidly owing to extensive genetic drift, restricted gene flow, and divergent natural selection (*8*). In the recent past, many such events have co-occurred with the emergence of modern civilizations and may in part even be driven by human activities (e.g., migration or trade). To improve the resolution in studying shallow divergences and their timing, a different class of molecular clocks is needed, whose tick rate is orders of magnitude faster than that of DNA. We recently proposed that DNA cytosine methylation could provide a biomolecular basis for such a clock in plants (*9*), but this possibility has not been explored rigorously.

DNA cytosine methylation is a conserved base modification in eukaryotes (*10*). Stochastic enzymatic failure or off-target DNA methyltransferase activity at CG dinucleotides leads to lasting methylation losses or gains (i.e., epimutations) in daughter cells and their descendant cell lineages (*11*). Such CG methylation (mCG) changes have been observed within the lifetime of mammals and have been extensively exploited as a DNA methylation clock of aging (*12*). However, unlike in mammals, many somatically acquired CG epimutations are stably inherited across clonal and sexual generations in plants (*13*–*15*) and thus hold high-resolution information about the evolutionary histories of cell lines or clonal and sibling lineages (*11*, *16*). Estimates in several plant species indicate that CG epimutations are effectively neutral at the genome-wide scale and occur at a rate that is ~10,000 to 100,000 times higher than the genetic mutation rate per unit time (*13*, *14*, *17*–*20*). Here we show that the rapid accumulation of CG epimutations in plant genomes defines a fast-ticking evolutionary clock (henceforth, epimutation clock) that can be used for the reconstruction and dating of phylogenies.

Discovery of clocklike regions in *A. thaliana*

We set out to construct a robust epimutation clock by first searching for genomic regions whose CG epimutation rates are invariant to genetic and environmental perturbations. To do this, we used the selfing plant *Arabidopsis thaliana* as a model to generate mutation accumulation lines (MA lines) from seven diverse natural accessions (genotypes) as founders (Fig. 1A and fig. S1A; and see the materials and methods (*21*)]. These MA pedigrees had a depth of 17 generations with nine whole-genome bisulfite sequencing (WGBS) measurements

[1]Department of Genetics, University of Georgia, Athens, GA, USA. [2]Plant Epigenomics, Technical University of Munich, Freising, Germany. [3]Marine Evolutionary Ecology, GEOMAR Helmholtz Centre for Ocean Research Kiel, Kiel, Germany. [4]School of Biosciences, University of Sheffield, Sheffield, UK. [5]Department of Statistics, University of Georgia, Athens, GA, USA. [6]Department of Evolution and Ecology, University of California, Davis, CA, USA.
***Corresponding author. Email: treusch@geomar.de (T.B.H.R.); schmitz@uga.edu (R.J.S.); f.johannes@tum.de (F.J.)**
†These authors contributed equally to this work.

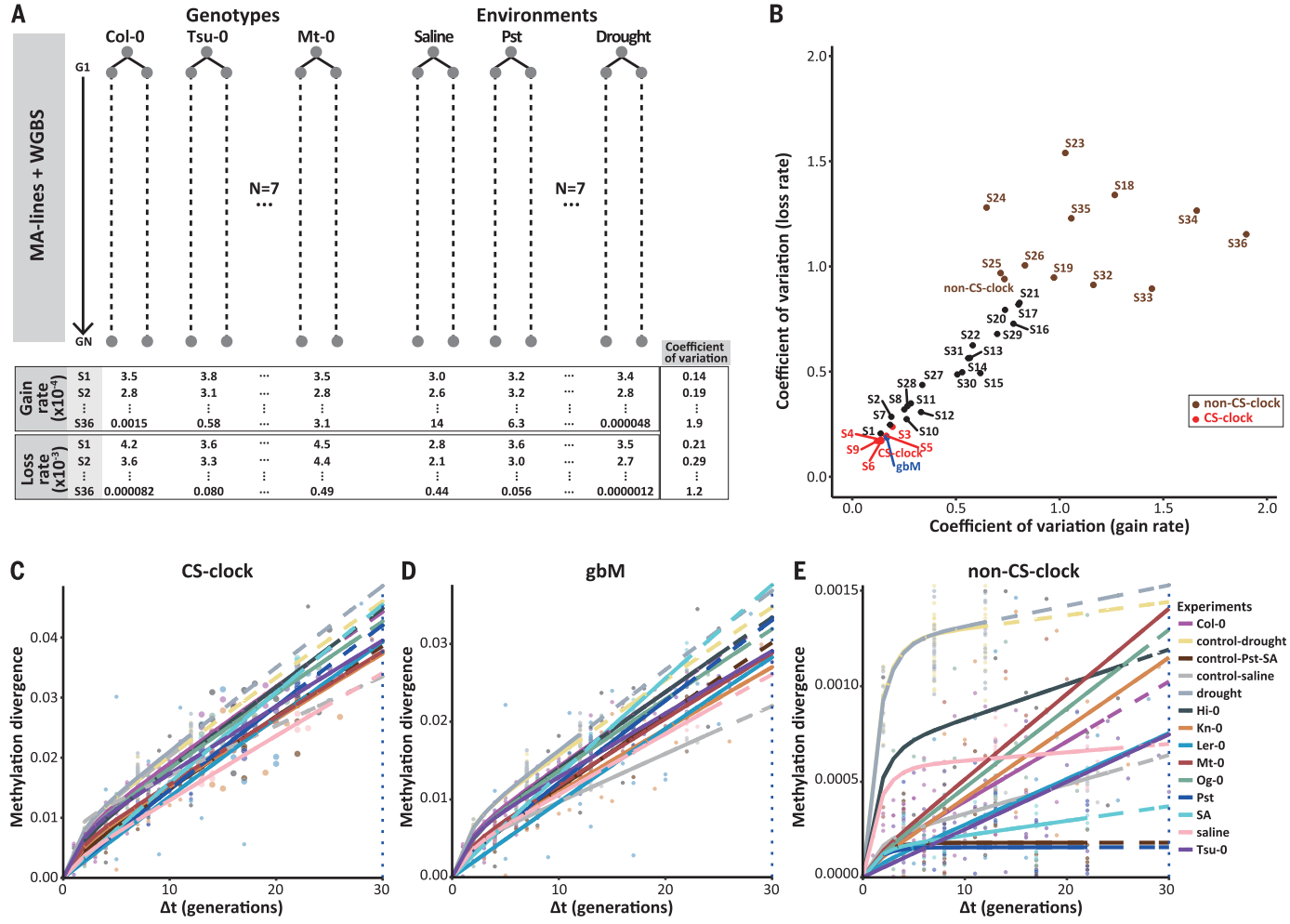

Fig. 1. Discovery of epigenetic clock regions. (**A**) We sought to identify genomic regions whose CG epimutation rates are invariable across genetic and environmental perturbations. To that end, we created seven MA pedigrees in various genetic backgrounds by using different natural accessions as founders (Col-0, Hi-0, Kn-0, Ler-0, Mt-0, Og-0, and Tsu-0). In addition, we generated MA lines grown under biotic stress [repeated exposure to *P. syringae* and salicylic acid (SA)] and combined these data with published MA lines grown under abiotic stress (exposure to high salinity and drought conditions). Using multigenerational WGBS data from these MA lines, we estimated CG epimutation rates in each of 36 annotated *Arabidopsis* chromatin states (CSs). Detailed information about pedigree topologies and WGBS sampling can be found in fig. S1. For each CS, the coefficient of variation (CV) in the gain and loss rates were calculated across pedigrees. (**B**) Low CV for the gain and the loss rates were identified in a cluster of CSs including S3, S4, S5, S6, and S9. Genomic regions indexed by these CSs were defined as epigenetic clock regions ("CS-clock"). For comparison, a cluster of CSs including S18, S19, S23, S24, S25, S26, S32, S33, S34, S35, and S36 displayed high CVs, which were defined as non-clock regions ("non–CS-clock"). (**C** to **E**) CG epimutation accumulation is plotted as a function of divergence time (Δt) for each MA pedigree. Dashed lines indicate model-based extrapolations of mCG divergence for MA lines with a Δt of <30 generations. For CS-clock regions (C), epimutation accumulation patterns were much more invariable across pedigrees than for non–CS-clock regions (E). Epimutation accumulation in gbM genes (D) closely resembled CS-clock regions, indicating that gbM genes can serve as a proxy for an epigenetic clock.

per pedigree, on average (see fig. S1A for details). To evaluate the impact of environmental factors, we also generated *A. thaliana* MA lines grown under biotic stress (repeated exposure to *Pseudomonas syringae* and salicylic acid) and combined these data with published MA lines grown under abiotic stress [exposure to high salinity and drought conditions (*22*, *23*)] (Fig. 1A and fig. S1, B to D). The depth of these latter MA pedigrees varied from 7 to 13 generations and had ~9 WGBS measurements per pedigree.

Epimutation analysis of these different MA lines revealed specific genomic regions whose CG epimutation rates were largely invariable across the 14 different genetic or environmental perturbation experiments (Fig. 1, B to E; fig. S2; tables S1 to S4; and materials and methods). These clocklike regions were in stark contrast with other regions where rates were fivefold more variable on average (Fig. 1B and tables S1 and S5). We found that clocklike regions displayed specific epigenomic features and made up about 16.1% of all CGs in the genome (~896,323 of all CG sites) (Fig. 1B, tables S2 and S3, and fig. S3). The majority of clocklike regions (~60%) were located within gene body methylated (gbM) genes (fig. S3B). In *A. thaliana*, gbM genes compose a subclass of ~5000 genes that display elevated CG methylation (*24*). Although the precise function of gbM genes is unclear, the nucleotide sequences and steady-state methylation levels of these genes are generally conserved across diverse plant species (*25*, *26*). We recently identified these same regions as epimutation hotspots in *A. thaliana* (*27*). Their average epimutation rates exceed the genome-wide average by about one order of magnitude. Hence, the biomolecular properties of these regions form the basis for a robust epimutation clock, whose fast mCG substitution rate can facilitate high-resolution

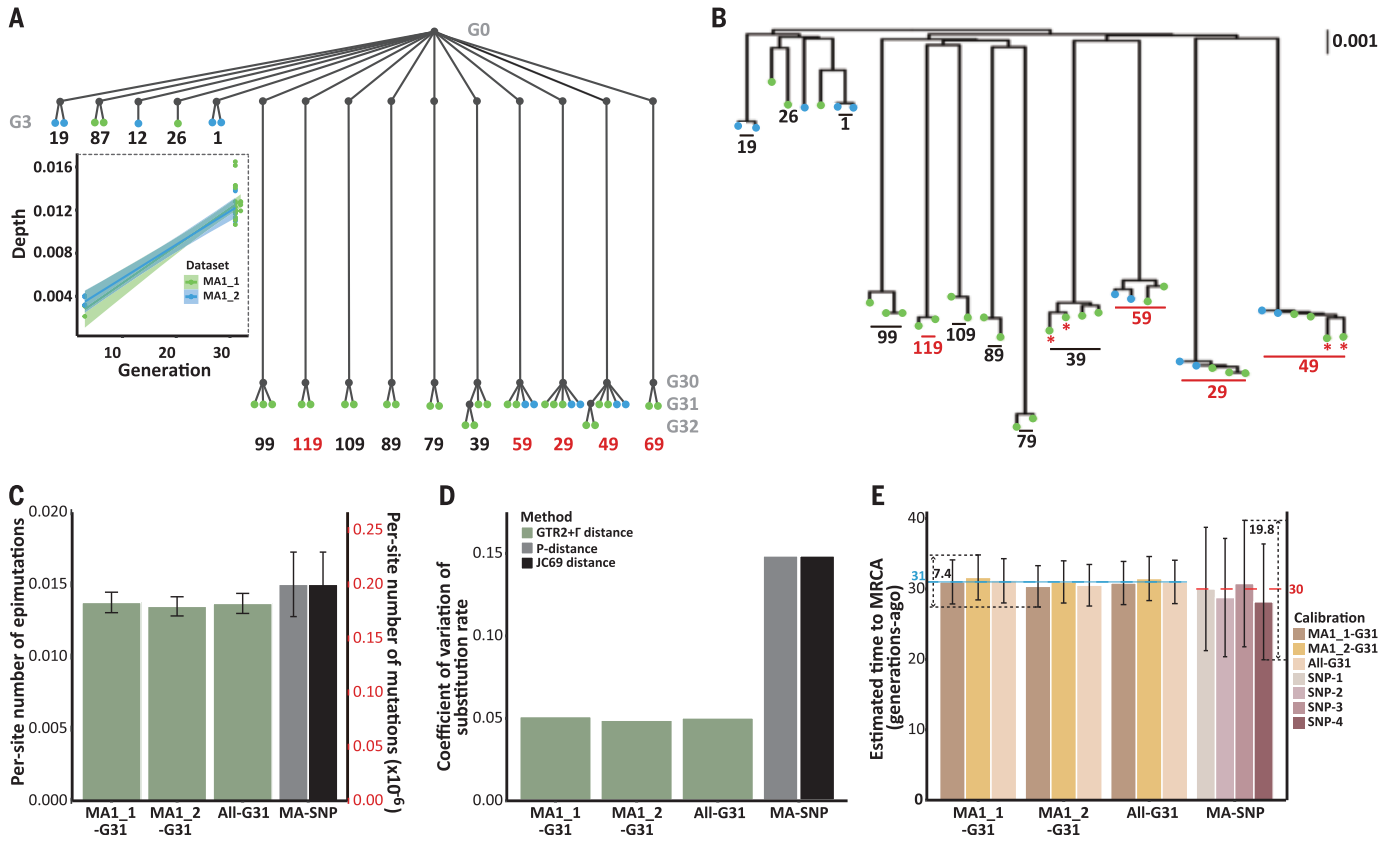

Fig. 2. Evolutionary histories of *A. thaliana* MA lines. (**A**) The MA lines shared a common ancestor and were maintained by single-seed descent for 3, 31, and 32 generations (G3, G31, and G32). Their DNA methylomes were sequenced by Becker *et al*. (*14*) (MA1_1, green dots) and Schmitz *et al*. (*13*) (MA1_2, blue dots) separately. In addition, Ossowski *et al*. (*28*) sequenced the genomes of five G30 individuals from 29, 49, 59, 69, and 119 (orange). (**B**) We inferred the phylogeny of these MA lines using our epimutation clock. The inferred topology recapitulates the known evolutionary relationships among the sequenced samples. The G32 individuals are marked with a red asterisk. (**C**) We estimated the number of accumulated substitutions on each lineage from the phylogeny (i.e., depth of tip node; materials and methods). The error bars represent the SE of accumulated substitutions per lineage. The average depth of G31 individuals is consistent with the clocklike accumulation of epimutations in the different MA lineages. For comparison, the number of SNPs per G30 lineage from the previous study (*28*) is also shown. (**D**) The CV of the estimated substitution rate. The CV of the substitution rate from segregating SNPs is significantly higher than the CV of the substitution rate from the epimutation clock. (**E**) With the estimated substitution rates, we inferred the time to the MRCA. The error bars show 95% CI. The blue line indicates 31 generations. The red dashed line indicates 30 generations. The epimutation clock not only estimates the correct time to the MRCA but also shows higher consistency than the times estimated with segregating SNPs. The SNP-1 is the mean of SNP substitution rates that was calibrated from the SNP phylogeny of the MA lines. SNP-2, SNP-3, and SNP-4 are three published estimates of SNP substitution rates (*28*, *32*).

inference about divergence events in the recent past. Here we use the term "mCG substitution rate" to refer to the number of fixed CG methylation changes that occur over a specific time interval.

Clock calibration and phylogenetic inference in *A. thaliana*

To confirm the existence of such clocklike regions, we analyzed the largest *A. thaliana* MA pedigree available (here named MA1_1 and MA1_2) (*13*, *14*) (Fig. 2A). This MA pedigree features 15 independent lineages with a maximum depth of 32 generations. WGBS samples were available from generations 3, 31, and 32. In total, we detected 46,597 segregating CG epimutations within the clocklike regions after ~31 generations. By contrast, only 99 segregating single-nucleotide polymorphisms (SNPs) were detected genome-wide over this timescale (*28*). This observation shows that epimutations in the relatively small clocklike regions are overall much more abundant than genome-wide SNPs. Using pairwise distances based on the GTR2 substitution model (general time reversible model for binary data; materials and methods), we performed neighbor-joining clustering of the samples on the basis of their mCG status within the clocklike regions and were able to recapitulate the known topology (Fig. 2B). Hence, the rapid accumulation of epimutations is highly informative about divergence events as recent as a few generations ago.

Estimates of the mCG substitution rates were highly consistent across lineages (Fig. 2, C and D), yielding rates of $4.43 \pm 0.229 \times 10^{-4}$ and $4.34 \pm 0.214 \times 10^{-4}$ [± SE; see the supplementary text (*21*) and table S6] for MA1_1-G31 and MA1_2-G31, respectively. We then applied the mean mCG substitution rate of MA1_1-G31 to the methylation data of MA1_2-G31 to infer the time until its MRCA. This estimate indicated that the MRCA lived approximately 30.4 ± 2.94 generations ago [95% confidence interval (CI)] (Fig. 2E, tables S7 and S8, and fig. S4), which is very close to the actual depth of the pedigree (31 generations). By contrast, attempts to date the MRCA using available SNP data from the MA lines were biased and more variable, yielding an estimate of 28.2 ± 8.22 generations (95% CI), an uncertainty of nearly ~29.19% of the total age of the phylogeny (Fig. 2E, table S7, and materials and methods). Together these results indicate that CG epimutations are much more robust and informative over these short timescales than are DNA mutations, a conclusion that is strongly supported

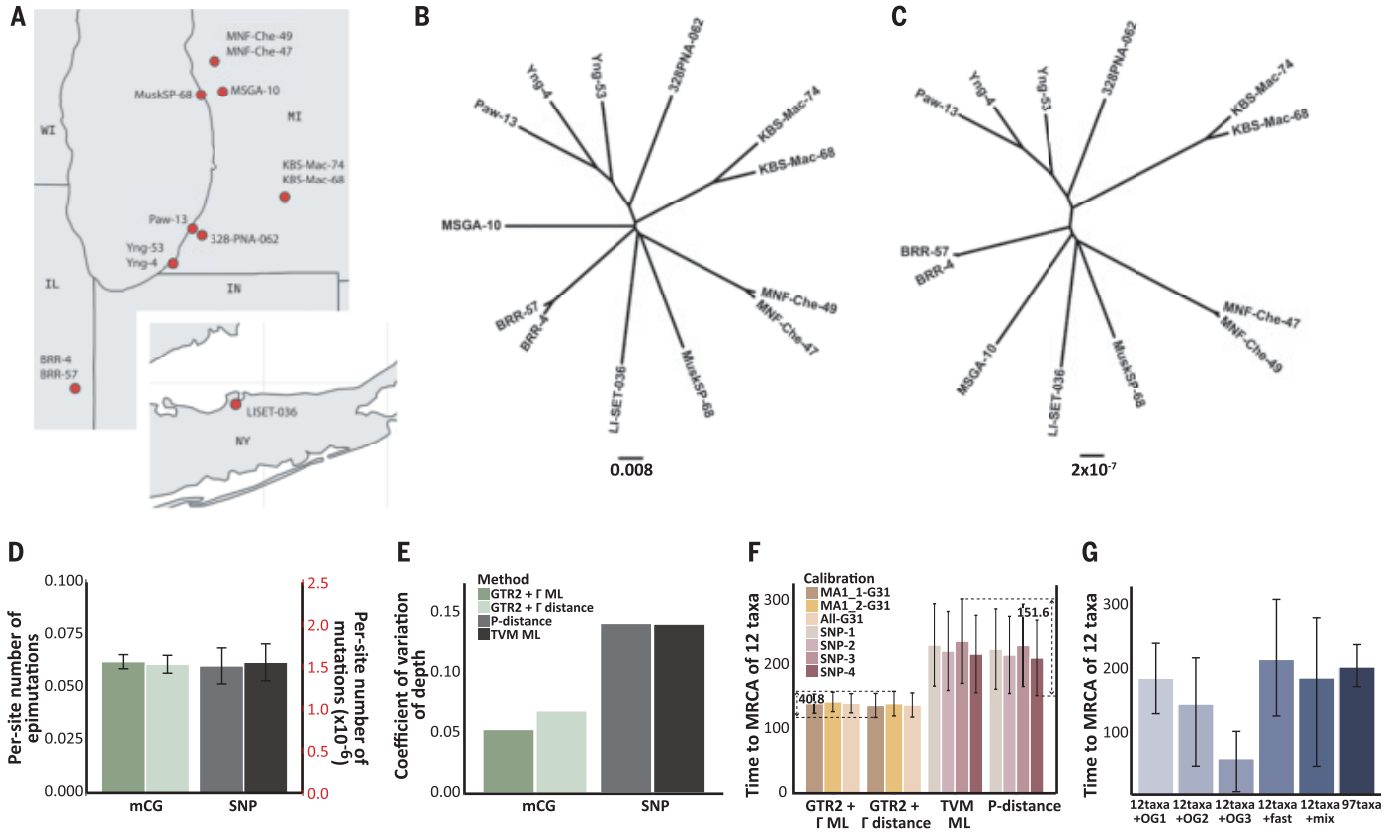

Fig. 3. Evolutionary histories of *A. thaliana* North American accessions. (**A**) We reanalyzed the DNA methylomes of 13 samples from (*30*) and used them for phylogenetic inference. The selected samples all belong to a single haplogroup, HPG1 (*30*, *31*). (**B**) The phylogeny was inferred with the same epimutation clock regions that were used in MA1_1 and MA1_2. (**C**) We reanalyzed the published set of segregating SNPs to generate the phylogeny of North American accessions (*30*). (**D**) The number of substitutions per lineage (± SE). We removed Yng-53, a hybrid taxon (*30*, *32*), and estimated the number of substitutions on the rest of the 12 lineages. (**E**) The coefficient of variation of depth suggests the SNP-based estimation has higher uncertainty than the estimation based on epimutation clock regions. (**F**) The estimated times between a modern taxon and the MRCA of 12 taxa. The error bars indicate 95% CI. All substitution rates of the epigenetic clock, which were calibrated from different data sources, indicate that the MRCA lived in 1864 ± 19 years. However, using four different published substitution rates of SNPs from (*28*, *32*) shows that the MRCA lived between 1700 and 1840 (materials and methods). (**G**) Dating divergence event of 12 taxa with Bayesian tip calibration. We reanalyzed segregating SNPs from a total of 70 modern and 27 herbarium specimen samples from a previous study (*32*). In the phylogeny with all 97 samples, the MRCA of 12 taxa lived between 1769 and 1835 [95% high posterior density interval (HPD); mean: 202 years ago]. However, the phylogenies with only the 12 modern taxa and a part of herbarium specimen samples produced larger HPD intervals. The mean values of the time to the MRCA varied with the sample collection dates and substitution rates on the lineages. Outgroups OG1, OG2, and OG3 are specimens that were collected in the 19th century, 1900–1950, and 1950–1985, respectively. The outgroup "fast" includes six fast-evolving taxa, and the outgroup "mix" has an extra three slow-evolving taxa.

by theoretical arguments and extensive simulation studies (*6*, *29*) (tables S9 and S10 and figs. S5 to S7).

We sought to extrapolate these insights to natural settings. Hagmann *et al.* (*30*) sequenced the genomes and DNA methylomes of 13 *A. thaliana* accessions collected around the Great Lakes and the East Coast of the United States (Fig. 3A), which all belong to the large haplogroup HPG1 (*30*, *31*). As *A. thaliana* is not native to North America, it has been hypothesized that these lineages were introduced with the arrival of the early European settlers (*30*, *32*). The average genetic distance between the 13 lineages and the HPG1 pseudo–reference genome is about 245 nucleotide positions, providing evidence for their close kinship. In line with previous work (*30*, *33*–*36*), clustering accessions based on mCG produced phylogenetic trees nearly identical to those produced by SNP-based clustering, which indicates that they can capture the same evolutionary relationships between lineages (Fig. 3, B and C). Attempts to date the MRCA for 12 nonrecombinant lineages (*30*, *32*) on the basis of the available SNP data and three published SNP substitution rates from mutation accumulation experiments (*28*, *32*, *37*) yielded estimates ranging from the year 1792 ± 59.2 years (95% CI) to 1766 ± 66.2 years (95% CI) (Fig. 3F and table S11). As an alternative method, we also combined SNP data from these 12 taxa (ingroups) with that of different herbarium samples (outgroups) as input for Bayesian tip calibration with BEAST (*38*). The mean values of the estimated divergence time of the 12 taxa ranged from ~1949 to ~1792, depending on the set of herbarium outgroups used (Fig. 3G, table S12, and supplementary text). This extensive uncertainty is partly corroborated by our simulation studies, which indicate that a DNA mutation rate of 10^{-9} would yield large estimation errors for founding events occurring as recently as a few centuries ago (table S9 and supplementary text).

To help resolve the temporal questions about the origin of these lineages, we reanalyzed the WGBS data and applied the experimentally calibrated epimutation clock. Our analysis placed the MRCA of these 12 lineages in the year 1864 ± 19 (95% CI) (Fig. 3, D to F, and table S11). This estimate provides solid evidence for a very recent MRCA. As North American herbarium samples of *A. thaliana* can be found that are older than this date (*32*), our

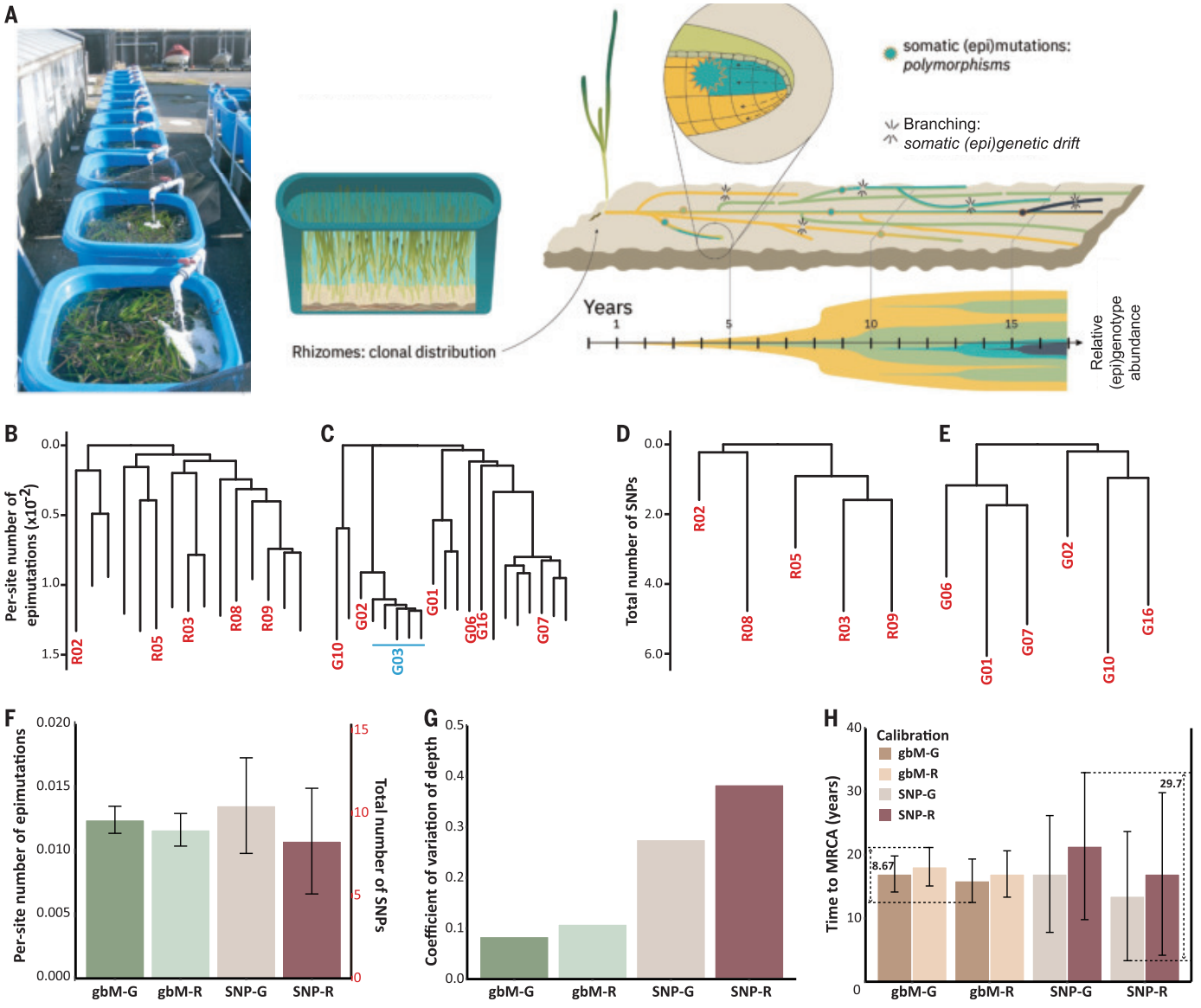

Fig. 4. Evolutionary histories of *Z. marina* experimental clones. (**A**) Two independent *Z. marina* clonal lines were established from Bodega Bay harbor in large tanks under ambient light, temperature, and flow-through of ocean water. They were maintained through clonal reproduction for 17 years. (**B** and **C**) DNA methylomes were sequenced for 15 and 16 ramets of the R and G clones [five technique replicates were generated with the same ramet, G03 (blue)]. Using CG sites within gbM genes as a proxy of the epimutation clock, we inferred the phylogeny of the R and G clones separately. We resequenced genomes from five samples from the R clone and six samples from the G clone. Only 31 and 47 segregating SNPs were identified for clones R and G, respectively. We inferred the phylogeny using the segregating SNPs, and the trees of the R clone and the G clone are shown in (**D**) and (**E**). (**F** and **G**) The average depth of two gbM-based trees is 1.246×10^{-2} and 1.168×10^{-2} with CVs less than 11%. However, the average depth in the SNP trees is much more variable, with CVs of >27%. (**H**) The estimated times to the MRCA were further calibrated with these depths and substitution rates.

results support the notion that these lineages belong to a clade of a larger phylogeny whose breadth has not been sufficiently sampled and/or are the result of serial founding events on this continent. Broader sampling of North American accessions would be necessary to further study the introduction time of *A. thaliana*.

Inference and timing of recent clonal phylogenies in *Z. marina*

The rapid formation and radiation of new plant lineages are particularly prevalent in species with facultative clonal reproduction through the production of runners, stolons, or tillers. These make up an estimated 40% of plant species on Earth (*39*), many of which are of considerable ecological relevance. The marine flowering plant *Zostera marina* is an important example of these. Like most seagrasses, *Z. marina* is the foundation of entire ecosystems (*40*). It has important ecosystem functions in carbon storage, biodiversity enhancement, and coastal protection and is currently being developed as a seagrass genomic model (*41*). Besides sexual reproduction that is carried out entirely under water—including subaqueous pollination—*Z. marina* is distinguished by clones that can grow to several football fields in size (*41*). Previously, the accumulation of somatic genetic variation (in the form of SNPs) has been observed in large mega-clones (*42*). However, a dating of clones less than a decade old is elusive but would be highly useful to elucidate the demographic structure, the longevity, and, ultimately, the vulnerability of seagrasses to a changing ocean environment.

To demonstrate that the epimutation clock is a powerful tool for the reconstruction and dating of clonal phylogenies over short timescales, we took advantage of two *Z. marina* clones that had been cultured since 2004 for ecological experiments in Bodega Bay harbor, California (materials and methods, supplementary text, and tables S13 and S14). These two clones (clone R and clone G) were initiated and propagated independently from each other in large tanks under ambient light, temperature, and flow-through of ocean water (Fig. 4A). Sixteen ramets were sampled from each clone in 2021, corresponding to a clonal age of 17 years (materials and methods). WGBS was performed for 15 ramets of clone R, as one ramet did not belong to this clone (*43*). As for clone G, all 16 ramets were sequenced using WGBS, and technical replicates were generated by sequencing five aliquots of one sample independently (materials and methods). As extensive epigenomic information is lacking for the de novo identification of clocklike regions in *Z. marina*, we used gbM genes as a proxy of the epimutation clock (materials and methods, figs. S4 and S8, and table S8). For comparison, we also generated deep (100×) resequencing data for SNP identification in a subset of these ramets (materials and methods).

Our analysis revealed that the clones have generated 20,713 (clone R) and 21,008 (clone G) fixed CG methylation changes in gbM genes over the course of 17 years, on average, compared with only 31 and 47 fixed SNP changes, respectively (materials and methods). Again, this constitutes a large excess of epimutations relative to SNPs per unit of time, even though the effective genome size of the former is orders of magnitude smaller. Although the true clonal phylogeny is unknown in this experiment, an epimutation clock–based analysis revealed high-confidence phylogenetic trees in both clones (Fig. 4, B and C, and supplementary text). We were unable to recapitulate the phylogenetic trees using fixed SNPs (Fig. 4, D and E). Instead, we observed that the bootstrap support values in the SNP-based trees were low (~0.6; supplementary text), which indicates that there is little phylogenetic information in the few SNPs captured among clonal ramets over these timescales.

To assess our ability to date the clones on the basis of DNA methylation data, we calibrated our epimutation clock in clone R, using its known age of exactly 17 years (Fig. 4, F to H, and materials and methods). Application of the calibrated clock to the phylogenetic tree of clone G estimates the MRCA at 18.14 ± 3.01 years ago (95% CI), which aligns well with the actual founding date of this clone (Fig. 4H and table S15). Applying the same approach using fixed SNPs led to variable estimates of 21.39 ± 11.59 years ago (95% CI), an uncertainty of one decade over this short timescale (Fig. 4H).

Discussion and outlook

The existence of a fast-ticking evolutionary epigenetic clock in plants opens previously unexplored research avenues at the interface between evolutionary biology and ecology (*9*). Our proof-of-principle study focused on the application of this clock to the reconstruction and dating of shallow intraspecies phylogenies that arise within clonal or selfing species over short timescales. The use of epimutation clocks may be extended to plant species with longer life cycles, as the necessary clock calibration could rely on DNA methylation data from F2 intercrosses rather than from mutation accumulation lines. A promising extension of our work would be to combine the clocklike regions with modified coalescent methods to infer recent demographic changes (i.e., bottlenecks) and selection at the population level. The rapid rate at which epigenetic diversity arises within the clocklike regions will facilitate unprecedented temporal resolution. This information can shed new light on microevolutionary questions that have been challenging to resolve, such as the timing of the introduction of invasive species, the rate of poleward and upslope spread of species after the retreat of the Pleistocene glaciers, and the consequences of anthropogenic activities for population divergence. In an era of climate change, plant biodiversity is transforming at a fast pace. The ability to monitor rapid population dynamics at the molecular level will help us gauge the fate of this diversity going forward.

REFERENCES AND NOTES

1. S. Kumar, S. B. Hedges, *Mol. Biol. Evol.* **33**, 863–869 (2016).
2. E. Zuckerkandl, L. B. Pauling, in *Horizons in Biochemistry*, M. Kasha, B. Pullman, Eds. (Academic Press, 1962), pp. 189–225.
3. S. Kumar, *Nat. Rev. Genet.* **6**, 654–662 (2005).
4. E. Zuckerkandl, L. Pauling, in *Evolving Genes and Proteins*, V. Bryson, H. J. Vogel, Eds. (Academic Press, 1965), pp. 97–166.
5. S. Y. W. Ho, S. Duchêne, *Mol. Ecol.* **23**, 5947–5965 (2014).
6. Z. Yang, *Syst. Biol.* **47**, 125–133 (1998).
7. P. Pyšek, D. M. Richardson, *Annu. Rev. Environ. Resour.* **35**, 25–55 (2010).
8. S. C. H. Barrett, R. I. Colautti, C. G. Eckert, *Mol. Ecol.* **17**, 373–383 (2008).
9. N. Yao, R. J. Schmitz, F. Johannes, *Trends Genet.* **37**, 699–710 (2021).
10. S. Feng *et al*., *Proc. Natl. Acad. Sci. U.S.A.* **107**, 8689–8694 (2010).
11. F. Johannes, R. J. Schmitz, *New Phytol.* **221**, 1253–1259 (2019).
12. S. Horvath, K. Raj, *Nat. Rev. Genet.* **19**, 371–384 (2018).
13. R. J. Schmitz *et al*., *Science* **334**, 369–373 (2011).
14. C. Becker *et al*., *Nature* **480**, 245–249 (2011).
15. A. Wibowo *et al*., *Proc. Natl. Acad. Sci. U.S.A.* **115**, E9145–E9152 (2018).
16. A. Vidalis *et al*., *Genome Biol.* **17**, 264 (2016).
17. A. van der Graaf *et al*., *Proc. Natl. Acad. Sci. U.S.A.* **112**, 6676–6681 (2015).
18. Y. Shahryary *et al*., *Genome Biol.* **21**, 260 (2020).
19. J. Denkena, F. Johannes, M. Colomé-Tatché, *Heredity* **127**, 190–202 (2021).
20. B. T. Hofmeister, K. Lee, N. A. Rohr, D. W. Hall, R. J. Schmitz, *Genome Biol.* **18**, 155 (2017).
21. Materials and methods are available as supplementary materials.
22. C. Jiang *et al*., *Genome Res.* **24**, 1821–1829 (2014).
23. D. R. Ganguly, P. A. Crisp, S. R. Eichten, B. J. Pogson, *Plant Physiol.* **175**, 1893–1912 (2017).
24. R. K. Tran *et al*., *Curr. Biol.* **15**, 154–159 (2005).
25. S. Takuno, B. S. Gaut, *Mol. Biol. Evol.* **29**, 219–227 (2012).
26. S. Takuno, B. S. Gaut, *Proc. Natl. Acad. Sci. U.S.A.* **110**, 1797–1802 (2013).
27. R. R. Hazarika *et al*., *Nat. Plants* **8**, 146–156 (2022).
28. S. Ossowski *et al*., *Science* **327**, 92–94 (2010).
29. S. Klopfstein, T. Massingham, N. Goldman, *Syst. Biol.* **66**, 769–785 (2017).
30. J. Hagmann *et al*., *PLOS Genet.* **11**, e1004920 (2015).
31. A. Platt *et al*., *PLOS Genet.* **6**, e1000843 (2010).
32. M. Exposito-Alonso *et al*., *PLOS Genet.* **14**, e1007155 (2018).
33. R. J. Schmitz *et al*., *Nature* **495**, 193–198 (2013).
34. V. N. Ibañez *et al*., *J. Evol. Biol.* **36**, 663–674 (2023).
35. I. Sammarco *et al*., Research Square [Preprint] (2023); https://doi.org/10.21203/rs.3.rs-2642365/v1.
36. J. Xu *et al*., *Genome Biol.* **20**, 243 (2019).
37. M.-L. Weng *et al*., *Genetics* **211**, 703–714 (2019).
38. M. A. Suchard *et al*., *Virus Evol.* **4**, vey016 (2018).
39. O. Honnay, B. Bossuyt, *Oikos* **108**, 427–432 (2005).
40. R. K. F. Unsworth, L. C. Cullen-Unsworth, B. L. H. Jones, R. J. Lilley, *Science* **377**, 609–613 (2022).
41. J. L. Olsen *et al*., *Nature* **530**, 331–335 (2016).
42. L. Yu *et al*., *Nat. Ecol. Evol.* **4**, 952–962 (2020).
43. L. Yu, J. J. Stachowicz, K. DuBois, T. B. H. Reusch, *Mol. Ecol. Resour.* **23**, 592–600 (2023).
44. N. Yao, schmitzlab/Evolutionary-epigenetic-clock: First release, version 1.0.0, Zenodo (2023); https://doi.org/10.5281/zenodo.8109580.

ACKNOWLEDGMENTS

We thank J. Anderson, A. Sweigart, K. Dyer, J. Leebens-Mack, and D. Weigel for useful comments, M. Expósito-Alonso for the SNP data, and S. Landis (www.scienstration.com) for help preparing the figures. **Funding:** T.B.H.R. acknowledges support from the HFSP project (PI TBHR; ADAPTASEX; RGP42/2020). R.J.S. acknowledges support from the National Science Foundation (MCB-2242696) and the National Institutes of Health (R01GM134682). F.J. acknowledges support from the Deutsche Forschungsgemeinschaft (DFG). F.J., R.H., and R.J.S. acknowledge support from the Technical University of Munich Institute for Advanced Study, funded by the German Excellence Initiative and the European Seventh Framework Programme under grant agreement no. 291763. J.J.S. acknowledges support from the National Science Foundation (OCE 1829976). Z.Z. and L.Y. hold fellowships from the China Scholarship Council (no. CSC202006380020 and no. CSC201704910807, respectively). J.T. acknowledges support from a consolidator grant of the European Research Council (ERC; no. 309944 "Prime-A-Plant") and a Research Leadership Award from the Leverhulme Trust (no. RL-2012-042). **Author contributions:** F.J. and R.J.S. conceived of the project. N.Y. developed phylogenetic models that incorporate epimutations, with support from L.L. Z.Z. analyzed WGBS data and identified clocklike regions. R.H., L.Y., C.Y., and H.J. analyzed data. L.M.S., J.T., and R.J.S. produced MA lines. J.J.S. collected and produced *Z. marina* clones, and L.Y. and T.B.H.R. produced *Z. marina* WGBS and SNP data. F.J., R.J.S., Z.Z., and N.Y. wrote the manuscript, with contributions from all authors. **Competing interests:** The authors have no competing interests to declare. **Data and materials availability:** The *A. thaliana* sequence data are located in NCBI Gene Expression Omnibus (MA accessions, GSE223810; and MA-Pst, MA-SA, and MA-control-Pst&SA, GSE223861). *Z. marina* WGBS sequence data are located in NCBI Sequence Read Archive under BioProject numbers PRJNA933356, PRJNA943354, and PRJNA943356. Code is located in GitHub (https://github.com/schmitzlab/Evolutionary-epigenetic-clock) and Zenodo (*44*).

License information: Copyright © 2023 the authors, some rights reserved; exclusive licensee American Association for the Advancement of Science. No claim to original US government works. https://www.science.org/about/science-licenses-journal-article-reuse

SUPPLEMENTARY MATERIALS

science.org/doi/10.1126/science.adh9443
Materials and Methods
Supplementary Text
Figs. S1 to S8
Tables S1 to S15
References (*45*–*86*)
MDAR Reproducibility Checklist

Submitted 24 March 2023; accepted 8 August 2023
10.1126/science.adh9443

GEOLOGY

A Bayesian inversion for emissions and export productivity across the end-Cretaceous boundary

Alexander A. Cox* and C. Brenhin Keller

The end-Cretaceous mass extinction was marked by both the Chicxulub impact and the ongoing emplacement of the Deccan Traps flood basalt province. To understand the mechanism of extinction, we must disentangle the timing, duration, and intensity of volcanic and meteoritic environmental forcings. In this study, we used a parallel Markov chain Monte Carlo approach to invert for carbon dioxide (CO_2) and sulfur dioxide (SO_2) emissions, export productivity, and remineralization from 67 to 65 million years ago using the LOSCAR (Long-term Ocean-atmosphere-Sediment CArbon cycle Reservoir) model. Our results closely match observed and proxy data and suggest decoupled CO_2 and SO_2 emissions, a two-step decline in export productivity with a protracted recovery, and no clear volatile impulse at the boundary. More broadly, our methods provide a potential path forward for efficient parallel inversion of complex Earth system models.

Four of the five mass extinction events in the Phanerozoic have been causally and temporally linked to large-scale volcanism in the form of continental flood basalts (*1*–*5*), a link generally thought to be mediated by volcanic volatiles such as CO_2 and SO_2. However, even though radiometric age constraints of flood basalts are sufficient to temporally link them with corresponding extinctions and perhaps estimate a bulk eruptive rate (*1*), substantial uncertainties persist. These include uncertainty regarding the detailed timing and tempo of eruptive and especially non-eruptive degassing, as well as uncertainties in the volatile budget of the magma, the degassing efficiency thereof, and associated metamorphism—all of which make it difficult to disentangle the exact mechanisms of extinction on timescales of less than 100 thousand years (kyr) (*1*, *6*, *7*). Furthermore, because flood basalts are far from the only cause of large-scale ecosystem change, many other planetary-scale disturbances have been proposed as agents of extinction, including large bolide impacts (*8*). The most notable mass extinction with two potential drivers is the end-Cretaceous [Cretaceous/Paleogene (K/Pg)] event, which resulted in the demise of all large tetrapods and non-avian dinosaurs (*9*). This extinction coincides with both Deccan Traps volcanism, which spanned approximately 66.3 million years ago (Ma) to 65.5 Ma (*10*–*12*), and the Chicxulub asteroid impact (*8*, *13*, *14*), whose ejecta deposits are found globally at sections that record the K/Pg boundary (66.052 ± 0.008/0.043 Ma) (*15*). Although the chronology of these events in relation to the boundary is relatively well understood, their respective roles as sole or joint causes of extinction in the context of a changing climate system (*16*) is still a subject of debate.

The emission of climate-active volatiles such as CO_2 and SO_2 has been proposed as a causal factor in both the impact and volcanism models of extinction (*17*), so learning the relative magnitude and timing of volatile emissions is crucial to understanding the K/Pg extinction from both perspectives. The asteroid impact is hypothesized to have caused a sudden heat stress on the environment resulting from molten ejecta followed by a prolonged impact winter (*14*, *18*), as well as ocean acidification and climate change due to the release of volatiles from the carbonate and anhydrite target rock (*17*, *19*). Artemieva *et al.* (*19*) estimate that about 425 billion tons (Gt) of CO_2, 325 Gt of SO_2, and

Department of Earth Sciences, Dartmouth College, Hanover, NH 03755, USA.
*Corresponding author. Email: ac.gr@dartmouth.edu

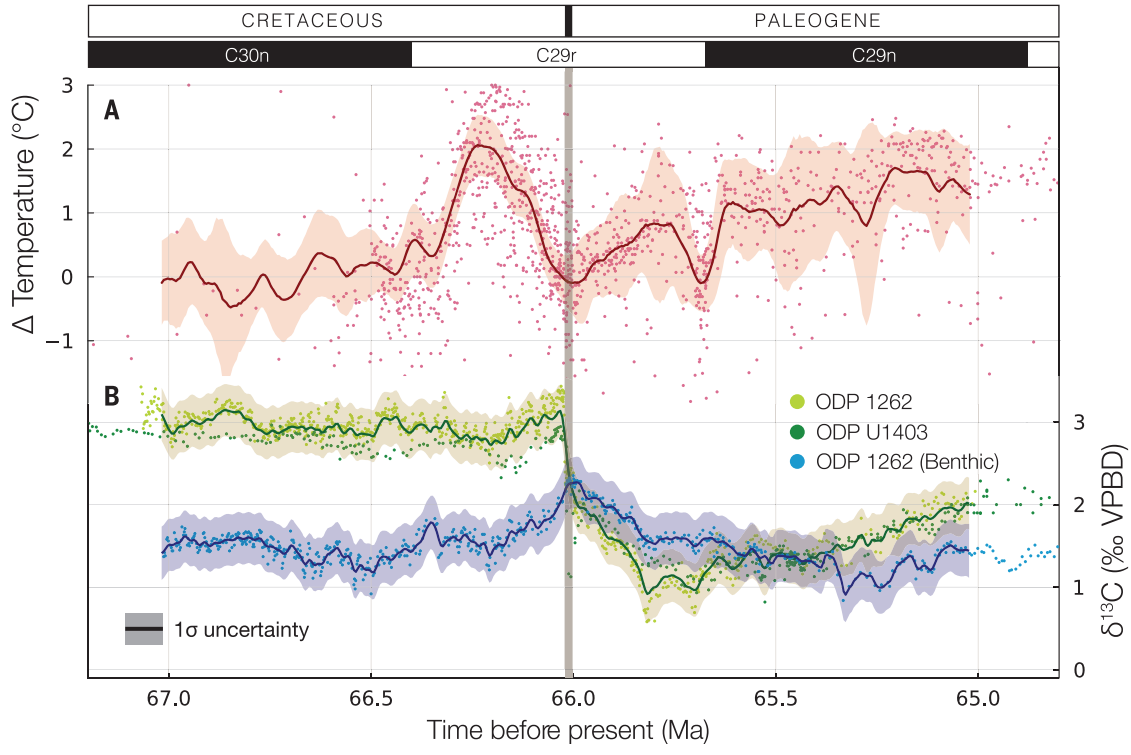

Fig. 1. Paleoenvironmental data. (**A**) Temperature records from marine sediments, marine carbonates, and terrestrial proxies from (*17*). Unweighted bootstrap resampling on these records with a bin width of 5000 years was performed 10,000 times on these data to create a trend line with an associated 2 standard deviation uncertainty (shown by shaded lines). (**B**) Carbon isotope dynamics from bulk carbonates [Ocean Drilling Program (ODP) site 1262 and ODP site U1403], which represent surface-ocean conditions, and benthic foraminifera (deep ocean), bootstrapped resampled 10,000 times using 5000-year time bins. C30n, C29r, and C29n refer to magnetic polarity chrons of the geomagnetic polarity time scale (GPTS). VPBD, Vienna Pee Dee belemnite.

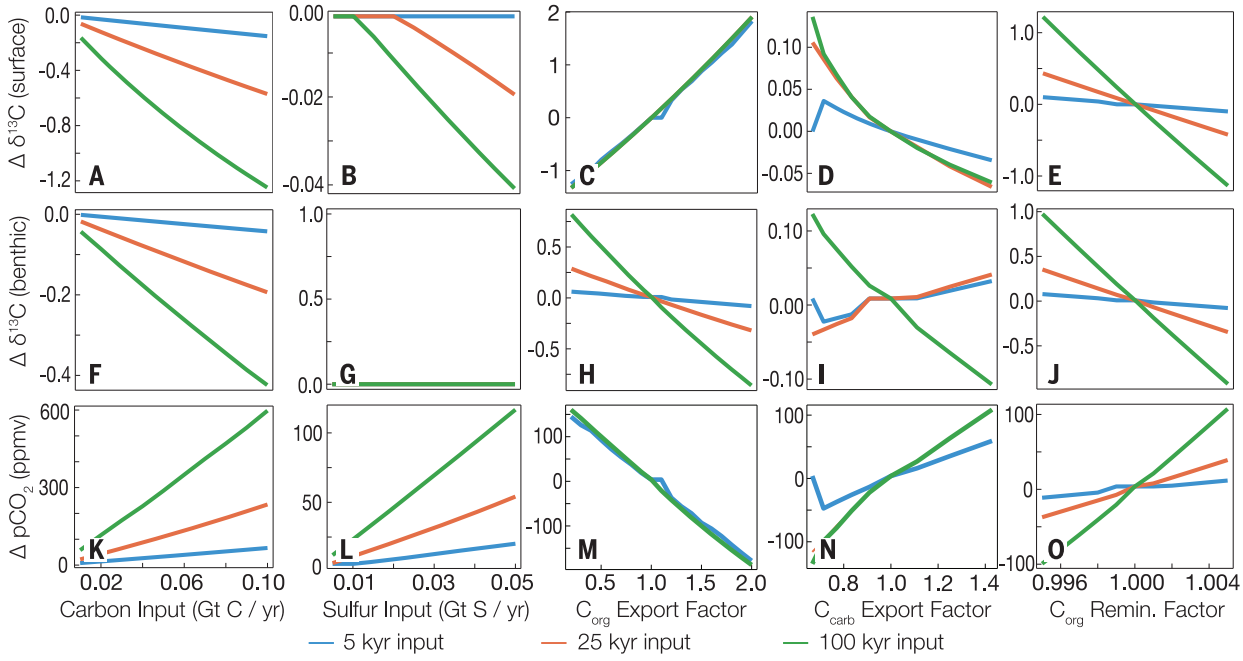

Fig. 2. Model sensitivity. Keeping every other input constant, in turn, these graphs show the relative impact of 5, 25, and 100 kyr pulses of the five LOSCAR input parameters on the three output values, surface $\delta^{13}C$ (**A** to **E**), benthic $\delta^{13}C$ (**F** to **J**), and atmospheric pCO_2 (**K** to **O**). For each test, the model was spun up to steady state for 2 million years, at which time the pulse was applied, and the maximum deviation of the output parameter was recorded before the model returned to steady state after a further 2 million years. ppmv, parts per million by volume; Remin., remineralization.

<50,000 km^3 of ejecta were released instantaneously upon impact. The relatively short residence time of sulfate aerosols (*20*) and dust in the atmosphere suggests a short-lived impact winter, with the CO_2 causing a more protracted effect on the global carbon cycle, which lasted around 5000 years, and disturbing an ecosystem already perturbed by Deccan volcanism (*21*). Both U-Pb and $^{40}Ar/^{39}Ar$ geochronology have constrained the timing of the Deccan Traps (*10*, *11*), although the volume of lava erupted before and after the boundary is still uncertain and depends on where the boundary is placed within the stratigraphic section of the Western Ghats (*11*, *12*). In total, about 1.3 million km^3 of basalt was erupted throughout the province (*22*), with one estimate suggesting between 4100 and 9500 Gt of carbon degassed, along with 3200 to 8500 Gt of sulfur (*23*). However, the weight percent of volatile gases in magmas may vary both between and within volcanic provinces (*24*) as may the CO_2:SO_2 ratio of the degassed volatiles (*25*). Indeed, much degassing in modern volcanic systems is noneruptive (passive), in which case, CO_2:SO_2 ratios vary systematically as a function of the depth of the magma chamber(s) from which volatiles are degassing (*25*–*27*). Such phenomena should not be absent from continental flood basalts. Consequently, the timelines of volcanic CO_2 and SO_2 emissions may be distinct and may both diverge from the underlying rate of basalt eruption.

Although the gas inputs are unknown, a high-resolution chronology exists of the changing pelagic and benthic carbon cycle from $\delta^{13}C$ values from foraminifera and other carbonates in ocean drill cores (*17*). This chronology forms an imperfect but improving record of paleoclimate from numerous marine and terrestrial climate proxies including marine carbonate $\delta^{18}O$ (Fig. 1, A and B). Previous studies have proposed gaseous emissions and changes in carbon export for the million years spanning the boundary and have used a carbon cycle model to assess their viability as a solution by comparing the calculated isotopic values to the fossil record (*17*, *24*, *28*). A commonly used model is the Long-term Ocean-atmosphere-Sediment CArbon cycle Reservoir (LOSCAR) model, which consists of four ocean basins (Atlantic, Indian, Tethys, and Pacific) at three depths, a high-latitude ocean, and atmosphere and sediment modules (*29*). However, forward modeling is necessarily constrained to the number of scenarios proposed, and the full gamut of potential solutions to the environmental conditions across the K/Pg boundary is only explored by using a more agnostic inverse modeling approach.

Inverse modeling

Because we have no a priori reason to impose any constraints on the timing of emissions at or around the boundary, we modify the LOSCAR model to accept continuously variable inputs of carbon and sulfur in 5000-year time bins from 67.0 to 65.0 Ma (the same bin width as the bootstrapped data) (Fig. 1). These time series (and time series of other biological changes described below) form a set of LOSCAR input parameters φ for which we invert in our Bayesian inverse model. We assign a prior distribution for the total amount of carbon emitted (normal distribution with mean and standard deviation of 25,000 Gt) and for the ratio of C:S (normal distribution with a mean of 2 and a standard deviation of 1), to avoid underdetermining our model system. The input parameters are given to the LOSCAR model, and we calculate a log-likelihood function $l(\varphi|y)$, which reflects how accurately this input can generate outputs of $\delta^{13}C$ and partial pressure of carbon dioxide (pCO_2) matching the observed values y (Fig. 1). Then, using a Markov chain Monte Carlo approach, we apply stepwise perturbations of random position and amplitude to the initial inputs to create a new set of inputs φ', with a corresponding log-likelihood $l(\varphi'|y)$. If the likelihood $l(\varphi'|y) > l(\varphi|y)$, then the new proposal is accepted with probability 1. Otherwise, the proposal is accepted with a probability equal to the ratio of the likelihoods. The log-likelihood estimator will eventually converge toward a correct solution after a suitable number of iterations, from which we can obtain a posterior distribution for these parameters that reflects the combination of our prior knowledge and the information we gained from the LOSCAR model outputs.

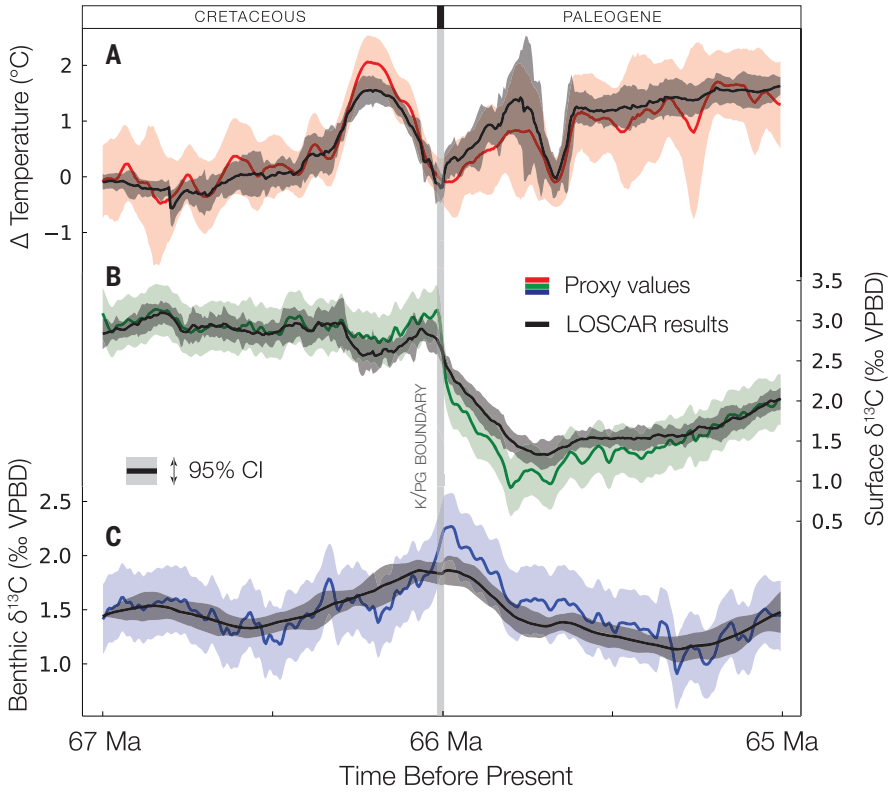

Fig. 3. Comparison of model outputs with paleoenvironmental data. After 10 separate runs of the parallel MCMC algorithm, the mean outputs of temperature deviation from late-Cretaceous values (**A**) and surface (**B**) and benthic (**C**) $\delta^{13}C$ were recorded for 10,000 sets of input parameters post-convergence, and their associated 95% credible interval was calculated. They are compared with the proxy and observed data from Fig. 1, spanning 2 million years, from 67 to 65 Ma.

Because one run of the LOSCAR model with variable inputs can take between 5 and 15 min, reaching convergence is not feasible using the serial MCMC algorithm. Therefore, we use a parallel implementation of the Metropolis algorithm (*30*), which includes elements of replica exchange (also known as parallel tempering) (*31*, *32*). By this method, cores can simultaneously run different proposals and at every iteration exchange their current states according to their relative log-likelihood. Parallelizing the MCMC algorithm results in an orders-of-magnitude speedup in convergence, allows for more potential solutions to be explored, and reduces the likelihood of the algorithm converging on a local maximum (*33*, *34*). While we do not prevent our model from exploring arbitrarily complicated inputs up to the model resolution of 5000 years, our inversion results are largely smooth given that our bootstrap-resampled means for $\delta^{13}C$ and temperature are smooth, and our proposal distribution perturbs in a piecewise-continuous fashion (*34*). Our approach may be considered as a weak form of regularization that diminishes as the number of steps in the Markov chain increases, which we do in lieu of an explicit smoothness constraint on the model output or input.

Biological and biogeochemical changes

Given the expected biotic and biogeochemical changes from 67.0 to 65.0 Ma apart from volatile input, we also allow the inversion to continuously vary the export of organic and carbonate carbon (C_{org} and C_{carb}, respectively) from the surface to the deep ocean and the remineralization of organic carbon at shallow and intermediate depth (C_{remin}, where the ratio of intermediate to other-depth remineralization is set at 80:20), all relative to an arbitrary pre-extinction value of 1.0, which is the initial proposal. We also invert for the CO_2 doubling rate, which we allow to vary freely from an initial guess of 3° of warming per doubling. Physically or chemically implausible proposals will be rejected by the LOSCAR solver, which imposes a further indirect smoothness constraint on our final inversion results (*34*).

In total, we invert for five parameters around the K/Pg boundary, which change the atmospheric and ocean carbon cycle system in different ways and impose two priors. CO_2 degassed from depth and emitted by volcanoes will have a $\delta^{13}C$ value of ~−5 per mil (‰), causing a depletion in surface-ocean $\delta^{13}C$ values and decreasing ocean alkalinity, as well as raising the atmospheric pCO_2 levels (Fig. 2, A, F, and K), until this CO_2 is consumed by silicate weathering to reattain a steady state pCO_2 of 600 parts per million (ppm). Following CO_2 perturbations, LOSCAR uses a steady-state atmospheric pCO_2 value of 600 ppm to adjust the silicate weathering feedback to maintain a mass balance of long-term carbon cycle fluxes on a timescale of 10^5 to 10^6 years (*29*). Similarly, SO_2 gas decreases ocean alkalinity, which in turn further raises the atmospheric pCO_2 (Fig. 2L). Additionally, we directly account for aerosol cooling of the atmosphere, which occurs when volcanogenic sulfur is converted to high-albedo atmospheric sulfate particles. Although the plume height and convection of sulfate is controlled by latitude and local environmental factors (*35*), we assume that the volcanic sulfur that causes a decrease in ocean alkalinity also makes it to the stratosphere, because the lava flows cause large-scale convection (*36*). The decrease in planetary albedo as a function of stratospheric sulfur injections has been studied in the modern era with the eruption of Mount Pinatubo in 1991 (*37*). Here, we treat SO_2 degassing as piecewise-continuous over each 5000-year timestep, in which case, the change in temperature ΔT (K) will be related to the amount of sulfur emitted

$$\Delta T = -11.3 \cdot \left(1 - e^{-5.18x}\right)$$

where x is the rate of sulfurous gas released in gigatons of sulfur per year. Our initial proposal involves emitting 0.02 and 0.01 Gt/year of carbon and sulfur, respectively, continuously from 66.8 to 65.2 Ma. The export of organic carbon (C_{org} export) from the surface to the deep ocean, known as the biological carbon pump, takes organic carbon [with a characteristic $\delta^{13}C$ of between −20 and −30‰ (*38*)] to the deep ocean through a wide range of gravitational and eddy-based pumps (*39*). A relative increase in C_{org} export implies that either the ocean is more biologically productive, because phytoplankton fix dissolved inorganic carbon to organic carbon, which then rains out (*40*), or export efficiency is increased, although both can happen in concert. Regardless, more C_{org} export increases the gradient between surface and benthic $\delta^{13}C_{carb}$ values and vice versa (Fig. 2, C and H). Conversely, an increase in C_{carb} export from surface to deep ocean will collapse the gradient (Fig. 2, D and I). Together, the rain ratio (the ratio of organic carbon to calcite export to the deep ocean) is an indicator of biological productivity and also influences the atmospheric pCO_2, as organic carbon burial sequesters CO_2 and the precipitation of calcite returns CO_2 to the atmosphere (*41*) (Fig. 2, M and N).

The final parameter we invert for, C_{org} remineralization, is a sink of oceanic O_2 and a

source of CO_2. Remineralization also reduces the $\delta^{13}C_{carb}$ values at all depths at which remineralization occurs (Fig. 2, E, J, and O). Together, these biological, biogeochemical, and gaseous parameters comprehensively describe the biotic and abiotic carbon cycle and can work together in concert to capture the large perturbations to the global environment that occurred across the K/Pg boundary.

Model results

Once the MCMC algorithm reaches a point where subsequent iterations result in diminishing increases in log-likelihood, we record the model inputs (the five gas and carbon cycle parameters) and outputs (temperature and $\delta^{13}C$ values). By initializing the algorithm multiple times at slightly different initial proposals and allowing it to reconverge, we reduce the potential for autocorrelation of the results and hedge against nonstationarity, in a process analogous to sieving. From 10 separate MCMC runs, we obtain 10,000 possible input scenarios that most closely reproduce the proxy data. Figure 3 shows the average output data from these LOSCAR model runs compared with the proxy temperature and the bulk and benthic $\delta^{13}C_{carb}$ values.

Approximately 32,000 and 15,000 Gt of carbon and sulfur emissions, respectively, are required by the model to reproduce K/Pg conditions with a CO_2 doubling rate of 2.9° ± 0.3° (Fig. 3A). One-third of this volume is before the boundary, with similar amounts of carbon and sulfur emitted from 66.8 to 66.3 Ma, reflecting potential passive degassing because these signals pre-date all but perhaps the very first known Deccan Traps eruptions (*42*, *43*) (Fig. 4A). At 66.3 Ma, a noticeable increase in carbon output and decrease in sulfur output occurs, coincident with the oldest Deccan flows dated by Eddy *et al.* (*42*) and the initiation of the late-Maastrichtian warming event. Post-extinction, the rate of gas emissions increases, with more carbon emission suppressing the surface $\delta^{13}C$ values, and more sulfur providing atmospheric cooling to offset the effect of the carbon. The 2:1 ratio of C:S is broadly observed, but two pulses of sulfur at 65.9 and 65.65 Ma potentially reflect increasing Deccan activity. Although the total ratio of the gases is 2:1, the instantaneous rates of carbon and sulfur emission are highly decoupled, reflecting the different timescales on which the gases affect the global carbon cycle.

The most notable result in the C_{org} export modeling is the 55 to 60% drop across the K/Pg boundary (Fig. 4B). This drop serves to collapse the surface-to-benthic gradient of $\delta^{13}C$. As we only model export productivity, our results cannot directly differentiate between the end-member hypotheses of the "Strangelove Ocean" (*44*) (decline in primary productivity) and the "Living Ocean" (*45*) (decline in export productivity only),

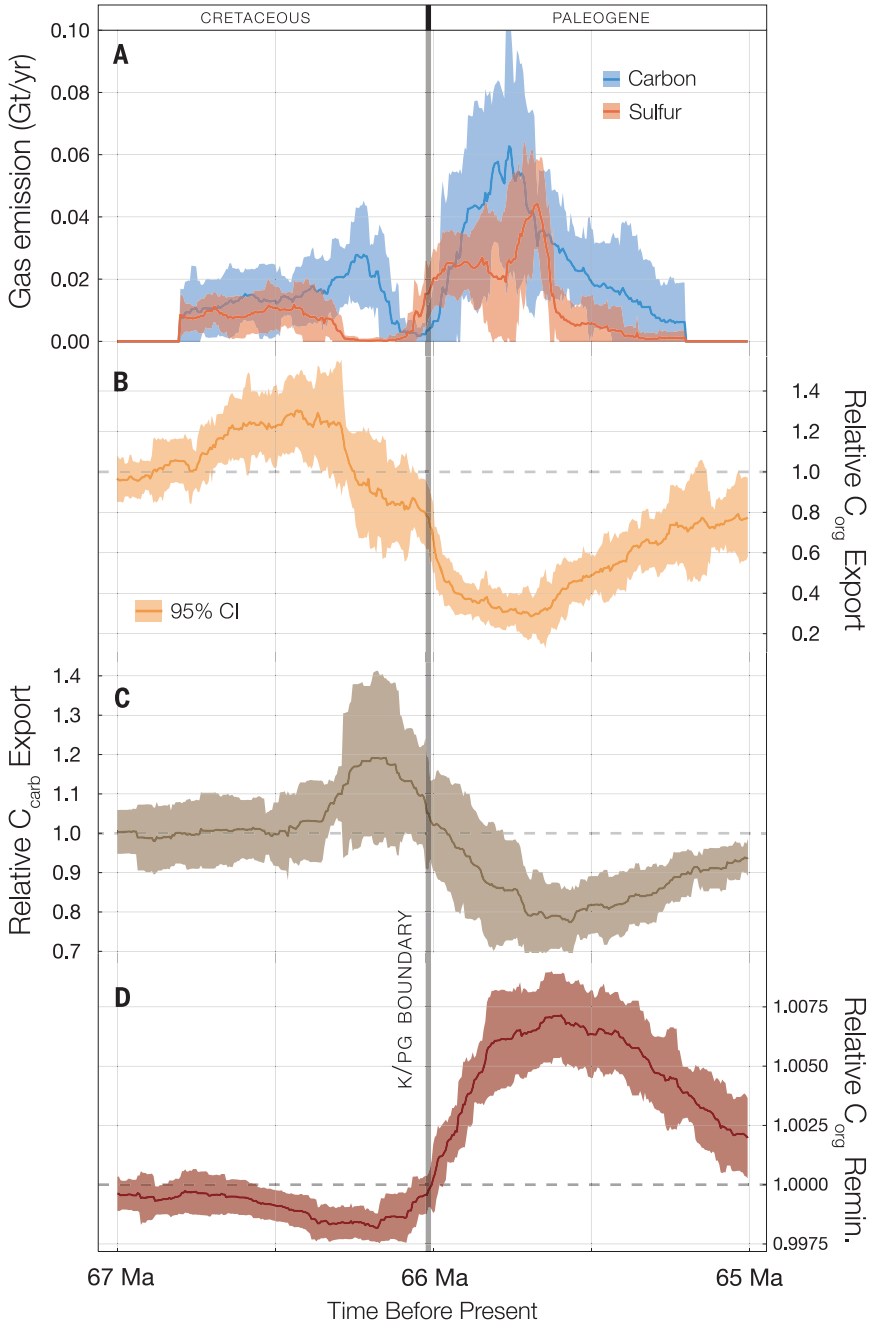

Fig. 4. Inversion results. For the 10,000 post-convergence model runs of the MCMC algorithm, their accepted inputs across the extinction boundary were recorded, and their mean and 95% credible interval were calculated. We show the accepted values of gas emissions [as carbon and sulfur (**A**)], organic carbon export relative to steady-state values (**B**), relative carbonate carbon export (**C**), and relative organic carbon remineralization (**D**), over a period spanning 2 million years, from 67 to 65 Ma.

or any heterogeneous variation thereof (*46*), but may place an approximate lower limit on decreases in primary productivity. The 55 to 60% decrease in export we observed would, however, notably remain consistent with the estimated 50% decline in primary productivity from Henehan *et al.* (*47*). This drop in C_{org} export is followed by a protracted recovery that reaches pre-extinction levels after 1 million years. The LOSCAR model likely favors this protracted recovery because surface $\delta^{13}C$ values remain low for the whole post-extinction period, and reducing export productivity is an efficient way to depress these values. An initial 30% relative drop in export productivity occurs before the boundary, lasting 100 kyr, from 66.28 Ma to 66.18 Ma. From a model perspective, this drop in export serves to increase the atmospheric

pCO_2 associated with the late Maastrichtian warming event (LMWE), because achieving this by adding more Deccan CO_2 would potentially violate the 2:1 CO_2:SO_2 prior. The sulfur flux remains low throughout the LMWE until ~66.08 Ma, suggesting that biological pump changes and an increased silicate weathering feedback (implicit in LOSCAR) may have played a greater role in its termination than did sulfate aerosol albedo effects.

Because marine primary productivity and export efficiency are the two major controls on both C_{org} and C_{carb} export, their trends are, unsurprisingly, roughly the same—with a decrease in C_{carb} export at the boundary followed by a protracted recovery (Fig. 4C). However, a ~20% increase in C_{carb} export is coincident with the drop in C_{org} export and the LMWE. This trend occurs because more export of carbonate releases more CO_2 to the atmosphere, causing warming, whereas C_{carb} export has a relatively small impact on the ocean $\delta^{13}C$ values compared with organic carbon export.

Our inversion results also reveal a minor increase of about half a percent in the proportion of organic carbon remineralized at all depths after the boundary. This shift, although minor in relative terms, has substantial isotopic impacts owing to the relatively large volume of organic carbon involved (i.e., C_{org} production and remineralization are relatively tightly coupled). The model favors more remineralization after the K/Pg boundary because it decreases both surface and benthic $\delta^{13}C$ values but delays this increase so that it can still somewhat recreate the spike in benthic $\delta^{13}C$ at the boundary (Fig. 3C). Physically, such a systematic change in remineralization could reflect a systematic change in community composition of the post-extinction ocean. If, as has been suggested, smaller phytoplankton (*48*), including cyanobacteria (*49*), were favored in the aftermath of the extinction, the slower Stokes settling velocities thereof would allow more time for their remineralization in the oxic water column and reduce export efficiency of both C_{org} and C_{carb}. Changes in community composition may likewise influence the molecular size distribution and reactivity of dissolved organic carbon, which, while less well understood, may also systematically influence remineralization rates (*50*).

Conclusions

Relative to previous modeling of volatile emissions around the K/Pg boundary, our parallel MCMC approach is an improvement in that it allows us to explore many possible biological and volatile input scenarios across the K/Pg boundary, allowing the parameters to vary independently by means of random perturbations from uniform initial proposals. This strategy has the benefit of removing the subjectivity associated with manually selecting model scenarios. Even though our results are model-dependent, our sensitivity plots (Fig. 2) show that our five input parameters change the carbon cycle in expected and physically reasonable ways, and we can reproduce extinction conditions using physically plausible timings of gas emissions, carbon export, and remineralization (Fig. 4). Furthermore, by allowing several separate model runs to reach convergence, we avoid local maxima and show that our approach is reproducible while only applying weak priors.

The gas volumes required are plausibly consistent with volcanism, although pre-eruptive degassing may be required, given the timing of emissions, and substantial C:S fractionation is required, given that the proposed ratios vary from 1:1 to as much as 20:1 in the time period preceding the impact. Notably, there is no clear impulse of volatile emissions at the boundary, suggesting that the impact may have had a negligible effect on the long-term carbon cycle. This observation is consistent with previous estimates of Chicxulub-induced degassing (*19*), which are almost two orders of magnitude smaller than our total proposed Deccan Traps CO_2 and SO_2 volumes. Because LOSCAR is designed to deal with carbon cycle changes on the order of centuries to millions of years (*29*), it might not be able to fully resolve environmental dynamics as a result of impact. Nonetheless, the contrast in magnitude between likely volcanic and impact degassing magnitudes suggests that environmental effects associated with the Chicxulub impact were driven more by rate than absolute magnitude, or else not mediated primarily by volatile emissions. Finally, our proposed two-stage decline in export productivity is somewhat consistent with macrofossil datasets from Seymour Island (*28*) that suggest a two-stage extinction, although the timing of the decrease in productivity in our results slightly pre-dates the Seymour Island estimate of 140 to 290 kyr before the boundary.

More generally, our results show that inverting a moderately computationally expensive (on the order of core-minutes) Earth system model using a parallel MCMC method, as we do here with LOSCAR, presents a promising means of obtaining insights into past Earth system events, because it allows one to efficiently and unbiasedly explore the large parameter space of potential model inputs that represent unknown environmental forcings. Such a method may in principle be applied using any variety of paleoenvironmental data that corresponds to model outputs, while using available priors on the model inputs. Consequently, our results may change given improved proxy data; enhancements to the forward model; or additional geological, chemical, or geochronological constraints that allow the incorporation of additional priors. Nevertheless, our output data are consistent with volcanism and other biological changes imparting a great stress on the global carbon cycle at long and short timescales across the K/Pg extinction boundary.

REFERENCES AND NOTES

1. T. Green, P. R. Renne, C. B. Keller, *Proc. Natl. Acad. Sci. U.S.A.* **119**, e2120441119 (2022).
2. D. P. G. Bond, S. E. Grasby, *Palaeogeogr. Palaeoclimatol. Palaeoecol.* **478**, 3–29 (2017).
3. V. E. Courtillot, P. R. Renne, *C. R. Geosci.* **335**, 113–140 (2003).
4. J. Kasbohm, *Nat. Geosci.* **15**, 342–343 (2022).
5. M. E. Clapham, P. R. Renne, *Annu. Rev. Earth Planet. Sci.* **47**, 275–303 (2019).
6. P. B. Wignall, *Earth Sci. Rev.* **53**, 1–33 (2001).
7. S. Self, M. Widdowson, T. Thordarson, A. E. Jay, *Earth Planet. Sci. Lett.* **248**, 518–532 (2006).
8. L. W. Alvarez, W. Alvarez, F. Asaro, H. V. Michel, *Science* **208**, 1095–1108 (1980).
9. G. P. Wilson, *Spec. Pap. Geol. Soc. Am.* **503**, 365–392 (2014).
10. B. Schoene *et al*., *Science* **363**, 862–866 (2019).
11. C. J. Sprain *et al*., *Science* **363**, 866–870 (2019).
12. B. Schoene, M. P. Eddy, C. B. Keller, K. M. Samperton, *Geochronology* **3**, 181–198 (2021).
13. A. R. Hildebrand *et al*., *Geology* **19**, 867–871 (1991).
14. P. Schulte *et al*., *Science* **327**, 1214–1218 (2010).
15. C. J. Sprain, P. R. Renne, W. A. Clemens, G. P. Wilson, *Geol. Soc. Am. Bull.* **130**, 1615–1644 (2018).
16. V. Gilabert, S. J. Batenburg, I. Arenillas, J. A. Arz, *Geology* **50**, 21–25 (2022).
17. P. M. Hull *et al*., *Science* **367**, 266–272 (2020).
18. A. A. Chiarenza *et al*., *Proc. Natl. Acad. Sci. U.S.A.* **117**, 17084–17093 (2020).
19. N. Artemieva, J. Morgan, Expedition 364 Science Party, *Geophys. Res. Lett.* **44**, 110–180 (2017).
20. L. Marshall *et al*., *J. Geophys. Res. Atmos.* **124**, 964–985 (2019).
21. P. R. Renne *et al*., *Science* **339**, 684–687 (2013).
22. A. E. Jay, M. Widdowson, *J. Geol. Soc. London* **165**, 177–188 (2008).
23. A. L. Chenet *et al*., *J. Geophys. Res.* **114**, B06103 (2009).
24. A. Hernandez Nava *et al*., *Proc. Natl. Acad. Sci. U.S.A.* **118**, e2007797118 (2021).
25. H. Shinohara, A. Aiuppa, G. Giudice, S. Gurrieri, M. Liuzzo, *J. Geophys. Res.* **113**, B09203 (2008).
26. P. Allard, *Geophys. Res. Lett.* **24**, 2219–2222 (1997).
27. A. Aiuppa *et al*., *Geology* **35**, 1115–1118 (2007).
28. T. S. Tobin, C. M. Bitz, D. Archer, *Palaeogeogr. Palaeoclimatol. Palaeoecol.* **478**, 139–148 (2017).
29. R. E. Zeebe, *Geosci. Model Dev.* **5**, 149–166 (2012).
30. N. Metropolis, A. W. Rosenbluth, M. N. Rosenbluth, A. H. Teller, E. Teller, *J. Chem. Phys.* **21**, 1087–1092 (1953).
31. J. Machta, *Phys. Rev. E* **80**, 056706 (2009).
32. D. J. Earl, M. W. Deem, *Phys. Chem. Chem. Phys.* **7**, 3910–3916 (2005).
33. B. Calderhead, *Proc. Natl. Acad. Sci. U.S.A.* **111**, 17408–17413 (2014).
34. Materials and methods are available as supplementary materials.
35. R. B. Stothers, J. A. Wolff, S. Self, M. R. Rampino, *Geophys. Res. Lett.* **13**, 725–728 (1986).
36. E. Kaminski, A.-L. Chenet, C. Jaupart, V. Courtillot, *Earth Planet. Sci. Lett.* **301**, 171–178 (2011).
37. B. M. Harris, E. J. Highwood, *J. Geophys. Res.* **116**, D05109 (2011).
38. A. W. A. Jeffrey, R. C. Pflaum, J. M. Brooks, W. M. Sackett, *Deep Sea Res. A* **30**, 971–983 (1983).
39. P. W. Boyd, H. Claustre, M. Levy, D. A. Siegel, T. Weber, *Nature* **568**, 327–335 (2019).
40. M. Nowicki, T. DeVries, D. A. Siegel, *Global Biogeochem. Cycles* **36**, e2021GB007083 (2022).
41. O. M. Bialik, G. Sisma-Ventura, N. Vogt-Vincent, J. Silverman, T. Katz, *Sci. Rep.* **12**, 15970 (2022).
42. M. P. Eddy *et al*., *Earth Planet. Sci. Lett.* **540**, 116249 (2020).
43. A. Tholt *et al*., "40Ar/39Ar dating of the Malwa Plateau subprovince, Deccan Traps, India," EGU General Assembly 2022, Vienna, Austria, 23 to 27 May 2022, EGU22-11928 (2022); https://doi.org/10.5194/egusphere-egu22-11928.
44. K. J. Hsü, J. A. Mckenzie, in *The Carbon Cycle and Atmospheric CO_2: Natural Variations Archean to Present*, E. T. Sundquist, W. S. Broecker, Eds., vol. 32 of *Geophysical Monograph Series* (AGU, 1985), pp. 487–492.
45. S. D'Hondt, P. Donaghay, J. C. Zachos, D. Luttenberg, M. Lindinger, *Science* **282**, 276–279 (1998).

46. P. M. Hull, R. D. Norris, *Paleoceanography* **26**, PA3205 (2011).
47. M. J. Henehan *et al.*, *Proc. Natl. Acad. Sci. U.S.A.* **116**, 22500–22504 (2019).
48. S. A. Alvarez *et al.*, *Nature* **574**, 242–245 (2019).
49. T. J. Bralower *et al.*, *Earth Planet. Sci. Lett.* **548**, 116476 (2020).
50. R. Benner, R. M. W. Amon, *Annu. Rev. Mar. Sci.* **7**, 185–205 (2015).

ACKNOWLEDGMENTS

We thank R. E. Zeebe for the use of his LOSCAR model and for fruitful discussions about how to interpret its parameters in the framework of the K/Pg extinction. Additional thanks go to D. E. Penman for supplying us with a modified version of the LOSCAR code, which paved the way for its ultimate inversion, and for his computational insights. The work benefited from further discussion with D. Rothman, A. Ridgwell, B. Schoene, J. A. Higgins, and I. Fendley. **Funding:** The authors have no funding to declare. **Author contributions:** Conceptualization: C.B.K. Methodology: A.A.C. and C.B.K. Software: A.A.C. and C.B.K. Writing – original draft: A.A.C. Writing – review & editing: A.A.C. and C.B.K. Visualization: A.A.C. **Competing interests:** The authors declare that they have no competing interests. **Data and materials availability:** All data and code are available in the supplementary materials. **License information:** Copyright © 2023 the authors, some rights reserved; exclusive licensee American Association for the Advancement of Science. No claim to original US government works. https://www.science.org/about/science-licenses-journal-article-reuse

SUPPLEMENTARY MATERIALS

science.org/doi/10.1126/science.adh3875
Materials and Methods
Supplementary Text
Figs. S1 to S3
Table S1
References (*51*, *52*)
Code Files

Submitted 28 February 2023; accepted 25 August 2023
10.1126/science.adh3875

GENOMICS

Genomic signatures of disease resistance in endangered staghorn corals

Steven V. Vollmer†*, Jason D. Selwyn†, Brecia A. Despard, Charles L. Roesel

White band disease (WBD) has caused unprecedented declines in the Caribbean *Acropora* corals, which are now listed as critically endangered species. Highly disease-resistant *Acropora cervicornis* genotypes exist, but the genetic underpinnings of disease resistance are not understood. Using transmission experiments, a newly assembled genome, and whole-genome resequencing of 76 *A. cervicornis* genotypes from Florida and Panama, we identified 10 genomic regions and 73 single-nucleotide polymorphisms that are associated with disease resistance and that include functional protein-coding changes in four genes involved in coral immunity and pathogen detection. Polygenic scores calculated from 10 genomic loci indicate that genetic screens can detect disease resistance in wild and nursery stocks of *A. cervicornis* across the Caribbean.

Increased global CO_2 emissions and the resulting ocean warming have devastated tropical reef corals by increasing the frequency and severity of thermal bleaching events (*1*–*3*) and disease outbreaks (*4*, *5*). Emergent infectious diseases in Caribbean corals cause high levels of coral mortality (*6*–*8*), with white band disease (WBD) killing up to 95% of the critically endangered Caribbean *Acropora* corals (*8*), and stony coral tissue loss disease (SCTLD) is, at present, decimating more than 20 key reef-building coral species (*6*, *7*). The rising toll of thermal bleaching and diseases on coral reefs globally has focused scientific efforts on identifying thermally resilient and disease-resistant coral species, individuals, genes, and symbionts that allow reef corals to adapt to future climate scenarios (*9*–*11*), including through human intervention (*9*). Adaptive polygenic variation for thermal tolerance with relatively high heritability exists in corals (*11*), although the identification of genetic markers that strongly influence thermal tolerance is more elusive (*12*). Less is known about the genetics of coral disease resistance. Phenotypic variation in disease resistance to WBD has been documented in the staghorn coral, *Acropora cervicornis* (*13*, *14*), and may be heritable and adaptive.

WBD is a highly transmissible, host-specific disease that infects the two sister species of Caribbean *Acropora* (*8*, *15*–*17*): the staghorn coral, *A. cervicornis*, and the elkhorn coral, *Acropora palmata*, as well as their hybrid species, *Acropora prolifera* (*18*, *19*). Since it was first observed in 1979 (*15*), WBD has killed up to 95% of Caribbean *Acropora* and is found throughout the greater Caribbean (*8*). WBD is caused by a bacterial pathogen or pathogens that can be arrested with antibiotics (*16*, *20*) and quorum-sensing inhibitors (*21*, *22*). Multiple putative bacterial pathogens have been associated with WBD (*20*, *23*), including *Vibrio* spp. (*24*, *25*), *Aquarickettsia* (*26*, *27*), and other bacteria (*23*). *A. cervicornis* genotypes display strong phenotypic variation in disease resistance (*13*, *14*) and mount a vigorous immune response to WBD infection (*28*, *29*), with highly resistant genotypes up-regulating genes involved in microRNA-induced posttranscriptional gene regulation (*29*).

We conducted a genome-wide association study (GWAS) to identify genetic variants associated with disease resistance to WBD in

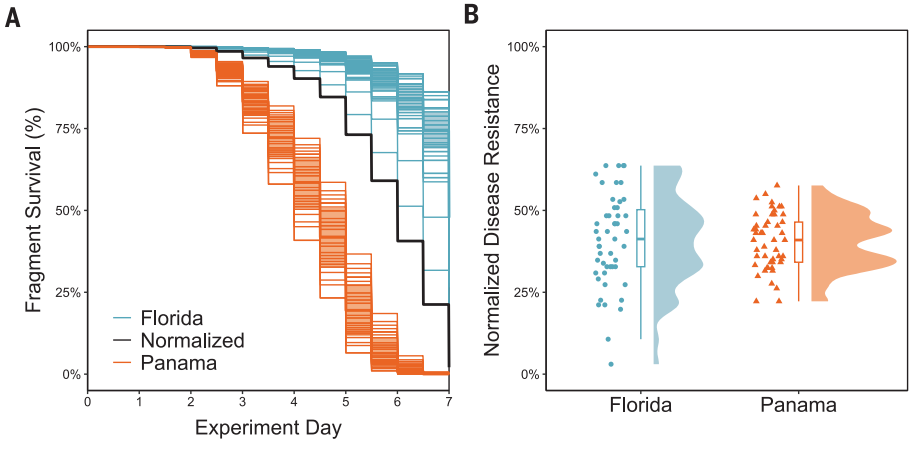

Fig. 1. Tank-based infection, survival, and disease resistance. (**A**) Fragment survival rates (%) from the two independent tank-based transmission experiments conducted in Florida (blue) and Panama (orange). A Cox proportional hazard model detected significant effects of genotype [χ^2(effective df = 65, reference df = 99) = 2392, $p < 0.0001$], experimental tank [χ^2(7.8, 9) = 4779, $p = 0.00008$], and experiment location and/or population [χ^2(0.99, 1) = 23,127, $p < 0.00001$] on fragment survival. Genotype explained 6.1% of the variation in survival, whereas experiment location and/or population (i.e., Florida versus Panama) explained 28.8% of the variation. (**B**) Normalized disease resistance (one minus the probability of infection; see methods for details) at day 6 of exposure for the 50 Florida and 50 Panama *A. cervicornis* genotypes that were surveyed. The center line represents the median, box limits are upper and lower quartiles, and whiskers are minimum and maximum values.

Department of Marine and Environmental Sciences, Northeastern University, 430 Nahant Road, Nahant, MA 01908, USA.
***Corresponding author. Email: s.vollmer@northeastern.edu**
†These authors contributed equally to this work.

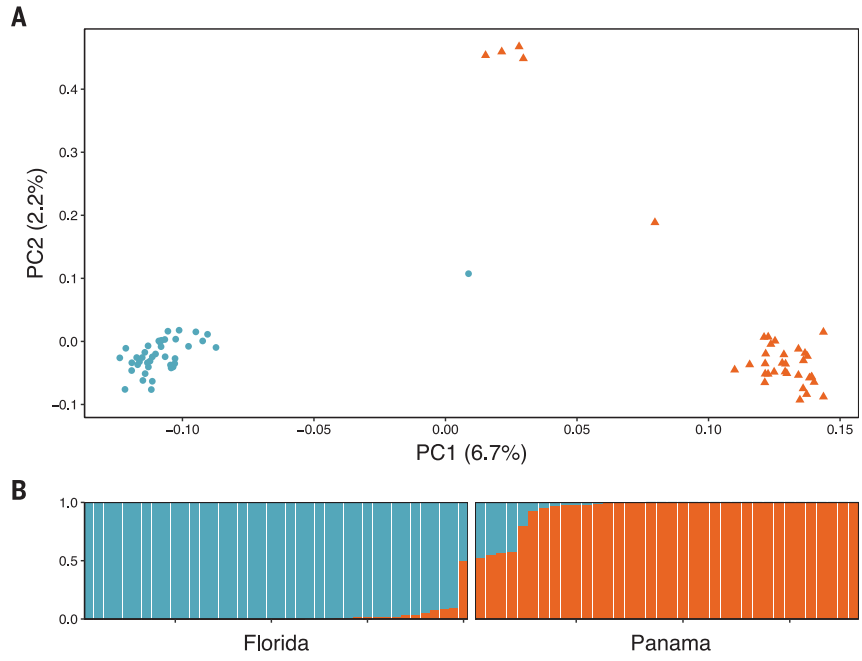

Fig. 2. Population structure and admixture between Florida and Panama. (**A**) PCA showing the strong genetic differences between *A. cervicornis* from Florida (blue) and Panama (orange) (F_{ST} = 0.04, p < 0.001). (**B**) Structure-based assignment analysis (k = 2 populations) showing greater than 10% admixture in six individuals.

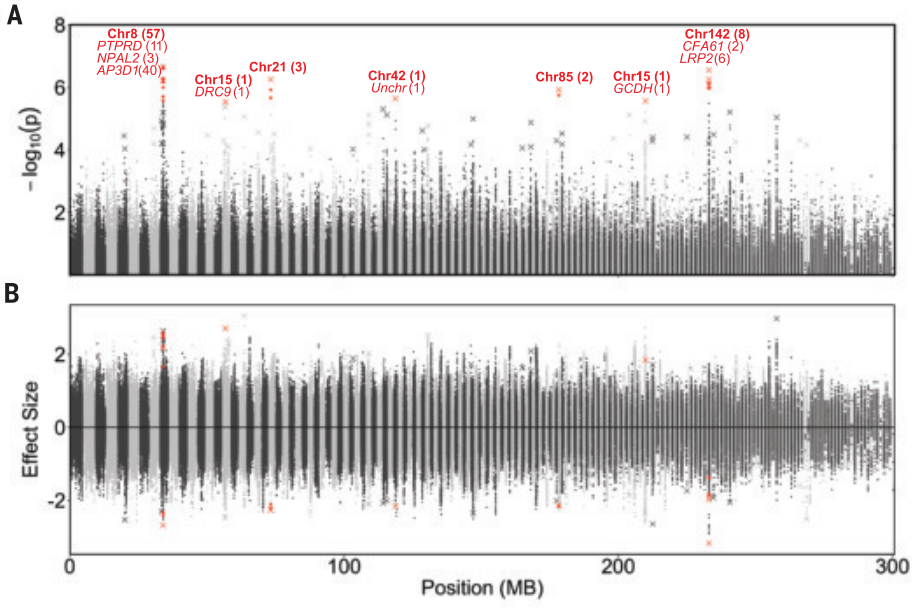

Fig. 3. Genome-wide SNP association analyses of disease resistance. (**A**) Manhattan plot of p values across 1.2 million high-quality SNPs in the *A. cervicornis* genome. (**B**) Effect-size plot across the genome, in which positive effect sizes indicate that the rare allele is associated with increased disease resistance and negative effect sizes indicate that the common allele is associated with increased disease resistance. Seventy-three significant disease-associated SNPs (adjusted p < 0.05) are labeled in red. The numbers of significant SNPs per chromosome (chr) and gene are summarized and labeled in red. The × symbol identifies the index SNP from each linkage group that was used to calculate polygenic scores, with red indicating the top 10 index SNPs from the significant linkage groups and gray indicating the 53 additional SNPs that were used to calculate the expanded polygenic score (p < 0.0001).

A. cervicornis from two geographically distant populations: Florida and Panama. Disease resistance was assayed in tank-based transmission experiments that were conducted separately in Florida and Panama with 50 coral genotypes from each location (Fig. 1A). Florida *A. cervicornis* were sourced from Coral Restoration Foundation nursery stocks, and the Panama *A. cervicornis* were sampled from wild populations in Bocas del Toro. A Cox proportional hazards model was used to calculate normalized disease-resistance scores across all 100 genotypes (Fig. 1B) while accounting for experimental and/or population effects of the two independent transmission experiments. Coral genotype explained 6.1% of the variation in disease resistance [χ^2(effective df = 65, reference df = 99) = 2392, p < 0.0001; df, degrees of freedom], experimental tank explained 8.4% of the variance [χ^2(7.8, 9) = 4779, p = 0.00008], and experiment location and/or population explained 28.8% of the variance [χ^2(0.99, 1) = 23,127, p < 0.00001]. The experiment location and population variation in the transmission experiments could result from a variety of factors (*30*), including differences in microbial exposure doses and host microbiomes as well as spatiotemporal environmental variation between the two study sites.

We randomly selected 48 genotypes from each population for whole-genome sequencing (WGS) and assembled and annotated a high-quality, de novo genome using adult tissue from the K2 genotype from Coral Restoration Foundation, Florida, with high-quality nanopore sequencing and short-read polishing. The 308-Mb scaffolded *A. cervicornis* K2 genome had an N50 of 2.8 Mb (where N50 is the minimum scaffold length needed to cover 50% of the genome) (fig. S1) and a BUSCO completeness of 92% and contains 28,059 genes on 398 scaffolded contigs (hereafter, chromosomes), 54% of which were annotated to known SwissProt reference proteins (E-value < 10^{-6}). The 308-Mb *A. cervicornis* genome is somewhat smaller than that of Pacific Acroporids (384 to 475 Mb) and has an intermediate number of gene annotations [23,467 to 41,860 (*31*)].

Using the K2 reference genome, we produced WGS data for 96 putative genotypes (48 from Florida and 48 from Panama) using Illumina paired-end 150–base pair sequencing. Four samples were removed because of low coverage, leaving 92 putative genotypes with high-quality WGS data (mean 74× coverage ± 3.6 SE) that included 1.2 million single-nucleotide polymorphisms (SNPs) [minor allele frequency >0.05] and 54,871 unlinked SNPs [linkage disequilibrium (r^2_{LD}) < 0.5, 250 kb]. A total of 76 unique staghorn coral genotypes (40 from Florida and 36 from Panama) were retained after filtering for clones based on 97% genetic similarity (fig. S2). *Symbiodinium* was the dominant algal symbiont in *A. cervicornis* (fig. S3),

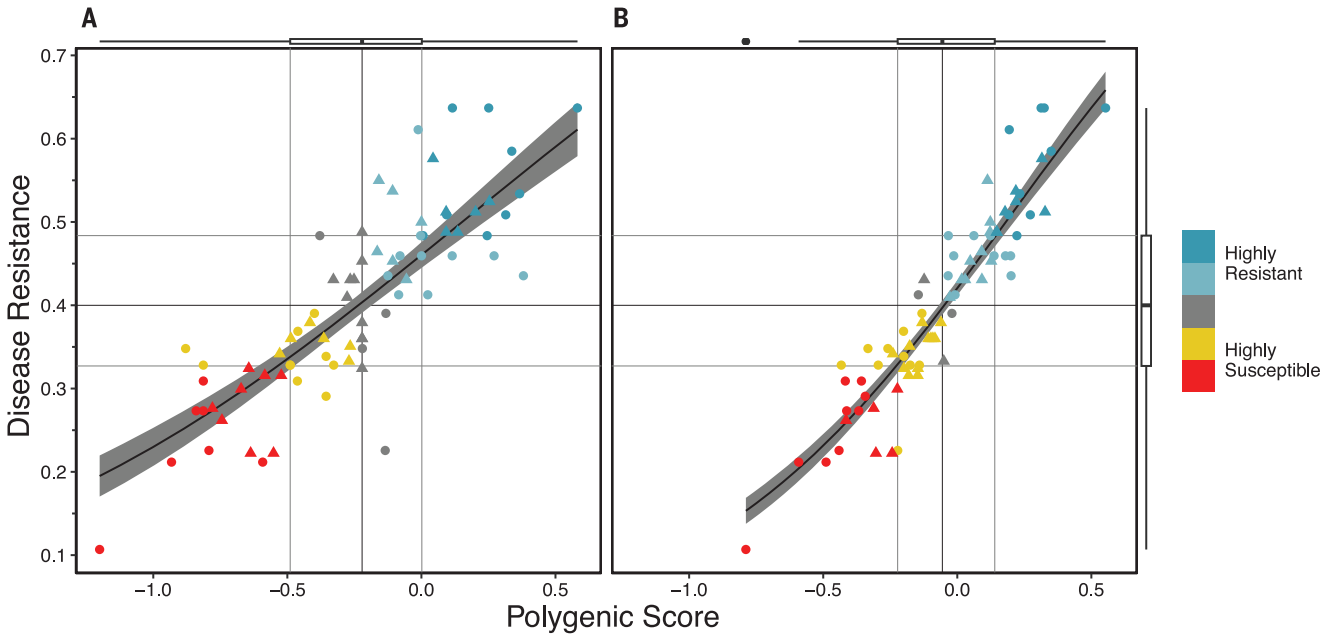

Fig. 4. Polygenic scores that predict disease resistance. (**A**) Polygenic scores for the top ten SNPs and genomic regions explain 66.9 ± 5.4% of disease resistance ($p < 0.0001$). (**B**) Polygenic scores based on the most important 63 SNPs and genomic regions ($p < 0.0001$) explain 85.3 ± 2.3% of the variation in disease resistance, showing that the inclusion of 53 additional loci improved disease-resistance predictions based on polygenic scores. Individuals represented by blue symbols have above-average polygenic scores and disease resistance; the dark blue points indicate individuals that are highly disease resistant, with polygenic scores and disease-resistance values in the top quartiles. Individuals represented by yellow and red symbols have lower-than-average polygenic scores and disease resistance, with red symbols indicating highly susceptible individuals. Coral genotypes from Florida are labeled with a circle and those from Panama are labeled with a triangle. The gray shaded area indicates ±1 standard error.

and the composition of algal symbionts did not differ by host disease resistance ($F_{1,72} = 0.04$, $p = 0.65$) or the interaction with location ($F_{1,72} = 0.02$, $p = 0.78$). There were significant compositional differences between Florida and Panama ($F_{1,72} = 5.65$, $p = 0.012$, $r^2 = 0.07$), with slight relative increases in *Breviolum* and *Fugacium* in Panama.

Principal components analysis (PCA) and admixture analysis (*32*) clustered *A. cervicornis* from Florida and Panama into two distinct populations (Fig. 2 and fig. S4) separated by an average population genetic difference (F_{ST}) of 0.038 ($p < 0.001$), which is similar to the population genetic structure that was detected using mitochondrial and nuclear sequencing data (*33*, *34*) and suggests restricted Caribbean-wide gene flow. Six genotypes—one from Florida and five from Panama—had greater than 10% population-level admixture (Fig. 2), but this admixture was not correlated to disease resistance (Kendall's rank correlation coefficient = 0.05, $p = 0.53$) (fig. S5) or recent introgressive hybridization (fig. S6).

Genetic variants associated with disease resistance

We used a latent factor mixed model to account for underlying population structure between Florida and Panama [inferred populations (k) = 2; fig. S4] and identify SNPs associated with disease resistance (table S1). Clumping and thresholding was used to organize all 1.2 million SNPs into linkage groups ($r^2_{LD} > 0.5$, 250 kb). Seventy-three SNPs in 10 linkage groups on seven chromosomes were significantly associated with disease resistance after false discovery rate correction (adjusted $p < 0.05$; Fig. 3 and table S1). Three linkage groups had SNPs with positive effect sizes, indicating that the rare allele is associated with increased disease resistance, whereas the remaining seven linkage groups had negative effect sizes in which the common allele was beneficial. Sixty-five disease resistance–associated SNPs occurred in annotated genes, including 54 SNPs in three genes—*AP3D1* (40), *PTPRD* (11), *NPAL2* (3)—on chromosome 8, and eight SNPs in two genes—*LRP2* (6) and *CFA61* (2)—on chromosome 142. Eight out of the 65 significant SNPs in annotated genes occurred in protein-coding regions. Only one significant SNP in *PTPRD* resulted in a functional, nonsynonymous (i.e., amino acid) change. *PTPRD* and *AP3D1* also contained one and three significant SNPs that resulted in synonymous changes, respectively. However, multiple nonsynonymous changes occurred in linkage groups that contained significant disease resistance–associated SNPs (fig. S7), including nonsynonymous changes in *PTPRD* (2), *AP3D1* (1), and *SECG* (1) on chromosome 8 and *LRP2* (7) and *CFA61* (1) on chromosome 142. The eight remaining significant SNPs that fell outside of annotated genes included three SNPs linked to the significant SNPs on genes in chromosome 8, three SNPs linked to an uncharacterized gene on chromosome 21, and two SNPs on chromosome 85 that were not linked to significant SNPs on genes.

Four of the five candidate disease-resistance genes with functional, protein-coding changes—*PTPRD*, *AP3D1*, *SECG*, and *LRP2*—have roles in coral immunity. Protein tyrosine phosphatase receptor type D (*PTPRD*) is a tumor suppressor gene (*35*) in the receptor protein tyrosine phosphatases (PTPs) family that regulates cell signaling through dephosphorylation and acts as an immune regulator (*36*). AP-3 complex subunit delta-1 (*AP3D1*) is part of the AP-3 complex, which regulates lysosomal trafficking and endocytosis and is specifically involved in the sorting of cargo molecules into clathrin-coated vesicles during endocytosis (*37*). Ankyrin repeat, PH and SEC7 domain–containing protein secG (*SECG*) is a cytohesin protein involved in signal transduction, immune regulation, and phagocytosis (*38*). Low-density lipoprotein receptor–related protein 2 (*LRP2*) is an innate immune gene that activates the complement system and nuclear factor κB (NF-κB) to initiate endocytosis (*39*). The fifth gene, cilia- and flagella-associated protein 61 (*CFA61*), is part of the calmodulin and spoke-associated complex that is involved in cilia motility (*40*).

PTPRD and *LRP* have previously been shown to be differentially expressed in WBD-infected

A. cervicornis (*28*) and *A. palmata* (*41*). *LRP* genes have also been reported to be up-regulated in multiple Caribbean corals infected with white plague (*42*). However, none of the five candidate disease-resistance genes with functional variants were constitutively or differentially expressed in six genotypes from the Florida transmission experiment (fig. S10 and table S6) as a result of the observed disease resistance; this effect was also not reported in prior research that examined the links between gene expression and disease resistance in *A. cervicornis* (*29*). The lack of gene expression polymorphisms at these five candidate disease-resistance genes suggests that the functional protein-coding changes in *PTPRD*, *AP3D1*, *SECG*, *LRP2*, and *CFA61* influence disease resistance rather than changes in their gene expression.

Shared polygenic variation explains disease resistance

Polygenic scores calculated for the 76 *A. cervicornis* genotypes, by using the top index SNP from each of the 10 linkage groups with significant SNPs, explained 67.9 ± 5.4% of the variation in observed *A. cervicornis* disease resistance (Fig. 4A and table S2). Thirty-three genotypes (44.6%; 19 from Florida and 14 from Panama) had above-average polygenic scores and displayed disease resistance, with 15 genotypes (20.2%; nine from Florida and six from Panama) scoring as highly disease-resistant and falling in the top 25% for both polygenic score and disease resistance. By contrast, 31 genotypes (41.9%; 17 from Florida and 14 from Panama) had below-average polygenic scores and disease resistance, with 15 genotypes (20.2% total; seven from Florida and eight from Panama) scoring as highly disease susceptible. Extending the polygenic score to 63 loci ($p < 0.0001$) captured 85.5 ± 2.3% of the observed variation in disease resistance (Fig. 4B and table S2), indicating that these 53 additional genetic loci have small, but measurable, effects on observed disease resistance.

Our data show that, similar to coral thermal tolerance (*43*), disease resistance within *A. cervicornis* is polygenic across multiple genomic regions and chromosomes. Although gene variants strongly associated with thermal tolerance have been difficult to identify with GWASs (*12*), we identified 10 genomic regions and 73 loci that were associated with *A. cervicornis* disease resistance, including linked functional protein-coding variation within five coral disease-resistance genes. Thus, natural selection for increased coral immunity and disease resistance may be higher than it is for thermal tolerance.

The shared adaptive polygenic variation in *A. cervicornis* disease resistance that is observed in Florida and Panama indicates that genetic variation for disease resistance is widely dispersed across the Caribbean, despite the restricted gene flow that we and others have found (*33*, *34*), and thus could be used to improve disease resistance through natural or assisted selection. *Acropora* populations throughout the greater Caribbean are under active conservation management and restoration because of their critically endangered status (*44*, *45*). Florida is a hotspot for *Acropora* restoration, with hundreds of *A. cervicornis* genotypes being actively propagated in land-based and in situ nurseries (*46*, *47*), including the Coral Restoration Foundation nurseries from which our Florida genotypes were sourced. More than 25,000 *A. cervicornis* fragments have been outplanted across Florida (*47*) and elsewhere in the Caribbean.

Our research shows that polygenic scores from the top 10 SNPs and genomic regions identified disease-resistant *A. cervicornis* genotypes. Future research is required to establish whether there are fitness trade-offs between disease resistance and other key metrics such as growth, fecundity, thermal tolerance, and survival (*48*). Although fitness trade-offs are, as of now, largely unknown, WBD prevalence and susceptibility often increase with temperature stress (*13*). Recent evidence indicates that *A. cervicornis* varies in its thermal tolerance (*46*), and thus future efforts need to determine how disease resistance, thermal tolerance, and their genetic bases influence the fitness and future resiliency of *A. cervicornis* across the Caribbean.

REFERENCES AND NOTES

1. T. P. Hughes *et al.*, *Science* **359**, 80–83 (2018).
2. J. F. Bruno *et al.*, *PLOS Biol.* **5**, e124 (2007).
3. O. Hoegh-Guldberg *et al.*, *Science* **318**, 1737–1742 (2007).
4. C. D. Harvell *et al.*, *Science* **285**, 1505–1510 (1999).
5. C. A. Burge *et al.*, *Annu. Rev. Mar. Sci.* **6**, 249–277 (2014).
6. L. Alvarez-Filip, F. J. González-Barrios, E. Pérez-Cervantes, A. Molina-Hernández, N. Estrada-Saldívar, *Commun. Biol.* **5**, 440 (2022).
7. W. F. Precht, B. E. Gintert, M. L. Robbart, R. Fura, R. van Woesik, *Sci. Rep.* **6**, 31374 (2016).
8. R. B. Aronson, W. F. Precht, in *The Ecology and Etiology of Newly Emerging Marine Diseases*, J. W. Porter, Ed., vol. 159 of *Developments in Hydrobiology* (Springer, 2001), pp. 25–38.
9. M. J. van Oppen, J. K. Oliver, H. M. Putnam, R. D. Gates, *Proc. Natl. Acad. Sci. U.S.A.* **112**, 2307–2313 (2015).
10. J. Kleypas *et al.*, *Biol. Conserv.* **257**, 109107 (2021).
11. E. Mcleod *et al.*, *J. Environ. Manage.* **233**, 291–301 (2019).
12. Z. L. Fuller *et al.*, *Science* **369**, eaba4674 (2020).
13. E. M. Muller, E. Bartels, I. B. Baums, *eLife* **7**, e35066 (2018).
14. S. V. Vollmer, D. I. Kline, *PLOS ONE* **3**, e3718 (2008).
15. W. B. Gladfelter, *Bull. Mar. Sci.* **32**, 639–643 (1982).
16. D. I. Kline, S. V. Vollmer, *Sci. Rep.* **1**, 7 (2011).
17. S. A. Gignoux-Wolfsohn, C. J. Marks, S. V. Vollmer, *Sci. Rep.* **2**, 804 (2012).
18. M. J. Van Oppen, B. L. Willis, H. W. Van Vugt, D. J. Miller, *Mol. Ecol.* **9**, 1363–1373 (2000).
19. S. V. Vollmer, S. R. Palumbi, *Science* **296**, 2023–2025 (2002).
20. M. J. Sweet, A. Croquer, J. C. Bythell, *Proc. Biol. Sci.* **281**, 20140094 (2014).
21. R. H. Certner, S. V. Vollmer, *Sci. Rep.* **5**, 11134 (2015).
22. R. H. Certner, S. V. Vollmer, *Environ. Microbiol.* **20**, 645–657 (2018).
23. S. A. Gignoux-Wolfsohn, F. M. Aronson, S. V. Vollmer, *FEMS Microbiol. Ecol.* **93**, (2017).
24. D. L. Gil-Agudelo, G. W. Smith, E. Weil, *Rev. Biol. Trop.* **54**, 59–67 (2006).
25. K. B. Ritchie, G. W. Smith, *Rev. Biol. Trop.* **46**, 199–203 (1998).
26. L. J. Baker *et al.*, *ISME J.* **16**, 400–411 (2022).
27. V. Casas *et al.*, *Environ. Microbiol.* **6**, 1137–1148 (2004).
28. S. Libro, S. T. Kaluziak, S. V. Vollmer, *PLOS ONE* **8**, e81821 (2013).
29. S. Libro, S. V. Vollmer, *PLOS ONE* **11**, e0146636 (2016).
30. R. Vega Thurber *et al.*, *Front. Ecol. Evol.* **8**, 575927 (2020).
31. C. Shinzato *et al.*, *Mol. Biol. Evol.* **38**, 16–30 (2021).
32. E. Frichot, F. Mathieu, T. Trouillon, G. Bouchard, O. François, *Genetics* **196**, 973–983 (2014).
33. E. M. Hemond, S. V. Vollmer, *PLOS ONE* **5**, e8652 (2010).
34. S. V. Vollmer, S. R. Palumbi, *J. Hered.* **98**, 40–50 (2007).
35. S. Veeriah *et al.*, *Proc. Natl. Acad. Sci. U.S.A.* **106**, 9435–9440 (2009).
36. T. Mustelin, T. Vang, N. Bottini, *Nat. Rev. Immunol.* **5**, 43–57 (2005).
37. S. J. Neuffer *et al.*, *Pigment Cell Melanoma Res.* **35**, 495–505 (2022).
38. R. Müller *et al.*, *Cell Commun. Signal.* **11**, 54 (2013).
39. A. Beenken *et al.*, *Cell* **186**, 821–836.e13 (2023).
40. P. Urbanska *et al.*, *Mol. Biol. Cell* **26**, 1463–1475 (2015).
41. B. D. Young *et al.*, *PLOS ONE* **15**, e0228514 (2020).
42. N. J. MacKnight *et al.*, *Sci. Adv.* **8**, eabo6153 (2022).
43. E. J. Howells, L. K. Bay, R. A. Bay, in *Coral Reef Conservation and Restoration in the Omics Age*, M. J. H. van Oppen, M. Aranda Lastra, Eds., in vol. 15 of *Coral Reefs of the World* (Springer, 2022), pp. 55–70.
44. National Marine Fisheries Service, *Federal Register* 71, no. FR26852 (8 June 2006), pp. 26852–26872.
45. J. Crabbe *et al.*, *Acropora cervicornis*, The IUCN Red List of Threatened Species 2022: e.T133381A165860142 (2022); https://www.iucnredlist.org/species/133381/165860142 [accessed 5 April 2023].
46. R. Cunning *et al.*, *Proc. Biol. Sci.* **288**, 20211613 (2021).
47. R. van Woesik *et al.*, *Restor. Ecol.* **29**, e13302 (2021).
48. W. C. Million *et al.*, *Proc. Natl. Acad. Sci. U.S.A.* **119**, e2203925119 (2022).
49. S. V. Vollmer, J. D. Selwyn, B. A. Despard, C. L. Roesel, Genomic signatures of disease resistance in endangered staghorn corals, Zenodo (2023); https://doi.org/10.5281/zenodo.8095056.

ACKNOWLEDGMENTS

We thank the staff of the Coral Restoration Foundation and Florida Keys Marine Lab in Florida and the staff of the Smithsonian Tropical Research Institute in Bocas del Toro, Panama, for their help with this project. We also thank S. Belliveau, A. Moura, and the Coral Restoration Foundation volunteers who assisted with the transmission experiments and E. Trytten, R. Aronson, and R. Gatins, who helped review the manuscript. Sample collections were permitted with the approval of Autoridad Nacional del Ambiente, Panama (CITES permit nos. SEX/A-03-08 and SEX/A-98-19), and samples were provided by the Coral Restoration Foundation (permit no. CRF-2021-001). **Funding:** Grant funding was provided to S.V.V. by a National Science Foundation Division of Ocean Sciences grant (NSF OCE-1924145). **Author contributions:** Conceptualization: S.V.V.; Methodology: S.V.V., J.D.S., B.A.D., C.L.R.; Investigation: S.V.V., J.D.S., B.A.D., C.L.R.; Visualization: S.V.V., J.D.S.; Funding acquisition: S.V.V.; Project administration: S.V.V.; Supervision: S.V.V.; Writing – original draft: S.V.V., J.D.S.; Writing – review and editing: S.V.V., J.D.S., B.A.D., C.L.R. **Competing interests:** The authors declare that they have no competing interests. **Data and materials availability:** Genome assembly and WGS reads can be accessed from NCBI BioProject with accession numbers PRJNA948411 and PRJNA950067, respectively. Analysis code with disease resistance calculations is available at Zenodo (*49*). **License information:** Copyright © 2023 the authors, some rights reserved; exclusive licensee American Association for the Advancement of Science. No claim to original US government works. https://www.science.org/about/science-licenses-journal-article-reuse

SUPPLEMENTARY MATERIALS

science.org/doi/10.1126/science.adi3601
Materials and Methods
Figs. S1 to S10
Tables S1 to S6
References (*50*–*103*)
MDAR Reproducibility Checklist

Submitted 21 April 2023; resubmitted 30 June 2023
Accepted 9 August 2023
10.1126/science.adi3601

FLUORINE CHEMISTRY

Handling fluorinated gases as solid reagents using metal-organic frameworks

Kaitlyn T. Keasler[1], Mary E. Zick[1]†, Emily E. Stacy[1]†, Jaehwan Kim[1], Jung-Hoon Lee[2], Lida Aeindartehran[3], Tomče Runčevski[3], Phillip J. Milner[1]*

Fluorine is an increasingly common substituent in pharmaceuticals and agrochemicals because it improves the bioavailability and metabolic stability of organic molecules. Fluorinated gases represent intuitive building blocks for the late-stage installation of fluorinated groups, but they are generally overlooked because they require the use of specialized equipment. We report a general strategy for handling fluorinated gases as benchtop-stable solid reagents using metal-organic frameworks (MOFs). Gas-MOF reagents are prepared on gram-scale and used to facilitate fluorovinylation and fluoroalkylation reactions. Encapsulation of gas-MOF reagents within wax enables stable storage on the benchtop and controlled release into solution upon sonication, which represents a safer alternative to handling the gas directly. Furthermore, our approach enables high-throughput reaction development with these gases.

Fluorinated organic molecules account for 20 to 30% of active pharmaceutical ingredients and >40% of agrochemicals owing to their improved metabolic stabilities and membrane permeabilities compared with their nonfluorinated analogs (Fig. 1A) (*1*–*6*). In addition, ^{18}F-labeled compounds are prominent radiotracers for positron emission tomography (*7*). Despite the importance of fluorine across numerous fields, the selective, late-stage introduction of fluoroalkyl and fluorovinyl groups into drug-like molecules remains a frontier in organic synthesis (*8*–*10*). Simple fluorinated commodity chemicals such as vinylidene fluoride (VDF), trifluoropropene (TFP), hexafluoropropene (HFP), and trifluoromethyl iodide (TFMI) represent inexpensive potential building blocks for the installation of fluoroalkyl and fluorovinyl groups (Fig. 1B). For example, VDF and TFP provide entry points for the synthesis of fluorinated alkenes, which are important bioisosteres for carbonyl groups in medicinal chemistry. As such, VDF has the potential to substantially streamline the synthesis of complex fluorinated molecules such as 5-(2,2-difluorovinyl)-2′-deoxyuridine (Fig. 1C) (*6*). However, these reagents remain underutilized because they are gases at room temperature (RT) and pressure. The use of gaseous reagents necessitates specialized equipment for safe handling (*11*, *12*). Fluorinated gases are also generally toxic, flammable, ozone depleting, and/or otherwise environmentally destructive (*13*), making them challenging to use for high-throughput reaction discovery. As such, a general strategy for safely using fluorinated gases would greatly facilitate the synthesis of fluorinated molecules that are relevant to medicinal chemistry, agriculture, biomedical imaging, and beyond.

The use of gaseous reagents in organic synthesis generally requires handling the gas directly (e.g., filling a balloon from a cylinder; Fig. 1D, left) or generating the gas in situ or ex situ from stable molecular precursors (Fig. 1D, center) (*14*–*17*). Both strategies suffer from key limitations. The former is simple, but it is low throughput, lacks stoichiometric control, and produces substantial gas waste, an issue that is exacerbated with toxic and environmentally

[1]Department of Chemistry and Chemical Biology, Cornell University, Ithaca, NY 14850, USA. [2]Computational Science Research Center, Korea Institute of Science and Technology (KIST), Seoul 02792, Republic of Korea. [3]Department of Chemistry, Southern Methodist University, Dallas, TX 75275, USA. *Corresponding author. Email: pjm347@cornell.edu
†These authors contributed equally to this work.

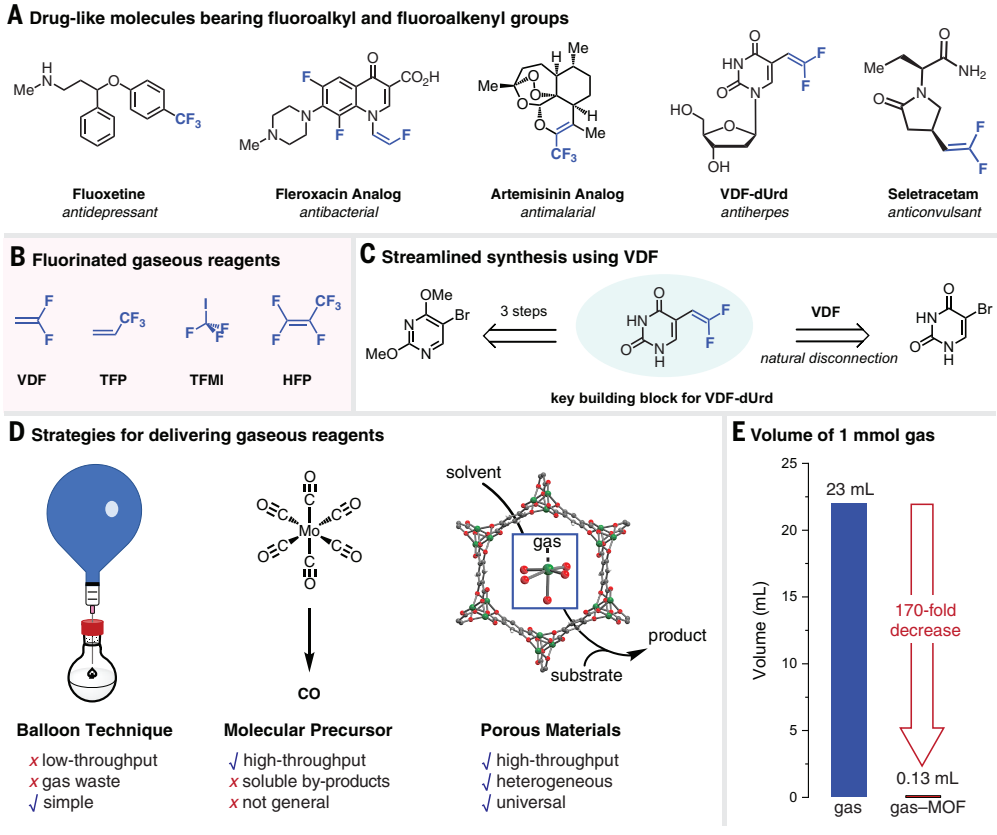

Fig. 1. Delivery of fluorinated gases using MOFs. (**A**) Examples of drug-like molecules bearing fluoroalkyl and fluoroalkenyl groups. dUrd, 2′-deoxyuridine; Me, methyl. (**B**) Fluorinated gaseous building blocks. (**C**) Streamlined synthesis using VDF (*6*). (**D**) Overview of gas-reagent delivery strategies, including balloons, generation from molecular precursors, and release from porous materials (this work). (**E**) The volume of 1 mmol of an ideal gas compared with 1 mmol of gas contained in a MOF [Mg_2(dobdc) with a crystallographic density of 0.909 g/cm^3 (*73*, *74*) and one gas molecule per metal site].

destructive gases. Although the latter approach is amenable to high-throughput screening, it requires the design of a new delivery strategy for each gas and results in soluble by-products that must be separated from the desired products. We hypothesized that the reversible adsorption of fluorinated gases within porous solids should allow for their facile handling as recyclable solid reagents, overcoming the limitations outlined above and facilitating the development of methods for fluorinating complex molecules (Fig. 1D, right). Among porous solids, metal-organic frameworks (MOFs), which are crystalline materials constructed from organic linkers and inorganic nodes, are distinctively modular, allowing for the optimization of storage capacity and enthalpy of adsorption ($-\Delta H_{ads}$) for any gas of interest (*18*–*20*). In particular, MOFs that bear coordinatively unsaturated metal centers (open metal sites) (*21*) should reversibly bind synthetically relevant fluorinated gases through strong metal-fluorine (M-F) interactions (*22*, *23*). Owing to the high theoretical gravimetric and volumetric capacities of MOFs such as Mg_2(dobdc) ($dobdc^{4-}$ is 2,5-dioxidobenzene-1,4-dicarboxylate) (*24*), 1 mmol (23 ml) of gas can be delivered with as little as 120 mg (0.13 ml) of MOF, resulting in a staggering ~170-fold volume reduction compared with a free ideal gas (Fig. 1E). In this work, we demonstrate that the commodity fluorinated gases VDF, TFP, HFP, and TFMI can be stored within MOFs and handled as solid reagents, enabling their facile use in otherwise challenging fluoroalkylation and fluorovinylation reactions.

Selection of the optimal MOF for fluorinated gas storage

To be useful for controlled fluorinated gas delivery, a porous material should possess a high gas sorption capacity, interact strongly with a range of fluorinated gases to prevent undesired gas leakage, and be stable toward long-term storage on the benchtop. Given the scarcity of available data regarding the adsorption of fluorinated commodity chemicals within porous solids, we commenced by studying VDF uptake in 12 representative open-metal-site MOFs, including HKUST-1 or Cu_3(btc)$_2$ (btc^{3-} is benzene-1,3,5-tricarboxylate) (*25*), MIL-100(Fe) or Fe_3(O)(OH)(btc)$_2$ (*26*), NH_2-MIL-101(Al) or Al_3(O)(OH)(NH_2-bdc)$_3$ (NH_2-bdc^{2-} is 2-aminobenzene-1,4-dicarboxylate) (*27*), MOF-74 or M_2(dobdc) (M is Mg, Mn, Fe, Co, Ni, Cu, or Zn) (*28*), and *m*-MOF-74 or M_2(*m*-dobdc) (M is Mg or Ni; *m*-$dobdc^{4-}$ is 4,6-dioxidobenzene-1,3-dicarboxylate) (*29*) (see fig. S2 for structures). We also investigated one commercially available zeolite that bears accessible Na^+ sites (Zeolite Y). To identify the optimal material for fluorinated gas delivery, VDF adsorption and desorption isotherms were collected for all materials at 30°, 40°, and 50°C. Notably, VDF adsorption was found to be fully reversible in every case. The isotherm data were used to determine the gravimetric VDF storage capacities at 30°C and 1 bar of VDF (vertical axis of Fig. 2A, fig. S80, and table S23). Among the tested materials, Mg_2(dobdc) (7.95 mmol/g, 34 wt %) and Cu_3(btc)$_2$ (7.64 mmol/g, 33 wt %) possess the highest VDF gravimetric capacities, which is expected given their high densities of open metal sites and low molecular weights. Beyond storage capacity, the enthalpy of adsorption ($-\Delta H_{ads}$) is critical for governing how readily fluorinated gases would be released in situ or under ambient conditions. To calculate $-\Delta H_{ads}$ values, all adsorption isotherms were fit using dual-site Langmuir models. Using the Clausius-Clapeyron equation, we determined the $-\Delta H_{ads}$ values as a function of VDF loading for each material; $-\Delta H_{ads}$ values at a loading of 1 mmol/g are included for comparison in Fig. 2A (horizontal axis). In general, materials that bear highly Lewis acidic Mg^{2+}, Ni^{2+}, or Na^+ sites—namely M_2(dobdc) (M is Mg or Ni), M_2(*m*-dobdc) (M is Mg or Ni), and Zeolite Y—demonstrate the strongest adsorption of VDF (38 to 41 kJ/mol). This is likely due in part to the hard-soft acid-base match of hard fluorine atoms with hard metal centers (*22*).

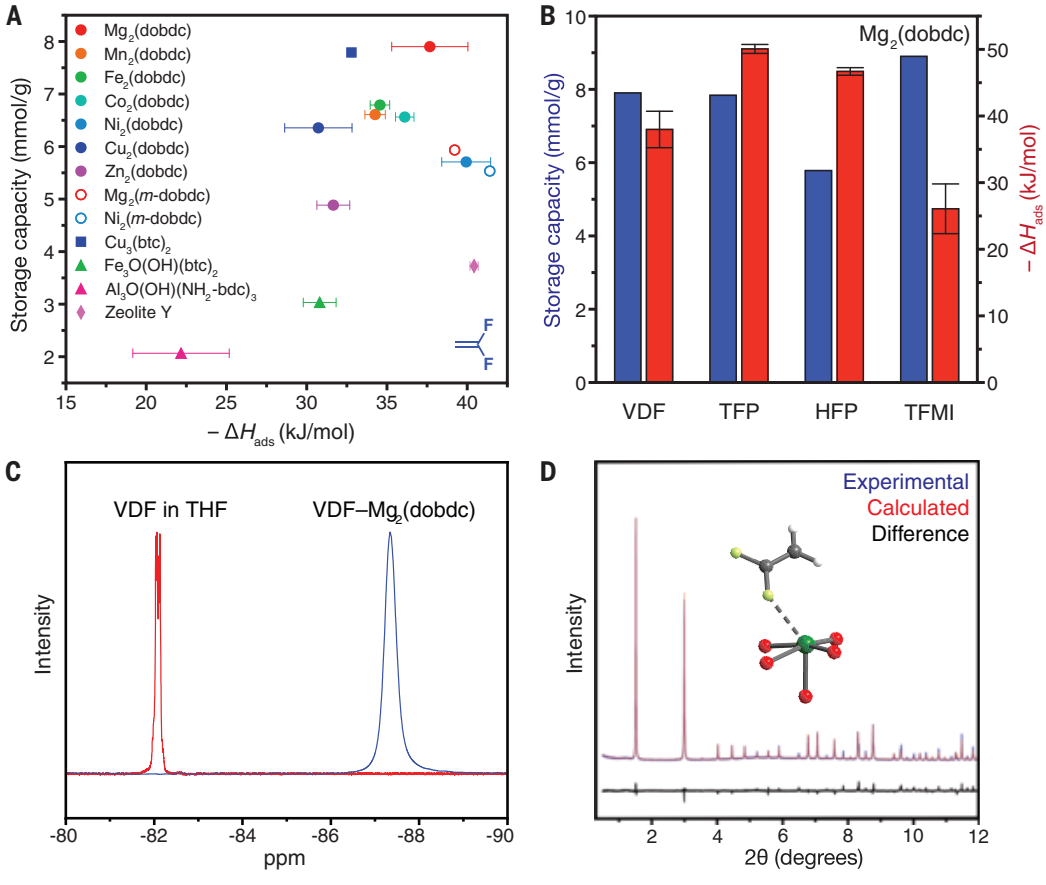

Fig. 2. Fluorinated gas adsorption in open-metal-site materials. (**A**) Comparison of storage capacity and binding enthalpy for VDF in porous materials. The binding enthalpies and associated errors were determined using linear fits to the Clausius-Clapeyron equation. (**B**) Comparison of storage capacity (blue) and binding enthalpy (red) for fluorinated gases in Mg_2(dobdc). The binding enthalpies and associated errors were determined using linear fits to the Clausius-Clapeyron equation. (**C**) MAS ^{19}F solid-state NMR spectrum of VDF-Mg_2(dobdc) (blue) compared with solution-state ^{19}F NMR spectrum of VDF in THF (red). (**D**) Rietveld refinement of VDF-Mg_2(dobdc). Measured diffraction data (blue), fitted pattern (red), and the difference (black) are shown. Weighted residual factor (R_{wp}) = 11.9%. The inset shows the structural model for VDF-Mg_2(dobdc).

Because Mg_2(dobdc), Ni_2(dobdc), and Ni_2(*m*-dobdc) display high VDF gravimetric storage capacities coupled with strong binding, their ability to adsorb the fluorinated gases TFP, HFP, and TFMI was also evaluated (Fig. 2B, fig. S81, and table S24). Because of its lower molecular weight, Mg_2(dobdc) exhibits a higher gravimetric capacity for each gas at 1 bar and 30°C than Ni_2(dobdc) and Ni_2(*m*-dobdc). In addition, the $-\Delta H_{ads}$ values for TFP and TFMI in Mg_2(dobdc) are larger in magnitude than the corresponding values in the Ni-based frameworks, whereas the strength of HFP binding is comparable across all three frameworks. Collectively, the adsorption data suggest that Mg_2(dobdc) is an ideal framework for the storage of fluorinated gases because of its high gravimetric capacity and strong interaction with multiple gases of synthetic interest. Further supporting its superiority as a practical gas storage medium, Mg_2(dobdc) retains its crystallinity and porosity after a week of standing on the benchtop at RT (figs. S93 and S94) and is stable in air at 120°C for 24 hours (*30*). To demonstrate the potential for commercialization of Mg_2(dobdc), we developed a new high-concentration aqueous synthesis that allows for >100 g of material to be prepared in a single batch (figs. S10 and S11).

The nature of the interaction between Mg_2(dobdc) and VDF (as a representative fluorinated gas) was probed using a range of experimental and computational techniques (Fig. 2, C and D; figs. S82 and S96; and table S25). Magic-angle spinning (MAS) ^{19}F solid-state nuclear magnetic resonance (NMR) measurements were performed on VDF-Mg_2(dobdc) (Fig. 2C and fig. S96). The resonance corresponding to VDF-Mg_2(dobdc) [−87.34 parts per million (ppm)] is shifted upfield and broadened relative to that of VDF dissolved in tetrahydrofuran (THF) (−82.09 ppm) (Fig. 2C and fig. S96). The greater shielding that is observed for VDF bound within the MOF is due to the proximity of π electron density from the aromatic linkers, and the signal broadening is due to immobilization (*22*, *31*). The preferred binding mode of VDF in Mg_2(dobdc) was further interrogated by synchrotron powder x-ray diffraction (PXRD) conducted on a sample of microcrystalline Mg_2(dobdc) dosed with ~100 mbar of VDF (Fig. 2D). Rietveld refinement of the obtained pattern corroborated a structural model in which VDF preferentially binds to the open Mg^{2+} site through a F···Mg interaction, not through the alkene π-bond (inset of Fig. 2D). The F···Mg distance is 2.67(3) Å, which is similar to the distances reported for related experimental and calculated structures (*22*, *23*). Density functional theory calculations further support that the F-bound structure for VDF-Mg_2(dobdc) possesses a predicted binding enthalpy ($-\Delta H_b$ = 37.5 kJ/mol) similar to the experimental value ($-\Delta H_{ads}$ = 37.7 kJ/mol) (fig. S82 and table S25). Indeed, the calculated F-bound structures for TFP, HFP, and TFMI all possess predicted binding enthalpies that are similar to the experimental values (fig. S82 and table S25). Overall, these data support that the strong binding of fluorinated gases in Mg_2(dobdc) is due to the favorable interaction between the hard Lewis basic F atoms and the hard Lewis acidic Mg^{2+} open metal sites in Mg_2(dobdc).

Application to solution-phase reactions

Building on these results, we investigated whether gas-Mg_2(dobdc) reagents can be used to deliver fluorinated gases under synthetically relevant conditions. Activated Mg_2(dobdc) was dosed with VDF, and the resulting gas-MOF reagent was loaded into a custom-built, air-free solid-addition funnel to enable controlled delivery into solution (Fig. 3A). ^{19}F NMR analysis confirmed that this approach facilitates rapid VDF release into solvents of varying polarity within 10 min (Fig. 3A and figs. S89 to S92). To further control the kinetics of gas release into solution, we loaded VDF-Mg_2(dobdc) into a gas-tight wax capsule (fig. S87) (*32*). When the encapsulated VDF-Mg_2(dobdc) was suspended in *N*,*N*-dimethylformamide (DMF), no VDF was detected in solution after an hour. This result suggests that the wax capsules are impermeable to VDF, representing a leak-proof encapsulation strategy. Simple sonication of the reaction mixture breaks the capsule open and dispenses VDF-Mg_2(dobdc), triggering the complete discharge of VDF into solution. These practical, single-use reagents enable high-throughput screening of reactions involving gases while preventing direct exposure to the gas and circumventing the need for complex equipment (*11*, *12*).

To explore the utility of gas-MOF reagents in synthetic chemistry, we envisioned that a desirable yet unrealized transformation would be the defluorinative coupling of VDF with easily handled (hetero)aryl nucleophiles to yield α-fluorostyrenes (*33*). Owing to their topological, electronic, and steric similarities (*34*), monofluoroalkenes have been widely used as amide bioisosteres in drug and peptidomimetic design (*34*–*36*). Traditional synthetic routes to access terminal α-fluoroalkenes through alkyne or alkene functionalization pathways suffer from key drawbacks such as multistep starting material syntheses, harsh or hazardous reaction conditions, poor regioselectivity, and/or modest scopes (*37*–*39*). Meanwhile, previously reported metal-catalyzed cross-coupling routes to prepare α-fluorostyrenes require air-sensitive starting materials and/or specialized equipment to handle gaseous VDF (*40*–*44*). To design a more streamlined protocol, we used VDF-Mg_2(dobdc) to enable a base-free, defluorinative Suzuki-Miyaura coupling (*45*) with (hetero)aryl boronic acids (Fig. 3B), representing a straightforward route to access α-fluorostyrenes. Without the need to handle gaseous reagents, we simply combined 4-biphenylboronic acid and VDF-Mg_2(dobdc) at RT using palladium trifluoroacetate [$Pd(TFA)_2$] as the catalyst, 4,4′-di-tert-butyl-2,2′-bipyridine (dtbbpy) as the ligand, and DMF as the solvent to obtain the α-fluorostyrene product in 23% yield (table S26, entry 1). Although reactions that involve reactive gases are typically low throughput, using VDF-Mg_2(dobdc) enables the setup of multiple reactions in parallel, streamlining the optimization process (table S26). An investigation of catalysts, solvents, temperatures, and concentrations revealed that the use of catalytic $Pd(TFA)_2$(dtbbpy) and a reaction concentration of 50 mM (with respect to the arylboronic acid) leads to nearly quantitative yield (table S26, entry 23). Critically, the equivalents of VDF can be adjusted by modifying the amount of VDF-Mg_2(dobdc) added to the reaction; doing so revealed that the reaction proceeds well using either four or eight equivalents of VDF (table S26, entries 23 and 24). The optimized defluorinative coupling protocol proceeds smoothly with a variety of (hetero)arylboronic acid substrates, furnishing the α-fluorostyrene products in good isolated yields (Fig. 3B). We obtained comparable yields using either freshly prepared VDF-Mg_2(dobdc) dispensed from a gas-tight solid-addition funnel or wax-encapsulated VDF-Mg_2(dobdc) reagents after a day of storage on the benchtop. After a successful reaction, the MOF was recovered and found to retain its crystallinity by PXRD, suggesting that it can potentially be recycled (fig. S95). Using a balloon of VDF in place of VDF-Mg_2(dobdc) affords the product in slightly lower yield [67% compared with 80% with VDF-Mg_2(dobdc)], demonstrating that our strategy is competitive with conventional gas delivery techniques. Given the simplicity of the protocol reported herein, we expect that it will find broad use for the synthesis of functionalized α-fluorostyrenes.

Scattered reports in the literature suggest that the coupling of HFP with aryl magnesium bromides (*46*) or arylboronic acid neopentylglycol esters (*47*) results in mixtures of stereo- and regioisomers. We sought to expand the scope of our defluorinative coupling of VDF and commercially available (hetero)arylboronic acids (Fig. 3B) to achieve a similar reaction using HFP-Mg_2(dobdc). Our preliminary efforts led to the defluorinative coupling of HFP and 4-biphenylboronic acid to furnish a 1:1 *E*:*Z* mixture of pentafluoropropene-substituted products (Fig. 3C). This result demonstrates how the use of gas-MOF reagents enables reaction development with multiple gases without needing to change cylinders attached to complicated manifolds.

Long-term stability of gas-MOF reagents

To probe the long-term storability of gas-Mg_2(dobdc) reagents, we evaluated their performance in the

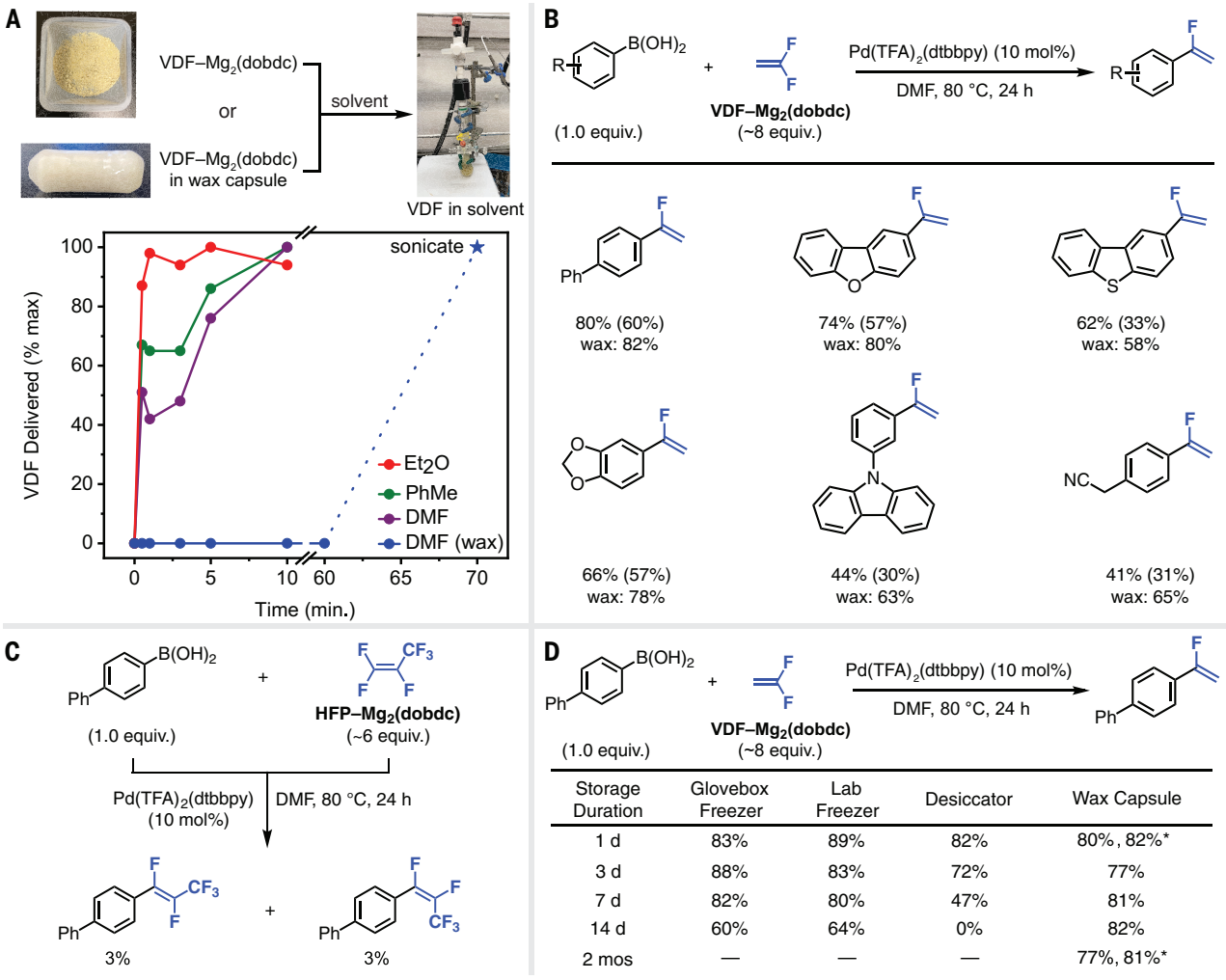

Storage Duration	Glovebox Freezer	Lab Freezer	Desiccator	Wax Capsule
1 d	83%	89%	82%	80%, 82%*
3 d	88%	83%	72%	77%
7 d	82%	80%	47%	81%
14 d	60%	64%	0%	82%
2 mos	—	—	—	77%, 81%*

Fig. 3. Delivery and synthetic transformations of VDF and HFP. NMR yields were determined by ^{19}F NMR integration using fluorobenzene as an internal standard. See supplementary materials for experimental details. (**A**) Percentage of VDF delivered to solution (determined by ^{19}F NMR) from freshly prepared VDF-Mg_2(dobdc) or wax-encapsulated VDF-Mg_2(dobdc). Ph, phenyl. (**B**) Scope of Pd-catalyzed defluorinative coupling of VDF and (hetero)arylboronic acids using VDF-Mg_2(dobdc). ^{19}F NMR yields are given with isolated yields shown in parentheses. For the reactions corresponding to the yields in the first row, VDF-Mg_2(dobdc) was freshly prepared and dispensed using a solid-addition funnel. For the reactions corresponding to the yields in the second row, VDF-Mg_2(dobdc) wax capsules were stored on the benchtop for 24 hours before they were broken to dispense VDF-Mg_2(dobdc). R, functional group. (**C**) Pd-catalyzed defluorinative coupling of HFP and arylboronic acids using HFP-Mg_2(dobdc). (**D**) Performance of VDF-Mg_2(dobdc) in defluorinative coupling with 4-biphenylboronic acid after storage under different conditions. An asterisk indicates that the wax capsule was cut open before dispensing VDF-Mg_2(dobdc); a dash indicates not determined.

defluorinative coupling of VDF and 4-biphenylboronic acid after storage under different conditions for up to 2 months (Fig. 3D). Bulk samples of VDF-Mg_2(dobdc) can be stored at −30°C under an inert atmosphere or at −20°C in air for up to 7 days with negligible loss in performance; only a minor decrease in yield was observed after storage for 14 days (glovebox and lab freezer in Fig. 3D and table S32). Storage of VDF-Mg_2(dobdc) in a desiccator at RT for 1 day resulted in the same yield as standard conditions, whereas storage in a desiccator for up to 1 week still afforded the product in good yield (desiccator in Fig. 3D and table S32). Leaving VDF-Mg_2(dobdc) on the benchtop in air at RT overnight before adding it to the reaction also produced a good yield of product (table S31, entry 3). Together, these results suggest that slow gas loss from bulk VDF-Mg_2(dobdc) is largely driven by entropic effects and that gas-MOF reagents are stable under ambient conditions as long as they are kept cold. To further improve the long-term stability and safety of the gas-MOF reagents at RT, we evaluated whether storage within wax capsules arrests gas loss under ambient conditions. Indeed, storage of VDF-Mg_2(dobdc) in a wax capsule on the benchtop at RT for 2 months before adding it to the reaction produced a comparable yield to that obtained using freshly prepared VDF-Mg_2(dobdc) (wax capsule in Fig. 3D and table S32). Either adding the wax capsule directly (followed by sonication) or cutting it open to dispense VDF-Mg_2(dobdc) to the reaction mixture resulted in similar yields of the product. As such, wax-encapsulated gas-Mg_2(dobdc) represents a bench-stable reagent for gas delivery on demand and provides a safer alternative to handling the gas-MOF powder directly.

Further synthetic applications

Beyond functionalizing the C–F bond of VDF to produce α-fluorostyrenes, we envisaged diversification of the C–H bond to produce β,β-difluorostyrenes as well. *Gem*-difluoroalkenes are of particular interest in medicinal chemistry because they are bioisosteres for carbonyl groups (*4*, *6*, *48*–*50*). For example, the antimalarial activity of artemisinin can be improved by replacing the ester carbonyl group with a *gem*-difluoroalkene (*4*). Standard protocols to install

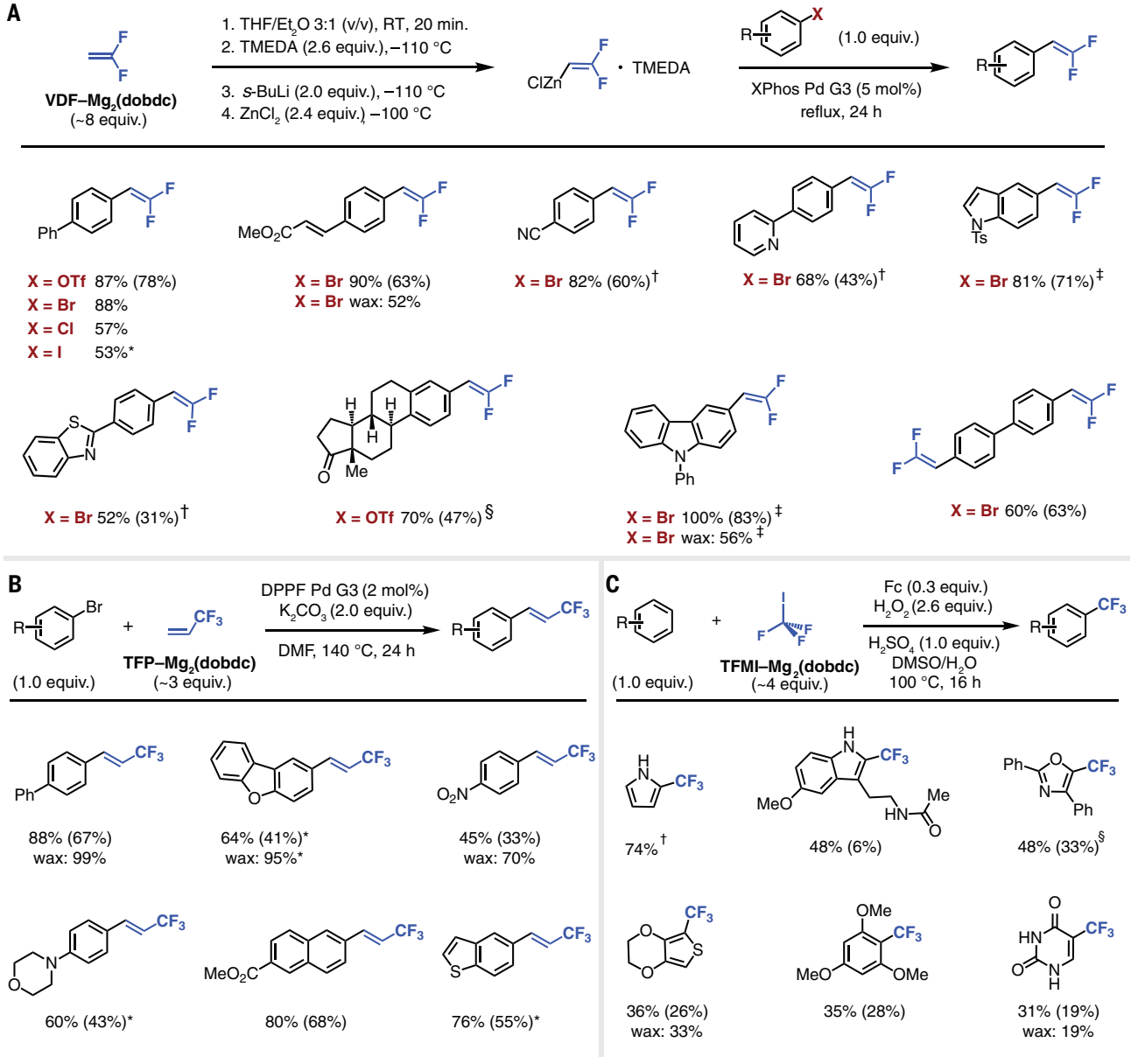

Fig. 4. Generalizability of gas-MOF delivery. ^{19}F NMR yields are given with isolated yields shown in parentheses. NMR yields were determined by ^{19}F NMR spectroscopy using fluorobenzene as an internal standard. See supplementary materials for experimental details. For the reactions corresponding to the yields in the first row, gas-Mg_2(dobdc) was freshly prepared and dispensed using a solid-addition funnel. For the reactions corresponding to the yields in the second row, gas-Mg_2(dobdc) wax capsules were stored on the benchtop for 24 hours before they were broken to dispense gas-Mg_2(dobdc). (**A**) Scope of Negishi coupling of (hetero)aryl halides and VDF-ZnCl•TMEDA synthesized from VDF-Mg_2(dobdc). OTf, trifluoromethanesulfonate; *s*-BuLi, *sec*-butyllithium; Ts, *p*-toluenesulfonyl. *$Pd(PPh_3)_4$; †8 hours, 10 mol % XPhos Pd G3; ‡18 hours, 10 mol % XPhos Pd G3; §11 hours, 10 mol % XPhos Pd G3. (**B**) Scope of Pd-catalyzed Heck coupling of (hetero)aryl bromides and TFP using TFP-Mg_2(dobdc). *XantPhos Pd G3 (2 mol %) and tetrabutylammonium bromide (1 equivalent). (**C**) Scope of Fe-catalyzed trifluoromethylation of (hetero)arenes using TFMI-Mg_2(dobdc). Fc, ferrocene. †0.15 mmol $FeSO_4{\cdot}7H_2O$ (0.3 equivalents), 50°C; §50°C.

gem-difluoroalkenes via carbonyl olefination reactions or defluorination of trifluoromethylated alkenes involve the use of complex starting materials or reagents and suffer from poor selectivity or modest scopes owing to the harsh reaction conditions (*51*–*57*). The development of cross-coupling methods has led to *gem*-difluorovinylating reagents, including 2,2-difluorovinyl pinacolboranes (*58*), 2,2-difluorovinylstannanes (*59*, *60*), and 2,2-difluorovinyl tosylates (*61*, *62*). However, these reagents are not bench stable, and their preparation entails complex synthesis and isolation procedures. As such, access to β,β-difluorostyrene analogs directly from readily available (hetero)aryl halides and VDF represents a desirable transformation. We used VDF-Mg_2(dobdc) to prepare 2,2-difluorovinylzinc chloride–*N*,*N*,*N*′,*N*′-tetramethylenediamine (VDF-ZnCl•TMEDA), which can be engaged in Pd-catalyzed Negishi couplings with (hetero)aryl halides to yield β,β-difluorostyrenes (*63*) (Fig. 4A). A brief reaction optimization revealed that the combination of VDF-ZnCl•TMEDA and catalytic amounts of XPhos Pd G3 (see fig. S1 for structure) in THF and Et_2O (Et_2O is diethyl ether) at reflux affords the β,β-difluorostyrene products from (hetero)aryl bromides in excellent yields (table S27, entry 3). Notably, despite exposure to strongly nucleophilic and basic conditions, Mg_2(dobdc) retains its crystallinity

after the reaction (fig. S95). Moreover, a variety of electrophilic functional groups (esters, nitriles, ketones) are compatible with this protocol, and they do not undergo nucleophilic attack by the organozinc reagent. Further, difluorovinyl groups can be successfully installed onto substrates containing *N*-heterocycles (pyridine, carbazole, indole, and thiazole) as well as biologically active molecules (estrone). Finally, this procedure can be extended to achieve a double coupling with an aryl dibromide, which produces the bis(difluorovinyl)ated product in good yield. Even with the use of air-sensitive reagents to generate VDF-ZnCl•TMEDA, delivery of VDF-Mg_2(dobdc) from day-old wax capsules results in comparable yields. The developed method represents a general approach to prepare β,β-difluorostyrenes under mild conditions.

We sought to further explore the generality of our delivery strategy by using Mg_2(dobdc) to deliver other fluorinated gases, namely TFP and TFMI. Similar to fluoroalkenes, trifluoromethylated alkenes have been used as amide mimics in medicinal chemistry (*64*). Conventionally, β-trifluoromethylstyrenes are constructed via the transition metal–catalyzed trifluoromethylation of β-halostyrenes (*65*); however, the lack of available β-halostyrene substrates severely limits the reaction scope. Previously reported Pd-catalyzed Heck reactions of TFP and aryl halides suffer from long reaction times, dependence on specialized equipment (e.g., high-pressure reactor autoclaves), the need to generate TFP in situ, and/or limited scopes (*16*, *66*). Building on these precedents, we used TFP-Mg_2(dobdc) reagents to deliver TFP for Heck coupling reactions with electronically diverse (hetero)aryl bromides to access a broad scope of β-trifluoromethylstyrenes (Fig. 4B). We investigated the Pd-catalyzed reaction of 4-bromobiphenyl with TFP under standard Heck coupling conditions using palladium acetate [$Pd(OAc)_2$] as the catalyst, potassium carbonate (K_2CO_3) as the base, and DMF as the solvent at 150°C, which afforded the β-trifluoromethylstyrene product in 17% yield (table S28, entry 1). During an investigation of a variety of Pd catalysts, we found that the use of DPPF Pd G3 (see fig. S1 for structure) leads to synthetically useful yields (table S28, entry 3). Although electron-neutral and -deficient aryl bromides react efficiently under these conditions, electron-rich derivatives exhibit sluggish reactivity. The simplicity of working with TFP-Mg_2(dobdc) enabled us to quickly survey different Pd catalysts and discover that the use of XantPhos Pd G3 (see fig. S1 for structure) in conjunction with tetrabutylammonium bromide (TBAB) as a phase transfer catalyst leads to improved yields for these challenging substrates (table S29, entry 6). With optimized conditions in hand, we expanded the reaction scope to an array of (hetero)aryl bromides bearing a variety of functional groups, which furnished the β-trifluoromethylstyrene products in good yields (Fig. 4B). Similar to VDF-Mg_2(dobdc), other gas-MOF reagents can be stored in wax capsules for 24 hours on the benchtop before use. Delivery of TFP-Mg_2(dobdc) from wax capsules results in excellent yields of β-trifluoromethylstyrenes.

We next used TFMI-Mg_2(dobdc) reagents to introduce valuable trifluoromethyl groups into (hetero)aromatic compounds (Fig. 4C). Trifluoromethyl groups are common in drugs (*67*) and appear in ~19% of fluorinated pharmaceuticals (*68*). TFMI represents an inexpensive and safe reagent for generating trifluoromethyl radicals (*17*, *69*–*72*). Compared with traditional Ru-based (*71*, *72*) or Ir-based (*70*) photoredox catalysis, Fe salts (*69*) are inexpensive potential catalysts for oxidatively generating trifluoromethyl radicals from TFMI under Fenton-like conditions without the need for complicated reaction setups or light irradiation. As such, we focused on developing a general procedure for radical, Minisci-like (hetero)arene trifluoromethylation using Fe catalysts. A brief optimization using uracil as the model substrate revealed that the combination of TFMI-Mg_2(dobdc), ferrocene, hydrogen peroxide (H_2O_2), and sulfuric acid (H_2SO_4) in dimethyl sulfoxide (DMSO) and H_2O at 100°C affords the trifluoromethylated product in good yield (table S30, entry 3). These conditions can be applied to a variety of substrates, including five-membered heteroarenes (pyrrole, indole, oxazole) and biologically active molecules (melatonin and uracil). Delivery of TFMI-Mg_2(dobdc) from wax capsules leads to similar yields as those obtained under standard conditions. Although the major product is accompanied by trifluoromethylation at other positions, isolation of the desired isomer in every case is possible with flash chromatography.

Collectively, we have demonstrated that gas-Mg_2(dobdc) reagents can be handled as free-flowing solids and used under synthetically relevant conditions to streamline a series of fluorovinylation and trifluoromethylation reactions. The bulk gas-Mg_2(dobdc) solids can be stored long-term (at low temperatures) for use in multiple reactions on different days or embedded within wax capsules to produce safer, indefinitely bench-stable reagents. Because gas-MOF powders are prone to slow gas loss over time, they should be generated on-site before use. As a safer option, we expect that wax-encapsulated gas-MOF reagents will be more widely adopted by synthetic chemists who are interested in reaction development using fluorinated gaseous reagents. Although we focus on fluorinated gases in this work, this strategy can, in principle, be generalized to the practical delivery of other gaseous reagents of interest to synthetic organic and medicinal chemists. We expect that these stable gas-MOF reagents will streamline the optimization of a myriad of transformations.

REFERENCES AND NOTES

1. E. P. Gillis, K. J. Eastman, M. D. Hill, D. J. Donnelly, N. A. Meanwell, *J. Med. Chem.* **58**, 8315–8359 (2015).
2. T. Fujiwara, D. O'Hagan, *J. Fluor. Chem.* **167**, 16–29 (2014).
3. Y. Asahina, K. Iwase, F. Iinuma, M. Hosaka, T. Ishizaki, *J. Med. Chem.* **48**, 3194–3202 (2005).
4. G. Magueur, B. Crousse, M. Ourévitch, D. Bonnet-Delpon, J.-P. Bégué, *J. Fluor. Chem.* **127**, 637–642 (2006).
5. J.-P. Bégué, D. Bonnet-Delpon, *ChemMedChem* **2**, 608–624 (2007).
6. M. Bobek, I. Kavai, E. De Clercq, *J. Med. Chem.* **30**, 1494–1497 (1987).
7. R. Halder, T. Ritter, *J. Org. Chem.* **86**, 13873–13884 (2021).
8. S. Caron, *Org. Process Res. Dev.* **24**, 470–480 (2020).
9. R. Szpera, D. F. J. Moseley, L. B. Smith, A. J. Sterling, V. Gouverneur, *Angew. Chem. Int. Ed.* **58**, 14824–14848 (2019).
10. T. Liang, C. N. Neumann, T. Ritter, *Angew. Chem. Int. Ed.* **52**, 8214–8264 (2013).
11. C. S. Shultz, S. W. Krska, *Acc. Chem. Res.* **40**, 1320–1326 (2007).
12. M. Shevlin, *ACS Med. Chem. Lett.* **8**, 601–607 (2017).
13. G. J. M. Velders, D. W. Fahey, J. S. Daniel, M. McFarland, S. O. Andersen, *Proc. Natl. Acad. Sci. U.S.A.* **106**, 10949–10954 (2009).
14. N.-F. K. Kaiser, A. Hallberg, M. Larhed, *J. Comb. Chem.* **4**, 109–111 (2002).
15. J. Demaerel, C. Veryser, W. M. De Borggraeve, *React. Chem. Eng.* **5**, 615–631 (2020).
16. G. K. S. Prakash, H. S. Krishnan, P. V. Jog, A. P. Iyer, G. A. Olah, *Org. Lett.* **14**, 1146–1149 (2012).
17. F. Sladojevich, E. McNeill, J. Börgel, S.-L. Zheng, T. Ritter, *Angew. Chem. Int. Ed.* **54**, 3712–3716 (2015).
18. H. Furukawa, K. E. Cordova, M. O'Keeffe, O. M. Yaghi, *Science* **341**, 1230444 (2013).
19. H. Li *et al.*, *Mater. Today* **21**, 108–121 (2018).
20. P. Kittikhunnatham *et al.*, *Angew. Chem. Int. Ed.* **61**, e202113909 (2022).
21. Ü. Kökçam-Demir *et al.*, *Chem. Soc. Rev.* **49**, 2751–2798 (2020).
22. M. E. Zick *et al.*, *J. Am. Chem. Soc.* **143**, 1948–1958 (2021).
23. J. Zheng *et al.*, *J. Am. Chem. Soc.* **142**, 3002–3012 (2020).
24. S. R. Caskey, A. G. Wong-Foy, A. J. Matzger, *J. Am. Chem. Soc.* **130**, 10870–10871 (2008).
25. S. S.-Y. Chui, S. M.-F. Lo, J. P. H. Charmant, A. G. Orpen, I. D. Williams, *Science* **283**, 1148–1150 (1999).
26. P. Horcajada *et al.*, *Chem. Commun.* **2007**, 2820–2822 (2007).
27. P. Serra-Crespo, E. V. Ramos-Fernandez, J. Gascon, F. Kapteijn, *Chem. Mater.* **23**, 2565–2572 (2011).
28. N. L. Rosi *et al.*, *J. Am. Chem. Soc.* **127**, 1504–1518 (2005).
29. M. T. Kapelewski *et al.*, *J. Am. Chem. Soc.* **136**, 12119–12129 (2014).
30. Z. Wang, A. Bilegsaikhan, R. T. Jerozal, T. A. Pitt, P. J. Milner, *ACS Appl. Mater. Interfaces* **13**, 17517–17531 (2021).
31. A. C. Forse, J. M. Griffin, V. Presser, Y. Gogotsi, C. P. Grey, *J. Phys. Chem. C* **118**, 7508–7514 (2014).
32. A. C. Sather, H. G. Lee, J. R. Colombe, A. Zhang, S. L. Buchwald, *Nature* **524**, 208–211 (2015).
33. M. Drouin, J.-D. Hamel, J.-F. Paquin, *Synthesis* **50**, 881–955 (2018).
34. M. Drouin, J.-F. Paquin, *Beilstein J. Org. Chem.* **13**, 2637–2658 (2017).
35. J. J. Urban, B. G. Tillman, W. A. Cronin, *J. Phys. Chem. A* **110**, 11120–11129 (2006).
36. S. Couve-Bonnaire, D. Cahard, X. Pannecoucke, *Org. Biomol. Chem.* **5**, 1151–1157 (2007).
37. K. Matsuda, J. A. Sedlak, J. S. Noland, G. C. Gleckler, *J. Org. Chem.* **27**, 4015–4020 (1962).
38. H. Suga, T. Hamatani, Y. Guggisberg, M. Schlosser, *Tetrahedron* **46**, 4255–4260 (1990).
39. J. R. McCarthy, D. P. Matthews, C. L. Barney, *Tetrahedron Lett.* **31**, 973–976 (1990).
40. J. Qiu, A. Gyorokos, T. M. Tarasow, J. Guiles, *J. Org. Chem.* **73**, 9775–9777 (2008).
41. T. Hanamoto, T. Kobayashi, M. Kondo, *Synlett* **2001**, 0281–0283 (2001).
42. T. Hanamoto, T. Kobayashi, *J. Org. Chem.* **68**, 6354–6359 (2003).
43. W. Heitz, A. Knebelkamp, *Makromol. Chem., Rapid Commun.* **12**, 69–75 (1991).

44. A. Knebelkamp, W. Heitz, *Makromol. Chem., Rapid. Commun.* **12**, 597–606 (1991).
45. C. A. Malapit, J. R. Bour, C. E. Brigham, M. S. Sanford, *Nature* **563**, 100–104 (2018).
46. W. Dmowski, *J. Fluor. Chem.* **18**, 25–30 (1981).
47. M. Ohashi, H. Saijo, M. Shibata, S. Ogoshi, *Eur. J. Org. Chem.* **2013**, 443–447 (2013).
48. C. Leriche, X. He, C. W. Chang, H. W. Liu, *J. Am. Chem. Soc.* **125**, 6348–6349 (2003).
49. J.-M. Altenburger *et al*., *Bioorg. Med. Chem.* **12**, 1713–1730 (2004).
50. S. Messaoudi *et al*., *J. Med. Chem.* **52**, 4538–4542 (2009).
51. X. Zhang, S. Cao, *Tetrahedron Lett.* **58**, 375–392 (2017).
52. B. Gao, Y. Zhao, M. Hu, C. Ni, J. Hu, *Chemistry* **20**, 7803–7810 (2014).
53. I. Nowak, M. J. Robins, *Org. Lett.* **7**, 721–724 (2005).
54. Y. Huang, T. Hayashi, *J. Am. Chem. Soc.* **138**, 12340–12343 (2016).
55. J. P. Phelan *et al*., *J. Am. Chem. Soc.* **141**, 3723–3732 (2019).
56. J. Ichikawa, *J. Synth. Org. Chem. Jpn.* **68**, 1175–1184 (2010).
57. J. Zhang, J.-D. Yang, J.-P. Cheng, *Nat. Commun.* **12**, 2835 (2021).
58. O. P. Blahun *et al*., *Eur. J. Org. Chem.* **2019**, 6417–6421 (2019).
59. L. Lu, D. J. Burton, *J. Fluor. Chem.* **133**, 16–19 (2012).
60. S. Y. Han, I. H. Jeong, *Org. Lett.* **12**, 5518–5521 (2010).
61. T. M. Gøgsig, L. S. Søbjerg, A. T. Lindhardt, K. L. Jensen, T. Skrydstrup, *J. Org. Chem.* **73**, 3404–3410 (2008).
62. B. Xiong *et al*., *ACS Catal.* **10**, 13616–13623 (2020).
63. T. Fujita, T. Ichitsuka, K. Fuchibe, J. Ichikawa, *Chem. Lett.* **40**, 986–988 (2011).
64. J. Xiao, B. Weisblum, P. Wipf, *J. Am. Chem. Soc.* **127**, 5742–5743 (2005).
65. T. Kitazume, N. Ishikawa, *J. Am. Chem. Soc.* **107**, 5186–5191 (1985).
66. T. Fuchikami, M. Yatabe, I. Ojima, *Synthesis* **1981**, 365–366 (1981).
67. A. S. Nair *et al*., *Processes* **10**, 2054 (2022).
68. M. Inoue, Y. Sumii, N. Shibata, *ACS Omega* **5**, 10633–10640 (2020).
69. T. Kino *et al*., *J. Fluor. Chem.* **131**, 98–105 (2010).
70. D. A. Nagib, M. E. Scott, D. W. C. MacMillan, *J. Am. Chem. Soc.* **131**, 10875–10877 (2009).
71. P. V. Pham, D. A. Nagib, D. W. C. MacMillan, *Angew. Chem. Int. Ed.* **50**, 6119–6122 (2011).
72. Y. Ye, M. S. Sanford, *J. Am. Chem. Soc.* **134**, 9034–9037 (2012).
73. J. A. Mason, M. Veenstra, J. R. Long, *Chem. Sci.* **5**, 32–51 (2014).
74. W. L. Queen *et al*., *J. Phys. Chem. C* **115**, 24915–24919 (2011).

ACKNOWLEDGMENTS

Computational resources provided by the KISTI Supercomputing Center (project no. KSC-2020-CRE-0361) are gratefully acknowledged (J.-H.L.). This work made use of the Cornell Center for Materials Research Shared Facilities, which are supported through the NSF MRSEC program (DMR-1719875). NMR data were collected on a Bruker INOVA 500-MHz spectrometer that was purchased with support from the NSF (CHE-1531632). We are grateful for the resources provided by the Advanced Photon Source, which is supported by the US Department of Energy, Office of Science, Office of Basic Energy Sciences, under contract no. DE-AC02-06CH11357. We thank the Cornell University Glass Shop for providing the custom-built, solid-addition funnels used in this work. We thank S. Meng, T. Hyster, T. Lambert, and S. Lin (Cornell University) for editorial assistance during the preparation of this manuscript. **Funding:** This work was funded by Cornell University (K.T.K., M.E.Z., E.E.S., J.K., P.J.M.); the National Institute of General Medical Sciences of the National Institutes of Health (R35GM138165) (K.T.K., M.E.Z., E.E.S., J.K., P.J.M.); a Bristol Myers Squibb fellowship (K.T.K.); the KIST Institutional Program (project no. 2E31801) (J.-H.L.); the National Center for Materials Research Data (NCMRD) through the National Research Foundation of Korea funded by the Ministry of Science and ICT (2021M3A7C2089739) (J.-H.L.); the NSF (CHE-1531632); the NSF MRSEC program (DMR-1719875); the Robert A. Welch Foundation (grant no. N-2012-20220331) (L.A., T.R.); the US Department of Energy, Office of Science, Office of Basic Energy Sciences (DE-AC02-06CH11357); and a Camille Dreyfus Teacher-Scholar Award (TC-23-048) (P.J.M.). The content is solely the responsibility of the authors and does not necessarily represent the official views of the National Institutes of Health. **Author contributions:** Conceptualization: P.J.M., K.T.K., M.E.Z., E.E.S.; Methodology: K.T.K., M.E.Z., E.E.S., J.K., J.-H.L., L.A.; Investigation: K.T.K., M.E.Z., E.E.S., J.K., J.-H.L., L.A.; Visualization: P.J.M., K.T.K., M.E.Z., E.E.S.; Funding acquisition: P.J.M., J.-H.L., T.R.; Project administration: P.J.M., J.-H.L., T.R.; Supervision: P.J.M., T.R.; Writing – original draft: K.T.K., P.J.M.; Writing – review and editing: K.T.K., M.E.Z., E.E.S., J.K., J.-H.L., L.A., T.R., P.J.M. **Competing interests:** P.J.M., K.T.K., and M.E.Z. are listed as inventors on a patent that includes gas-reagent delivery using MOFs (Cornell University, international patent application no. PCT/US2023/019456, filed 21 April 2023). **Data and materials availability:** All data are available in the main text or the supplementary materials.

License information: Copyright © 2023 the authors, some rights reserved; exclusive licensee American Association for the Advancement of Science. No claim to original US government works. https://www.science.org/about/science-licenses-journal-article-reuse

SUPPLEMENTARY MATERIALS

science.org/doi/10.1126/science.adg8835
Materials and Methods
Supplementary Text
Figs. S1 to S181
Tables S1 to S32
References (*75*–*113*)

Submitted 27 January 2023; resubmitted 12 June 2023
Accepted 24 August 2023
10.1126/science.adg8835

MYCOSES

A *Candida auris*–specific adhesin, Scf1, governs surface association, colonization, and virulence

Darian J. Santana[1,2], Juliet A. E. Anku[1,3,4], Guolei Zhao[1], Robert Zarnowski[5,6], Chad J. Johnson[5,6], Haley Hautau[7], Noelle D. Visser[1]†, Ashraf S. Ibrahim[7,8], David Andes[5,6], Jeniel E. Nett[5,6], Shakti Singh[7,8], Teresa R. O'Meara[1]*

Candida auris **is an emerging fungal pathogen responsible for health care–associated outbreaks that arise from persistent surface and skin colonization. We characterized the arsenal of adhesins used by *C. auris* and discovered an uncharacterized adhesin, Surface Colonization Factor (Scf1), and a conserved adhesin, Iff4109, that are essential for the colonization of inert surfaces and mammalian hosts. *SCF1* is apparently specific to *C. auris*, and its expression mediates adhesion to inert and biological surfaces across isolates from all five clades. Unlike canonical fungal adhesins, which function through hydrophobic interactions, Scf1 relies on exposed cationic residues for surface association. *SCF1* is required for *C. auris* biofilm formation, skin colonization, virulence in systemic infection, and colonization of inserted medical devices.**

Since the initial reports of its discovery in 2009, the emerging fungal pathogen *Candida auris* has become an increasingly common source of life-threatening infection worldwide (*1*, *2*). *C. auris* is frequently reported in association with nosocomial outbreaks, a characteristic rarely described with other *Candida* species, and is of urgent concern for public health authorities (*3*–*7*). *C. auris* outbreaks are characterized by persistent colonization of patient skin and abiotic surfaces, which can remain positive for extensive periods and serve as a source of contaminative transmission (*8*–*14*). *C. auris* also colonizes indwelling medical devices, which act as a risk factor for the development of invasive disease (*15*–*21*). Lapses in diagnostic screening and infection prevention measures are thought to contribute to the increasing rate of *C. auris* outbreaks (*20*). The ability of *C. auris* to robustly colonize a range of living and abiotic substrates is central to its emergence as a global health threat.

Colonization requires the initial physical association and attachment between fungal cells and substrate. For fungal pathogens, attachment is largely mediated by cell surface–exposed adhesin proteins (*22*). In *Candida* species, genetic expansion has resulted in the formation of adhesin families containing genes similar in sequence and domain architecture, with adhesive functions that are redundant or specific across family members (*23*, *24*). *C. auris* encodes genes similar to members of the conserved *ALS (Agglutinin-Like Sequence)* and *IFF/HYR (IPF Family F/Hyphally Regulated)* adhesin families found across the genus, although these genes may have expanded independently in *C. auris* and lack clear one-to-one homology with adhesins from well-characterized species. Moreover, their phenotypic importance in *C. auris* is not well understood (*24*–*26*).

To investigate the role of individual *C. auris* adhesins in colonization phenotypes, we

[1]Department of Microbiology and Immunology, University of Michigan, Ann Arbor, MI, USA. [2]Department of Epidemiology, University of Michigan, Ann Arbor, MI, USA. [3]West African Centre for Cell Biology of Infectious Pathogens (WACCBIP), Accra, Ghana. [4]Department of Biochemistry, Cell and Molecular Biology, University of Ghana, Accra, Ghana. [5]Department of Medicine, University of Wisconsin, Madison, WI, USA. [6]Department of Medical Microbiology and Immunology, University of Wisconsin, Madison, WI, USA. [7]Division of Infectious Disease, The Lundquist Institute for Biomedical Innovation at Harbor–University of California, Los Angeles Medical Center, Torrance, CA, USA. [8]David Geffen School of Medicine, University of California, Los Angeles, Los Angeles, CA, USA.
***Corresponding author. Email: tromeara@umich.edu**
†Present address: Department of Biology, University of Louisville, Louisville, KY, USA.

measured the adhesion between fungal cells and polymer substrates as a model for surface association. We found that *C. auris* does not primarily rely on conserved adhesins for surface attachment. Instead, we identified Surface Colonization Factor 1 (Scf1), an adhesin specific to *C. auris* that is necessary and sufficient for the robust attachment of its cells to polymer substrates. *C. auris* isolates from diverse and similar genetic lineages exhibit marked divergence in terms of substrate association, and this phenotypic plasticity is tightly correlated with strain-specific transcriptional control of *SCF1*. The nonspecific surface association driven by *Scf1* does not occur through

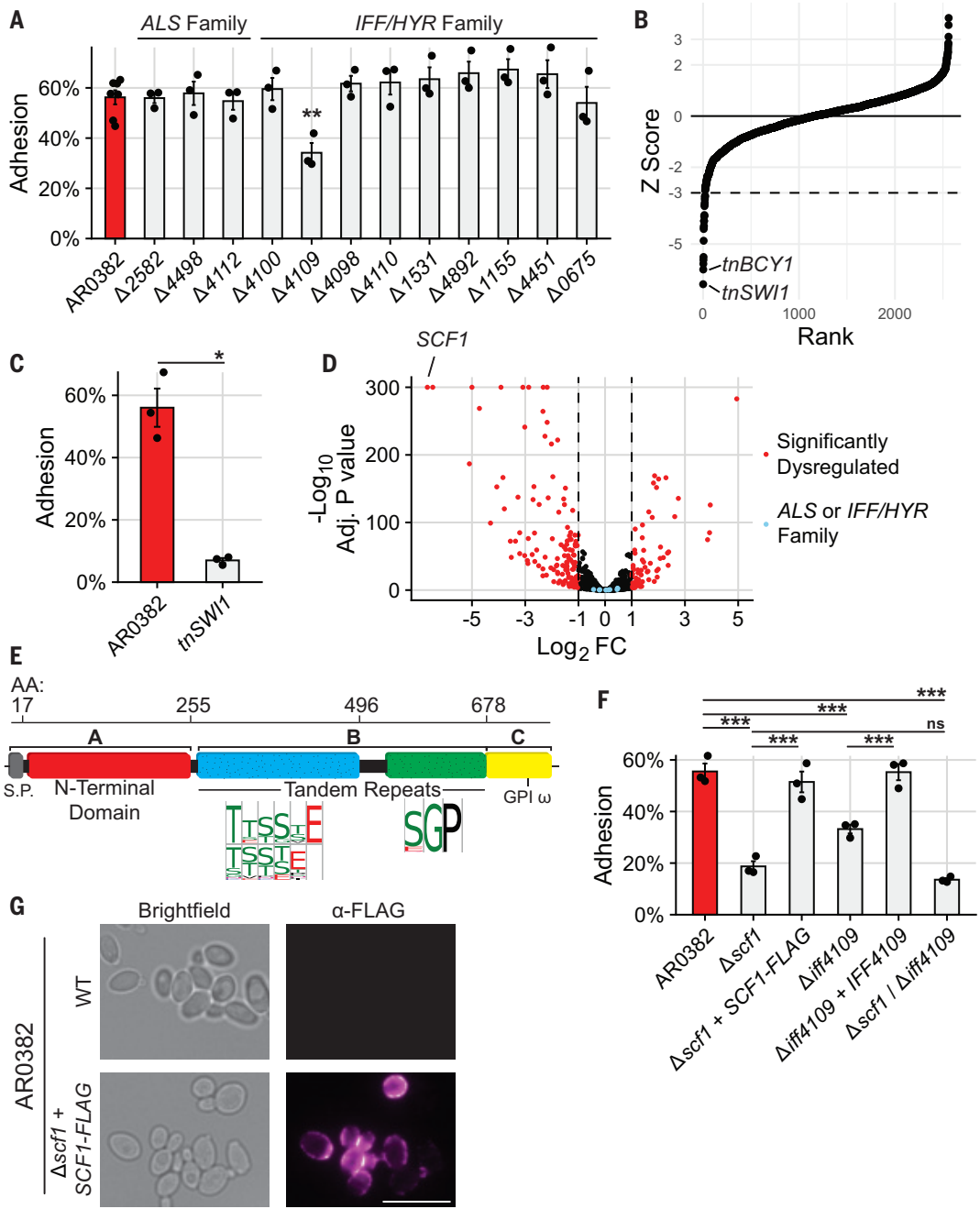

Fig. 1. SCF1 mediates *C. auris* adhesion to polymer surfaces. (**A**) Adhesion of wild-type AR0382 or mutants lacking one of 12 genes from the *ALS* or *IFF/HYR* adhesin families. (**B**) The 2560 insertional mutants in the AR0382 strain background were screened for adhesion defects by measuring the proportion of cells able to remain attached to a cyclic olefin polymer surface after three washes with phosphate-buffered saline. Strains are ordered by *Z*-score rank. Mutants with a *Z*-score more negative than −3 were considered to have a significant adhesive defect. (**C**) Adhesion of AR0382 and an insertional *SWI1* mutant. (**D**) RNA sequencing comparing the transcriptome of *tnSWI1* with that of AR0382. *SCF1* (B9J08_001458) is the strongest dysregulated gene. (**E**) Predicted domain architecture of Scf1 based on the clade I primary sequence is consistent with canonical fungal adhesins. (**F**) Adhesion of adhesin mutants and complements compared with AR0382. (**G**) Immunofluorescence microscopy using an α-FLAG antibody. Representative images shown for wild-type AR0382 and AR0382 Δ*scf1* + *SCF1-FLAG*. Scale bar, 5 μm. Statistical differences were assessed using one-way ANOVA with Dunnett's post hoc test (A), Student's *t* test (C), or one-way ANOVA with Tukey's post hoc test (F); $^{*}P \le 0.05$; $^{**}P \le 0.01$; $^{***}P \le 0.001$; ns: $P > 0.05$.

canonical hydrophobic interactions but rather through cation-substrate interactions. To explore the clinical relevance of these findings, we investigated the importance of *SCF1* in long-term colonization models. *SCF1* is critical for biofilm formation in vitro, robust colonization of in vivo central venous catheters, colonization of both human and murine skin, and virulence in disseminated infection. These findings offer insight into the genetic and molecular mechanisms by which *C. auris* mediates surface association, a trait critical to the increasing disease burden of this emerging pathogen.

Results

Polymer surface attachment by the adhesin SCF1

C. auris encodes 12 genes homologous to members of the characterized *ALS* and *IFF/HYR* adhesin families (*24*, *25*, *27*). We generated individual deletion mutants in the clade I AR0382 background for each adhesin gene to model their impact on surface association. We used a flow cytometric adhesion assay that measures the ability of cells to attach to dispersed polystyrene microspheres in suspension (fig. S1) (*28*). Of the 12 adhesin mutants, only deletion of *IFF4109* (B9J08_004109) conferred an adhesive defect while still failing to completely ablate attachment (Fig. 1A). To investigate the possibility that there were occult adhesive factors, we screened a library of 2560 insertional mutants, prioritizing those exhibiting the most significant defects (Fig. 1B). The greatest loss of adhesive capacity was observed in the *tnSWI1* (B9J08_003460) and *tnBCY1* (B9J08_002818) mutants (Fig. 1, B and C, and fig. S2). Compared with the AR0382 parent, the *tnSWI1* mutant exhibited no significant transcriptional dysregulation of the *ALS* or *IFF/HYR* adhesins, suggesting alternative mediators of adhesion (Fig. 1D). The strongest, most significantly dysregulated gene in *tnSWI1* was an uncharacterized open reading frame (ORF) (B9J08_001458) that had no significant primary sequence homology to characterized genes (Fig. 1D). This gene, however, exhibited a putative three-domain architecture consistent with canonical glycosylphosphatidylinositol (GPI)–anchored fungal adhesins (Fig. 1E) (*23*). This same gene was also strongly down-regulated in the *tnBCY1* mutant, whereas *IFF4109* was not (fig. S2). Deletion of the B9J08_001458 ORF in AR0382 conferred a substantial adhesive defect, so we refer to the gene as *Surface Colonization Factor* (*SCF1*) (Fig. 1F). Complementation with an epitope-tagged *SCF1* allele in the endogenous locus rescued the adhesive defect, and the epitope-tagged Scf1 protein localized to the cell surface, consistent with its role as an adhesin (Fig. 1, F and G). Deletion of *IFF4109* in the Δ*scf1* background did not significantly reduce attachment beyond deletion of *SCF1* alone, suggesting nonadditive roles for these adhesins (Fig. 1F).

The specific reliance on Scf1 and Iff4109 for adhesion despite potential redundancy with other adhesins is reminiscent of other fungal pathogens. For instance, loss of *ALS1* alone reduces *Candida albicans* adhesion despite the presence of seven other *ALS* genes (fig. S3A) (*29*). In *C. auris*, adhesins exhibit structural and transcriptional variation, which may explain their functional specificity (fig. S3B) (*25*, *26*). However, *IFF4892* encodes the entire canonical adhesin architecture and shows similar expression to *IFF4109*, but of the two, only *IFF4109* is required for adhesion, suggesting

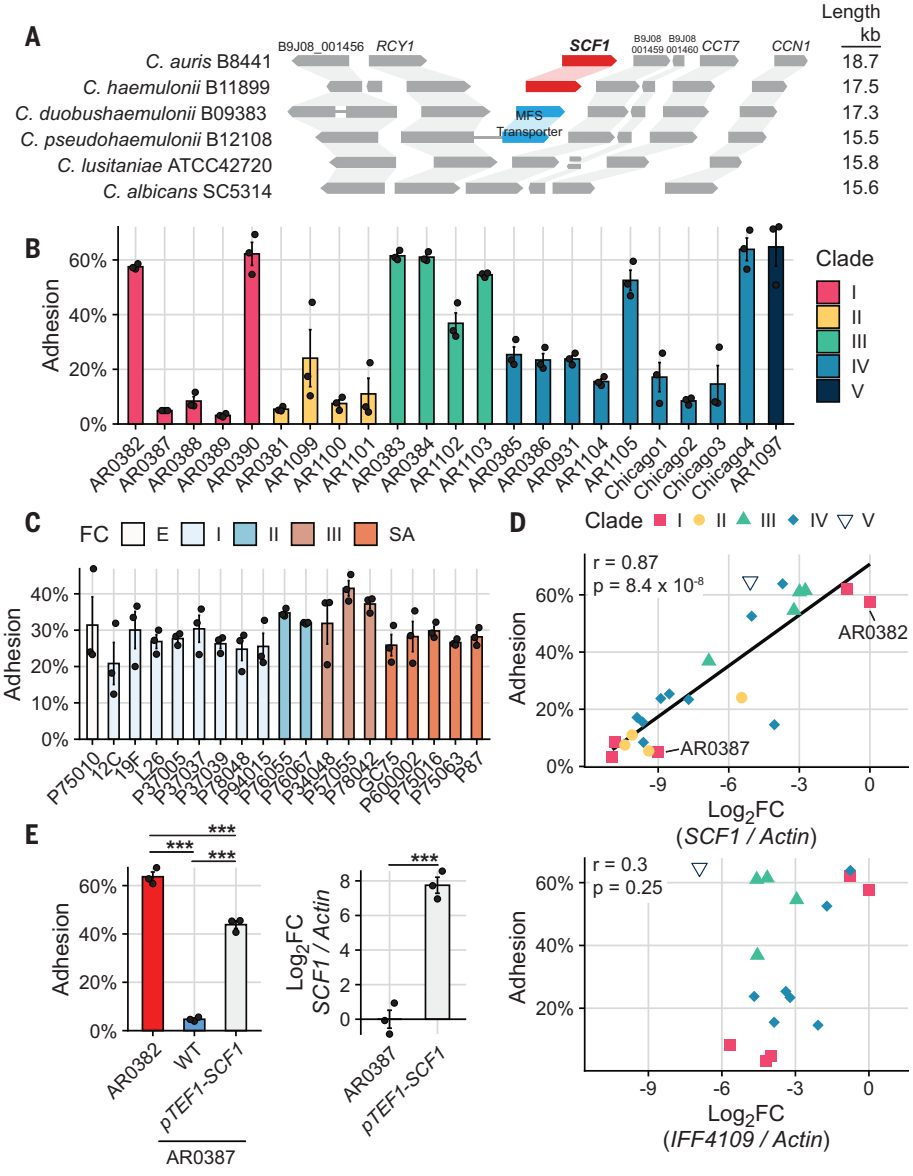

Fig. 2. *C. auris* alone relies on Scf1 for adhesive plasticity. (**A**) Synteny schema depicting *SCF1* and the conservation and orientation of adjacent ORFs. Genomic loci are shown compared with *C. auris*. Putative *SCF1* homologs were only identified in *C. auris* and *C. haemulonii*. (**B**) Adhesion of 23 *C. auris* clinical isolates from all five clades. (**C**) Adhesion of 19 *C. albicans* clinical isolates from five clades. FC, fingerprint clade. (**D**) *SCF1* transcript abundance (top panel), but not *IFF4109* transcript abundance (bottom panel), is associated with adhesion to polystyrene in the same 23 *C. auris* isolates from (A). Log_2 fold change (Log_2FC) values are expressed relative to AR0382. Each point signifies the mean of three biological replicates. Pearson correlation coefficient and *P* value are indicated. Isolates that do not encode *IFF4109* are not indicated in the bottom panel. (**E**) Comparison of adhesion between two clade I isolates: AR0382 and AR0387. Overexpression of *SCF1* using the strong *TEF1* promoter (right panel) is sufficient to drive adhesion in the poorly adhesive AR0387 background (left panel). Statistical differences were assessed using one-way ANOVA [(B) and (C)], Tukey's post hoc test (E), or Student's *t* test (E); $*P \le 0.05$; $**P \le 0.01$; $***P \le 0.001$; ns: $P > 0.05$.

that individual adhesins mediate specific adhesive mechanisms (Fig. 1A and fig. S3B) (*25*). Such functional specificity is shown by the increased flocculation and aggregation associated with overexpression of *ALS4112*, whereas these phenotypes are not associated with *SCF1* despite its transcriptional expression being among the highest 2.5% of all genes in this strain background (fig. S3, B to D) (*30*, *31*). These findings suggest functional specificity for surface association for Scf1 and Iff4109.

C. auris relies on Scf1 for adhesive plasticity

Although many *Candida* and *Saccharomyces* adhesins belong to conserved gene families, we identified homologs of *SCF1* only in *C. auris* and the closely related *Candida haemulonii* species and not in other members of the *haemulonii* complex (Fig. 2A). *SCF1* is encoded in a genomic locus in *C. auris* and *C. haemulonii* that is syntenic, lacking an *SCF1* homolog, even to distantly related species (Fig. 2A). Although the *C. haemulonii SCF1* homolog functionally complements Δ*scf1* in *C. auris,* it is not essential for adhesion in *C. haemulonii* and shows poor expression across isolates, indicating that reliance on *SCF1* for adhesion is specific to *C. auris* (fig. S4).

To investigate the generalizability of the reliance on *SCF1* and the variability between *C. auris* strains, we measured adhesion for 23 *C. auris* isolates representing all five clades and diverse geographic origins. These strains exhibited substantial adhesive variation regardless of clade ($P = 2 \times 10^{-16}$, $F = 35.06$, one-way ANOVA) (Fig. 2B). By contrast, a similar analysis of 19 genetically diverse *C. albicans* clinical isolates showed no significant adhesive variation ($P = 0.054$, $F = 1.856$, one-way ANOVA), indicating that the surface association strategies of *C. auris* are more plastic than those of *C. albicans* (Fig. 2C). Substantial variation in adhesion was observed even between genetically similar isolates of *C. auris*, e.g., AR0382 and AR0387, which differ by only 206 coding single-nucleotide polymorphisms (Fig. 2B). In the poorly adhesive AR0387, *SCF1* was the most down-regulated gene compared with the highly adhesive AR0382, reminiscent of the poorly adhesive *tnSWI1* mutant (fig. S5A and Fig. 1D). However, the transcriptome of AR0387 showed little overlap with that of the *tnSWI1* strain, indicating that dysregulation of *SCF1* in AR0387 is not caused by a *SWI/SNF* complex defect (fig. S5B). Furthermore, we observed no nucleotide variants in the *SCF1* ORF or neighboring intragenic regions between AR0382 and AR0387.

Transcript abundance of *SCF1* was tightly positively correlated with adhesion across isolates regardless of clade ($r = 0.87$, $P = 8.4 \times 10^{-8}$) (Fig. 2D). By contrast, we observed no association between transcriptional control of *IFF4109* and adhesion ($r = 0.3$, $P = 0.25$) (Fig. 2D). Experimentally, transcriptional overexpression of *SCF1* was sufficient to elevate adhesion in the otherwise poorly adhesive isolate AR0387 (Fig. 2E). The magnitude of overexpression using the *TEF1* promoter (~2^8-fold increase) was similar to and did not exceed the naturally varying magnitude of expression difference between the two wild-type isolates AR0382 and AR0387 (~2^9-fold change) (Fig. 2, D and E). These data show that adhesive variation between *C. auris* isolates is associated with *SCF1* expression variation.

In AR0382 and AR0387, the *SCF1* locus is invariant, but other isolates exhibit allelic variation, which is primarily concentrated in the low-complexity tandem repeats (table S1). We tested whether allelic variation also contributed to the adhesive variation among isolates. Overexpression of the native *SCF1* allele in AR0381, a poorly adhesive clade II isolate, was sufficient to increase attachment (fig. S6A). However, overexpression of the clade I *SCF1* allele from AR0382 further elevated adhesion despite similar levels of overexpression (fig. S6A). In the clade I AR0382 background, which relies strongly on *SCF1* for adhesion, complementation of the Δ*scf1* mutant with either the clade I or clade II *SCF1* allele resulted in similar levels of rescue of the adhesive phenotype (fig. S6B). These findings show that sequence variation between these two *SCF1* alleles does not intrinsically contribute to functional differences in adhesion, and that other factors may also influence adhesive capacity.

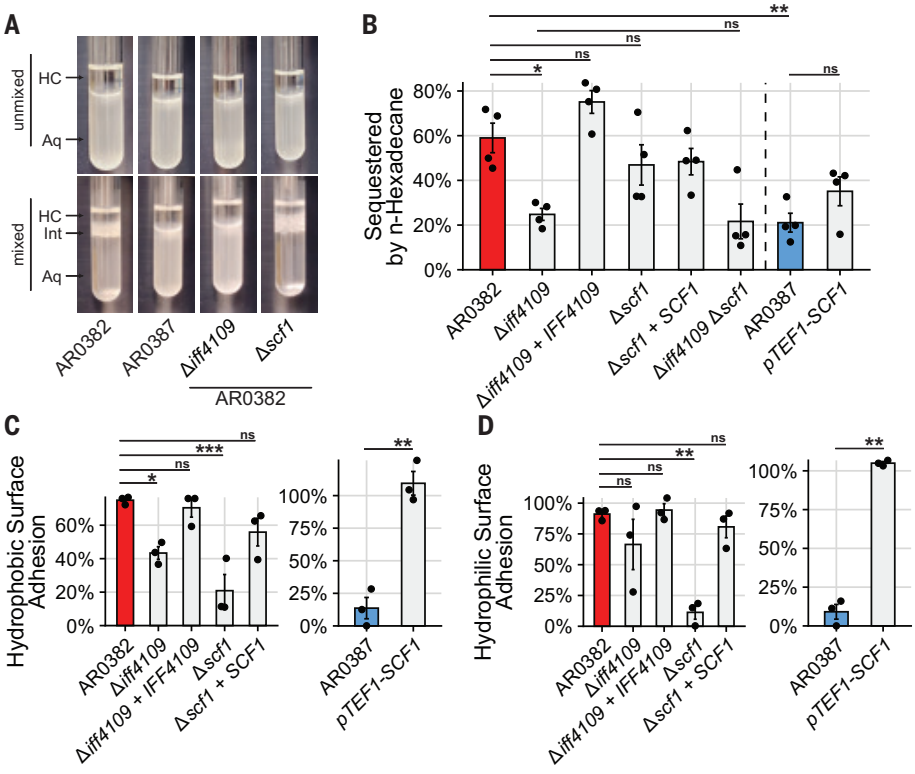

Fig. 3. Iff4109, but not Scf1, mediates adhesion through cell surface hydrophobicity. (**A**) Representative images from the microbial attachment to hydrocarbons (MATH) assay. Hydrophobic cells are sequestered from the aqueous phase (Aq) to the aqueous-hydrocarbon interface (Int) after mixing with the hydrocarbon phase (HC). (**B**) Proportion of cells sequestered out of the aqueous phase during the MATH assay. (**C** and **D**) Cells were allowed to attach to a hydrophobic, untreated polystyrene surface (C) or a hydrophilic, vacuum plasma–treated polystyrene surface (D) for 1 hour. The surface was then washed and the proportion of cells that remained attached after washing was measured. Statistical differences were assessed using one-way ANOVA with Tukey's post hoc test [(B), (C), and (D)] or Student's *t* test [(C) and (D)]; *$P \le 0.05$; **$P \le 0.01$; ***$P \le 0.001$; ns: $P > 0.05$.

Scf1 *and* Iff4109 *have distinct nonspecific mechanisms*

The reliance on *SCF1* for surface association is complicated by the genetic interaction with *IFF4109*, in which deletion of both does not result in a more severe adhesive defect than deletion of *SCF1* alone (Fig. 1F). Loss of one adhesin did not result in dysregulation of the other, suggesting that the interaction is not a regulatory one (fig. S7). One possibility is that the two genes contribute to adhesion through distinct but complementary physical mechanisms. For other *Candida* species, adhesion

to abiotic substrates is often nonspecific, with adhesins promoting affinity for hydrophobic substrates (*32*–*34*). The highly adhesive AR0382 strain exhibited elevated cell surface hydrophobicity compared with the poorly adhesive AR0387 (Fig. 3, A and B). Deletion of the *IFF4109* adhesin in AR0382 reduced cell surface hydrophobicity, which was rescued to wild-type levels by complementation (Fig. 3, A and B). By contrast, deletion or overexpression of *SCF1* did not significantly affect cell surface hydrophobicity in either AR0382 or AR0387 (Fig. 3, A and B).

Elevated cell surface hydrophobicity likewise promotes affinity for hydrophobic substrates (*33*). We measured the adhesion of *C. auris* isolates to both an untreated hydrophobic polystyrene surface and a polystyrene surface modified using vacuum plasma treatment to become strongly hydrophilic. Both Iff4109 and Scf1 mediated adhesion to the hydrophobic substrate (Fig. 3C); however, only Scf1 mediated adhesion to the hydrophilic substrate, showing that Scf1 is not dependent on hydrophobicity (Fig. 3D). AR0382 and AR0387 still exhibited differential adhesion to the hydrophilic surface, indicating that hydrophobic interactions are not primarily responsible for the differential strain phenotypes (Fig. 3D).

To investigate the mechanism of Scf1 adhesion, we examined the apical N-terminal domain using AlphaFold2, which suggested that this domain contains a core fibronectin type III fold similar to the *FLO11* family of adhesins characterized in *Saccharomyces cerevisiae* and conserved throughout *Ascomycota* (fig. S8A) (*32*, *35*). However, Scf1 does not exhibit significant primary sequence homology to *S. cerevisiae* Flo11 and lacks conservation of the canonical aromatic bands responsible for adhesive functions in true *FLO11* homologs (fig. S8, A and B) (*32*, *35*). Furthermore, model confidence dwindles outside of the fibronectin fold, suggesting substantial variation from Flo11 adhesins (fig. S9). In its primary sequence, the Scf1 N-terminal domain exhibits an enrichment of arginine and lysine residues compared with other yeast adhesins (table S2). Adhesive systems in many marine organisms rely on similarly cation-rich proteins, which act through the displacement of hydrated ions at the surface-liquid interface or direct cation-π interactions with substrates (*36*–*40*). We reasoned that if Scf1 relied on such interactions, then adhesion could be inhibited by a saturating concentration of cations at the substrate interface that could not be competitively displaced by SCF1. Consistent with this hypothesis, high concentrations of arginine in solution were sufficient to ablate AR0382 adhesion (Fig. 4A). Similar concentrations of NaCl or other noncationic amino acids did not produce the same effect, whereas exogenous lysine

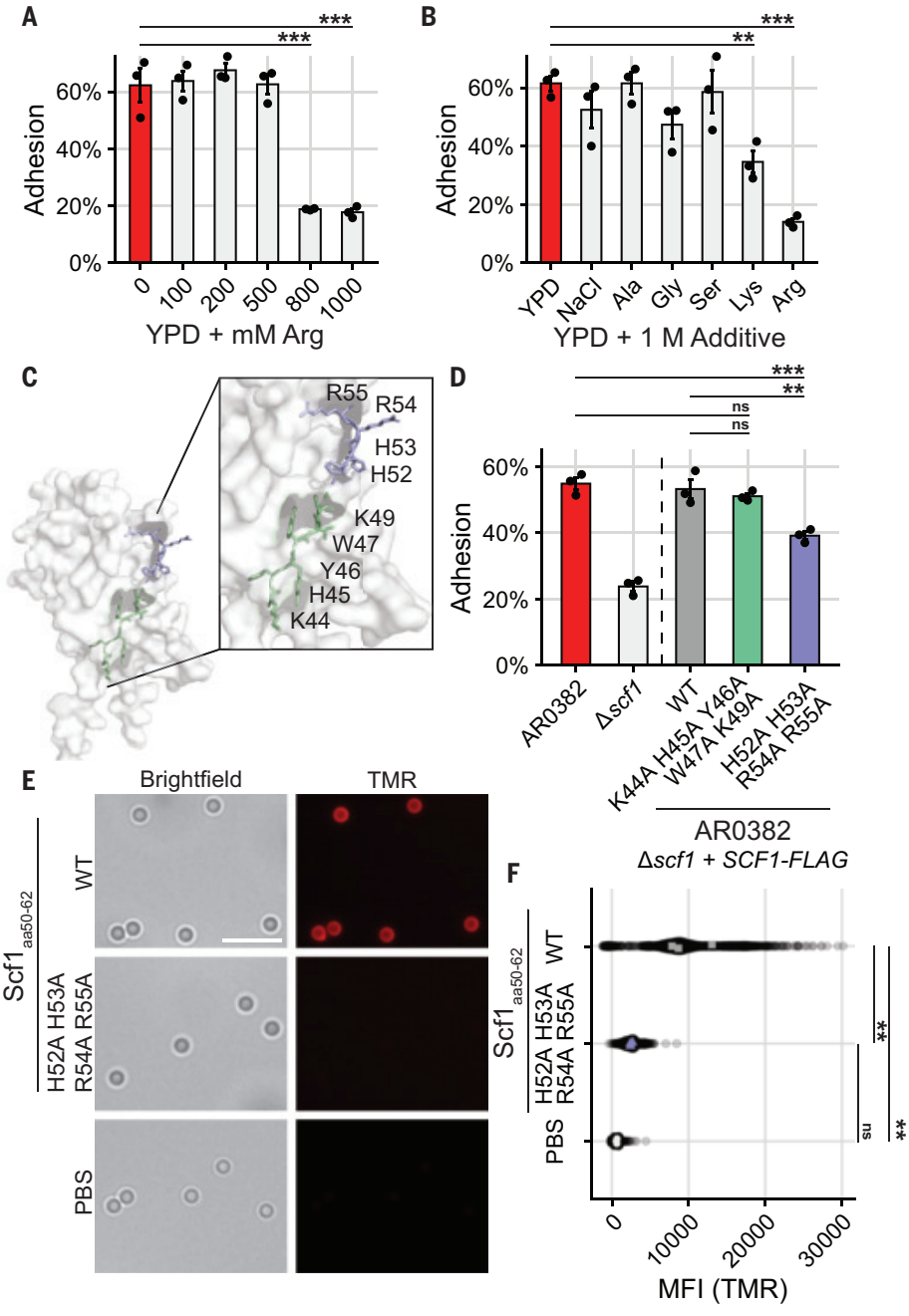

Fig. 4. Specific cationic residues are critical for Scf1-mediated surface association. (**A** and **B**) Wild-type AR0382 adhesion in the presence of increasing concentrations of arginine (A) or 1 M additives (B). (**C**) Predictive model of the Scf1 N-terminal domain with two neighboring cationic-aromatic clusters highlighted. (**D**) Adhesion of wild-type AR0382, a mutant lacking *SCF1*, or AR0382 Δ*scf1* + *SCF1-FLAG* mutants encoding the wild-type *SCF1* allele or alleles containing the indicated mutations. (**E**) Tetramethylrhodamine (TMR)–labeled 13–amino acid peptides corresponding to the wild-type Scf1 sequence (residues 50 to 62) or the same sequence with the indicated mutations incubated with the same polystyrene microspheres used to measure adhesion in (D). Scale bar, 5 μm. (**F**) Quantification (mean fluorescence intensity, MFI) of peptide binding to individual polystyrene microspheres as in (E) measured by TMR epifluorescence and corrected for background fluorescence. Each point represents an individual microsphere. Colored points represent averages of individual experiments used for statistical analysis. Statistical differences were assessed using one-way ANOVA with Dunnett's post hoc test [(A) and (B)] or one-way ANOVA with Tukey's post hoc test [(D) and (F)]; $^{*}P \le 0.05$; $^{**}P \le 0.01$; $^{***}P \le 0.001$; ns: $P > 0.05$.

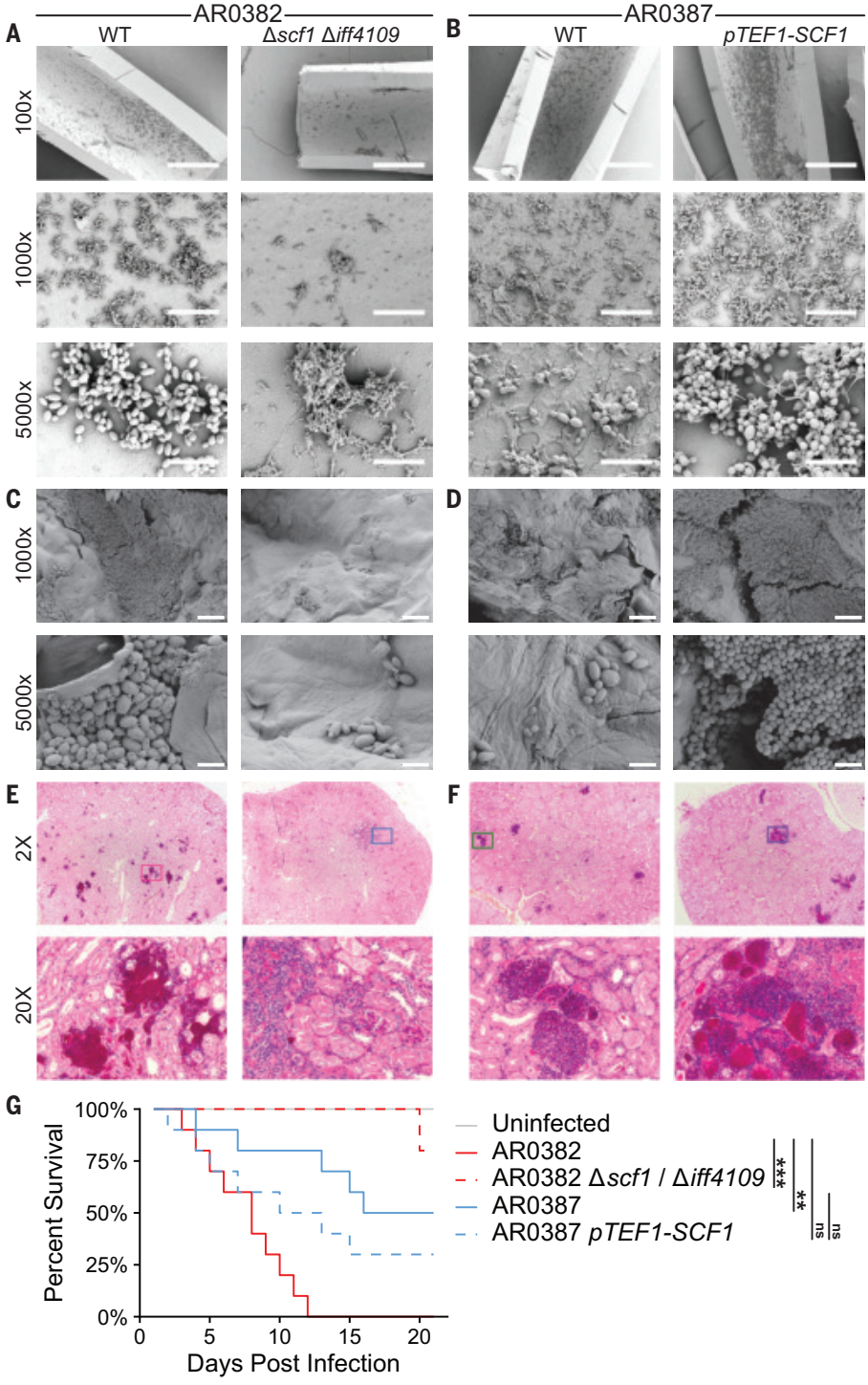

Fig. 5. Scf1 mediates host colonization and infection phenotypes. (**A** and **B**) Polyethylene central venous catheters were set in rat jugular veins and inoculated intraluminally with *C. auris*. Representative scanning electron microscopy images of the luminal catheter surface are shown from catheters collected 24 hours after infection. Scale bars: 400 μm (100×), 40 μm (1000×), and 5 μm (5000×). (**C** and **D**) Full thickness human skin explants were colonized with *C. auris* for 24 hours before washing to remove unassociated cells. Representative scanning electron microscopy images of the skin surface after washing are shown. Scale bars: 20 μm (1000×) and 4 μm (5000×). (**E** to **G**) Immunosuppressed mice were infected intravenously (through tail vein injection) with 5×10^7 *C. auris* cells. Histopathology sections of the kidneys 7 days after infection [(E) and (F)] were stained with periodic acid–Schiff. Magenta color indicates lesion areas. Ten infected mice for each strain were monitored for survival for 21 days (G). Statistical comparisons of overall survival were assessed using the Mantel-Haenszel log-rank test with Benjamini-Hochberg correction; *$P \leq 0.05$; **$P \leq 0.01$; ***$P \leq 0.001$; ns $P > 0.05$.

produced a more modest inhibition of attachment, consistent with lysine's weaker ability to form electrostatic interactions (Fig. 4B) (*41*).

We next investigated whether specific cationic regions or residues were critical for Scf1 activity. We generated point mutations in cationic residues in different areas of the N-terminal domain, focusing on residues that clustered with aromatic groups because this pattern potentiates electrostatic adhesion (fig. S10A) (*42*). Several mutations had no adhesive impact, but an R54A R55A mutant exhibited a modest adhesive defect while showing no discernable effect on Scf1 transcription, protein expression, or localization (fig. S10). Mutating the entire cation-aromatic cluster, H52 H53 R54 R55, resulted in a similar adhesive defect (Fig. 4, C and D, and fig. S11). A nearby cation-aromatic cluster, K44-K49, which was modeled to be less surface exposed, was not required for adhesion (Fig. 4, C and D, and fig. S11). To determine whether surface exposure of the HHRR cluster (residues 52 to 55) would be sufficient to promote adhesion, we synthesized peptides corresponding to Scf1 residues 50 to 62 with the intact wild-type cluster or the HHRR residues mutated. The wild-type peptide adhered to polystyrene microspheres, but mutation of the HHRR cluster completely ablated this ability (Fig. 4, E and F). Similar patterns of cation-aromatic clusters are also abundant in some lipid-binding proteins (*40*, *43*). The wild-type Scf1 peptide was similarly able to adhere to phosphotidylcholine microparticles, and *SCF1* expression potentiated lipid particle binding by *C. auris* cells, suggesting that Scf1 may also contribute to association with biotic substrates (fig. S12).

SCF1 promotes long-term colonization and virulence

We next investigated the impact of Scf1 and Iff4109 on other aspects of surface colonization. We measured the importance of these adhesins for biofilm growth, which can promote prolonged environmental persistence (*11*, *44*–*46*). The two adhesins were functionally redundant, and deletion of both was required to ablate biofilm formation in AR0382, suggesting that the partial adhesive contributions of each is sufficient to establish colonization (fig. S13A). Expression of *SCF1* alone in otherwise biofilm-incompetent isolates was sufficient to establish biofilm colonization (fig. S13, B to E). This pattern continued for in vivo biofilms, in which loss of *SCF1* and *IFF4109* ablated the ability of AR0382 to colonize the luminal surface of a polyethylene rat central venous catheter, and overexpression of *SCF1* was sufficient to potentiate AR0387 colonization (Fig. 5, A and B).

We then investigated whether biological surface association followed the same reliance on these adhesins. Again, we observed that loss of *SCF1* and *IFF4109* diminished the ability of

AR0382 to colonize ex vivo human skin explants and in vivo murine skin, whereas overexpression of *SCF1* potentiated skin colonization by AR0387 (Fig. 5, C and D, and fig. S14). Given this potential for interaction with host tissues, we also investigated the importance of these adhesins in disseminated infection. Histopathological examination of tissues collected from immune-compromised mice 7 days after intravenous *C. auris* infection revealed that the loss of *SCF1* and *IFF4109* reduced AR0382 dissemination to the kidneys and heart, whereas overexpression of *SCF1* in AR0387 was sufficient to increase fungal lesions (Fig. 5, E and F, and fig. S15). Loss of *SCF1* and *IFF4109* substantially attenuated the virulence of AR0382, with the wild type causing 100% mortality within 12 days of infection and the mutant causing 20% mortality after 21 days (Fig. 5G). Similarly, overexpression of *SCF1* reduced the median survival time of mice infected with AR0387 from 18.5 to 11.5 days and ablated the difference in overall survival between the less virulent AR0387 and the more virulent AR0382 (Fig. 5G).

Discussion

C. auris encodes genes similar to the conserved *ALS* and *IFF/HYR* adhesin families, and proposed models suggest that differential utilization of these adhesins may contribute to epidemiological differences among isolates (*25*, *27*). Our findings suggest that the *C. auris*–specific adhesin Scf1 and the conserved adhesin Iff4109 are the principal mediators of association with abiotic surfaces and additionally contribute substantially to infection and long-term colonization of both biological and abiotic surfaces. The other conserved adhesin genes did not appear to mediate surface association. Whether this is the product of functional or regulatory divergence remains to be explored. We observed widespread differential regulation of *SCF1* among *C. auris* isolates regardless of clade, suggesting that the transcriptional control of this adhesin has adapted more recently than clade separation. The widespread plasticity around a single genetic element responsible for diverse, clinically relevant phenotypes could be problematic in outbreak settings. Although Scf1 and Iff4109 contribute to host infection and colonization, the mechanisms of their interaction with host systems remain unclear. Understanding how variable adhesion allows *C. auris* to mediate infection is likely to offer therapeutic insights. Prior work suggests that vaccination or monoclonal antibody therapy targeting Als or Iff/Hyr adhesins may offer protection against lethal *C. auris* infection (*27*, *47*). Furthermore, the complementary function of Scf1 and Iff4109 with divergent mechanisms suggests that *C. auris* has evolved the capacity for promiscuous surface association and colonization. Mediation of hydrophobic interactions is largely conserved among fungal adhesins, consistent with the adhesive mechanism of the conserved Iff4109 (*32*–*34*). The cation-rich Scf1, however, appears to functionally resemble proteins from bivalve, barnacle, and *Vibrio* adhesion systems. For these organisms, cation-dependent surface interactions promote adhesion in aqueous and highly ionic environments (*36*–*39*). *C. auris* has been isolated from the coastal wetlands of the Andaman Islands and from a Colombian estuary, suggesting a possible marine natural habitat, and this ecological niche may have conferred similar selective pressures on adhesion mechanisms (*48*, *49*). Development of this specific adhesion biology may in part explain the tenacity of this organism on medically relevant substrates. Nevertheless, differential utilization of *SCF1* by different isolates suggests that an unknown selective pressure may govern its expression. Understanding this adaptation and its clinical consequences more fully may offer important insights into the outbreak potential of this pathogen.

Overall, our work characterizes of the adhesin machinery used by *C. auris* for surface association and colonization. The identification of Scf1 and the characterization of the genetic determinants of adhesion add to the growing understanding of the pathobiology of this emerging organism.

REFERENCES AND NOTES

1. A. Chakrabarti, P. Sood, *J. Med. Microbiol.* **70**, 001318 (2021).
2. A. B. Akinbobola, R. Kean, S. M. A. Hanifi, R. S. Quilliam, *PLOS Pathog.* **19**, e1011268 (2023).
3. L. Ashkenazi-Hoffnung, C. Rosenberg Danziger, *J. Fungi (Basel)* **9**, 176 (2023).
4. N. A. Chow *et al*., *Lancet Infect. Dis.* **18**, 1377–1384 (2018).
5. S. C. Roberts, T. R. Zembower, E. A. Ozer, C. Qi, *J. Clin. Microbiol.* **59**, e02252-20 (2021).
6. S. Vallabhaneni *et al*., *MMWR Morb. Mortal. Wkly. Rep.* **65**, 1234–1237 (2016).
7. World Health Organization, "WHO fungal priority pathogens list to guide research, development and public health action" (WHO, 2022); https://www.who.int/publications/i/item/9789240060241).
8. D. J. Sexton *et al*., *Clin. Infect. Dis.* **73**, 1142–1148 (2021).
9. D. M. Proctor *et al*., *Nat. Med.* **27**, 1401–1409 (2021).
10. E. Adams *et al*., *Emerg. Infect. Dis.* **24**, 1816–1824 (2018).
11. O. Dire, A. Ahmad, S. Duze, M. Patel, *J. Hosp. Infect.* **137**, 17–23 (2023).
12. J. N. de Almeida Jr *et al*., *Mycoses* **64**, 1062–1072 (2021).
13. D. W. Eyre *et al*., *N. Engl. J. Med.* **379**, 1322–1331 (2018).
14. C. A. Patterson *et al*., *Crit. Care Med.* **49**, 697–701 (2021).
15. T. Vila *et al*., *MSphere* **5**, e00760-20 (2020).
16. K. Vinayagamoorthy, K. C. Pentapati, H. Prakash, *Mycoses* **65**, 613–624 (2022).
17. E. Rajni, A. Jain, S. Gupta, Y. Jangid, R. Vohra, *Acta Med. (Hradec Kralove)* **65**, 83–88 (2022).
18. J. V. Mulet Bayona, N. Tormo Palop, C. Salvador García, M. D. R. Guna Serrano, C. Gimeno Cardona, *Mycoses* **66**, 882–890 (2023).
19. F. Allaw *et al*., *Microorganisms* **10**, 1011 (2022).
20. M. Lyman *et al*., *Ann. Intern. Med.* **176**, 489–495 (2023).
21. K. Benedict, K. Forsberg, J. A. W. Gold, J. Baggs, M. Lyman, *Emerg. Infect. Dis.* **29**, 1485–1487 (2023).
22. P. W. J. de Groot, O. Bader, A. D. de Boer, M. Weig, N. Chauhan, *Eukaryot. Cell* **12**, 470–481 (2013).
23. L.-O. Essen, M. S. Vogt, H.-U. Mösch, *Biol. Chem.* **401**, 1389–1405 (2020).
24. R. A. Smoak, L. F. Snyder, J. S. Fassler, B. Z. He, *Genetics* **223**, iyad024 (2023).
25. J. F. Muñoz *et al*., *Genetics* **218**, iyab029 (2021).
26. S.-H. Oh *et al*., *Front. Cell. Infect. Microbiol.* **11**, 794529 (2021).
27. S. Singh *et al*., *PLOS Pathog.* **15**, e1007460 (2019).
28. A. Silva-Dias *et al*., *Cytometry A* **81**, 265–270 (2012).
29. J. S. Finkel *et al*., *PLOS Pathog.* **8**, e1002525 (2012).
30. C. Pelletier, A. J. P. Brown, A. Lorenz, *bioRxiv* p. 2023.04.21.537817 (2023).
31. J. Bing *et al*., *PLOS Pathog.* **19**, e1011239 (2023).
32. T. Kraushaar *et al*., *Structure* **23**, 1005–1017 (2015).
33. S. El-Kirat-Chatel *et al*., *ACS Nano* **9**, 1648–1655 (2015).
34. C. Valotteau, V. Prystopiuk, B. P. Cormack, Y. F. Dufrêne, *MSphere* **4**, e00277-19 (2019).
35. S. Brückner *et al*., *eLife* **9**, e55587 (2020).
36. G. P. Maier, M. V. Rapp, J. H. Waite, J. N. Israelachvili, A. Butler, *Science* **349**, 628–632 (2015).
37. Y. Li *et al*., *Mater. Chem. Front.* **1**, 2664–2668 (2017).
38. C. Liang *et al*., *Front. Mar. Sci.* **6**, 565 (2019).
39. S. Kim *et al*., *ACS Nano* **11**, 6764–6772 (2017).
40. X. Huang *et al*., *Nat. Commun.* **14**, 2104 (2023).
41. S. Sokalingam, G. Raghunathan, N. Soundrarajan, S.-G. Lee, *PLOS ONE* **7**, e40410 (2012).
42. H. Fan *et al*., *Nat. Commun.* **10**, 5127 (2019).
43. S. McLaughlin, J. Wang, A. Gambhir, D. Murray, *Annu. Rev. Biophys. Biomol. Struct.* **31**, 151–175 (2002).
44. R. Kean *et al*., *Int. J. Antimicrob. Agents* **52**, 673–677 (2018).
45. R. Kean *et al*., *MSphere* **3**, e00334-18 (2018).
46. B. Short *et al*., *J. Hosp. Infect.* **103**, 92–96 (2019).
47. S. Singh *et al*., *J. Fungi (Basel)* **9**, 103 (2023).
48. P. Arora *et al*., *mBio* **12**, e03181-20 (2021).
49. P. Escandón, *J. Fungi (Basel)* **8**, 748 (2022).

ACKNOWLEDGMENTS

We thank J. Sexton (University of Michigan) for consultation on the development of a label-free high-throughput imaging-based adhesion assay, M. Siddiq (University of Michigan) for consultation in investigating *SCF1* homology and variants, and A. Abraham (University of Michigan) for consultation on surface modification and assistance with vacuum plasma treatment experiments.
Funding: This work was supported by the National Institutes of Health (grant R21AI169186 to D.J.S. and T.R.O.; grants T32AI007528 and F31AI169823 to D.J.S.; grant T32AI007413 to G.Z.; grant R01AI073289 to D.A.; grants R01AI145939 and R21AI159583 to J.E.N.; UCLA CTSI grant KL2TR001882 to S.S., and grant R01AI141202 to A.S.I.); the American Heart Association (grant 938451 to S.S.); and the WACCBIP (World Bank ACE Masters Fellowship and WACCBIP-NCDs Awandare to J.A.E.A.).
Author contributions: Conceptualization: D.J.S., T.R.O.; Funding acquisition: D.J.S., D.A., J.E.N., S.S., A.S.I., T.R.O.; Investigation: D.J.S., J.A.E.A., G.Z., R.Z., C.J.J., H.H., N.D.V., S.S.; Methodology: D.J.S., J.A.E.A., G.Z., R.Z., C.J.J., A.S.I., D.A., J.E.N., S.S., T.R.O.; Project administration: D.J.S., T.R.O.; Supervision: T.R.O., D.A., J.E.N., S.S., A.S.I.; Visualization: D.J.S., R.Z., C.J.J., S.S.; Writing – original draft: D.J.S., T.R.O., S.S., C.J.J., R.Z., J.A.E.A., G.Z.; Writing – review and editing: D.J.S., J.A.E.A., G.Z., R.Z., C.J.J., H.H., N.D.V., A.S.I., D.A., J.E.N., S.S., T.R.O. **Competing interests:** T.R.O. and D.J.S. are inventors on US Provisional Patent 63/502,704 filed on 17 May 2023 and US Provisional Patent 63/514,470 filed on 19 July 2023 related to this work. The remaining authors declare no competing interests. **Data and materials availability:** Data from Illumina sequences are available in the National Center for Biotechnology Information Sequence Read Archive (NCBI SRA; https://www.ncbi.nlm.nih.gov/sra/) under BioProject accession number PRJNA904261 (for RNA-sequencing data) or PRJNA904262 (for *Agrobacterium tumefaciens*–mediated transformation mutant whole-genome sequencing). Strains and constructs generated in this study will be provided for research purposes upon request. All remaining data are available in the main text or the supplementary materials. **License information:** Copyright © 2023 the authors, some rights reserved; exclusive licensee American Association for the Advancement of Science. No claim to original US government works. https://www.science.org/about/science-licenses-journal-article-reuse

SUPPLEMENTARY MATERIALS

science.org/doi/10.1126/science.adf8972
Materials and Methods
Figs. S1 to S15
Tables S1 to S5
References (*50*–*77*)
Data S1
MDAR Reproducibility Checklist

Submitted 5 December 2022; resubmitted 2 July 2023
Accepted 23 August 2023
10.1126/science.adf8972

NANOMATERIALS

3D printing of inorganic nanomaterials by photochemically bonding colloidal nanocrystals

Fu Li[1,2]†, Shao-Feng Liu[3]†, Wangyu Liu[1]†, Zheng-Wei Hou[4], Jiaxi Jiang[5], Zhong Fu[1], Song Wang[1], Yilong Si[1], Shaoyong Lu[1], Hongwei Zhou[3], Dan Liu[1], Xiaoli Tian[1], Hengwei Qiu[1], Yuchen Yang[1], Zhengcao Li[4], Xiaoyan Li[5], Linhan Lin[3]*, Hong-Bo Sun[3]*, Hao Zhang[1,6]*, Jinghong Li[1,7,8]*

3D printing of inorganic materials with nanoscale resolution offers a different materials processing pathway to explore devices with emergent functionalities. However, existing technologies typically involve photocurable resins that reduce material purity and degrade properties. We develop a general strategy for laser direct printing of inorganic nanomaterials, as exemplified by more than 10 semiconductors, metal oxides, metals, and their mixtures. Colloidal nanocrystals are used as building blocks and photochemically bonded through their native ligands. Without resins, this bonding process produces arbitrary three-dimensional (3D) structures with a large inorganic mass fraction (~90%) and high mechanical strength. The printed materials preserve the intrinsic properties of constituent nanocrystals and create structure-dictated functionalities, such as the broadband chiroptical responses with an anisotropic factor of ~0.24 for semiconducting cadmium chalcogenide nanohelical arrays.

Additive manufacturing, also known as 3D printing, has been a revolutionary technology with broad applications (*1*–*3*). Despite the substantial progress in the structural complexities and printing scalabilities (*4*–*6*), 3D printing is mostly limited to metals and plastics (*7*), especially for printing with nanoscale resolution. During printing, atomic bonds should form between the building blocks (atoms or molecules) at desired locations to produce three-dimensional (3D) shapes with sufficient mechanical support. For example, strong metallic bonds (e.g., W–W, ~800 kJ/mol) form during the powder bed fusion printing of metals, whereas covalent bonds (e.g., C–C, ~350 kJ/mol) are produced in the photopolymerization of 3D-printed plastics (*1*).

Such atomic bonding events do not directly occur with comparable resolution for other functional materials, especially inorganic semiconductors and metal oxides. For instance, metal–chalcogen/pnictogen bonding in corresponding II–VI and III–V semiconductors requires elaborate reactions between molecular or ionic building blocks (*8*, *9*), which cannot be triggered at specific locations under regular 3D printing conditions (supplementary text 1). One promising strategy is to use preformed colloidal inorganic nanocrystals (NCs) with compositions covering a broad scope of functional materials (*7*) and high solution processability as building blocks for 3D printing. Colloidal NC inks can be extruded from a micronozzle by inkjet or related techniques (*10*, *11*) and assembled into 3D microstructures joined by van der Waals forces. However, the printing resolution is limited by the nozzle size, and the weak interparticle forces are insufficient to support complex 3D structures. Alternatively, the two-photon polymerization process (*12*) can print arbitrary 3D structures of inorganic NC–polymer hybrids, where the NCs (especially the metal oxides) are physically embedded in (*13*, *14*) or chemically bonded to (*15*–*17*) photocurable resins. The inorganic mass fraction of these hybrids is below 50%. Consequently, the purity and intrinsic properties of inorganic materials cannot be preserved (*18*). 3D printing of perovskites and other materials shows impressive capability in the compositional control of printed materials but still requires glass (*19*) or 3D patterned hydrogels (*20*) as matrices for mechanical support.

Light-triggered direct chemical bonding between inorganic NCs represents a promising approach in producing 3D structures with improved material purity and properties. We demonstrated a 3D printing method for colloidal quantum dots (QDs), whereby the light-generated high-energy charge carriers from QDs induce a series of ligand detachment and rebinding processes to form nanoscale 3D architectures (*21*). However, it is limited to specific combinations of semiconductor QDs and surface ligands (supplementary text 2 and fig. S1). Nonspecific bonding between NCs through their native ligands by using photogenerated nitrene radicals, as shown in the 2D patterning of NCs in solid-state thin films (*22*–*24*), can potentially overcome the material constraints. Here we harness a femtosecond (fs) laser to trigger the dynamic delivery, local accumulation, and nitrene-mediated covalent bonding of colloidal NCs in solution states. This approach, termed 3D Pin, is general for direct 3D printing of inorganic nanomaterials into mechanically robust 3D structures with nanoscale resolution.

Printing mechanism

The core of 3D Pin is to establish strong covalent bonds between colloidal NCs photochemically at desired locations to form 3D structures (Fig. 1A). NCs are composed of inorganic cores coated with a layer of molecules called surface ligands. These ligands are "native" and indispensable because they are introduced before NC synthesis and preserved for providing surface passivation and colloidal solubility to NCs (*25*, *26*). They typically include hydrocarbon chains and terminal anchoring groups that bind to the NC surface (supplementary text 3 and fig. S2). In our work, stable colloidal solutions of various NCs with a small amount of bisazide molecules [e.g., 1,5-bis (4-azido-2,3,5,6-tetrafluorophenyl) penta-1,4-dien-3-one, or BTO; fig. S3] serve as inks (Fig. 1B). BTO has a broad absorption band between 300 and 400 nm (Fig. 1C) and high two-photon absorption cross-section (>10^3 Goeppert-Mayer units, or GM, at 780 nm, fig. S4). It generates nitrene radicals at both ends that readily bridge NC ligands through nonspecific C–H insertion when triggered by a continuous-wave ultraviolet (UV) laser (fig. S5) or a low-energy fs laser (780 nm, 0.009 nJ; table S1). Printing with a fs laser is preferred as the two-photon process permits longer penetration depth and higher printing resolution (supplementary text 4).

In contrast to previous 2D patterning of NC films by light (*22*–*24*, *27*) and other stimuli (*28*, *29*), the NCs are well separated (by several to >10 times the NC size) and undergo strong Brownian motion in the solution (supplementary text 5). Under irradiation, the ligand linking events on the same NCs may reduce the interparticle repulsive forces and improve the possibility for NCs interacting at a small separation. This facilitates the subsequent ligand bonding between NCs in close contact, which produces structures from the inks at the focal point. Such a bonding process also generates a concentration gradient that drives fast NC diffusion [e.g., ~10^{-10} m^2/s for CdSe NCs (*30*)]

[1]Department of Chemistry, Center for Bioanalytical Chemistry, Key Laboratory of Bioorganic Phosphorus Chemistry and Chemical Biology (Ministry of Education), Tsinghua University, Beijing 100084, China. [2]Shanghai Institute of Microsystem and Information Technology, Chinese Academy of Sciences, Shanghai 200050, China. [3]State Key Laboratory of Precision Measurement Technology and Instruments, Department of Precision Instruments, Tsinghua University, Beijing 100084, China. [4]Key Laboratory of Advanced Materials (MOE), School of Materials Science and Engineering, Tsinghua University, Beijing 100084, China. [5]Center for Advanced Mechanics and Materials, Applied Mechanics Laboratory, Department of Engineering Mechanics, Tsinghua University, Beijing 100084, China. [6]Laboratory of Flexible Electronic Technology, Tsinghua University, Beijing 100084, China. [7]Beijing Institute of Life Science and Technology, Beijing 102206, China. [8]Center for BioAnalytical Chemistry, Hefei National Laboratory of Physical Science at Microscale, University of Science and Technology of China, Hefei 230026, China.
†These authors contributed equally to this work.
*Corresponding author. Email: linlh2019@mail.tsinghua.edu.cn (L.L.); hbsun@tsinghua.edu.cn (H.-B.S.); jhli@mail.tsinghua.edu.cn (J.L.); hzhangchem@mail.tsinghua.edu.cn (Ha.Z.)

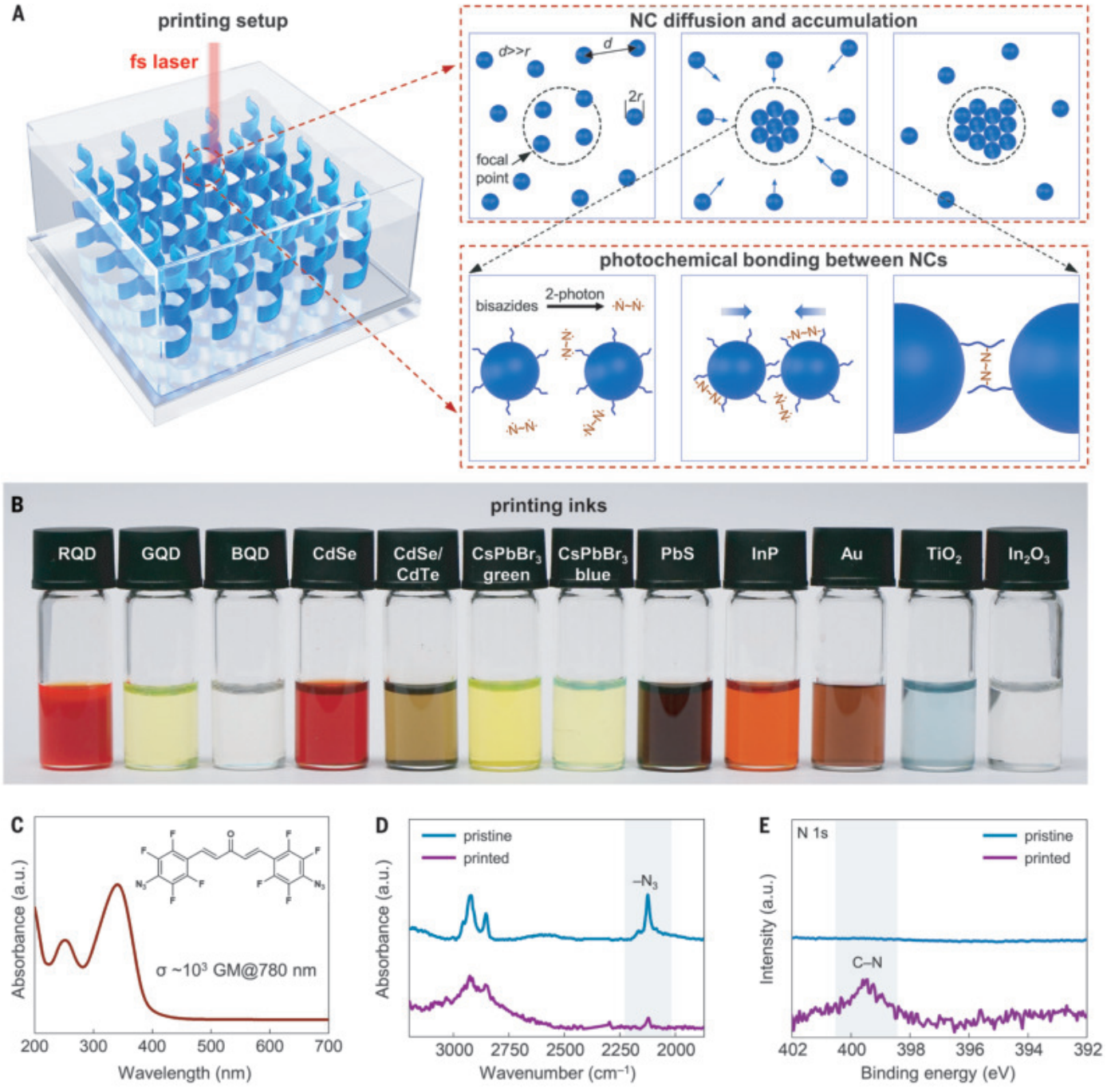

Fig. 1. Mechanism of 3D Pin. (**A**) Scheme illustrating 3D printing of inorganic nanomaterials from a solution containing NCs (blue spheres) and bisazides using a fs laser (left). NCs are initially separated at a distance (*d*) of up to >10 times their sizes (*r*). Diffusion and accumulation bring NCs to the focal point (top right). At reduced interparticle distance, the bonding photochemistry starts from the two-photon activation of bisazides, which then generate nitrene radicals (·Ṅ–Ṅ·) and covalently bond adjacent NCs by bridging their ligands (represented by the lines on the blue spheres) (bottom right). The bonded NCs constitute mechanically robust 3D structures that replicate the laser trajectory. (**B**) Photographs of solutions of various NCs as 3D Pin inks. BQD, GQD, and RQD are II–VI core–shell QDs emitting in blue (CdZnS/ZnS), green (CdSe/CdZnSeS), and red (CdSe/ZnS). (**C**) UV–visible absorption spectrum and molecular structure of BTO. (**D**) FTIR and (**E**) XPS (N1s) spectra of pristine CdSe NC films and printed CdSe structures confirm the underlying photochemistry in 3D Pin. Pristine samples in (D) and (E) refer to spin-coated CdSe NC films with (D) or without (E) BTO linkers. a.u., arbitrary units.

from the surroundings for the following printing processes (fig. S6). The bonding chemistry can be validated by Fourier-transformed infrared (FTIR) and x-ray photoelectron spectroscopic (XPS) spectra of both pristine and printed samples. The decomposition of BTO is confirmed by the substantially reduced resonance of the azido group (asymmetric stretching of $-N_3$ at ~2100 cm^{-1}, Fig. 1D), whereas the reaction between nitrene radicals and NC ligands (alkyl carboxylates in this case) is verified by the N 1s peaks from the produced C–N bonds (Fig. 1E). The preservation of C–H resonance and occurrence of F peaks (fig. S7A) in printed samples further exclude the

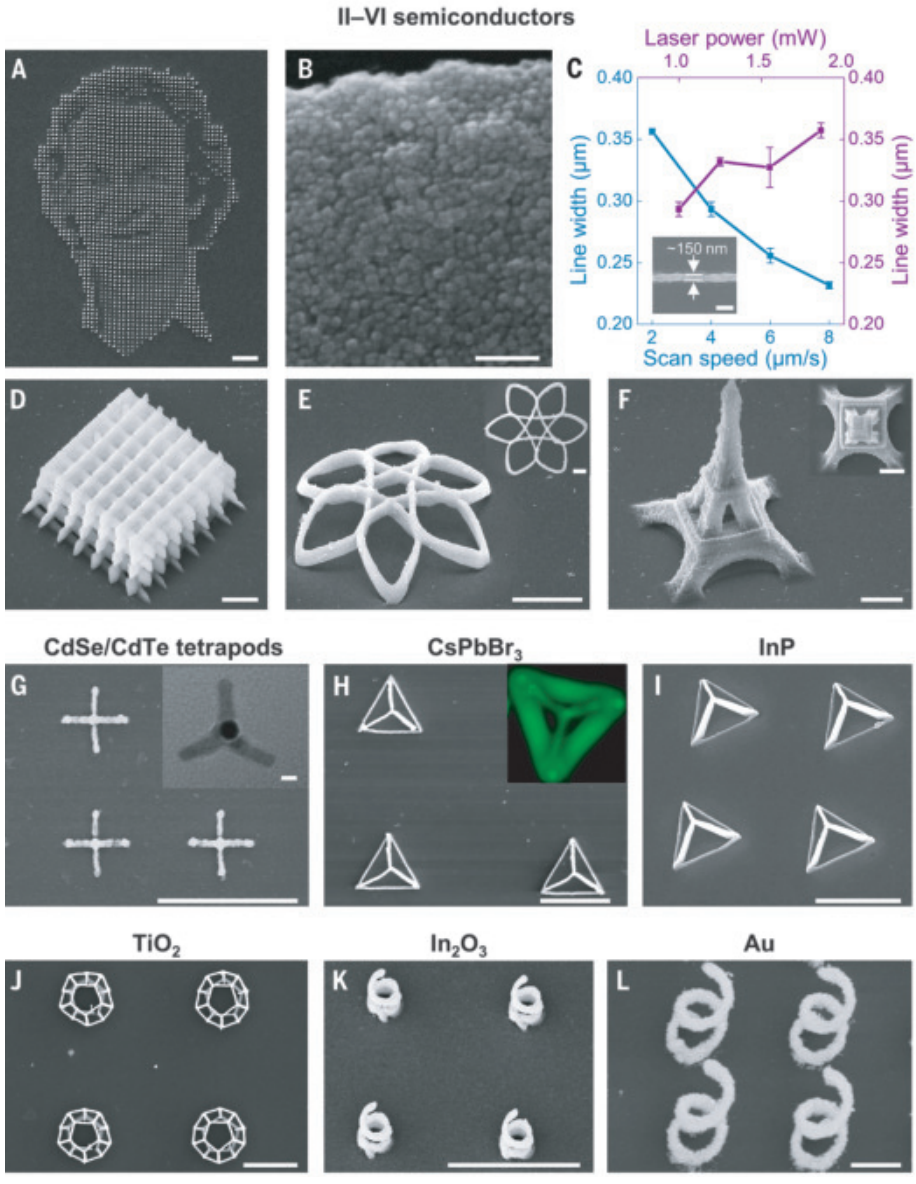

Fig. 2. 3D nanoprinting of various materials. (**A**) SEM image of a portrait of Richard P. Feynman printed with red-emitting CdSe/ZnS core–shell QDs. (**B**) Red QDs are densely distributed in the printed structures while maintaining their sizes and shapes. (**C**) Printing linewidth as a function of scan speed and laser power. The error ranges were from measurements of SEM images. For the scan speed series, the laser power was set as 1 mW. For the laser power series, the scan speed was set as 4 μm/s. Inset shows the SEM image of the finest line. Error bars represent the standard deviation. (**D** to **F**) SEM images of (D) woodpile structures, (E) a bulging flower structure containing both linear and curved components, and (F) the model of Eiffel Tower. Insets in (E) and (F) show the top view. (**G** to **I**) SEM and fluorescent images of structures of different semiconductors printed by 3D Pin, including (G) tetrapods of CdSe/CdTe nanotetrapods (inset, TEM image of a single tetrapod), (H) pyramidal frameworks of $CsPbBr_3$ NCs (inset, fluorescent image), and (I) pyramidal frameworks of InP NCs. (**J** to **L**) SEM images of 3D structures of metal oxides and metals, including (J) dodecahedra of TiO_2 NCs, (K) helices of In_2O_3 NCs, and (L) helices of Au nanorods. All structures shown in this figure were printed from NC solution in toluene containing BTO, except that (L) was printed from Au nanorod solution in water containing DBTAI. Scale bars, 10 μm [(A) and (G) to (L)], 100 nm (B), 2 μm [(D) and inset in (E)], 5 μm [(E) and (F), and inset in (F)], 400 nm [inset in (C)], and 5 nm [inset in (G)].

possibility of nitrene-mediated ligand stripping or other reaction pathways. The solvent of NC inks is toluene, whose reaction with nitrene is negligible and barely affects the printing (supplementary text 6 and fig. S7B). We also replaced BTO with other light-sensitive chemicals that are either nonresponsive to 780-nm fs laser or unable to bridge the ligands, which produced no or fragmented 3D structures (supplementary text 6 and fig. S8). This corroborates the proposed bonding chemistry that is initiated by the absorption of bisazides rather than the one- or two-photon processes of NCs (*21*).

3D nanoprinting of multiple materials

With a home-built apparatus (fig. S9), we printed semiconductor QDs (fig. S10) composed of CdZnSe/CdZnS/ZnS (or CdSe/ZnS for simplicity) core–shell structures into nanopillar arrays. Hundreds of nanopillars with tunable heights (0.3 to 3.3 μm) constitute the portrait of Richard P. Feynman (Fig. 2A). Such 3D pixels with diameters of ~0.6 μm and pitch sizes of ~1 μm remain intact during printing and the subsequent rinsing and drying steps, revealing the bonding-enabled mechanical rigidity. The printed structures are composed of densely packed QDs with preserved shapes and sizes (Fig. 2B and fig. S11). The interparticle distance is determined by the thickness of the ligand layers (<1 nm) and much reduced than those in the inks owing to the accumulation–bonding processes (fig. S12).

3D Pin requires a small amount of BTO additives (as low as ~0.2 wt % to the mass of QDs, fig. S13), which does not influence the original optical properties of QDs (fig. S14 and table S2). The printing resolution is determined by the combination of laser power and scan speed (Fig. 2C and fig. S15). The finest width of printed lines reaches ~150 nm. Consistent with other focus laser-based 3D printing techniques, the printing resolution is anisotropic, with a higher lateral resolution than the axial one (supplementary text 7 and fig. S16). We also noted that the typical printing speeds (1 to 10 μm/s) and lowest ink concentration (1 to 10 mg/ml) for printing are related to the NC diffusion rates, which determines the NC flux from the surroundings to the focal point (supplementary text 7). For example, inks with a low concentration of 0.5 mg/ml cannot provide adequate NCs for continuous printing, which correlates well with the proposed diffusion-limited printing process (fig. S17). Such printing speed achieved at relatively low pulse energy

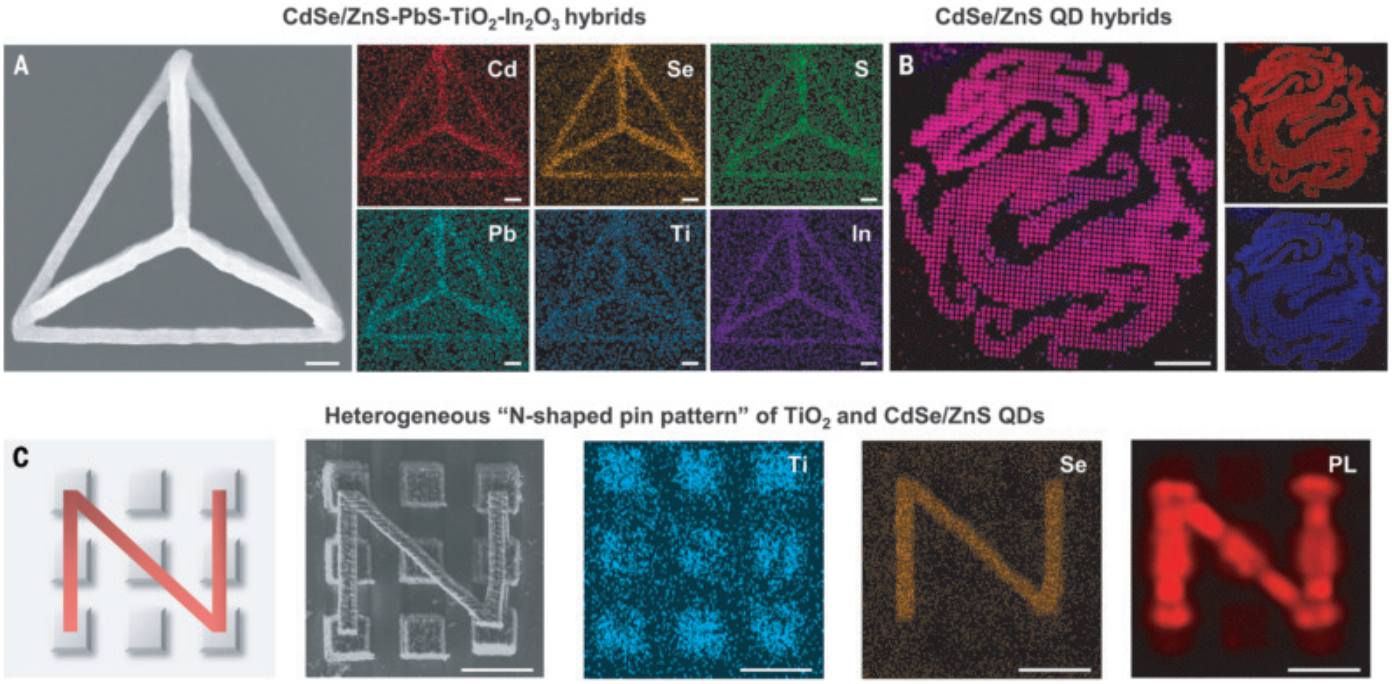

Fig. 3. Hybrid 3D printing of inorganic nanomaterials. (**A**) SEM image of the hybrid pyramidal framework printed from CdSe/ZnS, PbS, In_2O_3, and TiO_2 NCs. (**B**) Fluorescent "Loong" pattern composed of pixels of red- and blue-emitting QDs, displaying the merged magenta emission (left). The panels on the right were taken on the same image with selected color filters. (**C**) Heterogeneous printing of an "N"-shaped pin pattern. The N shape of red-emitting CdSe/ZnS QDs is drawn to connect some of the nine printed dots of TiO_2. From left to right: Design, SEM, EDS mapping (Ti and Se), and fluorescent images of the pin pattern. Scale bars, 1 μm (A), 10 μm (B), and 5 μm (C).

(~0.009 nJ) supports a decent printing throughput comparable to those for typical two-photon polymerization (supplementary text 7).

3D Pin can print QDs into complex nanostructures by steering the laser beam in 3D space. Figure 2D and figs. S18, A to D, show the scanning electron microscopy (SEM) images of woodpile and beam lattice structures printed in a layer-by-layer fashion. The linewidth of the woodpile structure is ~400 nm and the length-to-width ratio is >20. Figure 2E and fig. S18, E and I, show the overhanging structures, such as petal-like structures and nanohelices printed continuously in a single scan. 3D Pin can also produce volumetric objects, as exemplified by the model of Eiffel Tower with a height of ~34 μm (Fig. 2F). To investigate the reliability, we printed arrays of pyramidal frameworks, domes, and overhanging "L" shapes (length-to-width ratio between 10 and 20), which showed identical structures as designed. At a large length-to-width ratio of 30, 60% of the overhanging structures can maintain their shapes after printing and rinsing steps (fig. S19).

3D Pin adapts to NC semiconductors, metal oxides, and metals (figs. S10 and S20) with diverse morphologies, sizes, compositions, surface chemistries, and functionalities (*31*). In addition to the spherical QDs, NCs with more exotic structures, including the heterostructures of branched CdSe/CdTe tetrapods, can also be printed. This yields submicroscale tetrapods (Fig. 2G) composed of nanoscale tetrapods (Fig. 2G, inset). 3D Pin can be extended to other important semiconductors, including metal halide perovskite ($CsPbBr_3$) and III–V (InP) NCs (Fig. 2, H and I). InP shows a strong covalent bonding character and thus high formation energy, whereas $CsPbBr_3$ is ionic and easily crystalizes at room temperature. Bonding of these NCs via their ligands bypasses the complexities associated with their highly dissimilar crystallization energy. We also printed structures from NCs of metal oxides and metals. Figure 2, J and K, shows the structures composed of dielectric TiO_2 and conductive In_2O_3 NCs printed under similar conditions with the semiconductor NCs. Right-handed nanohelices composed of Au nanorods (Fig. 2L) were printed from their aqueous solution containing water-soluble bisazides, *N,N*-dimethyl-*N,N*-trimethylene bis (4-azido-2,3,5,6-tetrafluorobenzamide) ammonium iodide, or DBTAI. The relatively rough surface of Au helices may be due to the random orientation of Au nanorods (fig. S21).

The material versatility enables the "mix-and-match" of NC building blocks to form multimaterial 3D objects. We printed a hybrid of CdSe/ZnS, PbS, TiO_2, and In_2O_3, containing semiconducting, dielectric, and conductive components, into a pyramidal framework (Fig. 3A). Energy-dispersive spectrometry (EDS) mapping reveals the homogeneous distribution of all constituents. Similar to the 2D counterparts (*32*), mixing complementary inorganic nanomaterials in the printed 3D nanostructures can provide programmable tuning of their optical and electrical properties. As an example, printing a mixture of blue- and red-emitting QDs yields high-resolution (2.5×10^3 dots per inch) nanopillar pixels illuminating in magenta (Fig. 3B). Moreover, consecutive 3D Pin of NCs produces "heterostructures" with segments of different materials at desirable locations. Figure 3C shows the original design and SEM image of a nanoscale, 3D replica of a frequently used pin pattern (letter "N") to unlock the screen of a cell phone. The nine dots composed of TiO_2 were first printed, which were then connected by drawing the "N" pattern of red CdSe/ZnS QDs on the top. To show the resolution limit in making such hybrid heterostructures, we printed thin "polar" pillars (800 nm in diameter and ~2.8 μm in height) containing two segments of CdSe/ZnS QDs and $CsPbBr_3$ NCs (fig. S22).

Composition and density of printed structures

We quantified the inorganic mass fraction of printed structures by using core-only CdSe NCs (~6.1 nm) capped with oleic acid ligands as a model system. Details appear in supplementary materials and methods and

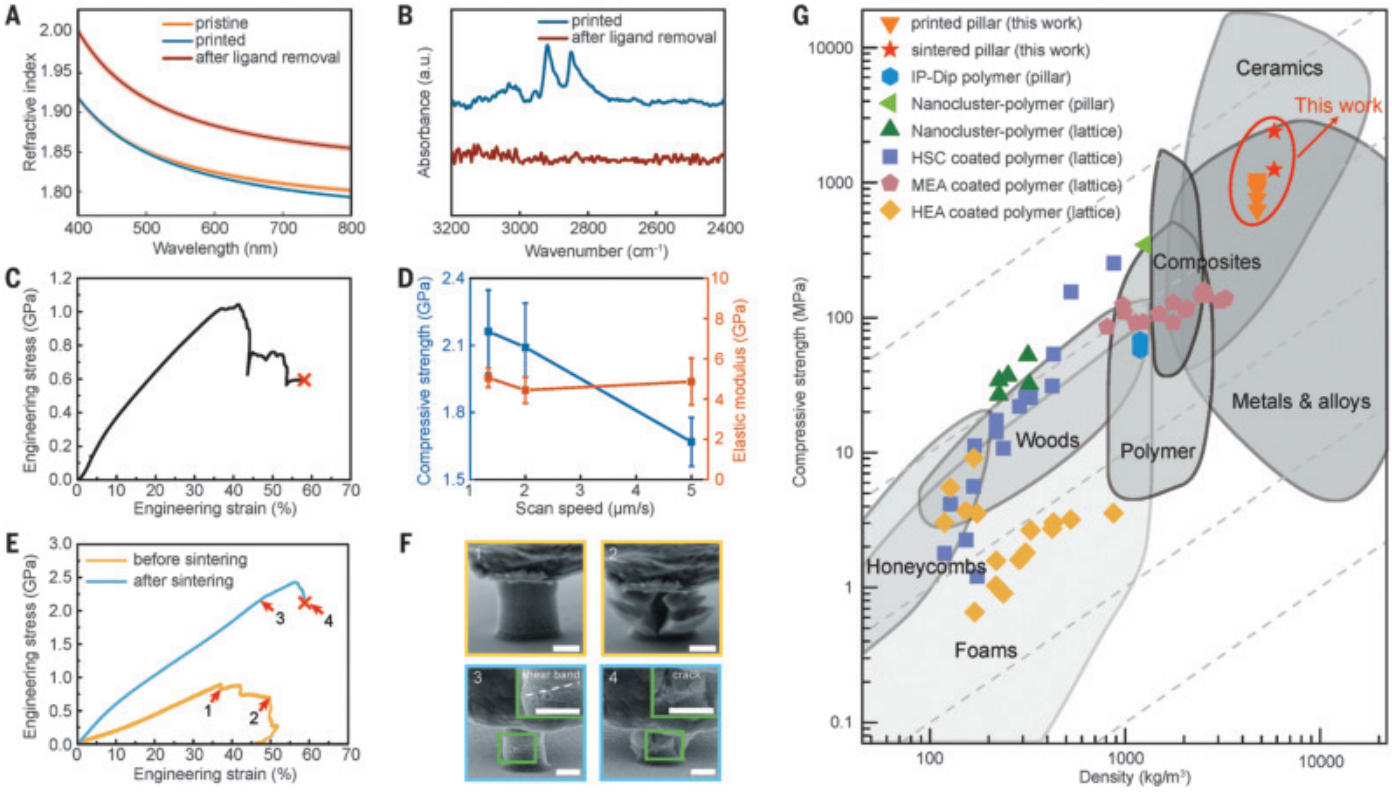

Fig. 4. Refractive indices of printed TiO_2 NC films and mechanical properties of printed pillars of II–VI core–shell QDs. (**A**) Refractive indices of printed TiO_2 NC films before and after ligand removal with nitrosyl tetrafluoroborate, and spin-coated films of pristine TiO_2 NCs with native ligands. The solid curves represent the mean value and the shades represent error bars of refractive indices, respectively. (**B**) FTIR spectra of printed TiO_2 films before and after ligand removal. (**C**) Compressive stress–strain curve. Fracture or failure of overall QD pillar is indicated by the red cross. (**D**) Dependence of compressive strength and elastic modulus of pillars on scan speed. (**E**) Stress–strain curves of pillars before and after sintering at 700°C. The numbers 1 to 4 correspond to different stages of deformation and failure, as monitored by (**F**) the snapshots during compression. The dashed line in the inset of (F) indicates the formation of shear band. (**G**) Compressive strength versus density Ashby plot of QD pillars in this work and other 3D printed pillars or lattices in previous reports (*38*–*42*). Scale bars, 1 μm. Error bars indicate standard deviations in (D).

supplementary text 8. The NC inks contain purified CdSe NCs with low contents of organic ligands (~6 wt % to the mass of NC–ligand complexes, fig. S23) and BTO linkers (<2 wt %). These NCs are colloidally stable with their ligands mostly bound to the NC surface (fig. S24), instead of behaving as "free" and unbound ligands in the solvents. This helps to achieve a high inorganic mass fraction (~91%) in the as-printed structures (fig. S25 and table S3), which well matches the ink formulation. Our analysis reveals that each pair of CdSe NCs in printed structures has ~100 BTO linkers, which are sufficient for interparticle bonding even in the presence of some ligand linking on the same NCs. Inorganic fraction of >90% can also be obtained in printed structures of core–shell QDs and other NCs (table S3). Moreover, the organic components can be removed by using thermal or chemical treatments. Annealing the printed structures at 400°C (typical for complete decomposition of NC ligands, fig. S26) leads to 3D objects composed solely of inorganic materials with preserved structural integrity. The size shrinkage of annealed lattice structures, measured on the basis of the width of entire structures (*15*, *33*), is ~8% (fig. S27). We also noted that parameters such as NC sizes and ligand density can also affect the inorganic fraction of printed structures, as detailed in supplementary text 8.

Taking TiO_2 nanorods containing ~24 wt % of ligands as an example, we estimated the density of printed structures by ellipsometry measurements (supplementary text 9). The as-printed TiO_2 films show a refractive index (n = 1.837) that is similar to those of the spin-coated, pristine films (Fig. 4A and fig. S28). On the basis of the Bruggeman mixing formula (*34*), the as-printed films of ligand-capped TiO_2 NCs possess a low porosity of ~5.0% and a nominal density of 2.09 g/cm^3. Postprinting chemical treatment with nitrosyl tetrafluoroborate (*35*) removes the organic species, as confirmed by the disappearance of C–H modes in FTIR spectra (Fig. 4B). This process reduces the thickness of TiO_2 films by ~32%, and the refractive index of the film is increased to 1.904. The volume fraction of TiO_2 in treated films also increases to ~56.7%, which is comparable with the theoretical limit for randomly packed rods with a similar length-to-diameter ratio (~50%–60%) (*36*). The density of the treated sample is improved to 2.40 g/cm^3. Such chemical treatment also works for 3D-printed TiO_2 or QD structures, which retain their shapes with comparable volume shrinkage (<4% in the width of the entire structure and ~20% in the linewidth, fig. S29). A combination of chemical and thermal treatment can lead to the NC fusion. For instance, the grains of printed CdSe structures grow from <10 to >200 nm after a sequence of $CdCl_2$ treatment and 600°C annealing (fig. S30).

Mechanical properties of printed structures

The strong covalent bonds (bond energy of C–N, ~300 kJ/mol) ensure robust mechanical properties of the printed 3D structures. Figure 4C shows a typical compressive stress-strain curve of micropillars (1.6 μm in diameter) printed from QDs with ~10 wt % of ligands. They show

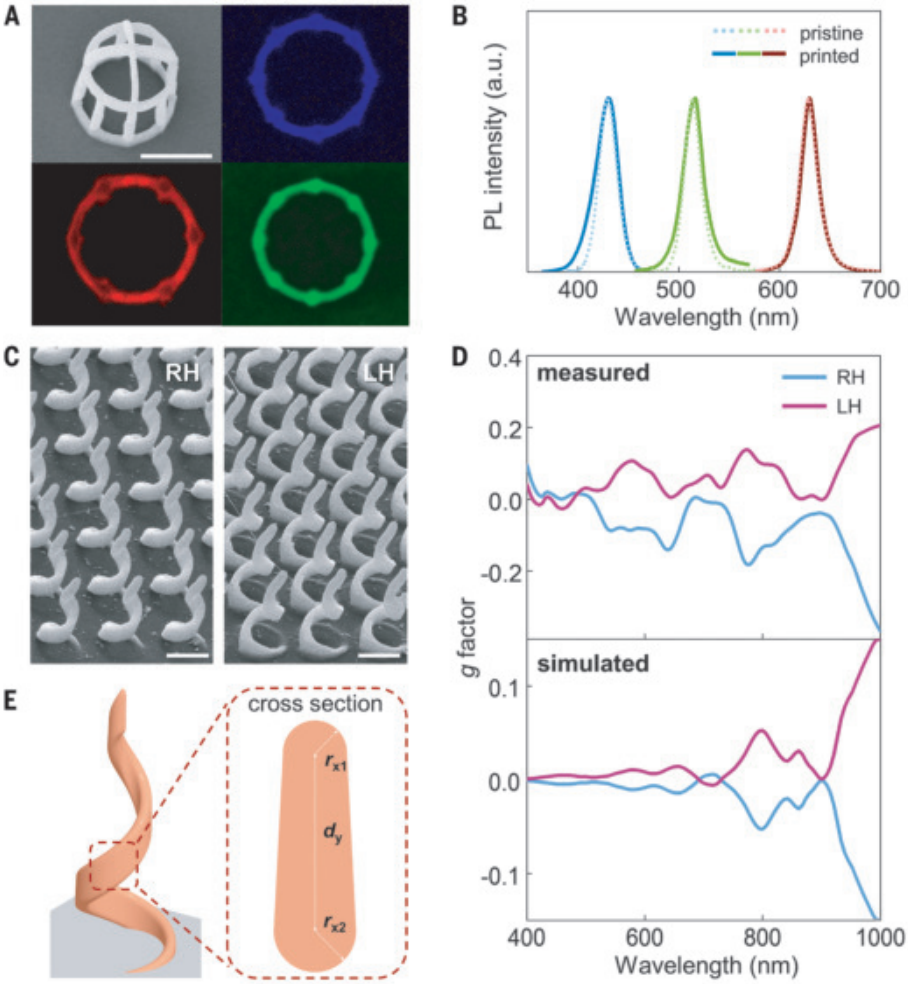

Fig. 5. Optical properties of printed 3D structures of semiconductors. (**A**) SEM and fluorescent images of dome structures of II–VI core–shell QDs emitting in red, green, and blue. (**B**) Corresponding PL spectra of printed QD structures. The spectra of spin-coated, pristine QD films are shown as dashed lines for reference. (**C**) SEM images of printed arrays of left- (LH) and right-handed (RH) nanohelices of red CdSe/ZnS semiconductor QDs. The diameter of the helices narrows with height, with a base diameter of ~2.4 μm. (**D**) Measured and simulated *g*-factor spectra of opposite-handed QD nanohelices. (**E**) 3D model of a single QD helix and its vertical cross-section slice and geometric parameters (r_{x1} = 139 nm, r_{x2} = 154 nm, d_y = 656 nm) used for the simulation. Scale bars, 5 μm (A) and 2 μm (C).

both high compressive strength (~1 GPa) and large fracture strain (~55%, taken from the peak stress of the stress-strain curve). Tailoring the ink compositions and printing parameters can further tune the mechanical properties. Increasing the scan speed leads to lower compressive strength, probably owing to the reduced degree of interparticle bonding (Fig. 4D). However, the moduli are not appreciably affected, because they are mainly determined by the fractions of inorganic and organic components. The pillars sintered at 700°C (Fig. 4, E and F) contain only inorganic grains and show higher compressive strengths (>2 GPa), larger moduli (~7 GPa), and a relatively brittle fracture mode owing to the formation of shear band and subsequent crack propagation. In comparison, the as-printed pillars containing ~20 wt % of organic ligands undergo plastic deformation and eventually fail owing to the nucleation and propagation of nanocracks. Encouragingly, the mechanical properties of 3D-printed samples compare favorably with previous micropillars and micro- or nanolattices composed of polymers and inorganic materials, as summarized in the Ashby plot (Fig. 4G).

Optical properties of printed structures

Printed structures preserve the encoded optical properties of NCs. Structures composed of core-shell QDs, core-only CdSe NCs or blue-emitting $CsPbBr_3$ QDs retain their composition- and size-dependent absorption and photoluminescence (PL) peaks (Fig. 5, A and B, and figs. S31 and S32). Beyond the intrinsic properties of the individual NCs, the 3D-printed objects also show structure-dictated functionalities, especially those based on the collective light-matter interactions at subwavelength scales. We printed arrays of nanohelices with ever-changing diameters based on red CdSe/ZnS QDs (Fig. 5C). Such uniform helical arrays of semiconductors are inaccessible by existing methods (supplementary text 10). The nanohelices show broadband visible and near-infrared chiroptical responses from 400 to 1000 nm with a high anisotropic (*g*) factor up to 0.24 (Fig. 5D). Opposite-handed helical arrays display *g* factor spectra with reverse signs, similar to those reported in self-assembled helices of CdTe NCs with chiral cysteine ligands (*37*). Compared with the self-assembled chiral semiconductor NCs, the *g* factors in our 3D-printed helical arrays are much higher, by ~20 times (0.24 versus 0.01), probably arising from the uniform geometry (*37*). We also calculated the *g* factor using finite-difference time-domain simulation (Fig. 5, D and E, and fig. S33). Although the relation between the geometry of chiral semiconductors and their chiroptical activities is still vague (*37*), the qualitatively matched simulated and experimental results suggest the effectiveness of light manipulation of the printed chiral structures. Moreover, we also harness the multimaterial printing capability to fabricate the Au NC–QD hybrid nanopillars (Au:QD = 1:1 in mass). The broad plasmonic resonance centered at ~580 nm covers the emission peak of green QDs (centered at ~540 nm), leading to plasmon-enhanced fluorescence (fig. S34). The PL intensity of the hybrid nanopillars is about twice as high as that of the QD-only pillars under identical measurement conditions.

In conclusion, 3D Pin yields arbitrarily complex structures of numerous inorganic nanomaterials and their mixtures with nanoscale resolution. The bonding photochemistry at the molecular level and NC building blocks at the nanoscale create "plenty of room" for the material toolbox of 3D printing. The printed structures preserve the intrinsic properties encoded in the NCs and also show additional functionalities stemming from their 3D geometries.

REFERENCES AND NOTES

1. J. R. Tumbleston *et al.*, *Science* **347**, 1349–1352 (2015).
2. S. V. Murphy, A. Atala, *Nat. Biotechnol.* **32**, 773–785 (2014).
3. F. Kotz *et al.*, *Nature* **544**, 337–339 (2017).
4. S. K. Saha *et al.*, *Science* **366**, 105–109 (2019).
5. D. A. Walker, J. L. Hedrick, C. A. Mirkin, *Science* **366**, 360–364 (2019).
6. M. Regehly *et al.*, *Nature* **588**, 620–624 (2020).
7. E. MacDonald, R. Wicker, *Science* **353**, aaf2093 (2016).
8. A. L. Efros, L. E. Brus, *ACS Nano* **15**, 6192–6210 (2021).
9. M. Ludowise, *J. Appl. Phys.* **58**, R31–R55 (1985).
10. B. Y. Ahn *et al.*, *Science* **323**, 1590–1593 (2009).
11. J. Bae *et al.*, *ACS Nano* **14**, 10993–11001 (2020).
12. S. Kawata, H.-B. Sun, T. Tanaka, K. Takada, *Nature* **412**, 697–698 (2001).

13. D. W. Yee, M. L. Lifson, B. W. Edwards, J. R. Greer, *Adv. Mater.* **31**, e1901345 (2019).
14. K. Liu *et al*., *Nat. Commun.* **13**, 4563 (2022).
15. A. Desponds *et al*., *Small* **17**, e2102486 (2021).
16. J. Im *et al*., *Adv. Funct. Mater.* 2211920 (2023).
17. A. Issa *et al*., *ACS Appl. Mater. Interfaces* **13**, 41846–41856 (2021).
18. D. W. Yee, J. R. Greer, *Polym. Int.* **70**, 964–976 (2021).
19. K. Sun *et al*., *Science* **375**, 307–310 (2022).
20. F. Han *et al*., *Science* **378**, 1325–1331 (2022).
21. S.-F. Liu *et al*., *Science* **377**, 1112–1116 (2022).
22. F. Li *et al*., *ACS Nano* **16**, 13674–13683 (2022).
23. S. Lu *et al*., *Angew. Chem. Int. Ed.* **61**, e202202633 (2022).
24. D. Liu *et al*., *Sci. Adv.* **8**, eabm8433 (2022).
25. M. A. Boles, D. Ling, T. Hyeon, D. V. Talapin, *Nat. Mater.* **15**, 141–153 (2016).
26. H. Zhang *et al*., *Nature* **542**, 328–331 (2017).
27. Y. Wang, I. Fedin, H. Zhang, D. V. Talapin, *Science* **357**, 385–388 (2017).
28. F. Palazon, Q. A. Akkerman, M. Prato, L. Manna, *ACS Nano* **10**, 1224–1230 (2016).
29. D. Pires *et al*., *Science* **328**, 732–735 (2010).
30. Z. Hens, J. C. Martins, *Chem. Mater.* **25**, 1211–1221 (2013).
31. C. R. Kagan, E. Lifshitz, E. H. Sargent, D. V. Talapin, *Science* **353**, aac5523 (2016).
32. W. Chen *et al*., *ACS Nano* **13**, 7493–7501 (2019).
33. X. Wen *et al*., *Nat. Mater.* **20**, 1506–1511 (2021).
34. V. A. Markel, *J. Opt. Soc. Am. A Opt. Image Sci. Vis.* **33**, 1244–1256 (2016).
35. A. Dong *et al*., *J. Am. Chem. Soc.* **133**, 998–1006 (2011).
36. S. R. Williams, A. P. Philipse, *Phys. Rev. E Stat. Nonlin. Soft Matter Phys.* **67**, 051301 (2003).
37. W. Feng *et al*., *Sci. Adv.* **3**, e1601159 (2017).
38. L. R. Meza *et al*., *Proc. Natl. Acad. Sci. U.S.A.* **112**, 11502–11507 (2015).
39. Q. Li *et al*., *Science* **378**, 768–773 (2022).
40. J. Bauer, S. Hengsbach, I. Tesari, R. Schwaiger, O. Kraft, *Proc. Natl. Acad. Sci. U.S.A.* **111**, 2453–2458 (2014).
41. X. Zhang *et al*., *Nano Lett.* **18**, 4247–4256 (2018).
42. X. Feng *et al*., *Mater. Today* **42**, 10–16 (2021).

ACKNOWLEDGMENTS

We thank TCL Inc. China for providing QDs (red CdZnSe/CdZnS/ZnS and green CdZnSe/ZnSe/ZnS); Y. Zhao and H. Fan (Tsinghua University) for designing the 3D chiral model and writing the program; X. Chen (Tsinghua University) for ellipsometry measurements of QDs; J.-X. Duan and W.-Q. Yao (Tsinghua University) for providing XPS measurements and analysis; S.-F. Yue (Tsinghua University) for assistance in AFM measurements; X.-Y. Wang (Micro-Nano Fabrication Laboratory of Peking University) and L. Zhao and Y. Tian (National Center for Nanoscience and Technology) for the tutorial in ellipsometry measurements; C. Ma (Tsinghua University) for assistance in TEM imaging; and J. Zhu and X. Wang (Tsinghua University) for the simulation of the laser intensity distribution after the objective. **Funding:** National Key Research and Development Program of China grant 2022YFB3602805 (Ha.Z.); National Natural Science Foundation of China grant 21974079 and 22274087 (Ha.Z.); Tsinghua University Initiative Scientific Research Program (L.L., Ha.Z.); Tsinghua University Dushi Program (Ha.Z.); Strategic Priority Research Program of Chinese Academy of Sciences grant XDB36000000 (J.L.); International Scientific Partnership Program grant ISPP-20-155(1) (J.L.); Tsinghua University Initiative Scientific Research Program (J.L.); National Key Research and Development Program of China grant 2020YFA0715000 (L.L.); National Natural Science Foundation of China grant 62075111 (L.L.); National Natural Science Foundation of China grant 61960206003 (H.-B.S.); Tsinghua-Foshan Innovation Special Fund grant 2021THFS0102 (H.-B.S.); State Key Laboratory of Precision Measurement Technology and Instruments (L.L., H.-B.S.). **Author contributions:** Ha.Z. conceived the study. Ha.Z., L.L., F.L., S.-F.L., and W.L. designed the experiments and analyzed the data. F.L., S.-F.L., and W.L. led the investigation and methodology with assistance from Z.-W.H., J.J., S.W., S.L., Y.Y., Ho.Z., Z.F., D.L., X.T., H.Q., Y.S., Z.L., and X.L. Ha.Z., L.L., F.L., S.-F.L., W.L., Z.-W.H., J.L., and H.-B.S. co-wrote the paper with input from all authors. Ha.Z., J.L., H.-B.S., and L.L. acquired the funding and supervised the study. **Competing interests:** The authors declare no competing interests. **Data and materials availability:** All data are available in the main text or the supplementary materials. **License information:** Copyright © 2023 the authors, some rights reserved; exclusive licensee American Association for the Advancement of Science. No claim to original US government works. https://www.sciencemag.org/about/science-licenses-journal-article-reuse

SUPPLEMENTARY MATERIALS

science.org/doi/10.1126/science.adg6681
Materials and Methods
Supplementary Text 1 to 10
Figs. S1 to S35
Tables S1 to S3
References (*43*–*93*)

Submitted 13 January 2023; accepted 9 August 2023
10.1126/science.adg6681

ORGANIC CHEMISTRY

Aromatic nitrogen scanning by *ipso*-selective nitrene internalization

Tyler J. Pearson, Ryoma Shimazumi, Julia L. Driscoll, Balu D. Dherange, Dong-Il Park, Mark D. Levin*

Nitrogen scanning in aryl fragments is a valuable aspect of the drug discovery process, but current strategies require time-intensive, parallel, bottom-up synthesis of each pyridyl isomer because of a lack of direct carbon-to-nitrogen (C-to-N) replacement reactions. We report a site-directable aryl C-to-N replacement reaction allowing unified access to various pyridine isomers through a nitrene-internalization process. In a two-step, one-pot procedure, aryl azides are first photochemically converted to 3*H*-azepines, which then undergo an oxidatively triggered C2-selective cheletropic carbon extrusion through a spirocyclic azanorcaradiene intermediate to afford the pyridine products. Because the *ipso* carbon of the aryl nitrene is excised from the molecule, the reaction proceeds regioselectively without perturbation of the remainder of the substrate. Applications are demonstrated in the abbreviated synthesis of a pyridyl derivative of estrone, as well as in a prototypical nitrogen scan.

Shape complementarity between a ligand and its target strongly influences binding phenomena in medicinal chemistry. Consequently, isoteric atom replacements that retain the three-dimensional contour of the molecule figure prominently in the discovery process. Within this class, the replacement of an aromatic carbon atom with a nitrogen to afford the corresponding pyridine (or higher azaarene) is privileged for its ability to impart critical drug-like properties through the modulation of physicochemical properties, introduction of hydrogen-bond acceptors, and management of oxidative metabolic liabilities (*1*–*3*). This effect has been so frequently observed by medicinal chemists that it has become known colloquially as the "necessary nitrogen effect" (*4*, *5*). With drug discovery still a largely empirical practice, the identification of such necessary nitrogens frequently requires the examination of each isomeric permutation—a practice referred to in discovery chemistry as a "nitrogen scan" (Fig. 1A). Specific nitrogen scans that were involved in the identification of three recently Food and Drug Administration (FDA)–approved pharmaceuticals are shown in Fig. 1B (*6*–*8*).

Although a nitrogen scan is conceptually simple, its practice is divorced from this ideal by a conspicuous lack of direct atom-replacement techniques. Conducting a nitrogen scan therefore almost invariably requires bottom-up synthesis of each azine isomer (*9*). Each of the analogs shown in Fig. 1B followed this template, requiring iterative syntheses to identify the final clinical candidate. This need for synthetic iteration represents a substantial bottleneck in the discovery of new medicines, and the availability of appropriate heterocycle syntheses can often limit the viability of the strategy altogether.

Accordingly, the development of synthetic methods that can enable the direct interrogation of such C-to-N replacements has attracted substantial interest (*10*–*12*). The reverse reaction (pyridine to benzene) has been reported with the use of stoichiometric titanium alkylidynes, and other atom-swapping approaches (for example, O to N) have been demonstrated in aliphatic systems (*13*–*15*). We recently reported a C2 selective carbon deletion of quinolines, which when paired with nitrogen insertion into the resulting indole, affords the corresponding replacement product, a cinnoline (*16*, *17*). This sequence, however, is currently limited to specific heterocyclic scaffolds and can only afford a single C-to-N replacement isomer.

In the search for a strategy that would enable arbitrary site-directable C-to-N replacement, we took inspiration from the literature of 2-amino-3*H*-azepines, synthesis of which from aryl azides (**1**) and protic nucleophiles dates back to Doering's seminal 1966 report (Fig. 1C) (*18*–*21*). Specifically, Sundberg's subsequent finding that photolysis in the presence of air leads to a mixture of pyridine products, including those featuring the formal "*para*"–

Department of Chemistry, University of Chicago, Chicago, IL 60637, USA.
***Corresponding author: Email: marklevin@uchicago.edu**

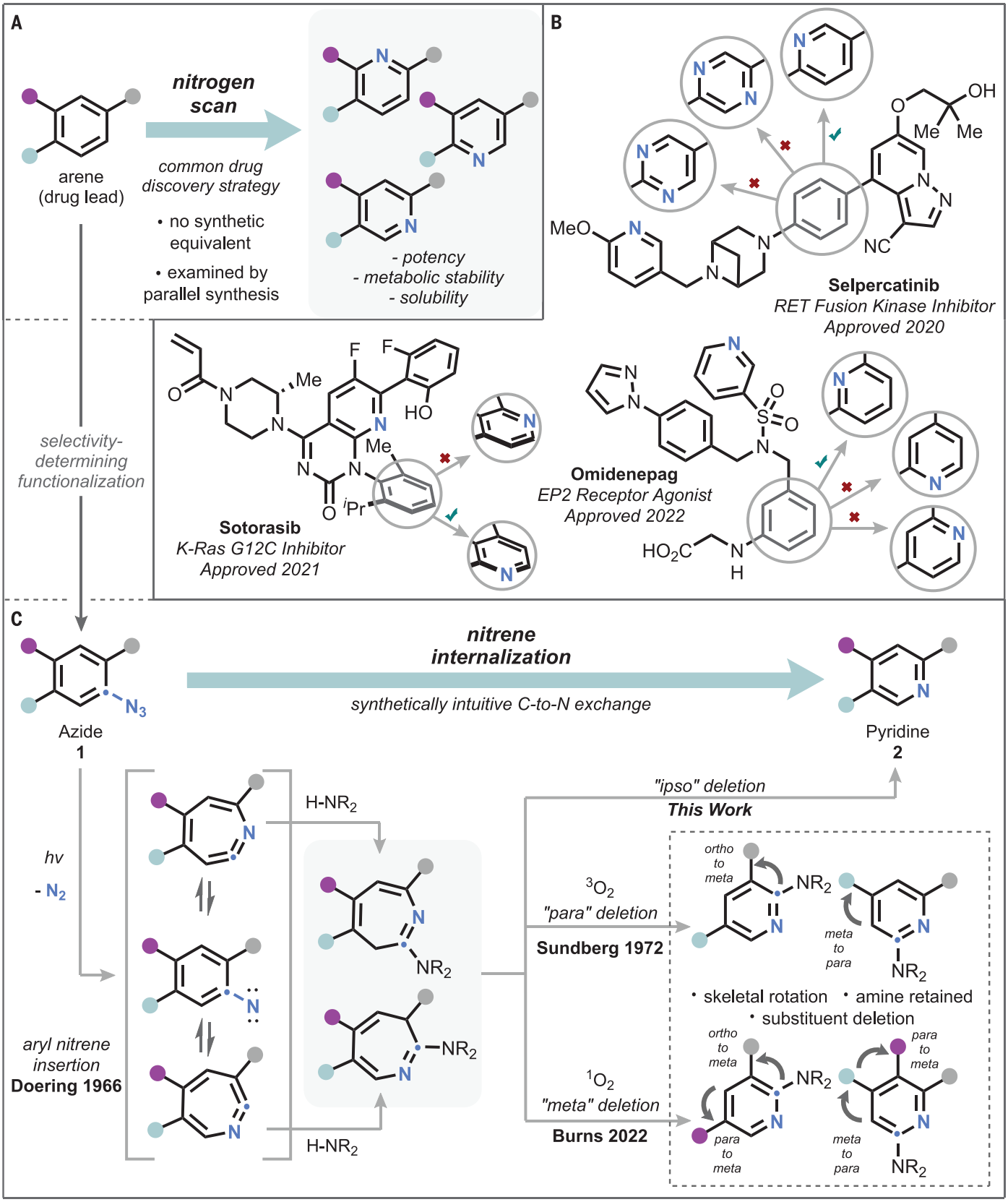

Fig. 1. Background and motivation. (**A**) General outline of the nitrogen scan strategy. (**B**) Examples of nitrogen scans examined in the discovery of recently approved pharmaceuticals. (**C**) Outline of relevant precedent for formal nitrene internalization, emphasizing drawbacks associated with the prior art. EP2, prostaglandin E_2 receptor; RET, rearranged during transfection proto-oncogene; K-Ras G12C, Kirsten rat sarcoma protein with glycine 12 to cysteine mutation; iPr, isopropyl; Me, methyl.

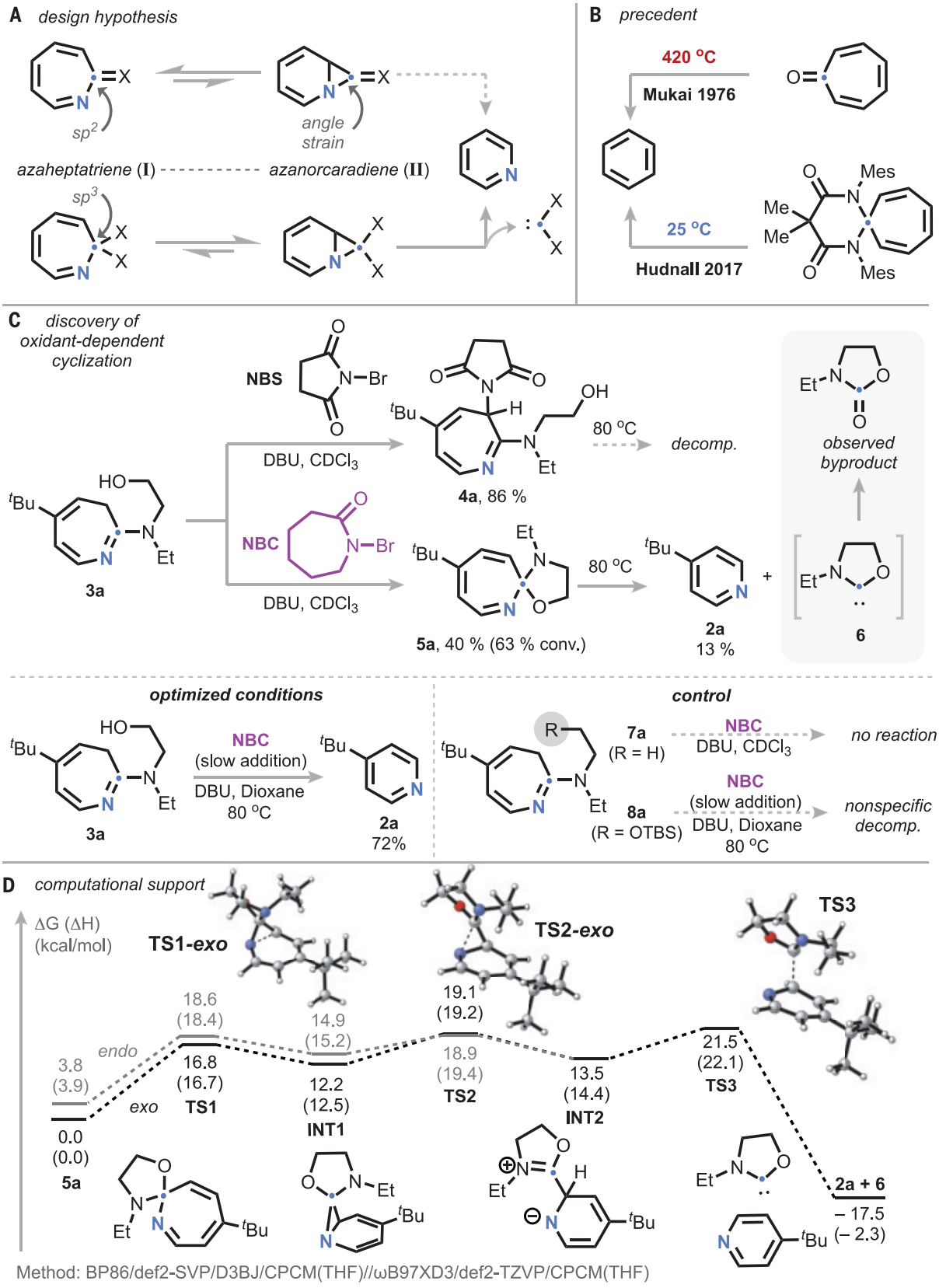

Fig. 2. Design and mechanism. (**A**) Design hypothesis for *ipso*-carbon deletion of azepines. (**B**) Precedent in benzenoid systems, demonstrating hybridization effects. (**C**) Discovery of oxidant-dependent cyclization and thermolytic extrusion of pyridine, with optimized conditions and control experiments lacking a pendant alcohol. (**D**) Computed mechanism for carbene extrusion from spirocyclic azahexatriene. NBS, *N*-bromosuccinimide; NBC, *N*-bromocaprolactam; decomp., decomposition; conv., conversion; DBU, diazabicycloundecene; OTBS, *tert*-butyldimethylsilyloxy.

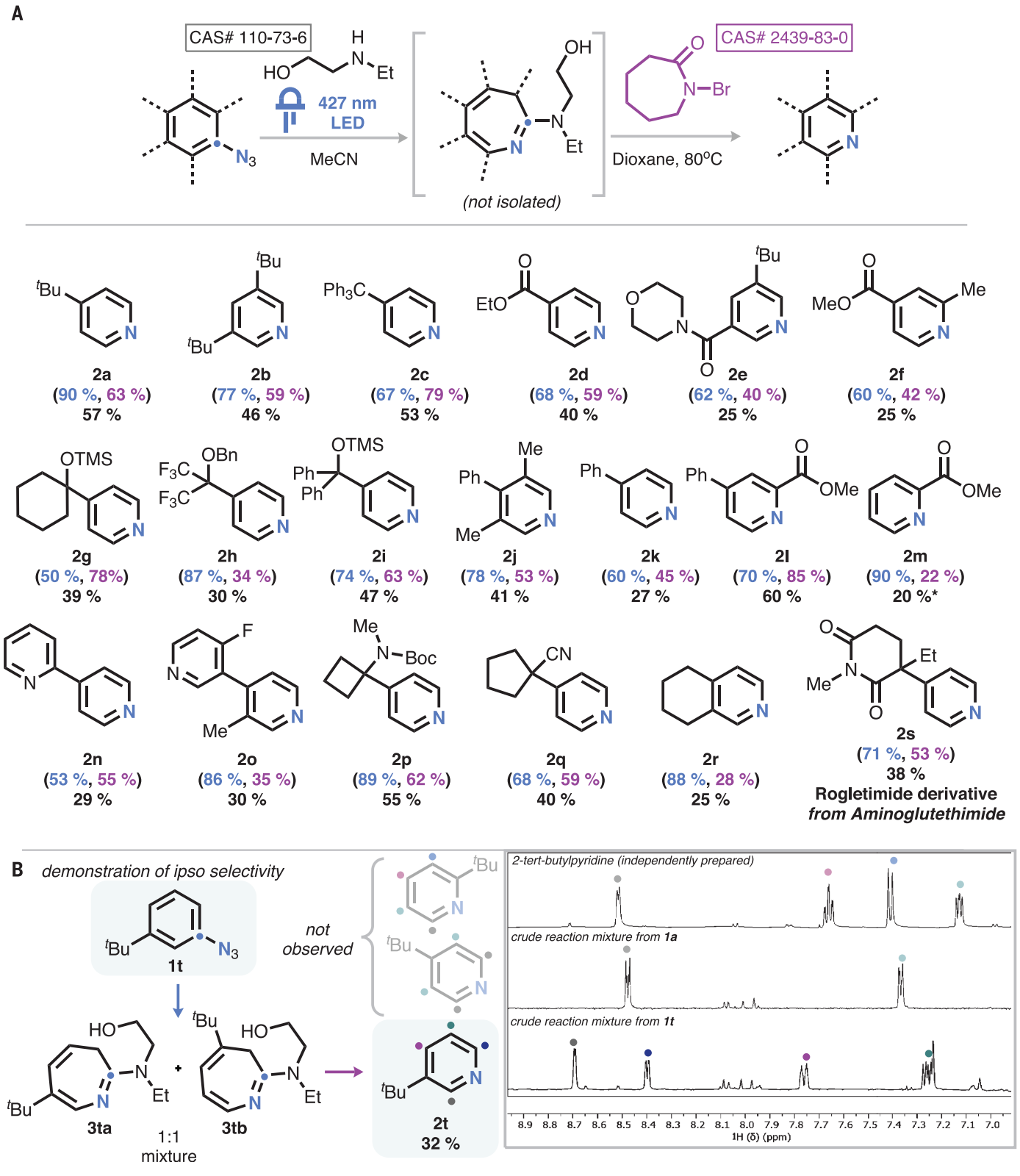
A
CAS# 110-73-6
427 nm LED
MeCN
(not isolated)
Dioxane, 80°C
CAS# 2439-83-0
2a (90 %, 63 %) 57 %
2b (77 %, 59 %) 46 %
2c (67 %, 79 %) 53 %
2d (68 %, 59 %) 40 %
2e (62 %, 40 %) 25 %
2f (60 %, 42 %) 25 %
2g (50 %, 78%) 39 %
2h (87 %, 34 %) 30 %
2i (74 %, 63 %) 47 %
2j (78 %, 53 %) 41 %
2k (60 %, 45 %) 27 %
2l (70 %, 85 %) 60 %
2m (90 %, 22 %) 20 %*
2n (53 %, 55 %) 29 %
2o (86 %, 35 %) 30 %
2p (89 %, 62 %) 55 %
2q (68 %, 59 %) 40 %
2r (88 %, 28 %) 25 %
2s (71 %, 53 %) 38 %
Rogletimide derivative from Aminoglutethimide
B demonstration of ipso selectivity
1t
not observed
3ta
3tb
1:1 mixture
2t 32 %
2-tert-butylpyridine (independently prepared)
crude reaction mixture from 1a
crude reaction mixture from 1t
1H (δ) (ppm)

Fig. 3. Scope and selectivity. (**A**) Scope of the reaction. Standard conditions: (i) 0.3 mmol aryl azide, 0.3 mmol ethylaminoethanol, 3 ml MeCN, and 427-nm light-emitting diode (LED); (ii) 0.3 mmol DBU, 3 ml dioxane heated to 80°C, and 0.6 mmol *N*-bromocaprolactam added dropwise at 80°C. Isolated yield of pyridine from aryl azide (black). Proton NMR (^{1}H-NMR) yield of photolysis (blue) and interpolated yield of pyridine based on azepine yield (purple), shown in parentheses. Asterisk indicates NMR yield. (**B**) Demonstration that nonsymmetric substrates form only one pyridine isomer.

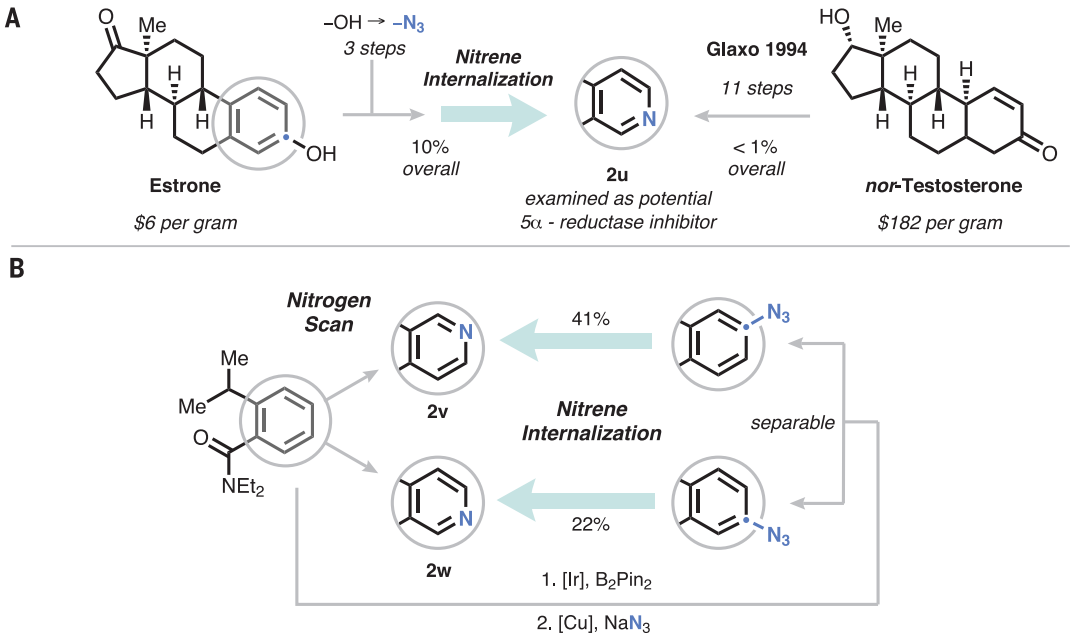

Fig. 4. Applications of nitrene internalization. (**A**) Synthesis of an azasteroid from estrone and comparison with published route from nortestosterone. (**B**) Demonstration of a prototypical nitrogen scan leveraging an unselective C–H borylation.

carbon deletion products, suggested that oxidation of the azepines could serve as a potential path forward (*22*). In a further development, Burns recently reported that singlet oxygen acts on the *3H*-azepines to induce formal "*meta*"-carbon deletion (*23*). Both of these approaches are problematic in that the nitrogen insertion and carbon deletions are conducted with differing selectivity, leading to an overall sequence that produces multiple products (in the case of nonsymmetric starting aryl azides), removes distal functional groups, retains the incoming amine nucleophile, and thereby promotes rearrangement of the arene skeleton. Indeed, such rearrangements are the norm in the handful of other ring-contraction reactions of azepines that have been reported (*24*–*34*). Whereas in certain instances this may be desirable, such skeletal rotation precludes straightforward structure-activity interrogation and complicates retrosynthetic analysis. We reasoned that selective *ipso*-carbon deletion of azepines would instead allow direct formation of a single pyridine isomer (**2**) with neither skeletal nor functional group perturbation. This would also enable nitrogen scanning because the site selectivity of azide installation would, in a predictable and straightforward manner, guide the final site of nitrogen placement. In effect, the net transformation would be internalization of the nitrene nitrogen, replacing the carbon atom to which it was formerly attached. We report the successful realization of such an *ipso*-selective nitrene-internalization reaction.

Development of an oxidative carbon extrusion

Our design centered on the hypothesis that oxidation of the azepine would lead to an azaheptatriene species (**I**) from which chelotropic extrusion of the *ipso* carbon could be achieved through the corresponding azanorcaradiene isomer (**II**) (Fig. 2A). In this regard, we were guided by precedent in the analogous benzenoid systems; whereas decarbonylation of tropone requires temperatures >400°C, spirocyclic diamido-aminal derivatives have been shown to extrude benzene at or near room temperature (Fig. 2B) (*35*–*37*). This difference in reactivity can be attributed to the change in angle strain of the differently hybridized azanorcaradiene intermediates. Accordingly, we envisioned that introduction of a second pendant donor to the amine nucleophile would enable spirocyclization and thereby facilitate carbene elimination through a similar reduction of angle strain. Initial attempts with 1, *n*-diamines (which would lead to N-heterocyclic carbene leaving groups) provided detectable quantities of pyridine but were consistently plagued by the oxidative sensitivity of the free amine. Consequently, we turned our attention to the aminoalcohol-substituted azepine derivative **3a**. On the basis of prior reports of nondestructive oxidation of azepines through the use of *N*-bromosuccinimide, we initially hypothesized that similar oxidants would facilitate oxidation and spirocycle formation in our system (*38*). However, treatment of **3a** with an organic base and *N*-bromosuccinimide led to the exclusive formation of the succinimide-trapped oxidation product **4a** (Fig. 2C). Having observed the noninnocence of the liberated conjugate anion upon formal Br^+ transfer, we hypothesized that further modulation of the oxidant could allow productive reactivity. Upon subsequent examination of *N*-bromocaprolactam, a less-oxidizing Br^+ equivalent, we observed the formation of the desired spirocyclic *N*,*O*-ketal **5a** (*39*). Heating of this species to 80°C resulted in the liberation of the corresponding pyridine in moderate yield, whereas thermolysis of **4a** led only to nonspecific decomposition. Because further oxidation of **5a** begins to compete with **3a** as the reaction proceeds, if the oxidation reaction is instead conducted at 80°C with slow addition of the oxidant, much higher yields of the desired pyridine can be obtained. Although the putative carbene byproduct (**6**) could not be detected, we could observe its oxidation product, *N*-ethyl oxazolidinone, with both nuclear magnetic resonance (NMR) and mass spectrometry. This oxidation can occur either from adventitious dioxygen or the Br^+ reagent, with the latter forming the oxazolidinone through hydrolysis upon aqueous workup.

Control experiments with aminoazepines that lacked the pendant alcohol function (**7a**) or in which the alcohol was silylated (**8a**) did not afford any detectable pyridine under analogous conditions, supporting the critical role of spirocyclization in the carbon-deletion process. Computational assessment of the formation of **2a** from **5a** at the BP86/def2-SVP/D3BJ/CPCM(THF)//ωB97XD3/def2-TZVP/CPCM(THF) level of theory revealed an energetic landscape roughly in line with our experimental observations (THF, tetrahydrofuran). The extrusion was predicted to proceed with an overall barrier of 21.5 kcal/mol through a stepwise carbene extrusion by means of a zwitterionic intermediate (**INT2**) (*37*). Although various levels of theory disagreed on the rate-determining step, all functionals that we examined afforded an energy surface with three similarly energetic transition states (details provided in supplementary materials). The two diastereomeric

pathways were found to be similar in energy, converging at **INT2**.

Reaction scope and applications

In seeking to translate these observations to a synthetic protocol starting from the aryl azide, we found that the crude photolysate from the initial azepine synthesis could be effectively carried forward to pyridine without intermediate purification, avoiding yield losses associated with purification of the azepine. This two-stage, one-pot transformation was found to be readily applicable to a range of aryl azides (Fig. 3). Various alkyl, aryl, and heteroaryl groups were compatible in a number of different substitution patterns (**2a** to **2c**, **2j**, **2k**, **2n**, **2o**, and **2r**). Electron-rich arenes (**2b**, **2j**, and **2r**) and those bearing both resonance (**2d** to **2f**, **2l**, and **2m**) and inductive (**2h**) acceptors were all viable for nitrene internalization. The reaction also tolerates protected amines (**2p** and **2s**), allowing conversion of aminoglutethimide into rogletimide and alcohols (**2 g**, **2h**, and **2i**), even those with delicate protecting groups such as silyl ethers. Strained and fused rings were also compatible (**2p** and **2r**).

A critically important feature of our protocol is that in cases in which two different azepine isomers are formed during photolysis, both converge to a common product. Indeed, for substrate **1t**, we could observe the formation of both azepine isomers in a 1:1 ratio. Treatment of these azepines, either as a mixture (Fig. 3B) or upon separation (supplementary materials), led to the formation of the *ipso*-substitution product **2t** as the exclusive pyridine product, with no detectable formation of its isomeric pyridines. Although isomers **3ta** and **3tb** both yielded pyridine, they proceeded with differing yields, suggesting that the specific steric profile of the azepine does influence the oxidation efficiency.

Limitations manifest in both steps of the reaction. For example, functionalities in the *ortho* position that can competitively react with the photogenerated nitrene (for example, Cadogan cyclization) are not well tolerated during photolysis (supplementary materials) (*40*, *41*). Some substrates also have limitations inherent to their photophysics. For example, 4-azidobiphenyl undergoes facile intersystem crossing relative to ring expansion and therefore generates substantial quantities of triplet nitrene products such as azobiphenyl and 4-phenylaniline (*42*). Furthermore, resonance donors such as alkoxy and amine substituents in the *ortho* and *para* positions of the aryl ring favor the formation of quinone-type resonance forms upon nitrene generation, which we have found not to productively form azepines. The oxidation carries a different set of limitations. Free alcohols and amines do not productively react with *N*-bromocaprolactam, even in the presence of excess base, necessitating their protection. In some instances, overoxidation of the intermediate azepine leads instead to bromopyridines or bipyridines as prominent by-products. In this regard, we found that substrates bearing sterically demanding groups in the *para* position tended to avoid these side reactions (compare **2l** versus **2m**; **2a** versus **2t**) and as such served as the most general substrate class.

To further demonstrate the applications of this protocol, we examined its use in a more complex setting (Fig. 4A). Estrone can be converted to the corresponding azide in three steps; upon subsequent application of our protocol, the pyridine analog (**2u**) can be accessed in 10% overall yield from the parent steroid. This compound had previously been synthesized en route to a potential 5α-reductase inhibitor and was prepared from nortestosterone (despite its homology to the far more widely available estrone) in 11 steps and <1% overall yield (*43*).

Lastly, we conducted a direct nitrogen scan on a simple model arene (Fig. 4B). Application of an unselective iridium-catalyzed C–H borylation of an asymmetrically 1,2-disubstituted benzene followed by Chan-Lam azidation afforded two separable, isomeric aryl azides. Subsequent nitrene internalization of each of these precursors afforded isomeric pyridines **2v** and **2w** from a single parent without contamination by any other pyridine isomers.

We have developed a transformation that enables site-specific replacement of a carbon atom in an aromatic ring with a nitrogen atom. Because installation of the requisite azide can proceed from a variety of conveniently installed functional groups, and because the reaction promotes deletion of the targeted *ipso* carbon, site-specific, predictable replacement reactions can be conducted, enabling nitrogen scan operations that serve as a direct chemical analog to the common medicinal chemistry strategy. We anticipate a wide range of exciting applications for this selective benzene-to-pyridine transformation, as well as the underlying spirocyclic azanorcaradiene mechanism that underpins it.

REFERENCES AND NOTES

1. Y. Hu, D. Stumpfe, J. Bajorath, *J. Med. Chem.* **60**, 1238–1246 (2017).
2. D. J. St Jean Jr., C. Fotsch, *J. Med. Chem.* **55**, 6002–6020 (2012).
3. N. A. Meanwell, *J. Med. Chem.* **54**, 2529–2591 (2011).
4. L. D. Pennington, D. T. Moustakas, *J. Med. Chem.* **60**, 3552–3579 (2017).
5. L. D. Pennington, P. N. Collier, E. Comer, *Med. Chem. Res.* **32**, 1278–1293 (2023).
6. B. A. Lanman *et al*., *J. Med. Chem.* **63**, 52–65 (2020).
7. S. W. Andrews, J. F. Blake, M. J. Chicarelli, A. Golos, J. Haas, Y. Jiang, G. R. Kolakowski, Substituted pyrazolo[1,5-A]pyridine compounds as RET kinase inhibitors. US Patent US10023570B2 (2018).
8. R. Iwamura *et al*., *J. Med. Chem.* **61**, 6869–6891 (2018).
9. J. A. Joule, K. Mills, *Heterocyclic Chemistry* (Wiley-Blackwell, ed. 5, 2010).
10. D. C. Blakemore *et al*., *Nat. Chem.* **10**, 383–394 (2018).
11. K. R. Campos *et al*., *Science* **363**, eaat0805 (2019).
12. J. Jurczyk *et al*., *Nat. Synth.* **1**, 352–364 (2022).
13. A. R. Fout, B. C. Bailey, J. Tomaszewski, D. J. Mindiola, *J. Am. Chem. Soc.* **129**, 12640–12641 (2007).
14. T. Morofuji, K. Inagawa, N. Kano, *Org. Lett.* **23**, 6126–6130 (2021).
15. H. Lyu, I. Kevlishvili, X. Yu, P. Liu, G. Dong, *Science* **372**, 175–182 (2021).
16. J. Woo *et al*., *Science* **376**, 527–532 (2022).
17. S. Liu, X. Cheng, *Nat. Commun.* **13**, 425 (2022).
18. W. von E. Doering, R. A. Odum, *Tetrahedron* **22**, 81–93 (1966).
19. N. P. Gritsan, M. S. Platz, *Chem. Rev.* **106**, 3844–3867 (2006).
20. W. T. Borden *et al*.. *Acc. Chem. Res.* **33**, 765–771 (2000).
21. R. K. Smalley, "Azepines: 3.1. Azepines, Cyclopentazepines and Related Systems" in *Hetarenes IV: Six-Membered and Larger Hetero Rings with Maximum Unsaturation*, vol. E9d of *Methods of Organic Chemistry (Houben-Weyl)*, E. Schaumann, Ed. (Georg Thieme Verlag, 1997), pp. 108–298.
22. R. J. Sundberg, S. R. Suter, M. Brenner, *J. Am. Chem. Soc.* **94**, 513–520 (1972).
23. S. C. Patel, N. Z. Burns, *J. Am. Chem. Soc.* **144**, 17797–17802 (2022).
24. J. W. Streef, H. C. van der Plas, Y. Y. Wei, J. P. Declercq, M. Van Meerssche, *Heterocycles* **26**, 685 (1987).
25. S. Bátori, R. Gompper, J. Meier, H.-U. Wagner, *Tetrahedron* **44**, 3309–3318 (1988).
26. M. Ogata, H. Matsumoto, H. Kanō, *Tetrahedron* **25**, 5217–5226 (1969).
27. M. Anderson, A. W. Johnson, *J. Chem. Soc. C Org.* **1966**, 1075–1078 (1966).
28. K. Satake *et al*., *Chem. Lett.* **25**, 1129–1130 (1996).
29. M. Anderson, A. W. Johnson, *J. Chem. Soc. Resumed* **1965**, 2411–2422 (1965).
30. R. J. Sundberg, B. P. Das, R. H. Smith, *J. Am. Chem. Soc.* **91**, 658–668 (1969).
31. C. Wentrup, *J. Chem. Soc. D* **0**, 1386–1387 (1969).
32. S. Karimi *et al*., *Tetrahedron* **69**, 147–151 (2013).
33. S. Karimi *et al*., *Tetrahedron Lett.* **56**, 6886–6889 (2015).
34. G. Li, M. N. Lavagnino, S. Z. Ali, S. Hu, A. T. Radosevich, *J. Am. Chem. Soc.* **145**, 41–46 (2023).
35. A. Amano, T. Mukai, T. Nakazawa, K. Okayama, *Bull. Chem. Soc. Jpn.* **49**, 1671–1675 (1976).
36. T. A. Perera, E. W. Reinheimer, T. W. Hudnall, *J. Am. Chem. Soc.* **139**, 14807–14814 (2017).
37. E. Vilsmaier, G. Kristen, C. Tetzlaff, *J. Org. Chem.* **53**, 1806–1808 (1988).
38. C. E. J. Cordonier *et al*., *J. Org. Chem.* **70**, 3425–3436 (2005).
39. D. H. Miles, M. Veguillas, F. D. Toste, *Chem. Sci.* **4**, 3427–3431 (2013).
40. J. M. Lindley, I. M. McRobbie, O. Meth-Cohn, H. Suschitzky, *J. Chem. Soc., Perkin Trans. 1* **1977**, 2194–2204 (1977).
41. P. A. S. Smith, B. B. Brown, *J. Am. Chem. Soc.* **73**, 2435–2437 (1951).
42. M.-L. Tsao *et al*., *J. Am. Chem. Soc.* **125**, 9343–9358 (2003).
43. C. Haffner, *Tetrahedron Lett.* **35**, 1349–1352 (1994).

ACKNOWLEDGMENTS

We thank S. Snyder (UChicago) for helpful discussions. We thank P. Kelly (UChicago) for assistance with separations. The University of Chicago's Research Computing Center is thanked for computational resources. **Funding:** M.D.L. acknowledges the NIH (R35 GM142768) for research support. J.L.D. thanks the NSF Graduate Research Fellowship (DGE: 2140001). **Author contributions:** T.J.P., J.L.D., and M.D.L. conceived of the work. T.J.P., R.S., J.L.D., B.D., and D.-I.P. designed and conducted synthetic experiments, including purification and characterization. T.J.P. conducted computational studies. M.D.L. and T.J.P. prepared the manuscript with input from all authors. M.D.L. directed the research. **Competing interests:** The authors declare that they have no competing interests. **Data and materials availability:** All data are available in the supplementary materials. **License information:** Copyright © 2023 the authors, some rights reserved; exclusive licensee American Association for the Advancement of Science. No claim to original US government works. https://www.science.org/about/science-licenses-journal-article-reuse

SUPPLEMENTARY MATERIALS

science.org/doi/10.1126/science.adj5331
Materials and Methods
Figs. S1 to S7
Table S1
NMR Spectra
References (*44*–*91*)

Submitted 1 July 2023; accepted 28 August 2023
10.1126/science.adj5331

HEART DISEASE

Fibroblasts in heart scar tissue directly regulate cardiac excitability and arrhythmogenesis

Yijie Wang[1,2,3,4,5,6], Qihao Li[7], Bo Tao[1,2,3,4,5,6], Marina Angelini[8], Sivakumar Ramadoss[1,2,3,4,5,6], Baiming Sun[1,2,3,4,5,6], Ping Wang[1,2,3,4,5,6], Yuliya Krokhaleva[9], Feiyang Ma[10], Yiqian Gu[3,11], Alejandro Espinoza[3,11], Ken Yamauchi[4,12], Matteo Pellegrini[3,11], Bennett Novitch[4,12], Riccardo Olcese[8,13], Zhilin Qu[1], Zhen Song[7], Arjun Deb[1,2,3,4,5,6]*

After heart injury, dead heart muscle is replaced by scar tissue. Fibroblasts can electrically couple with myocytes, and changes in fibroblast membrane potential can lead to myocyte excitability, which suggests that fibroblast-myocyte coupling in scar tissue may be responsible for arrhythmogenesis. However, the physiologic relevance of electrical coupling of myocytes and fibroblasts and its impact on cardiac excitability in vivo have never been demonstrated. We genetically engineered a mouse that expresses the optogenetic cationic channel ChR2 (H134R) exclusively in cardiac fibroblasts. After myocardial infarction, optical stimulation of scar tissue elicited organ-wide cardiac excitation and induced arrhythmias in these animals. Complementing computational modeling with experimental approaches, we showed that gap junctional and ephaptic coupling, in a synergistic yet functionally redundant manner, excited myocytes coupled to fibroblasts.

Myocardial infarction (MI) results in the formation of scar tissue that enables fibroblasts to come in close apposition to myocytes (*1*, *2*). Fibroblasts can electrically couple with myocytes (*3*) and promote myocyte excitability (*4*–*9*). However, the biological relevance of electrical coupling between fibroblasts and myocytes in vivo, as a mechanism of cardiac excitability and arrhythmogenesis, has not been demonstrated. Using genetically engineered animal models, optogenetics, and computational modeling, we report that fibroblasts couple with myocytes in heart scars to directly cause cardiac excitation and arrhythmogenesis in vivo.

[1]Division of Cardiology, Department of Medicine, University of California Los Angeles, Los Angeles, CA 90095, USA. [2]Cardiovascular Theme, David Geffen School of Medicine, University of California Los Angeles, Los Angeles, CA 90095, USA. [3]Department of Molecular, Cell and Developmental Biology, University of California Los Angeles, Los Angeles, CA 90095, USA. [4]Eli and Edythe Broad Center of Regenerative Medicine and Stem Cell Research, University of California Los Angeles, Los Angeles, CA 90095, USA. [5]Molecular Biology Institute, University of California Los Angeles, Los Angeles, CA 90095, USA. [6]California Nanosystems Institute, University of California Los Angeles, Los Angeles, CA 90095, USA. [7]Peng Cheng Laboratory, Shenzhen, Guangdong 518000, China. [8]Department of Anesthesiology and Perioperative Medicine, David Geffen School of Medicine, University of California Los Angeles, Los Angeles, CA 90095, USA. [9]UCLA Cardiac Arrhythmia Center, David Geffen School of Medicine, University of California Los Angeles, Los Angeles, CA 90095, USA. [10]Department of Cell and Developmental Biology, Feinberg School of Medicine, Northwestern University, Chicago, IL 60611, USA. [11]Institute for Quantitative and Computational Biosciences–The Collaboratory, University of California Los Angeles, Los Angeles, CA 90095, USA. [12]Department of Neurobiology, David Geffen School of Medicine, University of California Los Angeles, Los Angeles, CA 90095, USA. [13]Department of Physiology, David Geffen School of Medicine, University of California Los Angeles, Los Angeles, CA 90095, USA.
*Corresponding author. Email: adeb@mednet.ucla.edu

Optogenetic-driven depolarization of fibroblasts in scar tissue altered organ-wide cardiac excitability

To determine whether cardiac fibroblasts (CFs) in scar tissue can directly drive cardiac excitation and arrhythmogenesis, we first genetically engineered a mouse in which CFs, but not myocytes, expressed the optogenetic channel channelrhodopsin variant [ChR2(H134R)], a blue light–sensitive, nonselective cationic channel (*10*, *11*). The expression of ChR2 only in nonexcitable fibroblasts enabled us to determine changes in cardiac excitation after optical stimulation and depolarization of CFs in vivo. The mouse was engineered by crossing animals that harbored a tamoxifen-inducible fibroblast Cre recombinase (*TCF21*MerCreMer [MCM]) with animals that have the *ChR2*-enhanced yellow fluorescent protein (*eYFP*) gene knocked into the Rosa locus downstream of a floxed STOP codon (*10*) [*Rosa26:ChR2(H134)-eYFP* mouse]. The *TCF21*MCM driver is specific to fibroblasts and is efficient in labeling fibroblasts in scar tissue (*12*–*15*). Consistent with published reports (*14*, *16*), we analyzed single-nucleus transcriptomic datasets and observed *Tcf21* expression in fibroblasts and myofibroblasts in the infarcted heart (fig. S1, A to E). Cre-mediated recombination resulted in the *ChR2* gene being expressed in CFs (*TCF21*MCM-*ChR2-eYFP* or CF-ChR2 mouse). We subjected the CF-ChR2 mouse to MI by means of permanent ligation of the left anterior descending coronary artery (Fig. 1A) (*17*). Tamoxifen to induce Cre recombination was administered for 5 days, starting 3 days before cardiac injury (Fig. 1A). Immunofluorescent staining of the uninjured region of the heart demonstrated expression of ChR2 (eYFP expression) only in the myocardial interstitium, which is consistent with expression by CFs, with no expression of ChR2 by cardiomyocytes (Fig. 1B). At 10 days after MI, we observed robust expression of ChR2 in the injury region, with ChR2-expressing fibroblasts in close proximity to cardiomyocytes within scar tissue (Fig. 1C). Immunostaining with fibroblast marker vimentin confirmed expression of ChR2 by CFs (Fig. 1D).

For optogenetic studies, we harvested the heart at 10 days after MI and mounted it in an isolated Langendorff organ perfusion system (Fig. 1, E and F). An optical fiber that emitted blue light (473 nm) was placed just above the scar to photonically stimulate the scar tissue (Fig. 1, E and F). A pair of bipolar microelectrodes were inserted into the uninjured myocardium at the base of the heart (remote from the scar) to record changes in cardiac electrical activity (Fig. 1, E and F). We optically stimulated the cardiac scar tissue (Fig. 1G) at different frequencies starting at 7 Hz, with a pulse duration of 10 ms. Before optical stimulation, the heart rate was ~360 beats per minute (bpm), but during optical stimulation, the heart rate increased to 420 bpm, which exactly corresponded with the frequency of optical stimulation with 1:1 concordance (each optical stimulation pulse was followed by cardiac electrical activity, and each cardiac electrogram was preceded by an optical stimulation pulse) (Fig. 1H and movie S1). After cessation of optical stimulation, the heart rate returned to its pre–optical stimulation rate (Fig. 1H). The sinus rhythm noted before stimulation was replaced by a ventricular rhythm during optical stimulation, with dissociation of atrial and ventricular electrical activity, which demonstrated that fibroblast depolarization in scar tissue was sufficient to elicit organ-wide myocyte excitation (Fig. 1, I and J). Sinus rhythm resumed after cessation of optical stimulation (Fig. 1K). Optical stimulation at 9 Hz increased the heart rate to 540 bpm (Fig. 1L), with a return to prestimulation rates after cessation of optical stimulation (Fig. 1L).

Optical stimulation of the uninjured myocardium (remote from the scar tissue) of CF-ChR2 animals did not result in any change in heart rate (Fig. 1M). This is likely because the number of TCF21-labeled ChR2-expressing cells was significantly higher in the infarcted region than in remote myocardium ($P < 0.001$) (fig. S1, F to I). Neither did the heart rate change with optical stimulation of the scar tissue of the *Cre(–)Rosa26:ChR2(H134)-eYFP* animals (Fig. 1N).

Depolarization of fibroblasts in scar tissue elicited cardiac excitation in vivo and induced arrhythmogenesis

We next investigated whether optical stimulation of scar tissue altered cardiac electrical activity and heart rate in the live animal. We subjected the CF-ChR2 animal to MI and performed open thoracotomy on the live

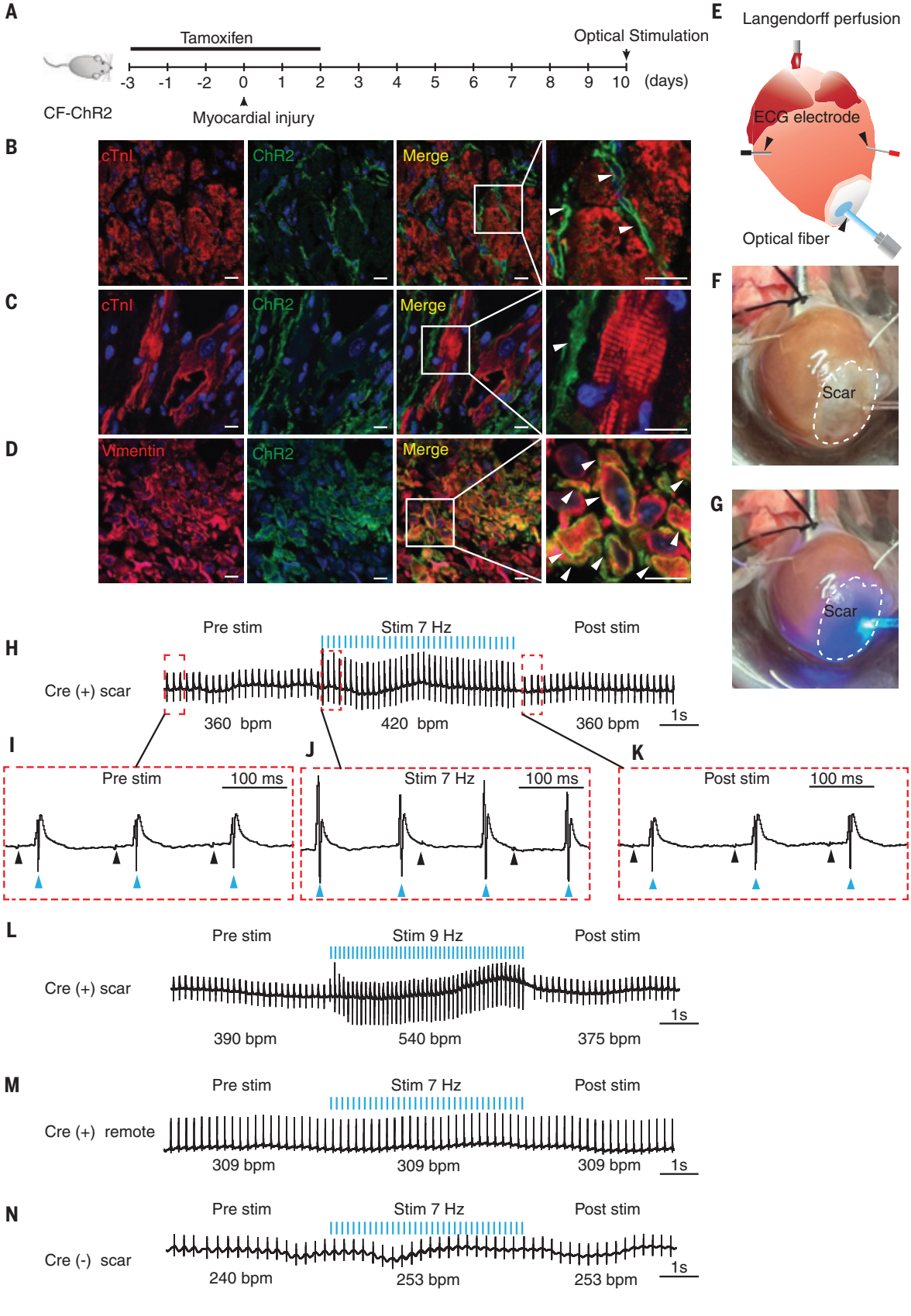

Fig. 1. Optical stimulation of scar tissue of CF-ChR2 animal drives organ-wide cardiac excitation. (**A**) Schematic of experiment outlining administration of tamoxifen to induce Cre-mediated recombination and harvesting of heart at 10 days after MI. (**B** and **C**) Immunofluorescent staining of heart of CF-ChR2 animal harvested at 10 days after MI that demonstrates cardiomyocyte (red, Troponin I) and ChR2-expressing cells (green, eYFP) in uninjured myocardium remote to scar tissue (B) and scar tissue (C). Merged image and magnified inset demonstrating spatial relationship of fibroblasts (arrows) to myocytes. Scale bar, 20 μm. (**D**) Immunostaining for vimentin (red) and ChR2 (green) that demonstrates colocalization of ChR2 in vimentin-expressing cells (merged image and magnified inset [arrows, yellow]). (**E** to **G**) (E) Schematic of optical stimulation of scar tissue of the perfused heart before (F) and at the onset of (G) optical stimulation with blue light. (**H**) Cardiac electrical recording before, during, and after optical stimulation of scar tissue at 7 Hz (blue lines indicate pulses of optical stimulation, bpm: recorded cardiac electrical activity in beats per minute). (**I** to **K**) Magnified atrial (black arrows) and ventricular electrograms (blue arrows) from recordings before (I), during (J), and after (K) optical stimulation. Note the dissociation of atrial and ventricular rhythm during stimulation with atrial activation not preceding ventricular activation. (**L**) Cardiac electrical recording after optical stimulation of scar at 9 Hz. (**M** and **N**) Cardiac electric recording after stimulation of myocardium remote to scar tissue in CF-ChR2 animal (M) or scar in Cre (−) animal (N). Representative tracings shown; *n* = 20 Cre (+) scar, *n* = 6 Cre (−) scar, and *n* = 10 Cre (+) remote.

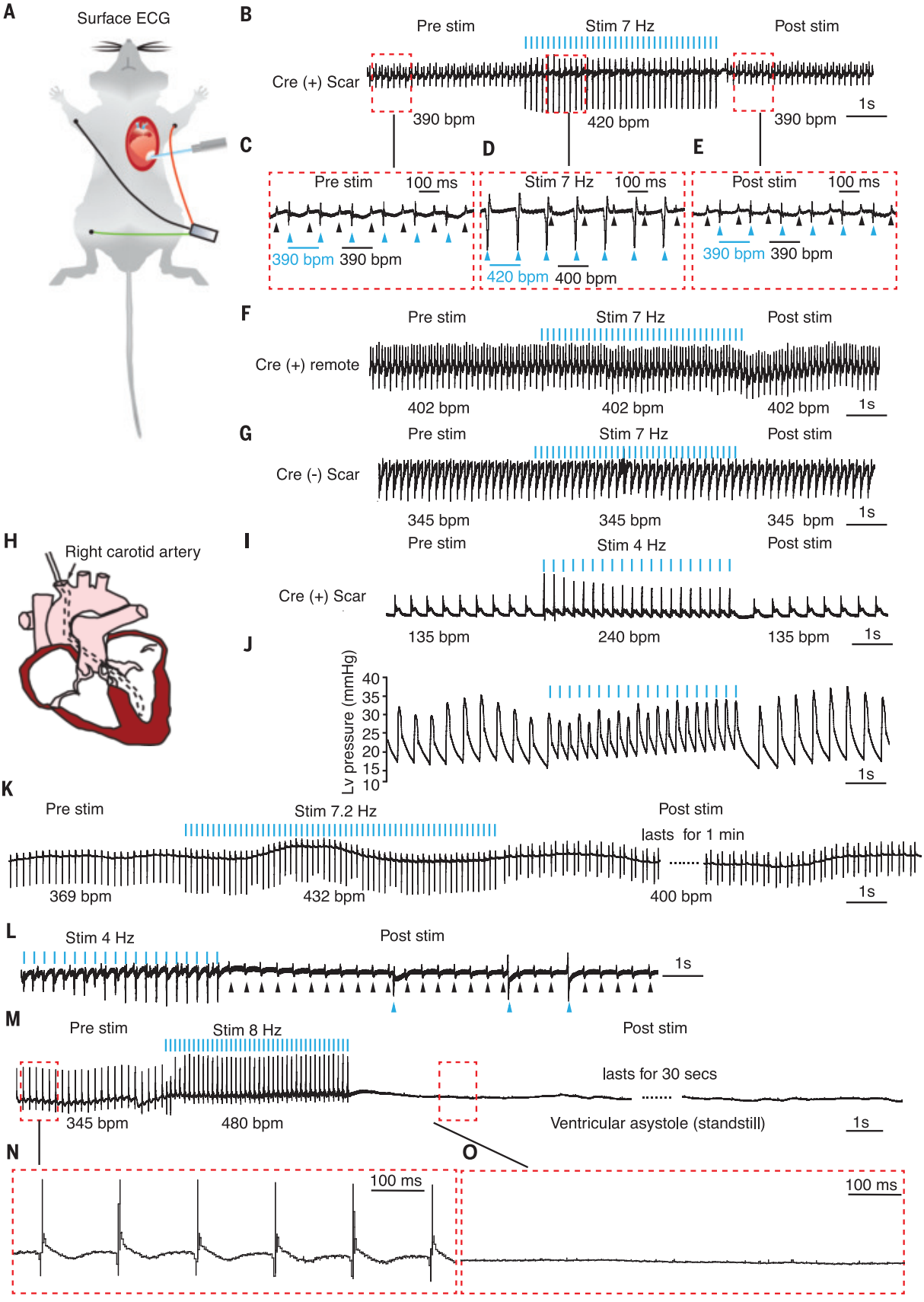

Fig. 2. Depolarization of fibroblasts in scar tissue drives cardiac excitation in vivo and induces arrhythmogenesis. (**A**) Schematic of experiment that demonstrates anesthetized CF-ChR2 animal subjected to open thoracotomy with optical stimulation of scar tissue and simultaneous surface ECG recording by

using limb leads. (**B**) ECG recording before, during, and after optical stimulation of scar tissue at 7 Hz (blue bars represent optical stimulation pulses). (**C** to **E**) Magnified recordings demonstrating atrial (P waves, black arrows) and ventricular activity (QRS complexes, blue arrows) from recordings before (C), during (D), and after (E) stimulation. Note that atrial (P-P) rate and ventricular (R-R) rates are different in (D), which confirms the dissociation of atrial and ventricular rhythm during optical stimulation followed by resumption of sinus rhythm poststimulation. (**F** and **G**) Surface ECG recording after optical stimulation of myocardium remote to scar tissue (F) or scar in Cre (−) animal (G). (**H** to **J**) LV pressure recording before and after optical stimulation in live CF-ChR2 animal. (H) Technical schematic showing introduction of pressure catheter through the carotid into the LV. (I) Surface ECG demonstrating electrical activity before, during, and after optical stimulation. (J) Simultaneous recording of LV pressures (note that increased cardiac electrical activity is associated with increased frequency of synchronous beats that generate LV pressure). (**K** to **O**) Arrhythmogenesis noted in a subset of animal hearts after optical stimulation of scar tissue. (K) Electrical recording from intact perfused heart before, during, and after optical stimulation, which demonstrates ventricular bigeminy (paired beats) that was sustained for 1 min in the absence of any further perturbations. (L) Surface ECG from live animal subjected to optical stimulation of scar that demonstrates high-grade AV block. Note the loss of 1:1 conduction between atrial (P wave, black arrows) and ventricular (QRS complex, blue arrows) activity. (M to O) Heart of CF-ChR2 animal harvested 3 months after MI and subjected to optical stimulation demonstrates ventricular asystole after cessation of optical stimulation (M), and magnified view of ventricular rhythm before (N) and after (O) stimulation demonstrates absence of any ventricular rhythm poststimulation (representative tracings, n = 15 per group).

animal 10 days after MI. The light source was positioned directly over the scar tissue (Fig. 2A), and surface electrocardiogram (ECG) electrodes were attached to the skin of the animal to record cardiac rate and rhythm (Fig. 2A). Before optical stimulation, the ECG demonstrated a rate of 390 bpm (Fig. 2B), but upon optical stimulation at 7 Hz, the rate increased to 420 bpm, which exactly corresponded to the frequency of optical stimulation with a 1:1 concordance, with a return to prestimulation rate after cessation of optical stimulation (Fig. 2B). We next looked at the rhythm and relationship of atrial (P) and ventricular activation (QRS) complexes on the surface ECG. Sinus rhythm with normal 1:1 atrioventricular (AV) conduction before optical stimulation (Fig. 2C) was replaced by a ventricular rhythm during stimulation, with clear dissociation of atrial and ventricular electrical activity, differing atrial and ventricular rates, and altered QRS morphology (Fig. 2D). Sinus rhythm with normal 1:1 AV conduction resumed after stimulation (Fig. 2E). Optical stimulation of the uninjured region of the CF-ChR2 animal did not change heart rate (Fig. 2F), and neither did the heart rate change with optical stimulation of scar tissue of *Cre(−)Rosa26:ChR2(H134R)-eYFP* animal (Fig. 2G).

We next investigated whether increased heart rate in vivo after optogenetic stimulation of CFs was associated with increased rate of cardiac contraction or electromechanical association. We optically stimulated the scar tissue in the live animal and placed a pressure transducer through the carotid artery, into the left ventricular (LV) cavity (Fig. 2H). Optical stimulation increased the heartbeat in the live animal from 135 bpm to 240 bpm (Fig. 2I), and simultaneous pressure recordings showed 1:1 concordance between each ventricular electrogram and LV contraction, which thus confirmed an electromechanical association (Fig. 2J).

We next studied whether the depolarization of fibroblasts in scar tissues can lead to arrhythmogenesis. We optically stimulated the scar of the isolated perfused CF-ChR2 heart (day 10 after MI) at different frequencies and observed that ~40% of the hearts developed postoptical stimulation rhythm disturbances. Many of these hearts developed ventricular ectopic beats after cessation of optical stimulation, and among the hearts that demonstrated poststimulation arrhythmias, 20% had ventricular bigeminy (ventricular beats in pairs) that was sustained and lasted from 30 s to 1 min (Fig. 2K). We also observed arrhythmias in the live anesthetized animal. In a subset of animals, after cessation of optical stimulation of scar tissue, surface ECG recordings demonstrated high-grade AV conduction block (Fig. 2L). During high-grade AV block, we observed multiple atrial activation signals (P waves) and occasional ventricular activation signals (QRS complexes) with loss of normal 1:1 AV conduction (Fig. 2L). Scar tissue undergoes dynamic remodeling over months after MI (*18*, *19*). We next examined the arrhythmogenicity of the scar tissue ~12 weeks after MI and optically stimulated perfused hearts of CF-ChR2 mice, 78 to 85 days after MI. In a subset of animals, after cessation of optical stimulation of scar tissue, there was prolonged ventricular standstill or asystole (Fig. 2M) with complete cessation of all ventricular electrical activity (Fig. 2, N and O). Ventricular asystole likely occurred because rapid and repetitive ventricular activation from fibroblast depolarization caused high-grade or complete AV conduction block (Fig. 2L) with poor or no ventricular escape rhythm of the infarcted ventricle. These observations demonstrate that depolarization of fibroblasts in scar tissue can result in changes in cardiac excitation and conduction, which together create a permissive environment for the occurrence of sustained arrhythmias in vivo.

Electrical coupling of fibroblasts and myocytes is not mediated by connexin 43

Connexin 43 (Cx43) is a gap junctional (GJ) protein that is the most abundant connexin in the heart, is expressed by fibroblasts in the infarcted heart, and is thought to mediate fibroblast-myocyte coupling (*20*, *21*). To determine whether Cx43 and/or other GJ proteins mediated fibroblast-myocyte coupling, we adopted an unbiased approach. We first performed single-nucleus RNA sequencing (RNA-seq) on the injured hearts of wild-type mice 7 days after MI. *Cx43* was the predominant connexin isoform expressed by cardiomyocytes (Fig. 3A). Compared with myocytes, the degree of connexin expression in CFs was much lower, but CFs and myocytes did express *Cx43*, *Cx45*, and to a lesser extent *Cx40*. *Panx1* was the only GJ-related gene, and it was expressed more highly in CFs (Fig. 3, A and B). Immunofluorescent staining confirmed Cx43 expression in fibroblasts in scar tissue of infarcted animals (fig. S2, A to D). To determine the role of Cx43 in fibroblast-myocyte coupling, we crossed the CF-ChR2 mouse with animals that have both *Cx43* alleles floxed (*22*) to create Cx43CKO-CF-ChR2 (CKO, conditional knockout) animals. Animals were subjected to MI, and tamoxifen was administered for 5 days to delete Cx43 in ChR2-expressing CFs (Fig. 3C). Fibroblasts harvested from the scar tissue of Cx43CKO-CF-ChR2 hearts demonstrated ~98% reduction of *Cx43* expression compared with CF-ChR2 fibroblasts (Fig. 3D). Cx43CKO-CF-ChR2 hearts (day 10 after MI) were subjected to perfusion (Fig. 3E), and at 7 Hz of optical stimulation, the heart rate exactly corresponded to the stimulation frequency with 1:1 concordance (Fig. 3E). Electrical recordings in the Cx43CKO-CF-ChR2 animals demonstrated sinus rhythm before optical stimulation (Fig. 3F), with replacement of sinus rhythm by ventricular rhythm during stimulation (Fig. 3G) and resumption of sinus rhythm after stimulation (Fig. 3H). Optical stimulation of scar tissue at higher frequencies (9 Hz) increased cardiac electrical activity from 345 bpm to 540 bpm, which exactly corresponded to the optical stimulation frequency (Fig. 3I).

We next subjected the live Cx43CKO-CF-ChR2 animal to open thoracotomy at 10 days after MI and optically stimulated the scar tissue at 7 Hz in vivo (Fig. 3J). The surface ECG demonstrated increase in heart rate to exactly correspond with the optical stimulation frequency (Fig. 3J). Sinus rhythm (Fig. 3K) was replaced by a ventricular rhythm during optical

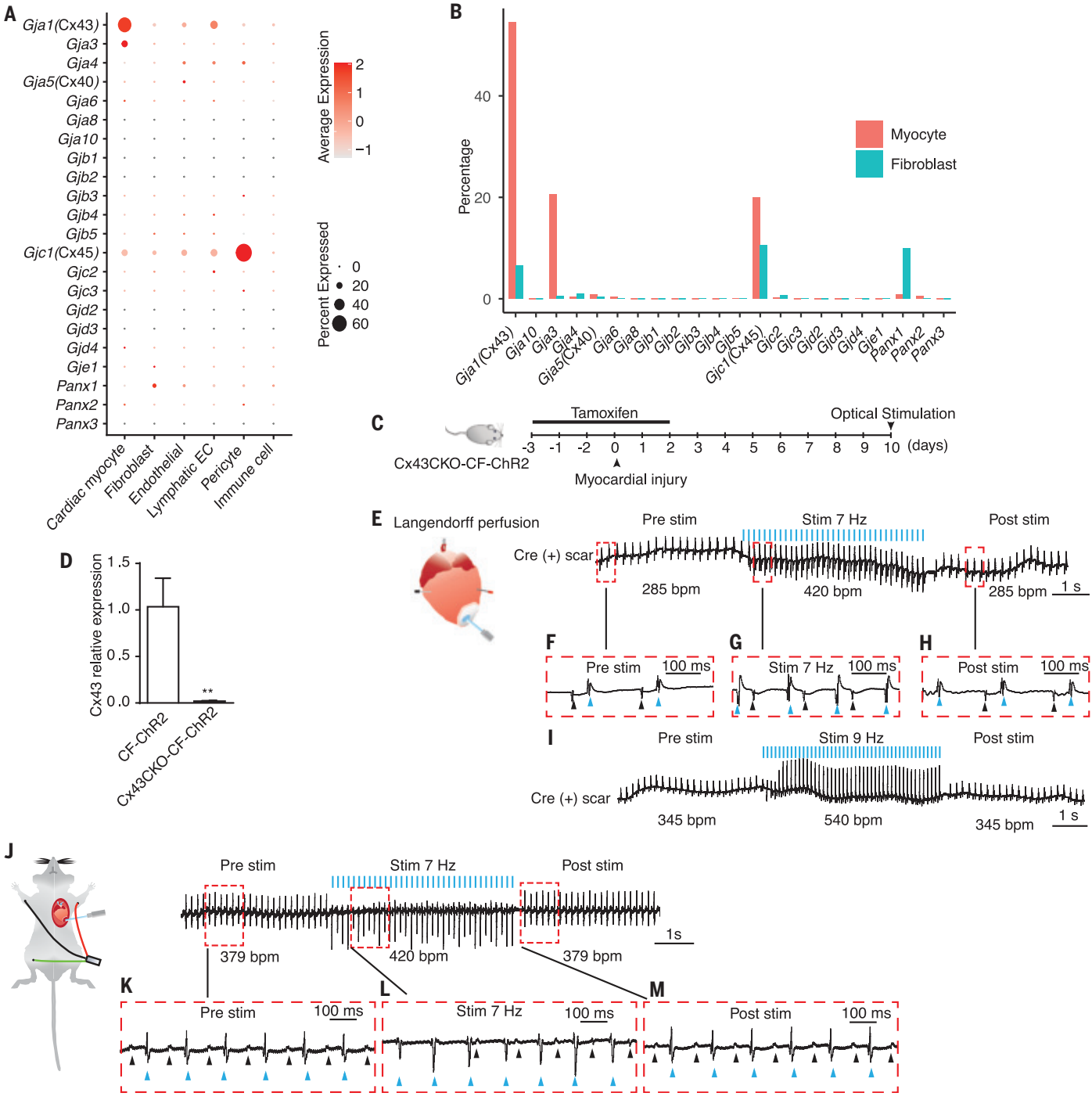

Fig. 3. Connexin 43 is not required for fibroblast-myocyte coupling in vivo. (**A**) Dot plot from single-nuclear RNA-seq that shows gene expression of various connexins and pannexins across cardiac cell population in the heart harvested 7 days after MI. EC, endothelial cell. (**B**) Comparison of expression of connexins/pannexins in CFs and myocytes shown as a percentage of cells expressing the gene of interest. (**C**) Schematic of generation of the Cx43CKO-CF-ChR2 animal with administration of tamoxifen to induce Cre-mediated recombination. (**D**) Quantitative polymerase chain reaction (qPCR) that demonstrates *Cx43* expression in CFs from Cx43CKO-CF-ChR2 animals compared with CFs from CF-ChR2 control animals (data are represented as mean ± SD, $^{**}P < 0.01$, $n = 3$). (**E** to **H**) Intact perfused hearts of Cx43CKO-CF-ChR2 animals harvested 10 days after MI were subjected to optical stimulation of scar tissue. (E) Electrical recording of heart before, during, and after optical stimulation at 7 Hz (blue bars represent optical stimulation pulses; representative tracings, $n = 8$). (F to H) Magnified electrograms demonstrate atrial (black arrows) and ventricular activity (blue arrows) before (F), during (G), and after (H) stimulation. Note dissociation of atrial and ventricular activity during optical stimulation. (**I**) Cardiac electrical recording after optical stimulation of scar at 9 Hz. (**J** to **M**) Surface ECG of live Cx43CKO-CF-ChR2 animal subjected to optical stimulation of scar at 10 days after MI. (J) ECG recording before, during, and after stimulation at 7 Hz. (K to M) Atrial (P wave, black arrows) and ventricular (QRS complexes, blue arrows) activity before (K), during (L), and after (M) stimulation. Note dissociation of atrial and ventricular activity during stim followed by resumption of normal sinus rhythm after stimulation (representative tracings, $n = 9$ per group).

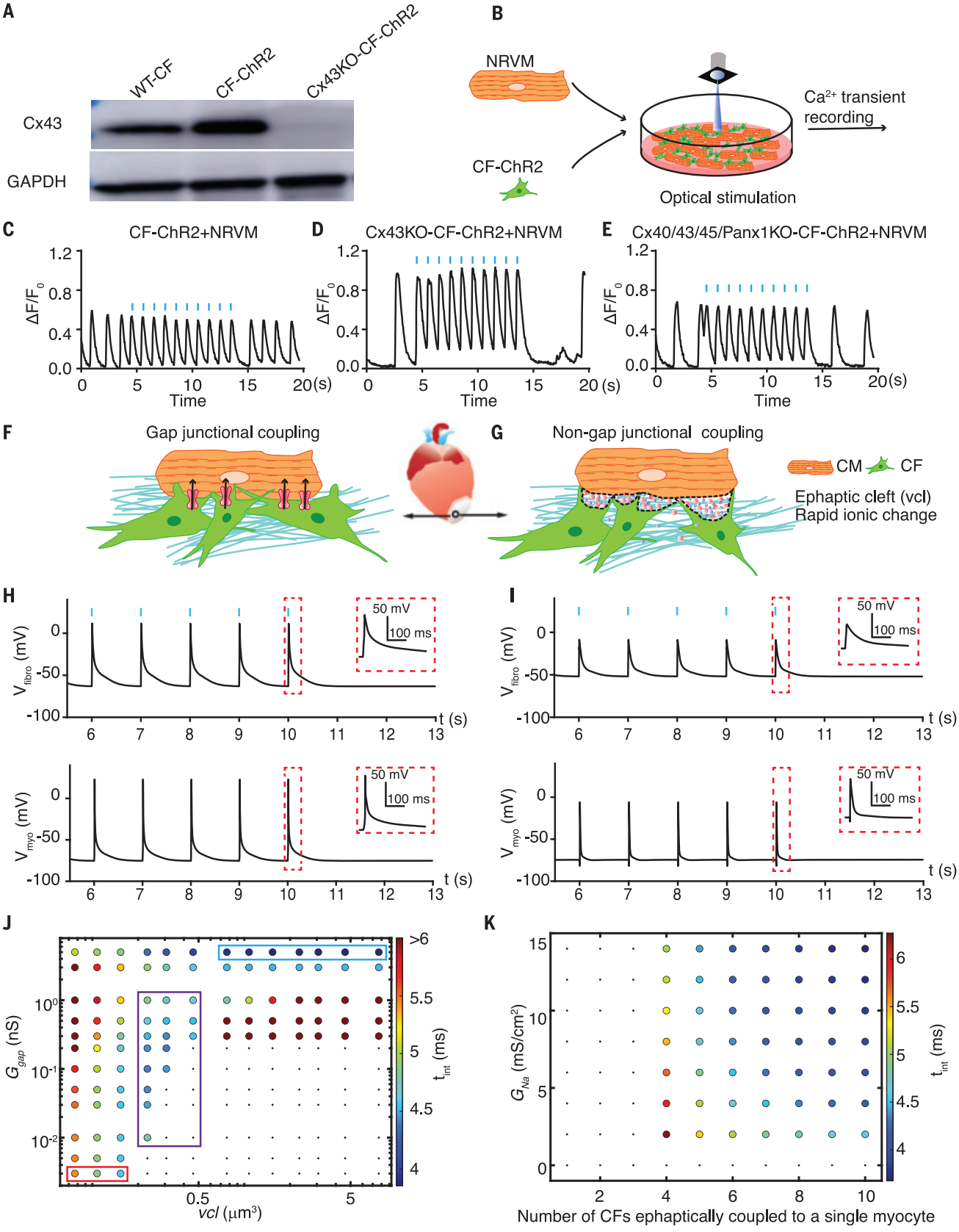

Fig. 4. Connexin-dependent GJ coupling is dispensable for fibroblast-myocyte electrical coupling. (**A**) Western blot demonstrating expression of Cx43 in wild-type (WT) CFs, CF-ChR2 (Cx43fl/fl) CFs, and after transfection of Cx43fl/fl CFs with Cre plasmid to generate Cx43KO CFs. (**B**) Schematic of optical stimulation of CF-ChR2 cocultured with NRVMs loaded with x-Rhod-AM dye to record calcium transients. (**C** to **E**) Recording of calcium transients in

cardiomyocytes after optical stimulation of CF-ChR2 (C), Cx43KO-CF-ChR2 (D), and Cx40/43/45/Panx1KO-CF-ChR2 (E) fibroblasts (blue bars represent optical stimulation pulses). Representative tracings, n = 5 per group. (**F** to **K**) Modeling of GJ (F) and non-GJ (ephaptic) (G) coupling, with simulation demonstrating successful depolarization of fibroblasts (V_{fibro}) and myocytes (V_{myo}) with either GJ (H) or non-GJ (I) coupling. Blue bars indicate pulses of optical stimulation applied to fibroblasts. (H and I, insets) Differences in membrane depolarization of fibroblast and myocyte with GJ and non-GJ coupling. (J) Simulation showing myocyte excitation with variation in GJ and ephaptic coupling (*vcl*). Ten fibroblasts were connected to the myocyte for this simulation. The red box represents low GJ conductance but strong ephaptic coupling, and the blue box represents strong GJ conductance with weak ephaptic coupling. The purple box indicates where ephaptic and GJ coupling synergize to excite myocytes. (K) Simulation showing myocyte excitation with variation in Na^+ channel conductance of CFs and the number of CFs coupled to the myocyte solely through ephaptic coupling. In (J) and (K), colored circles represent successful myocyte excitation, and dots represent unsuccessful myocyte excitation. Color of the circles represents delay (time interval) to myocyte excitation t_{int} (milliseconds).

stimulation with altered QRS morphology (Fig. 3L), which was followed by the resumption of sinus rhythm after stimulation (Fig. 3M).

Myocyte-fibroblast coupling is likely not connexin dependent

We next isolated CFs from uninjured hearts of $Cx43^{fl/fl}$ animals and transfected the CFs with a plasmid that expressed Cre recombinase, followed by transfection with a lentivirus that expressed *ChR2(H134R)-eYFP*. We confirmed the deletion of Cx43 in these cells (Cx43KO-CF-ChR2) by Western blotting compared with controls (CF-ChR2 fibroblasts) (Fig. 4A). Both the Cx43KO-CF-ChR2 fibroblasts and control fibroblasts were immortalized to prevent primary culture–associated artifacts as previously described (*15*). The fibroblasts were then cocultured with neonatal rat ventricular cardiomyocytes (NRVMs), which were loaded with a calcium-sensitive rhodamine-based dye to record intracellular calcium transients (Fig. 4B) (*23*). Optical stimulation of fibroblasts generated calcium transients in the myocytes at a rate concordant with the frequency of optical stimulation, but the deletion of Cx43 did not affect excitation of myocytes (Fig. 4, C and D). Next, we treated a coculture of myocytes and CF-ChR2 fibroblasts with a connexin-mimetic peptide, Gap 26, which behaves as a pharmacological antagonist of Cx43 and other GJ channels (*24*, *25*). On optical stimulation, Gap26 did not affect the response rate of the myocytes to optical stimulation of fibroblasts (fig. S2E). CFs not expressing ChR2 did not excite myocytes after optical stimulation (fig. S2F).

We then explored the hypothesis that there could be functional redundancy between the connexins in mediating fibroblast-myocyte electrotonic coupling. To address this question, we subjected Cx43KO-CF-ChR2 fibroblasts to CRISPR-Cas9–mediated genome editing to sequentially delete *Cx45*, *Cx40*, and *Panx1*. Sequencing confirmed biallelic deletion of *Cx45*, *Cx40*, and *Panx1* in colonies of CFs isolated from single-cell clones after CRISPR-Cas9 targeting (fig. S3, A to C). ChR2-expressing CFs deficient in *Cx40/43/45* and *Panx1* were then cocultured with NRVMs, but myocytes were excited at a rate that corresponded to the optical stimulation frequency despite the lack of these connexins (Fig. 4E).

Mathematical modeling demonstrates synergy and functional redundancy between GJ and non-GJ (ephaptic) coupling of fibroblasts and myocytes

We next performed mathematical modeling to examine the feasibility of non-GJ mediated mechanisms of myocyte-fibroblast coupling. Ephaptic coupling is a form of non-GJ coupling that has been proposed as a mechanism of propagation of the depolarization wave across the heart (*26*, *27*). Ephaptic coupling or electric field coupling occurs when rapid changes of ionic current in a junctional cleft after depolarization of one cell can lead to membrane depolarization of the adjacent cell across the cleft (*28*). We adapted computational models of ephaptic and GJ coupling (fig. S4) to our experimental design that involved depolarization of fibroblasts by using optogenetic means (*29*, *30*). In our models, multiple CFs were electrically coupled to a single myocyte either through GJ (Fig. 4F) or through ephaptic coupling (Fig. 4G). To better inform our models, we first patch clamped ChR2 fibroblasts and observed the membrane potential of ChR2 fibroblasts to change approximately from −32 mV to 0 mV during optical stimulation (fig. S5, A to C). In our simulations, optical stimulation of ChR2-expressing fibroblasts led to fibroblast depolarization and myocyte depolarization either with GJ (Fig. 4H) or ephaptic mechanisms (Fig. 4I). Differences were observed in the fibroblast and myocyte membrane potential changes between ephaptic and GJ-mediated coupling, which is suggestive of differences in electrical activation between these coupling mechanisms (Fig. 4, H and I, insets).

Subsequently, we created a mathematical model to determine the relative contribution of GJ and ephaptic coupling to myocyte depolarization (Fig. 4J). The strength of the GJ coupling was represented by the GJ conductance (G_{gap}). Ephaptic coupling is critically dependent on the cleft volume between the cell membranes of adjacent cells and so the strength of ephaptic coupling was quantified by the volume of the cleft (*vcl*) between CFs and the myocyte (Fig. 4J). When the GJ conductance is low or close to zero (Fig. 4J, red box), fibroblast-induced myocyte depolarization fails when the *vcl* is >0.2 μm^3, which suggests that, at low GJ conductance, ephaptic coupling between fibroblasts and myocytes mediates myocyte excitation. At higher GJ conductance (Fig. 4J, blue box), ephaptic coupling was not needed, which demonstrates functional redundancy. At *vcl* of ~0.2 to 0.5 μm^3 and intermediate GJ conductance (Fig. 4J, purple box), GJ and ephaptic coupling synergized to excite the myocyte. At this *vcl* range, ephaptic coupling alone failed to conduct. With decreased ephaptic coupling (larger *vcl*), conduction failed if GJ conductance was <0.3 nS. However, when both coupling mechanisms contributed, conduction was faster than with GJ alone (see sudden color change at right of purple box), which thus demonstrates synergy.

We next investigated the impact of fibroblast Na^+ channel conductance and the number of CFs for effective fibroblast-myocyte ephaptic coupling. Myocyte excitation occurred when the fibroblast Na^+ channel conductance exceeded 2 mS/cm^2, and the number of fibroblasts coupled only by ephaptic mechanisms to a myocyte exceeded four (Fig. 4K). At a similar Na^+ channel conductance, a greater number of CFs coupled to a myocyte through ephaptic mechanisms led to faster conduction (Fig. 4K). Immunostaining for fibroblasts and myocytes in infarcted hearts of CF-ChR2 animals demonstrated a significant alteration of the myocyte/fibroblast ratio in the infarcted zone compared with uninjured myocardium ($P < 0.001$), which would potentially enable greater coupling between myocytes and fibroblasts and support the proposed model (fig. S6, A to C).

In the uninjured heart, propagation of depolarization is thought to occur by means of GJs (*31*). Our computational model predicted that ephaptic or GJ coupling between fibroblasts and myocytes was less resilient when compared with myocyte-to-myocyte conduction through GJ. The simulation results demonstrated that the myocyte-myocyte coupling through GJ (fig. S7A) or ephaptic coupling (fig. S7B) was superior to fibroblast-myocyte coupling either through GJ (fig. S7, C and E) or ephaptic coupling (fig. S7, D and F), respectively. To test this prediction, we generated a transgenic mouse that expressed ChR2 in cardiomyocytes only (*αMHCMerCreMer* animals crossed with *Rosa26:ChR2(H134)-eYFP* animals). Tamoxifen was administered for 5 days to induce ChR2 expression in cardiomyocytes (αMHC-ChR2 animals) (fig. S8A). Perfused hearts responded to optical stimulation frequencies as high as

14 Hz, with 100% of the hearts tested exhibiting an increase in cardiac electrical activity with a 1:1 concordance (fig. S8, B to I). We subsequently infarcted these animals (fig. S8J) and optically stimulated the scar tissue of the αMHC-ChR2 animals (fig. S8K) and observed that a 1:1 concordance between optical stimulation and cardiac excitation could be maintained at a frequency of 11 Hz (fig. S8L), but at 14 Hz, the fraction of injured animals that were able to maintain 1:1 concordance was significantly decreased compared with the uninjured αMHC-ChR2 animals ($P < 0.001$) (fig. S8, M and N). However, when the scar tissue of hearts from CF-ChR2 animals was optically stimulated at progressively increasing frequencies, in contrast to the αMHC-ChR2 animals, the hearts did not respond to optical stimulation at 1:1 concordance at or beyond 11 Hz (fig. S8N). These experimental data suggest that fibroblast-myocyte coupling is less robust than myocyte-myocyte coupling and validates a prediction of the computational model.

Discussion

Our study showed that fibroblast-myocyte coupling in scar tissue was robust enough to elicit cardiac excitation and arrhythmogenesis in vivo after fibroblast depolarization. Even in the absence of optogenetic channels, fibroblasts are known to be depolarized by stimuli such as cell stretch, hypoxia (*32*), and various neurohumoral signals (*3*). Scar tissue is vulnerable to rapid changes in mechanical properties (*15*), and fibroblast compression induces membrane depolarization by activating inward currents through nonselective cation conductance (*33*). Our data suggest that such pathophysiological insults that cause fibroblast depolarization in scar tissue could be potentially arrhythmogenic by means of fibroblast-myocyte coupling.

Cx43 and related GJ proteins were surprisingly dispensable for myocyte-fibroblast electrical coupling. Ephaptic and GJ conductance have been proposed to contribute to electrical coupling of adjacent myocytes (*28*, *34*), and recent simulations suggest that ephaptic coupling can occur in all areas of small extracellular space between two adjacent cells (*26*). Activated CFs express voltage-gated sodium channel Nav1.5 and have sodium and potassium rectifier currents similar to those recorded from myocytes, which potentially enables ephaptic coupling (*35*). Our study demonstrates that ephaptic and GJ coupling can act in a synergistic yet functionally redundant manner to excite myocytes, but it does not exclude other proposed coupling mechanisms such as cellular nanotubes (*36*) or the possibility that a connexin-like protein expressed in low abundance in scar tissue compensates for the concomitant loss of the most highly expressed GJ genes.

Our findings potentially have clinical implications for treatment of arrhythmias. Scar-related ventricular arrhythmias are treated with radio frequency catheter ablation. Ablation reduces the number of myocytes but activates fibroblasts and induces fibrosis. Approximately 50% of patients who are treated with radio frequency ablation of scar-related ventricular tachycardia have arrhythmia recurrence. Our data suggest that increased fibroblast accumulation and remodeling of the scar may create fresh coupling foci between fibroblasts and residual myocytes and lead to new substrates for arrhythmogenesis.

REFERENCES AND NOTES

1. P. Christia *et al*., *J. Histochem. Cytochem.* **61**, 555–570 (2013).
2. N. G. Frangogiannis, *J. Clin. Invest.* **127**, 1600–1612 (2017).
3. V. M. Mahoney, V. Mezzano, G. E. Morley, *Prog. Biophys. Mol. Biol.* **120**, 128–133 (2016).
4. T. P. Nguyen, Z. Qu, J. N. Weiss, *J. Mol. Cell. Cardiol.* **70**, 83–91 (2014).
5. T. P. Nguyen, Y. Xie, A. Garfinkel, Z. Qu, J. N. Weiss, *Cardiovasc. Res.* **93**, 242–251 (2012).
6. P. Camelliti, T. K. Borg, P. Kohl, *Cardiovasc. Res.* **65**, 40–51 (2005).
7. E. Ongstad, P. Kohl, *J. Mol. Cell. Cardiol.* **91**, 238–246 (2016).
8. Y. Xie *et al*., *Heart Rhythm* **6**, 1641–1649 (2009).
9. E. A. Rog-Zielinska, R. A. Norris, P. Kohl, R. Markwald, *Trends Mol. Med.* **22**, 99–114 (2016).
10. L. Madisen *et al*., *Nat. Neurosci.* **15**, 793–802 (2012).
11. J. Y. Lin, *Exp. Physiol.* **96**, 19–25 (2011).
12. A. Acharya, S. T. Baek, S. Banfi, B. Eskiocak, M. D. Tallquist, *Genesis* **49**, 870–877 (2011).
13. A. Acharya *et al*., *Development* **139**, 2139–2149 (2012).
14. O. Kanisicak *et al*., *Nat. Commun.* **7**, 12260 (2016).
15. T. Yokota *et al*., *Cell* **182**, 545–562.e23 (2020).
16. M. D. Tallquist, J. D. Molkentin, *Nat. Rev. Cardiol.* **14**, 484–491 (2017).
17. S. Li *et al*., *J. Clin. Invest.* **132**, e149711 (2022).
18. J. S. Burchfield, M. Xie, J. A. Hill, *Circulation* **128**, 388–400 (2013).
19. M. Xie, J. S. Burchfield, J. A. Hill, *Circulation* **128**, 1021–1030 (2013).
20. A. Rodríguez-Sinovas, J. A. Sánchez, L. Valls-Lacalle, M. Consegal, I. Ferreira-González, *Int. J. Mol. Sci.* **22**, 4413 (2021).
21. P. Camelliti, G. P. Devlin, K. G. Matthews, P. Kohl, C. R. Green, *Cardiovasc. Res.* **62**, 415–425 (2004).
22. Y. Liao, K. H. Day, D. N. Damon, B. R. Duling, *Proc. Natl. Acad. Sci. U.S.A.* **98**, 9989–9994 (2001).
23. G. M. Kostecki *et al*., *Sci. Rep.* **11**, 4430 (2021).
24. M. Hulsmans *et al*., *Cell* **169**, 510–522.e20 (2017).
25. T. Desplantez, V. Verma, L. Leybaert, W. H. Evans, R. Weingart, *Pharmacol. Res.* **65**, 546–552 (2012).
26. J. Lin, J. P. Keener, *IEEE Trans. Biomed. Eng.* **60**, 576–582 (2013).
27. J. P. Kucera, S. Rohr, Y. Rudy, *Circ. Res.* **91**, 1176–1182 (2002).
28. R. G. Gourdie, *Anat. Rec.* **302**, 93–100 (2019).
29. C. Ly, S. H. Weinberg, *Chaos* **32**, 033123 (2022).
30. S. Morotti, A. G. Edwards, A. D. McCulloch, D. M. Bers, E. Grandi, *J. Physiol.* **592**, 1181–1197 (2014).
31. D. Eckardt *et al*., *J. Mol. Cell. Cardiol.* **41**, 963–971 (2006).
32. A. Kamkin *et al*., *Pflugers Arch.* **446**, 169–174 (2003).
33. A. Kamkin, I. Kiseleva, G. Isenberg, *Cardiovasc. Res.* **57**, 793–803 (2003).
34. R. Veeraraghavan, R. G. Gourdie, S. Poelzing, *Am. J. Physiol. Heart Circ. Physiol.* **306**, H619–H627 (2014).
35. A. Chatelier *et al*., *J. Physiol.* **590**, 4307–4319 (2012).
36. T. A. Quinn *et al*., *Proc. Natl. Acad. Sci. U.S.A.* **113**, 14852–14857 (2016).

ACKNOWLEDGMENTS

We thank E. Olson (University of Texas Southwestern) for sharing the TCF21MCM mice with us. We thank G. Salama (University of Pittsburgh) for assisting with ephaptic experiments. We thank the following colleagues from UCLA: K. Shivkumar and P. Rajendran for helping us establish an optogenetic suite, B. Khakh for insights into ephaptic signaling, and J. Lusis and J. Weiss (professor emeritus) for providing helpful suggestions on the manuscript. **Funding:** This study was supported by grants from the US Department of Defense (W81XWH-20-1-0238) and the US National Institutes of Health (HL149658, HL152176, HL149687, AR075867, and DK132735 to A.D.; HL134709, HL157116, and HL139829 to Z.Q.; and HL134346 and HL152296 to R.O.), from the American Heart Association (postdoctoral fellowship 906531 to Y.W.), and from the Natural Science Foundation of China (no. 82172067 to Z.S.). **Author contributions:** Y.W. performed and designed experiments related to optogenetics both in vitro and in vivo, performed CRISPR-Cas9 targeting, and performed all relevant analyses; B.T., B.S., and P.W. performed animal surgeries, and B.T. recorded LV pressure tracings; S.R. performed single-nuclear sequencing; F.M analyzed nuclear sequencing data; Y.G., A.E., and M.P. assisted with data interpretation and contextualization; Y.K. advised on optical stim protocols and interpretation of electrical recordings; K.Y. and B.N. assisted in recording of calcium transients; M.A performed and designed single-cell electrophysiology experiments; M.A. and R.O. assisted in interpretation and designing of coupling experiments; Q.L., Z.S., and Z.Q. designed and performed computational simulation and analyzed simulation results; A.D. conceptualized the project, designed all experiments, supervised all data collection and optogenetic experiments, interpreted all cardiac electrical tracings, and wrote the manuscript. **Competing interests:** All authors declare that they have no competing interests. **Data and materials availability:** All data are available in the manuscript or the supplementary materials. Single-nucleus RNA-seq data were deposited to the Gene Expression Omnibus database under accession number GSE235434 (https://www.ncbi.nlm.nih.gov/geo/query/acc.cgi?acc=GSE235434). Requests for material and correspondence should be addressed to A.D. **License information:** Copyright © 2023 the authors, some rights reserved; exclusive licensee American Association for the Advancement of Science. No claim to original US government works. https://www.science.org/about/science-licenses-journal-article-reuse

SUPPLEMENTARY MATERIALS

science.org/doi/10.1126/science.adh9925
Materials and Methods
Figs. S1 to S8
Tables S1 and S2
References (*37*–*55*)
MDAR Reproducibility Checklist
Movie S1

Submitted 27 March 2023; accepted 11 August 2023
10.1126/science.adh9925

ScienceCareers.org
ScienceCareers

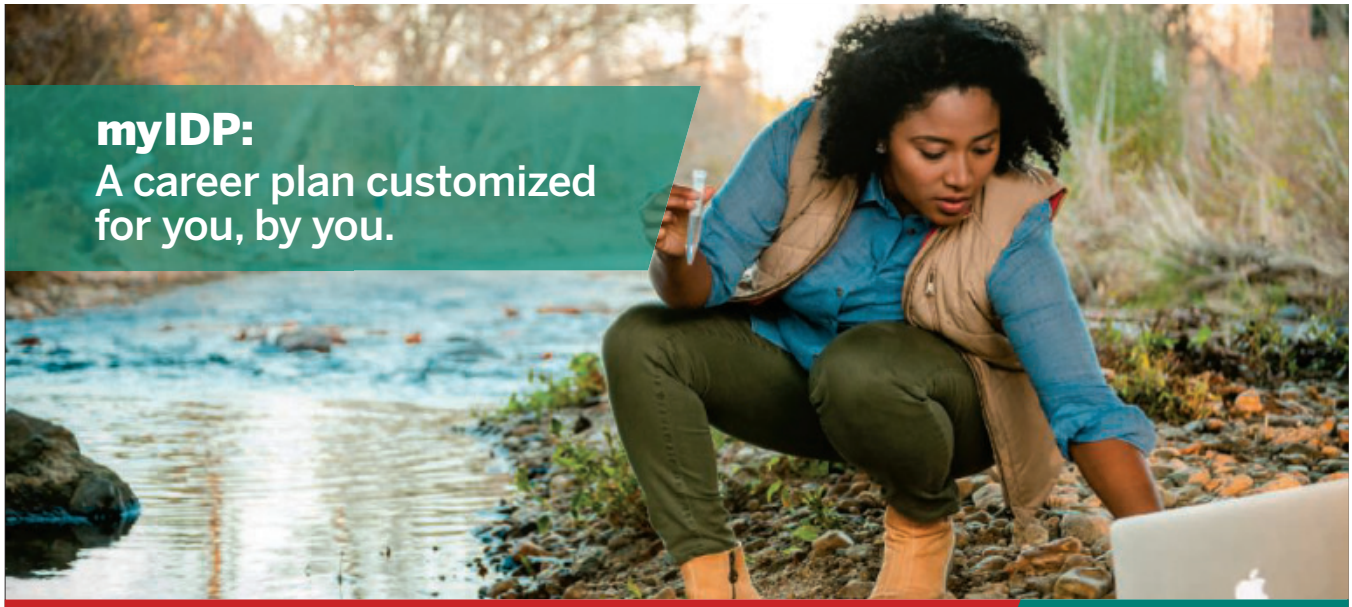

For your career in science, there's only one Science

Features in myIDP include:

- Exercises to help you examine your skills, interests, and values.
- A list of 20 scientific career paths with a prediction of which ones best fit your skills and interests.
- A tool for setting strategic goals for the coming year, with optional reminders to keep you on track.
- Articles and resources to guide you through the process.
- Options to save materials online and print them for further review and discussion.
- Ability to select which portion of your IDP you wish to share with advisors, mentors, or others.
- A certificate of completion for users that finish myIDP.

myIDP

Visit the website and start planning today!
myIDP.sciencecareers.org

ScienceCareers AAAS In partnership with:

FASEB Federation of American Societies for Experimental Biology
University of Massachusetts Medical School
UCSF University of California San Francisco
UIC
BURROUGHS WELLCOME FUND

School of Life Sciences
University of Dundee

We are recruiting!

Join the top university Biological Sciences department in the UK
(REF 2014 and REF 2021)

The School of Life Sciences, at the University of Dundee, Scotland, is looking to recruit up to 45 research active Group Leaders/Principal Investigators over the next five year period. Appointments will be made at all career stages (tenure-track, senior lecturer, reader and professorial) across all molecular life sciences research.

We are particularly looking to expand in the following thematic areas:

- Ageing and Neurodegeneration
- Microbiology, Immunology and Infectious Disease.
- Computational Biology.
- Drug Discovery/Chemical Biology/ Computational Chemistry.
- Plant Sciences for Sustainability and Climate Change.

Successful candidates will be joining the School at an exciting time of significant expansion providing the opportunity to contribute to our future direction. We are also keen to attract researchers with an aptitude for broader research leadership.

We offer a stimulating research environment, with state-of-the-art technologies in a highly collaborative research community. All in a fabulous location in Scotland.

Contact: SLS_PI_recruitment@dundee.ac.uk
Find out more: dundee.ac.uk/life-sciences/join-us

VANDERBILT
School *of* Medicine Basic Sciences

Vanderbilt University (VU) invites applications for a **senior faculty member to direct the Vanderbilt Institute for Chemical Biology (VICB)**. This position is based in the School of Medicine – Basic Sciences led by Dean John Kuriyan. However, the highly collaborative activities of the VICB and its faculty span multiple schools of the University as well as the adjacent Vanderbilt University Medical Center (VUMC).

The VICB was founded in 2002 and provides intellectual focus and infrastructure for research and education in chemical biology and drug discovery at Vanderbilt. There are currently 95 members from a broad range of departments in VU and VUMC. The VICB operates two complementary core facilities (High-Throughput Screening and Molecular Design and Synthesis). These cores are professionally managed and staffed with skills ranging from assay development, high-throughput screening, lead optimization, and chemical tool design and synthesis. VICB members and cores have played an important role in discovering and developing multiple drug candidates, some of which are in human clinical trials. The VICB also plays a vital role in educating undergraduate and graduate students across campus. VICB members serve as mentors on several chemical biology-focused training grants, complementing numerous other training grants based in the School of Medicine.

VU and VUMC are home to a myriad of investigators with expertise spanning the basic-to-translational research continuum for a wide range of human disorders. This includes microbial pathogenesis, particularly the emergent challenge of antimicrobial resistance (AMR). This is reflected, for example, by the research of the faculty of the Vanderbilt Institute for Infection, Immunology and Inflammation (VI4) and the Division of Infectious Disease in the Department of Medicine.

QUALIFICATIONS
Competitive candidates will have a track record of excellence in chemical biology, broadly defined, and an interest in leading the VICB and its affiliated cores in the broad mission of growing and nurturing the development and application of chemical biological approaches. The Director is also expected to lead a vibrant research program that leverages the highly collaborative environment at Vanderbilt and its numerous core and training resources to generate high-impact discoveries at the interface between molecular biosciences and human health and disease. We welcome applications from all qualified investigators, with candidates having a research interest in the problem of antimicrobial resistance especially being encouraged to apply. Significant resources will be available to the successful director to support and further develop the VICB and the Director's research program. Confidentiality will be maintained to the greatest extent possible.

APPLICATION INSTRUCTIONS
Applicants should provide a cover letter, curriculum vitae, and 2-3 page research statement that includes your commitment to inclusive excellence. All materials must be submitted through Interfolio (Director, Vanderbilt Institute for Chemical Biology). **https://apply.interfolio.com/132175**

If you have any questions or wish to schedule a call to discuss this position, email **VICB_search@vanderbilt.edu**.

Vanderbilt University is an equal opportunity employer. All qualified applicants will receive consideration for employment without regard to race, color, religion, sex, sexual orientation, gender identity, national origin, disability, or status as a protected veteran, or any other characteristic protected by law.
https://www.vanderbilt.edu/eoa/

By **Georgios Louloudis**

Finding a different path

When I hit play, I had no idea the podcast would feel so personal. The hosts shared stories of children who were intent on succeeding in one specific career and whose worlds came crashing down when they failed to live up to their own expectations. Their experiences resonated with me. After spending years being singularly focused on my goal of becoming a scientist, I made the difficult decision to quit my Ph.D. I viewed it as a devastating setback, and I wish I'd been aware then of the podcast hosts' recommendation: They said it's important for everyone to be open to multiple paths for the future and to see that they've got "alternative selves."

As a child I dreamed of becoming a stereotypical scientist—wearing a lab coat and studying brains, with "Dr." as my formal salutation. I mapped my life out: I'd study neuroscience at a top university and proceed to do a master's, a Ph.D., and a postdoc, all of which would somehow lead to a prosperous career. But it didn't go quite as planned.

During the research portion of my master's degree, I found myself putting in 8 hours of work per day with little enthusiasm. I found lab work monotonous. I wasn't ready to let go of my dream, however. I loved my courses and didn't think one disheartening project could tell me what it would be like to work as a researcher long term. So, I decided to apply to Ph.D. programs. After numerous rejections, I got accepted into a program in Zürich.

I was relieved, but I also doubted whether I was the right person for the job. I wasn't coming into the project with experience doing the kinds of experiments I would be expected to do. Still, I was hopeful that I'd learn on the job and perhaps enjoy trying something new.

Within 2 years, though, it became clear that I was failing to master the skills I needed, and I found the work no more satisfying than during my master's. My mental health deteriorated. I would lie in bed wide awake for hours. There I was, in one of the top 10 most livable cities in the world, and yet I was unhappy.

I struggled with whether to quit, influenced by the sunken cost fallacy: If I gave up, I thought it would render all the years I had devoted to academia a waste of time. But it was clear what I had to do when my psychotherapist noticed my mental and physical exhaustion. "Is this you, George?" he asked one day. After hearing those words, all of my hesitation about quitting vanished. I resigned the next day.

"I began to think I could have a career in science regardless of how I fared in the lab."

It felt liberating to finally be honest with myself about a path that wasn't meant for me. Still, by making this tough decision, I was replacing old problems with new ones. I needed to decide what to do next.

I thought about a symposium I had recently attended. A lecture on brain organoids had left me awestruck. "If only we could get the general public to feel the awe that I'm feeling," I remember thinking at the time. That got me wondering whether writing and communicating about science might be a viable profession.

I looked around and came across exceptional news features in science magazines, written by individuals without a Ph.D. I began to think I could have a career in science regardless of how I fared in the lab. Maybe all my years studying science wouldn't be a waste after all.

I signed up for a feature writing course, which confirmed my interest in writing. After that I went on to become a regular contributor at a volunteer-run science publication. I worked as an independent contractor, helping edit scientific content for clients. And I've started a master's program in public health, which I'm hoping to leverage into a career communicating about public health.

I feel as though I'm on the right path now. But I wish I'd been more open to it—and the notion of "alternative selves"—earlier in my career. Perhaps I would have felt less despair about my lack of interest in laboratory research, and struggled less with the decision to leave it. Because the reality is that there are many paths open for those interested in science. ■

George Louloudis is a master's student at University College Cork. Do you have a career story to share? Send it to SciCareerEditor@aaas.org.

ILLUSTRATION: ROBERT NEUBECKER

Pushing the Boundaries of Knowledge

As AAAS's first multidisciplinary, open access journal, *Science Advances* publishes research that reflects the selectivity of high impact, innovative research you expect from the *Science* family of journals, published in an open access format to serve a vast and growing global audience. Check out the latest findings or learn how to submit your research: **science.org/journal/sciadv**

Science Advances
AAAS

GOLD OPEN ACCESS, DIGITAL, AND FREE TO ALL READERS

BII | Prize for Science | Innovation

Bringing research to life –and science to market

Behind every life-changing solution is an entrepreneurial scientist–a creative mind who developed an idea in the lab and dared to carry it out in the world.

To encourage more scientists to translate their research, BioInnovation Institute (BII) and *Science* collaborate to host an annual award.

Up to three winners will have their essays published in *Science* magazine and will be invited into BII's entrepreneurial ecosystem. In addition, the Grand Prize winner will receive a prize of USD 25,000, and each finalist will receive USD 10,000 at a grand award ceremony in Copenhagen, Denmark.

The call for applications has just opened.

Apply before November 1, 2023

bii.dk/scienceprize

"I was offered an incredible and career-accelerating opportunity."

PhD Kaira Wagoner, Finalist 2023
Helping honey bees help themselves